



华东师范大学
EAST CHINA NORMAL UNIVERSITY



NYU
上海



SHANGHAI
纽约大学

NYU-ECNU Joint Graduate Training Programme

NYU Quantum Technology Lab

Kondappan Manikandan
PhD Thesis

Quantum non-demolition based entanglement of
cold atoms on atom chip

Supervisor: Prof. Tim Byrnes

Class of 2024 PhD Thesis for Graduate Students

Category Number: _____

Confidentiality Level: _____

ECNU University Code: 10269

NYUSH University Code: 002785

ECNU Student ID: 52180920029

NYU Student NET ID: mk6942



PhD DISSERTATION

Title: Quantum non-demolition based entanglement of cold atoms
on atom chip

Department: Physics

Category: Doctor of Philosophy

Field: Quantum Computation and Information

Supervisor: Prof. Tim Byrnes

Candidate: Kondappan Manikandan

March, 2024

Originality Statement of the Thesis from East China Normal University

Solemn Declaration: The thesis titled "Quantum non-demolition based entanglement of cold atoms on atom chip," submitted for the Doctoral degree at East China Normal University (ECNU), is a result of my own work under my supervisor's guidance. Apart from cited content, this thesis contains no other individuals' published or written research results. Significant contributions from individuals and collectives are acknowledged in the text.

Author's Signature:

Date: Year Month Day

Thesis Copyright Usage Statement of East China Normal University

This Doctoral thesis "Quantum non-demolition based entanglement of cold atoms on atom chip" was completed at East China Normal University (ECNU) under my supervisor's guidance. The research belongs to both institutions. I agree to their right to use this thesis as per their policies, including submitting it to relevant authorities and institutions, allowing library and database access, and including it in national doctoral thesis databases. It may be reproduced for academic purposes.

This thesis is categorized as (please tick):

() 1. "Internal" or "Confidential," approved by relevant departments*, declassified on
_____ Year _____ Month _____ Day.

() 2. Not confidential.

Supervisor's Signature Author's Signature Date: Year Month Day

* "Confidential" theses must be approved by the Academic Degree Evaluation Committee or Security Committee of ECNU and NYUSH, valid with the approved application form. Theses not approved as such are considered public.

华东师范大学学位论文原创性声明

郑重声明：本人提交的学位论文《量子非破坏基础上的冷原子纠缠在原子芯片上》，是在华东师范大学攻读博士学位期间，在导师的指导下进行的研究工作及取得的研究成果。除文中已经注明引用的内容外，本论文不包含其他个人已经发表或撰写过的研究成果。对本文的研究做出重要贡献的个人和集体，均已在文中作了明确说明并表示谢意。

作者签名

日期 年 月 日

华东师范大学学位论文著作权使用声明

《量子非破坏基础上的冷原子纠缠在原子芯片上》是本人在华东师范大学攻读博士学位期间在导师指导下完成的博士学位论文，本论文的研究成果归华东师范大学所有。本人同意华东师范大学根据相关规定保留和使用此学位论文，并向主管部门和相关机构如国家图书馆、中信所和“知网”（CNKI）送交学位论文的印刷版和电子版；允许学位论文进入华东师范大学图书馆及数据库被查阅、借阅；同意学校将学位论文加入全国博士、硕士学位论文共建单位数据库进行检索，将学位论文的标题和摘要汇编出版，采用影印、缩印或者其它方式合理复制学位论文。

本学位论文属于（请勾选）

1. 经华东师范大学相关部门审查核定的“内部”或“涉密”学位论文 *，于

_____ 年 _____ 月 _____ 日解密，解密后适用上述授权。

2. 不保密，适用上述授权。

导师签名

作者签名

; 日期 年 月 日

“涉密”学位论文应是已经华东师范大学学位评定委员会办公室或保密委员会审定过的学位论文（需附获批的《华东师范大学研究生申请学位论文“涉密”审批表》方为有效），未经上述部门审定的学位论文均为公开学位论文。此声明栏不填写的，默认为公开学位论文，均适用上述授权。

PhD Thesis Defense Committee Members

Name	Title	Institutions	Notes
Prof. Tim Byrnes	Professor	NYU, ECNU	Supervisor
Prof. Bing Qi	Professor	NYU	
Prof. Chandrashekhar Radakrishnan	Professor	NYU	
Prof. Zheyu Shi	Professor	ECNU	
Prof. JiaXing Wang	Professor	ECNU	
Prof. Jin-Ming Liu	Professor	ECNU	Chair

Abstract

This thesis introduces a theoretical and experimental framework for Quantum Non-Demolition (QND) measurement-induced quantum control in the Bose-Einstein Condensates (BECs) on atom chips. The core of this research involves the manipulation of ultracold atoms to form BECs at nanokelvin temperatures, performed with laser cooling and magnetic field manipulation. This framework allows for generating entangled states between distinct BEC clouds on atom chip, marking a departure from traditional single-cloud entanglement studies. First, this study presents a new experimental setup featuring a compact, high-power-efficiency optical circuit design. It accommodates five different frequency-detuned laser source generations into a significantly reduced experimental footprint. This circuit is used for generating optical source lines, enabling BEC realization and QND measurements in BECs on atom chips. The QND measurements are utilized for entanglement by creating a Mach-Zehnder interferometer on an atom chip. Second, this thesis develops a novel theory of QND measurements which allows for a simple yet powerful way of understanding the quantum states that are generated. The nonlinear nature of the QND measurement, which allows for producing interactions between systems, is explicitly derived in terms of measurement operators. We apply this theory of QND measurements to realize measurement-based imaginary time evolution. In our proposed scheme, repeated weak QND measurements are used to estimate the energy of a given Hamiltonian. Based on this estimated energy, adaptive unitary operations are applied such that only the targeted energy eigenstates are fixed points of the evolution. In this way, the system is deterministically driven towards the desired state. We show that for suitable interaction times, single-qubit QND Hamiltonians can be converted to effective multiqubit imaginary time operations. We illustrate our techniques with the example of preparing a four-qubit cluster state, which is prepared using only collective single-qubit QND measurements and single-qubit adaptive operations.

Keywords: BEC, Atom chip, Quantum Entanglement, Quantum Non-Demolition, Quantum Technology.

Acknowledgement

I would like to express my deepest appreciation to my supervisor, Prof. Tim Byrnes, whose expertise, understanding, and patience significantly contributed to my graduate experience. His guidance and financial support were invaluable in the shaping and completion of my thesis.

I appreciate Dr. Valentin Ivannikov's guidance in the lab. Interactions with him fostered a journey of self-discovery, enriched by the overlapping of our contrasting yet distinctly rich emotional bandwidths.

Special gratitude is extended to my doctor, Dr. Arif Hussain, a Chennai native. His help, particularly in providing the only good meal I had in a week in Shanghai, a place unfamiliar with vegetarianism, was a beacon of comfort.

I dedicate my PhD honor to my late mother, Suseela, who passed away on May 15th, 2023. My mom was everything to both me and my brother; she taught us how to be kind and responsible. Even though I lived several thousand kilometers apart, I used to maintain frequent communication with my mother through phone calls, virtually on a daily basis. It was her dream to see me achieve a Doctorate in Physics, and it is with her spirit in my heart that I complete this journey. Her belief in me has been a source of unwavering strength and inspiration.

I remember my father, Kondappan, who passed away during my BSc in Physics. His memory and values continue to be a constant beacon throughout my academic and personal life.

Special thanks to my only lovely brother, Vijayakumar Kondappan, for his support and encouragement. His companionship, understanding, and love have been invaluable throughout this process.

In memory of my beloved late grandparents, Ramasamy Nayakkar (Ramulu), Papathi Ammal (Rangammal), Muthu Nayakkar, and Erraai Ammal, whose wisdom and encouragement have been a guiding light in my life. The recent passing of my grandmother, Papathi Ammal, in March 2023, is a poignant reminder of the strength and resilience they

all embodied.

I am thankful to the Indira Ravindran, Sridhar Srinivasan family for their hospitality and kindness during the first four years of my PhD. Special thanks to Indira ma'am for her special care and advice on my well-being. I am also thankful to Chandra Anna (Chandrashekhar Radhakrishnan), CS prof., NYU Shanghai, for introducing me to Shanghai during my initial days in China and the dinners we shared provided a sense of familiarity in an unfamiliar environment. I remember my former supervisor late Sri.Prof.Hemaramachandran and her teachings at this very momentous time.

I'd like to thank my colleagues Shuai Gao, Jingyan, Manish Chaudhary, and the kindest postdoctoral fellow Ebubechukwu Ilo-Okeke, as well as my sweet lab mates, Yuping and Ping.

I extend my thanks to my cousin, Ravikumar Chinnarasu, a fellow experimental quantum physicist, Kumar Anna, Jayaprakash Pothan, another cousin of mine who is a quantum machine learning physicist, and my childhood friend, the mathematician Samivel Chidambaram, as well as my uncles and cousin sisters in Rasipuram, Tamil Nadu, for their camaraderie and support. Additionally, I am also thankful for the enduring friendship from Chen LiShan (陈利山), Chen SiBei, Pei QuTing and extending my thanks to my lovable friend 邢玉婷 (Xing YuTing aka Anita) for her kindness and support during my end days in China. I am equally grateful to my friend Max (杨晓军), a businessman and chemist.

Special appreciation goes to my dear friends Shalini M.G and Phebe Kokila. Since meeting them as colleagues during my Master's, they have stood by me through thick and thin. Their constant support, encouragement, and love have been a pillar of strength, especially during the more challenging periods of my journey.

Finally, but certainly not least, my gratitude goes to all those who have been involved in the successful completion of this thesis, including friends, colleagues, and the NYU Shanghai- ECNU academic community at large. Your support has been a vital part of my journey.

Contents

Abstract	iv
Acknowledgement	v
List of figures	xviii
List of tables	xix
Publications of the author during the PhD studies	xx
List of main symbols	xxii
1 Introduction	1
1.1 Ultracold atoms	1
1.2 Quantum computing	3
1.3 Quantum computing models and strategies	5
1.4 Cold atom quantum computing	8
1.5 Topics of this thesis	11
Organisation of the thesis structure	14
2 Introduction to cold atom physics	15
2.1 Introduction to Bose-Einstein Condensates (BEC)	15
2.2 Introduction to laser cooling	16
2.3 Three-dimensional cooling and sub-doppler techniques	19
2.4 Introduction to atom chip physics	21
2.4.1 Working principles of atom chips	21
2.5 Progress with BEC atom chip combination and quantum entanglement	27

3	Quantum information with atomic ensembles control	29
3.1	Introduction to spatial entanglement and EPR steering in BECs	29
3.2	Entanglement of macroscopic objects	30
3.3	Spatial entanglement and EPR steering in BECs	32
3.4	Quantum entanglement in spatially separated atomic modes	35
3.4.1	Analysis and implications.....	35
3.5	Spatial distribution of entanglement in atomic clouds.....	36
3.6	Advantages of our BEC qubits entanglement approach	38
4	Atom chip and experimental apparatuses design evolution	40
4.1	Global schema of the experimental setup	40
4.2	Our atom chip's specific design elements	42
4.2.1	Atom chip installation	46
4.2.2	Rb dispensers installations and operational parameters	48
4.3	AOM drivers.....	50
4.3.1	RF synthesizers	50
4.3.2	Amplifier and filters for DDS AD9958 and AD9959	50
4.3.3	Characterization of the amplifier NWDZ RF-PA V2.0	51
4.4	Experimental apparatus	53
4.4.1	Vacuum chamber and bake-out procedures	53
4.4.2	Anti-Helmholtz (quadrupole) coils design	55
4.4.3	Helmholtz coils design.....	57
4.5	Main experimental scheme	60
4.5.1	BEC preparation on atom chip	60
4.6	Complete setup	61
4.6.1	Experimental geometry	61
4.6.2	Preparation of atoms in the atom chip	63
4.6.3	Vacuum recovery and optimization.....	64
4.6.4	BEC formation process	64
4.6.5	Advanced cooling techniques	64
4.6.6	Imaging the atoms	64

4.6.7	Expected BEC production stages.....	65
4.6.8	BEC-BEC entanglement and QND measurements on atom chip.....	66
4.7	Entanglement scheme and measurement design on BECs in the systems....	68
4.8	Future experimental design trajectory	71
5	Optical circuit scheme and development	73
5.1	Required optical sources for ultracold atom preparation	73
5.2	Optical system	74
5.2.1	Overall optical scheme	74
5.2.2	Optical source generation	76
5.3	Circuit characterization	79
5.3.1	Lasers and frequency locking.....	79
5.3.2	Detuning ranges of the AOMs	80
5.3.3	Beam profile and power loss.....	82
5.3.4	Optical circuit power efficiencies with fiber coupling	82
5.3.5	Optimization of fiber coupling	83
5.4	QND implementation inside vacuum chamber.....	84
5.4.1	Entanglement generation complexities in experimental setup	84
5.4.2	Summary and conclusions	88
6	QND background theory	90
6.1	Introduction to entangled states in BECs	90
6.2	Experimental design for BEC entanglement generation	91
6.2.1	Setup and Hamiltonian	91
6.2.2	State preparation and measurement.....	91
6.3	Analysis of short-time interaction dynamics	95
6.3.1	Analytic approximation for $n_d = 0$	95
6.3.2	Analytic approximation of photon probability	96
6.3.3	Analytic approximation for states with $n_d > 0$	96
6.3.4	Characteristics of the approximate state	97
6.4	Spin squeezed states.....	101
6.4.1	Random vs. correlated spin states.....	101

6.4.2	Quantitative description	103
6.5	Two-axis two-spin squeezed spin states	104
6.6	The two-axis two-spin squeezed state	105
6.7	Violation of Bell Inequality in 2A2S squeezed states	108
6.7.1	Bell-CHSH inequality	108
6.7.2	Results	109
7	Introduction to quantum non-demolition measurements and imaginary time evolution	110
7.1	Outline and basic idea of this section	111
7.2	Generalized quantum nondemolition measurements	113
7.2.1	Wavefunction evolution	113
7.2.2	QND measurement operators	116
7.3	Imaginary time evolution	118
7.3.1	Ancilla qubit based measurement operators.....	118
7.3.2	QND based imaginary time evolution.....	120
7.4	QND measurement induced effective interactions	122
7.4.1	Short interaction time regime	123
7.4.2	Long interaction time regime.....	124
7.5	Example: Generation of a four qubit cluster state	126
7.5.1	Stabilizer Hamiltonian	127
7.5.2	Measurement and correction operators	127
7.5.3	Numerical evolution	131
7.6	Summary on QND measurements analysis	132
8	Conclusion	135
Bibliography		138
Appendix		164
Funding and Acknowledgments		164

Appendix A: Saturated absorption spectroscopy and laser locking	165
0.1 Saturated absorption spectroscopy and laser locking	165
Appendix B: Control electronics	169
0.2 The Mini-Circuits switch ZASWA-2-50DRA+.....	169
0.3 The control circuit	170
0.4 Shutter drivers	171
0.5 Automation and reverse engineering element	173
0.6 Control VI scheme	175
Appendix : Foundational equations and their context from our works [1–3]	179
0.7 Referenced equations	179
International Conferences	182

List of figures

Figure 1-1 Superconducting Qubit Technology for Quantum Computing. Credits : IBM	6
Figure 1-2 This figure illustrates advanced quantum state manipulation techniques, showcasing Fig (a) Spatial splitting of spin-squeezed BEC from Pezzè et al, Rev Mod Phys 90, 035005 (2018), (b) Chip ion trap for quantum computing from 2011 at NIST.....	10
Figure 2-1 Bose-Einstein Condensates(BEC), Image credit JILA	16
Figure 2-2 Schematic representation of the laser cooling process: in Fig (a) A photon with momentum $\hbar k$ is absorbed by a ^{87}Rb atom, causing the atom to move in the opposite direction due to conservation of momentum. In Fig (b) The atom is in an excited state after absorbing the photon, having a momentum of $m\mathbf{v} - \hbar k$. In Fig (c) Spontaneous emission occurs in random directions, resulting in a net recoil momentum that averages to zero in all directions except along the atom's initial movement. Continuous absorption and re-emission of photons in the direction of motion lead to a gradual reduction in the atom's velocity, effectively cooling it down as the kinetic energy decreases.....	19

Figure 2-3 Fig (a) is an illustration of a magneto-optical trap (MOT) for an atom with a $J = 0 \rightarrow J = 1$ transition. The laser frequency ω is red-detuned by δ against the atomic resonance ω_0 . The Zeeman shifts, which are exaggerated for clarity, contribute to a restoring force that drives the atom towards the zero-point of the magnetic field. This force, combined with Doppler cooling, effectively traps and cools the atoms within the MOT. Fig (b) is a schematic representation of a three-dimensional magneto-optical trap (MOT) configuration. The MOT employs a pair of anti-Helmholtz coils to generate a magnetic field gradient necessary for spatial confinement of atoms. The coils carry currents I in opposite directions, creating a quadrupole magnetic field. Circularly-polarized laser beams with σ^+ and σ^- polarizations intersect at the center of the trap, where the field gradient is zero (indicated by the red dot of trapped MOT atoms), to provide the optical cooling and trapping forces..... 20

Figure 2-4 Atom chip design by Böhi et al. Nature Phys. 5, 592 (2009). 22

Figure 2-5 A concise illustration of a wire-based magnetic trap that yields planar confinement is presented. Panel (a) demonstrates that a homogeneous bias field, superimposed with the magnetic field emanating radially from a linear conductor, culminates in a planar quadrupole configuration perpendicular to the conductor's axis. The left column depicts the magnetic flux contours, whereas the right column reveals the variation in magnetic field intensity $B(z)$ along the $y = 0$ plane, computed for a current $I = 2$ A through the wire and a bias field $B_b = 40$ G. This representation is adapted from [4, 5]. In panel (b), a lithographic technique is employed to construct a wire on the atom chip, which in turn forms a magnetic waveguide. This guide suspends neutral atoms at an established standoff distance z_0 from the wire, offering a conduit for controlled atomic transit..... 23

Figure 2-6 Presents two configurations of magnetic traps used for atom confinement in three-dimensional space: (a) displays a Quadrupole "U"-shaped trap, and (b) shows an Ioffe-Pritchard "Z"-shaped trap. The illustrations on the left detail the wire arrangements for both traps, emphasizing their distinct geometrical structures, with the bias magnetic field orientation indicated for clarity. The Quadrupole "U" design and the Ioffe-Pritchard "Z" design each create unique magnetic environments that are conducive to confining neutral atoms. These environments are generated through precise current flows and the application of an external bias magnetic field. The specific field strengths represented by dashed and solid lines correspond to bias fields of 54 G and 162 G, respectively. This figure is an adaptation from source [4,5], highlighting the practical realization of magnetic trapping through wire layout and magnetic field application. 26

Figure 3-1 Shows an experimental setup for the entanglement of two macroscopic cesium gas samples. The setup features two glass cells placed within a homogenous magnetic field (B -field) with the mean spin values (J_{x1} and J_{x2}) oriented along and against the x-axis, respectively. Optical pumping is performed using circularly polarized light (σ_+ and σ_-), creating coherent spin states in each cell. A linearly polarized probe light (entangling and verifying beams) detuned by 700 MHz interacts with the atomic samples, inducing a Faraday effect observable as a rotation of the probe's polarization $\mathbf{S}_{\text{out}}^y$. This interaction is used for non-demolition measurements of the collective spin, facilitating entanglement and subsequent verification. The time sequence below the setup indicates the duration of optical pumping, entangling, and verifying pulses with a 0.5 ms interval between entanglement and verification. Julsgaard, Polzik, et al. Nature 413, 400 (2001) 31

Figure 3-2 Shows an experimental sequence for spin-squeezed state creation and measurement in a Bose-Einstein condensate using an atom chip. (1) A BEC is confined in a trap and a squeezing operation is applied. (2) The trap is released, and under the influence of gravity, the BEC undergoes time-of-flight expansion. (3) A microwave field prepares the atomic spin state, followed by a Rabi pulse to select the spin component for measurement. The spatially resolved detection is performed using a camera, capturing the distribution of spin orientations within the expanded BEC cloud. Time of flight in Fadel et al., Science 360, 409–413 (2018)	34
Figure 3-3 Shows a single-shot absorption images showing atomic density distributions in a spin-squeezed Bose-Einstein condensate. The left panel represents the number of atoms in state $ 2\rangle$, while the right panel corresponds to atoms in state $ 1\rangle$. Regions A and B are delineated by dashed lines, with a gap of $1.3 \mu\text{m}$, indicating the spatial separation of the atomic densities. The color gradient quantifies the atom count per pixel, with warmer colors representing higher densities, thereby visualizing the spin correlations between the separated regions A and B. BEC splitting in Fadel et al., Science 360, 409–413 (2018)	34
Figure 3-4 Creation of multiparticle entanglement ensemble by naturally dividing the trapping potentials into two thus divided two clouds (red and blue) in Lange et al., Science 360, 416–418 (2018)	36
Figure 3-5 EPR steering between spin degree of freedoms in a tightly trapped BEC by local spin-mixing interactions, which evinces the presence of bipartite and multipartite entanglement in Kunkel et al., Science 360, 413–416 (2018)	37
Figure 4-1 Global view of the experimental schema	41
Figure 4-2 Fig (a) show the schematic design of multi-traps version of our atom chip depicting only the core specifics of U and Z wires of the chip. Fig (b) shows the 3D version of schematic design	42

Figure 4-3 a) Z trap is being dissected into a part made up of 3 pieces of wire each of length L, Width is 0.3mm and Height is 0.3 mm as it's wire dimensions., b) Standard Z-wire: B_{yz} field in y-z plane for current $I = 2 \text{ A}$, bias field $B_{bias} = 0.0002\text{T}$ and length $L = 0.002\text{m}$ in x,y and z diminutions with measured in meters. c) Standard Z-wire: Magnitude of $|B|$ field in 3D view d) Standard Z-wire: Magnitude of $|B|$ field slices 44

Figure 4-4 The atom chip installation process. (a) Bottom view of the atom chip installed inside the vacuum chamber. (b) Side view of the atom chip. (c) Shows the chamber design along with the chip install view through the bottom view port of the chamber, designed atom chip and chip holder being assembled together. This assembly seals the bottom of the vacuum chamber, and following the successful assembly of the chip, wire connections, and connector insulators, it will be mounted on top of the vacuum chamber. 47

Figure 4-5 U- and Z-wire connections scheme with TDM implementation 48

Figure 4-6 Evaluation board featuring the Analog Devices AD9958 multi channel Direct Digital Frequency Synthesizer IC. The AD9958 incorporates two synchronous DDS cores with many user-programmable functions. Evaluation board software provides a graphical user interface for easy communication with the DDS device along with many user-friendly features and in the right side of the figure RF amplifier NWDZ RF-PA which is employed in the scheme of AOM driver circuits developed to drive the AOMs in the optics blocks 52

Figure 4-7 Home made design of our experiments' AOM drivers scheme. This Unit is being designed to drive one 350Mhz AOM and three 200MHz AOMs 52

Figure 4-8 Home made design of our experiments' AOM drivers scheme. This Unit is being designed to drive one 80Mhz AOM and three 100MHz AOMs 54

Figure 4-9 3D design of our experimental setup, showing quadrupole coils in brown. The protruding cylindrical copper bar on the upper flange of the vacuum chamber is part of the cooling system for the atom chip, mounted on the bottom edge of the copper holder. The quadrupole-field gradient $ \mathbf{B} $ is shown along the y-axis in units of G/m, calculated against the coil separation distance along the x-axis.....	54
Figure 4-10 Field gradient of the quadrupole (Anti-Helmholtz) coil. The plot was generated with the following parameters per coil: current of 20A, number of turns $n = 600$, and effective outer radius $R = 9\text{cm}$ (inner radius $R = 7\text{cm}$, outer radius $R = 10.3\text{cm}$). The operating point is marked as a black dot. $ \mathbf{B} $ is shown.....	56
Figure 4-11 Magnetic field potential $ \mathbf{B} $ of the quadrupole trap.....	56
Figure 4-12 Fig. (a) Helmholtz coil design alongside the vacuum chamber. The coil alignment ensures the Helmholtz field is directed across the face of the chip. Given the radius of the Helmholtz coils is much larger than the length of the chip, the coils are intentionally tilted at an 8° angle with respect to the y-axis to match the cigar rotation of the z-wire in the atom chip ($\arcsin(1/7) = 8^\circ$). The on-axis approximation for the magnetic field of a wire coil is justified in this configuration. Fig. (b) shows the assembly design of the 3 pairs of correction coils	58
Figure 4-13 The Helmholtz coil design progress steps.....	59
Figure 4-14 The designed Helmholtz coil steps being mounted around the vacuum chamber design	59
Figure 4-15 Magnetic field potential $ \mathbf{B} $ of the Helmholtz coil.....	60
Figure 4-16 A basic timeline diagram for a BEC-BEC entanglement generation experiment, outlining the four stages: i) Cooling and trapping, ii) Vacuum recovery, iii) Transfer of atoms to a strong-field trap, and iv) BEC hold [6].	62

Figure 4-17 Fig.(a) is illustration of the chip and flying beams on top with their appropriate dimensions. Red and blue solid lines are schematically depicted with the atom chip representing mixed MOT and RP beams except the horizontal blue beam will be approaching the chip from the bottom, the z-branch of MOT and RP beams. Fig.(b) is the illustration of the bottom view of chip with the flying beams orientation 62

Figure 4-18 shows the configuration scheme for establishing QND effective interactions in an experimental setting. The beamsplitter BS_1 divides coherent light into two modes, top and bottom. Through the QND Hamiltonian, each mode interacts with BEC qubits 1(3rd positioned from left to right) and 2 (4rd positioned from left to right) on their path to BS_1 and mirror, resulting in interfered modes both being projected in parallel towards the lens followed by the camera [3, 7]. Thus the setup configuration would aim for BEC-BEC entanglement of 2 BEC targets with MZI setup 67

Figure 4-19 BEC-BEC entanglement generation on the chip. The 2- BEC qubits entangled $|00\rangle + |11\rangle$ states produced by two consecutive pulses of ENT beam. The blue mirrors in the MZI setup near the BECs are metal mirrors in the setup and the rest of the mirrors are dielectric mirrors. The wires connecting U and Z wire are not depicted in the picture. 70

Figure 5-1 ^{87}Rb energy level diagram and required laser lines. Zeeman sublevels show a linear splitting in a weak magnetic field. M Kondappan, V Ivannikov, T Byrnes, Rev Sci Instrum 95, 1 (2024) 74

Figure 5-2 Compactified optical source generation for ultracold atoms. The five outputs (highlighted in pink) are generated from two input laser sources (top right) from the Schafter+Kirchhoff collimators. The outputs are labelled as MOT + RP, OP + RP, ENT, PGC + RP, and IMG + RP. Output generations are fiber-coupled, and fiber output fixtures are integrated within the circuit. There are lens sets involved in the circuit, with a corresponding lens acting as a beam focal point for AOMs and shutters. The beams are naturally focused and re-collimated with a lens to have focal spots of around one mm to be matched in the AOM and shutter transmission apertures. The three circular spots depict vertically polarized light and three parallel lines show horizontally polarized light in the diagram.

M Kondappan, V Ivannikov, T Byrnes, Rev Sci Instrum 95, 1 (2024) 75

Figure 5-3 Our innovative optical circuit is being built on Viewport table for compactified optical sources generation. The outputs are generated from two input laser sources (top right) from the Schafter+Kirchhoff collimators. The outputs are labelled as shown are being fiber-coupled, and fiber output fixtures are integrated within the circuit. 77

Figure 5-4 Detuning ranges of AOMs and their working positions shown for various optical sources. Four different scales are being used in the plot. The bottom horizontal axis is the frequency for detuning ranges in MHz. The right side vertical axis shows the AOM combined work positions and colored bars as work position ranges as a function of the colored horizontal scale inside the plot. The left vertical scale gives the normalized amplitudes of detuning ranges. The detuning range maximum and minimum of the Gaussian curve shows the AOM transmission amplitude resulting from the combined detuning range. The ENT detuning range is shown here as $\Delta_{\text{ENT}} = +350$ MHz as a simplified representation of $\Delta_{\text{ENT}} = -18$ to $+682$ MHz. The colored numbers inside the plot represent the actual work done by the AOMs from their respective work positions. M Kondappan, V Ivannikov, T Byrnes, Rev Sci Instrum 95, 1 (2024) 81

Figure 5-5 Measured cooling MOT beam diameter as a function of displacement from the beam waist. Dots show data points and solid lines show a fit to a diffraction limited spot size calculation for Gaussian and homogeneous profile beams (Airy model). This beam profile of our MOT beam is characterized by a lens of f number of 0.510102, numerical Aperture (NA) 0.7 for the waist size measurements along the focal point axis and fitting data to M^2 Gaussian model, 20cm focal length lens used for the wavelength $\lambda = 780$ nm. M Kondappan, V Ivannikov, T Byrnes, Rev Sci Instrum 95, 1 (2024) 83

Figure 5-6 Development of full optical setup and entanglement circuit integration 85

Figure 6-1 Illustration of the experimental setup for generating two-spin squeezed states in two BECs. Coherent light enters a beam splitter, interacts with each BEC, and is then measured in modes c and d at Juan E Aristizabal-Zuluaga, M Kondappan, T Byrnes, et al. J. Phys. B 54 105502 (2021) 92

Figure 6-2 The function $C_{n_c n_d}(\chi)$ defined in (0-3) for (a) $\chi = 0.1$; (b) $\chi = \pi/4$; (c) $\chi = \pi/2$; (d) $\chi = 5\pi/4$. All plots use $\alpha = 5$. The dashed line indicates the line $n_c + n_d = |\alpha|^2$, the dominant region where the coefficients have the largest magnitude. at Juan E Aristizabal-Zuluaga, M Kondappan, T Byrnes, et al. J. Phys. B 54 105502 (2021) 97

Figure 6-3 Photon probability distribution. (a) Approximate probability distribution (6-15) for the interaction times as marked. (b)(c)(d) Exact probability distribution (0-10) for (b) $\tau = 0.1$; (c) $\tau = 0.23$; (d) $\tau = \pi/4$. All plots use parameters $N = 20$, $\alpha = 5$. The dashed line indicates the line $n_c + n_d = |\alpha|^2$, the dominant region where the coefficients have the largest magnitude. (Juan E Aristizabal-Zuluaga, M Kondappan, T Byrnes, et al. J. Phys. B 54 105502 (2021)) 98

Figure 6-4 (a)(b)(c) Probability distribution for measurements of the state $|\psi_{n_c}^{\text{approx}}(\tau)\rangle$ given in (0-2) for $N = 20$, $n_c = 20$, $\tau = 0.23$, $\alpha = \sqrt{20}$. (d)(e)(f) Probability distribution for measurements of the state (0-9) using the approximation (6-16) for $N = 20$, $n_c = 18$, $n_d = 2$, $\tau = 0.23$, $\alpha = \sqrt{20}$. (g)(h)(i) the 2A2S state given in (6-21) for $N = 20$, $\tau = 2/N$. Measurements are made in the eigenstates of the (a)(d)(g) S^x ; (b)(e)(h) S^y ; (c)(f)(i) S^z operators. (Juan E Aristizabal-Zuluaga, M Kondappan, T Byrnes, et al. J. Phys. B 54 105502 (2021)) 99

Figure 6-5 Entanglement produced between two BECs using the optical protocol. The von Neumann entropy for (a) the approximate state (0-2) for $N = 20$; (b) the exact state (0-9) for parameters $N = 20$, $n_c = 20$, $n_d = 0$, $\alpha = \sqrt{20}$ and the two-pulse state at [3] for parameters $N = 50$, $n_c^{(1)} = n_c^{(2)} = 50$, $n_d^{(1)} = n_d^{(2)} = 0$, $\tau^{(1)} = 0.1$, $\tau^{(1)} = \tau$, and $\alpha = \sqrt{50}$ as plotted in the figure. (Juan E Aristizabal-Zuluaga, M Kondappan, T Byrnes, et al. J. Phys. B 54 105502 (2021)) 102

Figure 6-6 Shows the squeezing in spin systems and coherent states, (a) is from Wikipedia: Coherent states and (b*) is spin squeezing from Kitagawa et al., PRA 47, 5138 (1993) 102

Figure 6-7 Variances of EPR-like observables in the two-axis two-spin squeezed state. The variances of the (a)(b) squeezed variables $\tilde{S}_1^x + \tilde{S}_2^x$ and $\tilde{S}_1^y - \tilde{S}_2^y$. (J Kitzinger, M Kondappan, T Byrnes et al. PRR, 2, 033504 (2020)) 108

Figure 6-8 Fig. **a** is the entanglement of the two-axis two-spin squeezed state, as measured by the von Neumann entropy E normalized to the maximum value $E_{\max} = \log_2(N + 1)$, as a function of the interaction time τ . The number of atoms in each BEC is $N = 10$. Fig. **b** is Optimized violation of the Bell-CHSH inequality $C - 2$ as a function of $\frac{1}{N}$ for the 2A2S squeezed state. Dots show the numerically calculated values and the solid line is the linear fit. (J Kitzinger, M Kondappan, T Byrnes et al. PRR, 2, 033504 (2020)) 109

Figure 7-1 Experimental setup for performing a QND measurement. (a) Coherent light $|\alpha\rangle$ is divided into two modes a, b at beamsplitter B_1 . In this generalized scheme of QND of an arbitrary system, the interaction is only through mode a which interacts with qubit via the QND Hamiltonian as depicted in the figure which is an atom cloud in this case (7-5). The modes are then interfered at beamsplitter B_2 that are detected using photon counters with outcomes n_c and n_d respectively. While we show the Mach-Zehnder configuration for conceptual simplicity, any equivalent configuration can also be implemented to realize the QND measurement.

M Kondappan, T Byrnes, et al, Phys Rev A 107, 042616 (2023) 114

Figure 7-2 Approximating functions to the function $C_{n_c n_d}(\chi)$. The two approximate expressions (7-20) and (7-23) which we call “approx 1” and “approx 2” respectively, are shown for the measurement outcomes (a) $n_c = 25, n_d = 0$; (b) $n_c = 20, n_d = 5$; (c) $n_c = 13, n_d = 12$; (d) $n_c = 0, n_d = 25$. The dotted line is the exact function (7-11) for comparison. We use $\alpha = 5$ for all plots. $C_{n_c n_d}$ and χ are dimensionless. M Kondappan, T Byrnes, et al, Phys Rev A 107, 042616 (2023) 119

Figure 7-3 Effects of short and long interaction times for QND measurements.

The C -function is plotted for different measurement outcomes as marked in the context of the energy levels τE_n marked by the dashed vertical lines. The energy levels are those given by (7-46) with $N = 3$ with the offset (7-41). The interaction times are chosen as (a) $\tau = \pi/12$; (b) $\tau = \pi/4$. The parameters for (a) satisfy the short time regime as $0 \leq \tau E_n \leq \pi/2$, while for (b) the interaction times are in the long time regime. We use $\alpha = 10$ for all calculations. $C_{n_c n_d}$ and χ are dimensionless. M Kondappan, T Byrnes, et al, Phys Rev A 107, 042616 (2023) 126

Figure 7-4 Preparing a four qubit cluster state with imaginary time evolution. (a)-(d) show fidelities as defined in (7-72) and (7-73) as marked. (e)-(h) show the energy estimates (7-37) based on the cumulative measurement outcomes (7-40). The procedure starts from a random initial state and applies the imaginary time evolution corresponding to (a)(e) $e^{\sigma_1^z \sigma_2^z \tilde{t}}$, (b)(f) $e^{\sigma_3^x \sigma_4^x \tilde{t}}$, (c)(g) $e^{\sigma_1^x \sigma_2^x \sigma_3^x \tilde{t}}$, (d)(h) $e^{\sigma_2^z \sigma_3^z \sigma_4^z \tilde{t}}$ in sequence. We use parameters $\alpha = 1$, $\delta_{tgt} = 0.5$ throughout. Numerically we impose a photonic cutoff of 5 photons. Here, the fidelities F and energy E are dimensionless. t is a dimensionless time step parameter (the same as that appearing in Sec. 7.3.2). M Kondappan, T Byrnes, et al, Phys Rev A 107, 042616 (2023) 134

Figure 0-1 SAS scheme used in our experimental setup. A similar configuration is being employed for both the primary and secondary laser to achieve frequency locking. The sub-kHz linewidth diode laser is locked to the cycle transitions $5^2S_{1/2}(F_g = 2) \rightarrow 5^2P_{3/2}(F_e = 3)$ for the cooling cycle. However, it is locked at a detuned wavelength -18 MHz and $5^2S_{1/2}(F_g = 1) \rightarrow 5^2P_{3/2}(F_e = 2)$ is being locked at the exact transition for repumping laser. Of the primary laser's output power, ~ 70 mW is used in the SAS circuit and 1 mW is utilized for repumping locking after the completion of the circuit and utilizing the laser in production mode. 167

Figure 0-2 Frequency locking of the primary laser. The output of this circuit is sent to the optical circuit of Fig. 5-3. The sub-kHz linewidth diode laser is locked to the cycle transition $5^2S_{1/2}(F_g = 2) \rightarrow 5^2P_{3/2}(F_e = 3)$ with a high polarization resonance. It runs at a detuning of 18 MHz, with a few milliwatts of power being used in this setup branch. The output power of the laser is being maintained at ~ 1.812 W. The frequency scanning range is 7 GHz. 168

Figure 0-3 The Mini-Circuits switch ZASWA-2-50DRA+ 170

Figure 0-4 Generalized driver control circuit 171

Figure 0-5 UF3SC120009K4S from UnitedSic 172

Figure 0-6 Shows the components of finger bot, (a) is dismantled finger bot and (b) is finger bot's MOSFET	174
Figure 0-7 LEM transducer	175
Figure 0-8 LabVIEW control buttons in the main control program's front(vi) page.....	178

List of tables

Table 0-1 Selected fundamental constants and properties of ^{87}Rb from [8] if no other source is specified.	xxii
Table 0-2 Selected properties of ^{87}Rb from [8]	xxii
Table 4-1 Operational parameters for Rb dispenser	49
Table 4-2 Test Results for NWDZ RF-PA V2.0 Amplifier.....	51
Table 4-3 Experimental target steps for ^{87}Rb BEC formation and transferring to atom chip.	66
Table 5-1 Relationship between the component numbers (COMP) in Fig. 5-3 for the primary and secondary lasers and the five outputs of the optical circuit. The labeled components send portions of the input light to different outputs, being processed suitably along the way.	78
Table 5-2 Table shows the efficiencies of fiber coupled outputs	82

Publications of the author during the PhD studies

During this thesis I have been an author and co-author of the following works:

1. M. Kondappan, V. Ivannikov, and T. Byrnes. Optical circuit compactification for ultracold atoms, *Review of Scientific Instruments*, 2024, AIP Publishing, 95(1).
2. M. Kondappan, M. Chaudhary, E. O. Ilo-Okeke, V. Ivannikov, and T. Byrnes. Imaginary-time evolution with quantum nondemolition measurements: Multiqubit interactions via measurement nonlinearities, *Physical Review A*, 2023, American Physical Society, 107(4), 042616.
3. E. O. Ilo-Okeke, M. Kondappan, P. Chen, Y. Mao, V. Ivannikov, and T. Byrnes. Hybrid approximation approach to the generation of atomic squeezing with quantum nondemolition measurements, *Physical Review A*, 2023, American Physical Society, 107(5), 052604.
4. J. Kitzinger, M. Chaudhary, M. Kondappan, V. Ivannikov, and T. Byrnes. Two-axis two-spin squeezed states, *Physical Review Research*, 2020, APS, 2(3), 033504.
5. Y. Mao, M. Chaudhary, M. Kondappan, J. Shi, E. O. Ilo-Okeke, V. Ivannikov, and T. Byrnes. Measurement-based deterministic imaginary time evolution, *Physical Review Letters*, 2023, American Physical Society, 131(11), 110602.
6. M. Chaudhary, Y. Mao, M. Kondappan, A. S. P. Paz, V. Ivannikov, and T. Byrnes. Stroboscopic quantum nondemolition measurements for enhanced entanglement generation between atomic ensembles, *Physical Review A*, 2022, American Physical Society, 105(2), 022443.
7. J. E. Aristizabal-Zuluaga, I. Skobleva, L. Richter, Y. Ji, Y. Mao, M. Kondappan, V. Ivannikov, and T. Byrnes. Quantum nondemolition measurement based generation

- of entangled states in two Bose–Einstein condensates, *Journal of Physics B: Atomic, Molecular and Optical Physics*, 2021, IOP Publishing, 54(10), 105502.
8. S. Mandal, M. Narozniak, C. Radhakrishnan, M. Kondappan, Z. Jiao, X. Jin, and T. Byrnes. An observable based approach to evaluating quantum coherence, *AIP Conference Proceedings*, 2020, AIP Publishing, 2241(1).
 9. J. E. Aristizabal Zuluaga, I. Skobleva, L. Richter, Y. Ji, Y. Mao, M. Kondappan, and V. Ivannikov. Generating two-spin squeezed states of separated Bose-Einstein condensates, 2020, Grupo de Física Atómica y Molecular.
 10. E. O. Ilo-Okeke, Y. Ji, P. Chen, Y. Mao, M. Kondappan, V. Ivannikov, Y. Xiao, and T. Byrnes. Deterministic preparation of supersinglets with collective spin projections, *Physical Review A*, 2022, American Physical Society, 106(3), 033314.
 11. G. Shuai, M. Prest, E. O. Ilo-Okeke, M. Kondappan, J. E. Aristizabal-Zuluaga, V. Ivannikov, and T. Byrnes. Optically mediated entanglement between Bose-Einstein condensates, *Journal of East China Normal University (Natural Science)*, 2022(2), 93.
 12. G. Shuai, E. O. Ilo-Okeke, Y. Mao, M. Kondappan, J. E. Aristizabal-Zuluaga, V. Ivannikov, and T. Byrnes. Decoherence effects in quantum nondemolition measurement induced entanglement between Bose–Einstein condensates, *Journal of Physics B: Atomic, Molecular and Optical Physics*, 2022, IOP Publishing, 55(19), 195501.

List of main symbols

Table 0-1 Selected fundamental constants and properties of ^{87}Rb from [8] if no other source is specified.

Constant/Property	Symbol	Value
Planck's constant	h	$6.626 \times 10^{-34} \text{ J s}$
Reduced Planck's constant	$\hbar = \frac{h}{2\pi}$	$1.054 \times 10^{-34} \text{ J s}$
Bohr magneton	μ_B	$9.274 \times 10^{-24} \text{ J/T}$
Speed of light	c	$2.998 \times 10^8 \text{ m/s}$
Permeability of vacuum	μ_0	$4\pi \times 10^{-7} \text{ N/A}^2$
Permittivity of vacuum	ϵ_0	$8.854 \times 10^{-12} \text{ F/m}$
Bohr radius	a_0	$0.529 \times 10^{-10} \text{ m}$

Table 0-2 Selected properties of ^{87}Rb from [8]

Property	Symbol	Value
Atomic mass	m	$1.443 \times 10^{-25} \text{ kg}$
Nuclear spin	I	$3/2$
Natural abundance		27.83%
D2 transition wavelength (vacuum)	λ	780.241 nm
Natural line width	Γ	6.065 MHz
Saturation intensity	I_s	1.669 mW/cm^2
Hyperfine structure constant	A_{hfs}	3.417 GHz
Zero-field hyperfine splitting	E_{hfs}	6.835 GHz
Electron spin g-factor	g_J	2.002
Nuclear spin g-factor	g_I	-0.000995
Static polarizability	α_0	$0.0794 \text{ Hz}/(\text{V/cm})^2$
S-wave scattering length $ 1, -1\rangle - 1, -1\rangle$	a_{00}	$100.40 a_0$
S-wave scattering length $ 2, 1\rangle - 1, -1\rangle$	a_{10}	$97.66 a_0$
S-wave scattering length $ 2, 1\rangle - 2, 1\rangle$	a_{11}	$95.00 a_0$

1 Introduction

1.1 Ultracold atoms

The exploration of the physics of ultracold atoms has ushered in a new era of technology, where atoms can be manipulated at the quantum level. Such atoms, using techniques such as laser cooling [9–14], are cooled to nanokelvin temperatures and below, where quantum mechanics is the dominant mechanism explaining the properties of the many-body system. These form the foundation for quantum experiments with applications to quantum technology [15]. Engineered quantum systems can be used to enhance measurement accuracy beyond the standard quantum limit [16, 17], imitate other quantum systems and controlling their fundamental parameters [18–22], and be even used as a platform for quantum computation [23–25]. For such applications, one of the starting points is to form a Bose-Einstein condensate (BEC), which forms at sufficiently low temperatures such that quantum degeneracy of bosonic particles occurs [26–28].

Atom optics field can be traced back to the advancements in laser cooling techniques during the 1980s. This pioneering development paved the way for exploring the wave-like behavior of matter at ultralow temperatures. The foundational work in this field, leading to the realization of atom-optical elements analogous to those in classical light optics, was recognized with the award of the 2001 Nobel Prize in Physics [27, 29]. Central to these developments has been the use of inhomogeneous magnetic fields to manipulate and confine laser-cooled atom clouds. The integration of magnetic traps with evaporative cooling techniques was a breakthrough, allowing the achievement of temperatures where atoms undergo a phase transition to form a Bose-Einstein condensate (BEC). In this phase, a significant number of atoms share the same quantum state, offering a new state of matter for study. Since then, the field has seen a continuous diversification, with a variety of atomic and molecular species being cooled to quantum degeneracy. Efforts

have also been directed toward refining the apparatus and techniques for creating and investigating BECs in more complex and exotic potentials [22, 25, 30, 31].

In 1995, the concept of the ‘atom chip’ was proposed, drawing inspiration from the success of microelectronics in miniaturization [32–34]. These chips use the large magnetic field gradients near current-carrying wires to confine ultracold atom clouds within $100\ \mu\text{m}$ of a micro-fabricated conductor surface, thus providing a compact, robust, and efficient platform for creating BECs. The proximity of the atoms to the field sources on these chips allows for the creation of intricate, micron-sized magnetic potentials, ideal for investigating quantum systems in custom-made environments. The first production of BECs using atom chips was successfully carried out in 2001 by the groups led by T. Hänsch and C. Zimmermann [35, 36]. More than 20 experiments worldwide are now actively exploring various aspects of BECs on chips [37]. These studies range from developing microfabricated atomic waveguides [38–40], to realizing BECs in portable vacuum cells [41], studying quantum degenerate Fermi gases and atomic mixtures [42], integrating sensitive detection techniques [43], utilizing BECs for novel magnetic field microscopy [44], and demonstrating on-chip atom interferometry [3, 15, 45].

However, atom chips are not without their limitations. Small deviations in the current flow can lead to the fragmentation of ultracold atom clouds in the vicinity of the wire surface [46]. Research has linked this issue to imperfections in the current-carrying wires [47, 48]. Efforts to minimize this effect have focused on high-quality fabrication techniques [49, 50], but the inherent properties of the wire materials, such as impurities or granular structure, might impose new limitations [20]. Additionally, Johnson noise-induced thermal current fluctuations are a fundamental loss mechanism when atoms are placed close to the wire surface [51, 52]. Optimizing wire thickness and material type has been a strategy to mitigate this, but non-conductors are emerging as a more effective solution [53]. Currently, the use of permanent magnetic materials on atom chips is being investigated to overcome these challenges. Ultracold atomic systems require isolation and confinement of the system from its surroundings, as well as advanced quantum entanglement techniques to manipulate them [54–58]. As a macroscopic matter wave, BECs naturally possess high degrees of coherence, making them a promising candidate for future quantum technologies [28, 31, 59]. To mention a few examples, in Refs. [60, 61], spin squeezing has been studied in the context of quantum-enhanced magnetometry with Bose-Einstein condensates. In Refs. [62–64], counter-rotating vortex superpositions to realize the atom-optical quantum gyroscope were carried out. In Ref. [65], the atom in-

terferometer gyroscope was demonstrated on an atom chip setup. Moreover, macroscopic quantum systems may allow for experimental testing of theories that explore the border between quantum mechanics and classical physics [22, 25, 30, 31], exploring the fundamental upper limits on the physical scale of quantum mechanical superposition states [66, 67]. Magneto-optical trapping (MOT) [9–14] and evaporative cooling [68] are primary techniques to realize BEC. Generation of ultracold atoms requires optical beams that play different roles, including those performing laser cooling, control, and imaging of the atoms. Generating these optical beams in a compact experimental setup requires a distinct and complex optical circuit. If there were an improved way to generate all the required optical beams, this would be beneficial to many ultracold atomic experiments.

1.2 Quantum computing

A qubit, the cornerstone of quantum computing, differs significantly from a classical computing bit. Qubits are capable of existing simultaneously in a superposition state, rather than just in binary 0 or 1 [69–71]. Entanglement is another quintessential quantum property, where qubits are interlinked in such a way that the state of one immediately affects the other, irrespective of distance. A typical example of an entangled state is $|\Phi_+\rangle = \frac{|01\rangle + |10\rangle}{\sqrt{2}}$, where measuring one qubit within the pair instantaneously sets the state of its counterpart [72]. This phenomenon exhibits correlations beyond the scope of classical physics. In entanglement, where the quantum states of entities are interconnected, rendering separate descriptions impractical. These correlations occur over potentially large spatial distances [73]. The concept of "steering," as named by Schrödinger [74–76], captures the concept of "spooky action at a distance" coined by Einstein [73]. It denotes a significant deviation of quantum theory from the local realist view, allowing predictions in one location based on local measurements elsewhere, surpassing limits set by the Heisenberg uncertainty principle [72, 77]. Despite these challenges, collective measurements have revealed entanglement and EPR Bell correlations in atomic clouds, and direct observation of these correlations in spatially separated subsystems has been achieved [78–82]. The role of entanglement in systems of indistinguishable particles extends beyond metrology, though its utility in other areas remains a subject of debate [83].

Since quantum computers operate fundamentally differently from classical computers, allowing quantum computers to perform many calculations simultaneously, poten-

tially solving certain problems much faster than classical computers [69–72]. For example, a specific task of factoring a 2,000-bit number, is highly relevant because many encryption systems, such as RSA, rely on the difficulty of factoring large numbers [84, 85]. RSA, in particular, often uses keys that are 2,048 bits long. A quantum computer that can efficiently factor these large numbers would be able to break these encryption systems. Quantum computing leverages these principles — superposition, entanglement, and interference — to potentially address complex problems in various domains including cryptography, fluid dynamics, and pharmaceutical development through the simulation of quantum systems. Despite ongoing advancements, quantum computers have not yet surpassed classical computers in practical applications [69, 71, 86, 87].

Quantum algorithms [69, 72, 88], intrinsic to quantum computing, contrast with conventional algorithms due to the qubits' probabilistic nature. DiVincenzo's criteria [86, 87, 89] , formulated in 1996, set forth the foundational requirements for a quantum computer, including a defined set of quantum states for information encoding, initial state preparation, the execution of two-qubit logic gates, long decoherence times, and accurate read-out capabilities for individual qubits. Due to the inherent noise sensitivity of qubits, these days it is widely believed that quantum error correction is a critical aspect [90–92]. While various physical systems are being developed, each exhibits different degrees of adherence to these criteria.

Achieving a fully operational quantum computer as described by DiVincenzo [86, 87, 89] continues to be challenging, particularly due to scalability and control issues. Some research groups are making progress towards simulating small-scale quantum systems, which may soon reach computational capabilities beyond those of classical simulators. At the advancement of the 50-100 qubit level, termed as 'quantum supremacy' or 'quantum advantage', is marks the first time that a quantum computer is able to outperform a classical computer — a feat that was achieved for the first time in 2019 by Google [93]. The last decade has witnessed significant experimental progress in quantum computing, particularly in scaling up quantum computing systems from a handful (less than 10) to the ~ 100 mark. Subsequent sections will explore diverse topics relevant to this evolving field.

The 100-million-qubit system as a hypothetical quantum computer that is significantly more powerful than any currently existing system. However, the current largest quantum computers as we know only have a fraction of this number of qubits. The chal-

lenge is not just in increasing the number of qubits but also in maintaining their coherence and managing error correction [87, 89–92]. Quantum error correction is crucial because qubits are prone to errors due to their highly sensitive nature. A large portion of the qubits in a quantum system would be dedicated to error correction, to ensure that the computation is reliable. This is why, in the scenario, out of 100 million physical qubits, only about a thousand might serve as stable logical qubits for actual computation. The prospect of such powerful quantum computers raises significant concerns about current cryptographic practices [84, 85] and is driving research into post-quantum cryptography, which aims to develop new algorithms that are secure against the potential capabilities of quantum computers.

1.3 Quantum computing models and strategies

The progression of quantum computing research parallels classical computing to an extent, but unique complexities arise from applying quantum theory principles [69, 87, 89, 94]. This ongoing research is crucial for the development of quantum computing technology. Concurrently, the semiconductor industry has achieved significant advancements in transistor fabrication, reducing feature sizes from $10\mu\text{m}$ to 10nm from 1971 to 2017. This progress has increased transistor density and computing power, in line with Moore’s Law [69, 87, 89]. Despite this growth, certain applications remain beyond the scope of even advanced classical computers.

Error correction, encoding strategies, and algorithmic advancements in quantum computing

Quantum error correction [90, 92, 95], crucial for safeguarding information from decoherence and noise, adapts classical concepts to the quantum domain, addressing the unique challenges posed by quantum systems. Techniques such as the use of entangled states for error correction have been developed, striving for fault tolerance where error impacts are minimized. Worldwide research in quantum computing explores controlling qubits through diverse physical systems such as superconductors, photons, quantum dots, and trapped ions. The goal is to meet DiVincenzo’s [86] criteria with minimal noise for scalable systems. Choosing an appropriate encoding for information in quantum systems

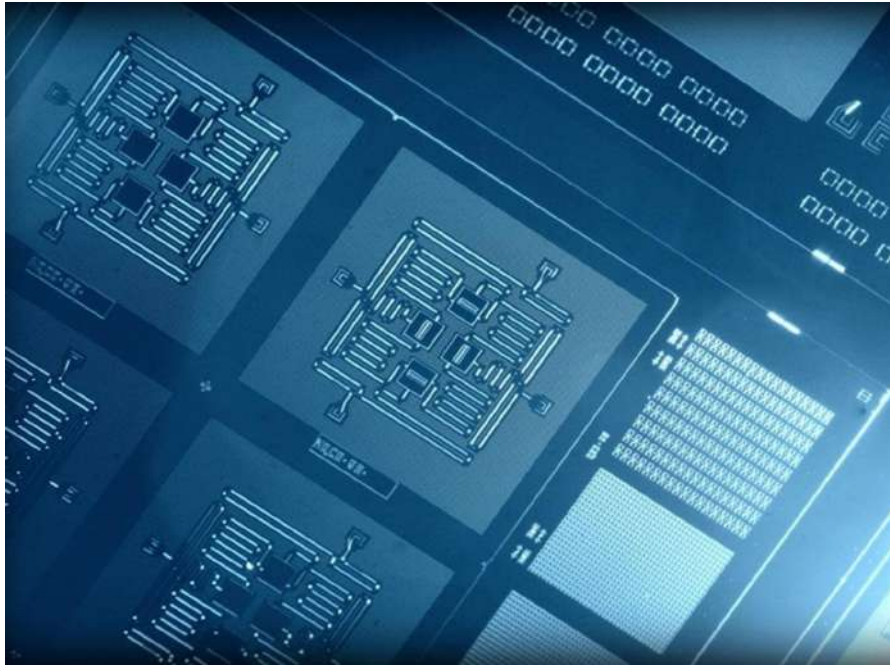


Fig 1-1 Superconducting Qubit Technology for Quantum Computing. Credits : IBM

varies; options range from simple two-level systems to complex continuous-variable encodings in systems like harmonic oscillators [96–98]. The success of encoding schemes becomes evident when managing multiple quantum bits. Quantum algorithms offer advantages over classical computing in tasks like search algorithms, prime number factorization [92, 99], and quantum simulations. Quantum computers, increasingly utilized in areas like quantum machine learning and quantum chemistry simulations [18], promise significant advancements. The computational power of quantum algorithms is growing, with the potential to surpass classical computers once sufficient error-corrected logical qubits are available.

All current quantum computer architectures that aim to perform complex and reliable computations require the transformation from physical qubits to logical qubits [90–92, 100]. This transformation is a central part of quantum error correction, which is essential due to the error-prone nature of layers of stacks of qubits. Logical qubits [95] layers are necessary since qubits' extreme sensitivity to their environment leading to decoherence and other quantum noise. These errors can quickly render the computations meaningless. On the other hand, in the case of scalability and reliability, for a quantum computer to perform complex calculations reliably and at scale [98, 101–103], it must manage and correct these errors. Logical qubits are formed by entangling multiple physical qubits in a way that allows the system to detect and correct errors without disturbing the

computation [95]. And considering fault-tolerance, to create a fault-tolerant quantum computer, meaning it can continue to operate correctly even when some of its physical qubits fail or behave erratically.

Near-term quantum computers, known as Noisy Intermediate-Scale Quantum (NISQ) devices [104], do not have full error correction and hence do not extensively use logical qubits. They are limited in the complexity and length of computations they can perform reliably. Converting physical qubits to logical qubits is a key step in quantum computing for achieving error correction. Logical qubits are formed by grouping several physical qubits, making a single, more stable unit [90–92, 104]. The physical qubits within this group are entangled, so their quantum states are interconnected, and a change in one affects the others. Information is encoded across the group of qubits, not just in one, creating redundancy. This setup aids in error correction by enabling the detection of errors when a qubit flips its state, as the error becomes evident by comparing the states of other qubits in the group [95]. It also allows for the correction of errors in individual qubits without altering the overall stored information. Logical qubits are less prone to errors than individual physical qubits [90, 92, 95] because it is unlikely all qubits in a group will fail at the same time, thereby increasing stability and reliability.

Near-future obstacles and error correction in quantum computing

Building quantum computers presents significant challenges, as it involves working with qubit systems on the atomic scale. The main issue is balancing the protection of qubits from environmental noise, which affects their quantum state and coherence time, against the need for their controlled interaction and entanglement for algorithm execution. Achieving high fidelity [92] in these operations while maintaining isolation is a contradictory yet necessary task in quantum computing. After years of research, several systems have shown promise for large-scale quantum information processing, including superconducting systems, trapped atomic ions, optical lattices, and semiconductors. Each of these has its own strengths and weaknesses concerning coherence, fidelity, and scalability [91, 92, 101]. A critical aspect across all platforms is the development of robust error correction protocols, a major research area. Experimental implementation has seen notable advancements, and while large-scale quantum computers [91, 101] are still years away, progress is evident. Various physical systems are under development, and it's yet to be determined which will be most successful. Companies such as IBM, Google, IonQ,

and start-ups like Rigetti and Cold Quanta have developed small, non-error-corrected quantum computers with tens of qubits [93], some accessible via the cloud. Quantum simulators are also advancing, with applications in molecular energetics and many-body physics [18, 105, 106]. As smaller systems become available, a new field focusing on near-term quantum computer applications is emerging, potentially realizing some benefits and insights of computation even before the completion of large-scale, error-corrected quantum computers.

1.4 Cold atom quantum computing

The discovery of Bose Einstein condensation (BEC) in 1995 marked a significant advance in quantum physics at macroscopic scales [25, 30, 107]. The study of nonclassical correlations in systems with limited numbers of particles has been substantial. Nevertheless, generating and observing these correlations in many-body systems poses challenges due to the susceptibility of such correlations to external noise, the intricacies involved in controlling many-body quantum systems, and the necessity to individually address and detect constituent particles. BECs are attractive as they naturally form a system with high coherence among all particles. There has been substantial theoretical and experimental work suggesting the utility of cold atoms, ultracold ensembles, and BECs for future quantum computing applications [31, 108, 109]. Atom-light interaction has been a fundamental aspect of quantum information processing and quantum state engineering, primarily explored within cavity QED, where light is efficiently coupled to a few or a single atom. Despite the complexity and challenges of cavity-based systems [110, 111], atomic ensemble-light interfaces have emerged as a powerful alternative, leading to significant advancements in experiments involving quantum memory for light, entanglement between atomic ensembles and light, and quantum teleportation with atomic ensembles.

In ultracold atomic ensembles, various nonclassical states such as spin-squeezed states are routinely created using techniques involving collisional interactions, quantum non-demolition measurements, or interactions mediated by cavity modes. These methods facilitate the preparation of states such as spin squeezed states, Dicke states [112], and Schrödinger cat states [113]. Atomic ensemble squeezed states are crucial for quantum metrology, enabling interferometry that surpasses classical limits in sensitivity scaling with $\frac{1}{\sqrt{N}}$. Additionally, in quantum simulation, ultracold atoms in optical lattices are

instrumental in studying quantum many-body systems. Characterizing the correlations among constituent atoms is also of fundamental interest. Notably, Julsgaard, Kozhekin, and Polzik [114, 115] demonstrated the first spatially separated entanglement between two atomic ensembles, forming a two-mode squeezed state mediated by an optical pulse in a short interaction timeframe. Based on this, continuous variable teleportation and spin-wave teleportation have been realized [116].

Atom chips are a compact platform for achieving BECs and entanglement generation, integrating electric, magnetic, and optical fields to confine and manipulate ultracold atomic ensembles or BECs [5, 40, 117, 118]. These chips represent a convergence of quantum optics, quantum measurement, and quantum information processing technologies. Atom chips in ultra-high vacuum chambers, equipped with micro fabricated wire structures, magnetically confine neutral atoms. These chips are initially loaded from laser-cooled atomic ensembles, followed by evaporative cooling to achieve the BEC phase. By manipulating the currents through the chip's wires, diverse magnetic trapping potentials are created. The atom chips' advantage lies in their reliance on DC, RF, and microwave currents for trapping and manipulation. The compactness of these setups enables practical applications of BECs [6, 119–121] in portable atomic clocks and sensors for metrology, paving the way for technological advancements in quantum computing with cold ensembles and BECs.

Spinor quantum computing

Spinor quantum computing [111, 122–124] is a framework for quantum computing where ensembles of qubits, typically composed of neutral atom ensembles, are used to store quantum information. In this framework, spin coherent states and their generalizations are used to store quantum information in a highly redundant way. This approach differs from other quantum computing methods since the operations must be performed at the ensemble (as opposed to single qubit) level [100, 125]. Key advantages include the high stability of spin coherent states against decoherence, and the high redundancy of quantum information that leads to logical error suppression [100, 126]. The primary challenge lies in precisely controlling and measuring the spin states [127], which is critical for effective quantum computation and error correction. In spinor quantum computing, leveraging atomic ensembles and BECs, emerges as a potent approach in quantum information processing. The uniqueness of BECs, highlighted in Klemp et al. (2009) [128] and

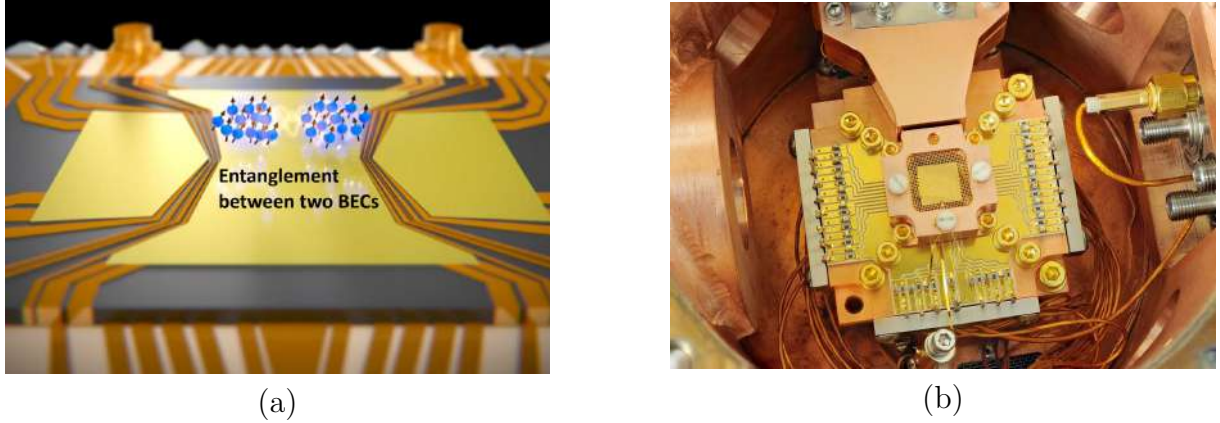


Fig 1-2 This figure illustrates advanced quantum state manipulation techniques, showcasing Fig (a) Spatial splitting of spin-squeezed BEC from Pezzè et al, Rev Mod Phys 90, 035005 (2018), (b) Chip ion trap for quantum computing from 2011 at NIST.

Stamper-Kurn and Ueda (2013) [129], lies in their macroscopic quantum states and tunable interactions, facilitating quantum phenomena exploration. Idlas et al. (2016) [130] illustrate the practicality of BECs in complex quantum operations through entanglement generation between spinor BECs using Rydberg excitations. Kronjäger (2007) [131] and Ueda and Kawaguchi (2010) [132] explore the coherent dynamics of spinor BECs, essential for maintaining coherence in quantum computing. Furthermore, the theoretical framework by Ilo-Okeke and Byrnes (2014) [133] for phase contrast imaging in spinor BECs and Rousseau et al. (2014) [111]’s research on entanglement generation in cavity QED underscore the versatility of BECs. Contributions of [22, 25, 30] in this field, particularly in advancing the understanding of quantum dynamics in BECs, play a pivotal role in reinforcing BECs as a prime candidate for effective and scalable quantum computational systems.

In spinor quantum computing, the redundancy of the quantum information leads to a type of error suppression, while it is not formally a quantum error correcting code. Information is redundantly encoded across an array of qubits, forming a logical qubit with appropriate logical encoding [90–92, 100]. Various error-correction techniques have been explored to prolong the lifespan of information in logical qubits, surpassing the durability of individual physical qubits. Building more complex systems with logical qubits as foundational elements enables the implementation of more robust algorithms. This thesis delves into the macroscopic performance of qubits, explores strategies for encoding information resilient to decoherence, and proposes relevant applications in quantum computing using macroscopic qubits [1, 2, 22, 25, 30, 31].

1.5 Topics of this thesis

In this section we discuss on our methods which we have developed for using BECs and QND measurements [1–3, 25] in quantum computing, with a focus on atom chips. Utilizing atom chips, we generate complex magnetic potentials, facilitating in-depth studies of quantum systems [5, 117, 118]. A significant capability of this approach is entangling multiple BEC clouds on an atom chip [5, 6], which is an improvement over single-cloud entanglement methods. Maintaining qubit coherence and stability is a critical challenge in quantum computing. We have shown our theoretical simulation as well as the chip design progress made by involving a Z-wire trapping potential on atom chips, ensures controlled and stable interactions between BECs [1, 3]. This contributes to better coherence maintenance compared to previous techniques and is essential for the practical solutions for quantum technologies [134]. Additionally, we have showed that the robustness and scalability of our experimental setups such as optical circuit development for addressing the atoms [2] are key benefits. It supports the development of complex quantum computing systems and enables the integration of multiple qubits. This nature is crucial for transitioning quantum computing from experimental setups to practical applications. The theoretical analysis of QND measurements provided here adds to the understanding of their role in quantum systems [1]. Combining practical applications with theoretical insights, this approach represents a meaningful contribution to the field of quantum computing. It addresses several core challenges and lays groundwork for future progress in developing advanced, efficient quantum computing technologies.

Quantum non-demolition measurements method and optical scheme for multi-trap atom chip development

In quantum computing, efficient entanglement generation and manipulation are crucial. Our work explores quantum nondemolition (QND) measurements for measurement-based imaginary time evolution (MITE) [1, 2, 135], critical for entangling neutral atoms and creating complex quantum states. Using QND measurements, we demonstrated a method for deterministically driving a system towards desired quantum states, such as the four-qubit cluster state, vital for quantum information processing [136–138]. Our modular optical circuit development addresses experimental challenges in multi-trap atom chips, leading to an efficient optical system for cooling, imaging, and controlling ultracold

atoms [26–28]. This advancement facilitates the BEC preparation process and enables complex quantum experiments. Precise control of ultracold atomic gases is fundamental in quantum computing, especially for atom chips [32–34].

Significance of our work towards quantum computing

Our research focuses on encoding information into macroscopic qubits and enhancing their robustness against decoherence [54–56], aligning with quantum computing’s goal of developing robust qubits and effective error correction. Our methods for quantum information encoding and error-correction techniques contribute to prolonging logical qubits’ lifetimes, improving quantum computing systems’ reliability [83, 139]. We address practical challenges in quantum control and error correction, contributing to quantum computing models from gate-based to measurement-based [70]. Our exploration of quantum algorithms extends to quantum chemistry and quantum machine learning [140, 141], showcasing quantum computing’s potential in complex problem-solving.

This thesis also covers about the robustness with scalability of our design in handling multiple Bose-Einstein Condensates addresses key challenges in the field [2]. Further explaining our methods which show potential in advancing quantum technology, setting new benchmarks in optical circuit development. Our optical schema for creating Bose-Einstein Condensates (BEC) on atom chips, involving cooling, vacuum control, and atom trapping techniques.

In summary, this thesis aims to clearly narrate the experimental and theoretical work that has been done in our research group, particularly focusing on the author’s contributions. It concludes with an analysis of the manipulation of ultracold atoms to form BECs, achieved using laser cooling and magnetic fields. A significant part of the work involves designing a compact, high-power-efficiency optical circuit integrating multiple laser frequencies, which facilitates conducting experiments in a smaller space. This setup is crucial for realizing BECs and conducting QND measurements on atom chips [5, 6]. Additionally, the thesis introduces a new theory of QND measurements, which explains the nonlinear aspects of these measurements and their role in generating complex quantum states. A key application of this theory lies in implementing measurement-based imaginary time evolution [1, 3, 142]. By using repeated weak QND measurements [142] combined with imaginary time evolution to estimate the energy of a Hamiltonian, and

then applying adaptive unitary operations [106], the system is effectively directed towards specific energy eigenstates. The practical application of this theory is demonstrated in the preparation of a four-qubit cluster state [1], using collective single-qubit QND measurements and single-qubit adaptive operations. Our intention is that this work not only contributes to the understanding of QND measurements and their applications but also opens avenues for advanced studies in quantum control and manipulation.

Organisation of the thesis structure

This thesis is structured to systematically present the research and its findings. The arrangement of the chapters is as follows:

- Chapter 1 provides a concise introduction to the thesis, setting the stage for the detailed discussions that follow. It also gives a broader context of how this thesis fits into the area of quantum information
- In Chapter 2 , an introduction to the field of cold atom physics and Bose-Einstein Condensates (BEC) is presented, laying the foundational knowledge necessary for understanding the subsequent chapters.
- Chapter 3 compares the current progress of our work with previous studies in the same field. It highlights the unique advantages and improvements our research offers over existing methods.
- Chapter 4 delves into the specifics of atom chip design, including the electrical circuits and components. This chapter outlines the framework for the final GHZ qubits preparation setup [143] and Quantum Non-Demolition (QND) measurement optics [136], crucial aspects of the research.
- Chapter 5 introduces a modular and compact optical circuit. This circuit is pivotal for generating the optical beams required for the preparation, control, and imaging of ultracold atomic gases [26–28]. The chapter not only details a compact circuit design but also analyzes the design and gain margins, as elaborated in our recent publications [2, 3, 136].
- In Chapter 6 , there is an overview of our previous works and publications that are relevant to the current study. The chapter concludes with an analysis of the complete optical setup integration for BEC-BEC entanglement inside the vacuum chamber on the atom chip.
- Chapter 7 presents a theoretical analysis of quantum non-demolition techniques applied in our experiment, a topic which was also the subject of a publication last year.
- Finally, Chapter 8 synthesizes the conclusions drawn from all the chapters, offering a cohesive and comprehensive understanding of the research conducted.

2 Introduction to cold atom physics

2.1 Introduction to Bose-Einstein Condensates (BEC)

Bose-Einstein Condensates (BECs) represent one of the most fascinating states of matter, exemplifying quantum mechanics on a macroscopic scale. A BEC forms when a gas of bosonic particles is cooled to temperatures close to absolute zero, causing a large fraction of the atoms to occupy the lowest quantum state. At such low temperatures as shown in Fig. 2-1, the quantum mechanical nature of the particles becomes dominant, and they behave as a single quantum entity with observable wave-like properties [10, 11]. The journey towards understanding and creating BECs has been marked by significant advancements in cooling techniques, particularly laser cooling and evaporative cooling [9–14]. These methods have enabled researchers to achieve the ultracold temperatures necessary for BEC formation, where the thermal de Broglie wavelengths of the atoms overlap, and quantum degeneracy occurs [26–28].

BECs are not only of theoretical interest but also have practical applications. They serve as a foundation for a variety of quantum experiments, from quantum simulations to the development of quantum sensors and computers [18–25]. The concept of BECs, as predicted by Satyendra Nath Bose and Albert Einstein in the 1920s, found a broadly acknowledged experimental manifestation in the work of Eric Cornell and Carl Wieman in 1995 [27, 29], which was later honored with the Nobel Prize in Physics. However, it is worth noting that some in the scientific community regard the superfluid phase of helium, discovered earlier in the 20th century, as an example of BEC behavior. The 1995 experimental verification of BECs in dilute atomic gases ushered in a new era in atomic physics, leading to an explosion of research into ultracold atoms and their application in quantum technologies [15]. These systems offer unprecedented control over the fundamental parameters, making them excellent candidates for probing the quantum world and

enhancing measurement accuracy beyond the standard quantum limit [16, 17]. Central to the creation of BECs is the ability to trap and manipulate atoms. The use of inhomogeneous magnetic fields and atom chips has been revolutionary in this regard [32–36]. Atom chips, in particular, have facilitated the creation of BECs in compact, robust, and efficient ways, allowing for the study of quantum systems in custom-made environments [37–40]. The study of BECs continues to evolve, with research pushing the boundaries of our understanding of quantum mechanics. The manipulation of BECs using atom chips has become an integral part of this exploration, enabling researchers to probe new quantum states and interactions in unprecedented detail.

2.2 Introduction to laser cooling

Laser cooling is a technique used to lower the kinetic energy of particles, such as atoms, thereby reducing their temperature. The principle behind laser cooling involves the manipulation of atomic motion using the radiation pressure exerted by light. Specifically, this method typically utilizes lasers to slow down the atoms, which cools them. The process begins when an atom absorbs a photon from a laser beam. The momentum of the photon is transferred to the atom, leading to a change in the atom's velocity. If the laser light is tuned to a frequency slightly below an atomic transition, atoms moving towards the light will see the laser frequency Doppler-shifted closer to resonance and preferentially absorb photons. This absorption results in a force that opposes the atom's motion, effectively slowing it down, as depicted in Figure 2-1(a). This step is essential for laser cooling and is known as the Doppler cooling mechanism.

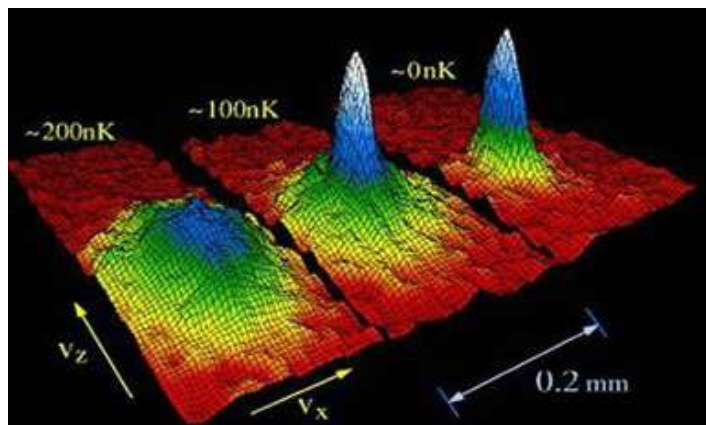


Fig 2-1 Bose-Einstein Condensates(BEC), Image credit JILA

After the photon is absorbed, the atom is in an excited state, as shown in Figure 2-1(b). It then spontaneously emits a photon in a random direction. Due to the conservation of momentum, the emission of the photon causes a recoil of the atom. However, since the emission direction is random, the average recoil momentum over many absorption-emission cycles is zero in all directions except along the direction of the laser light. As a result, there is a net cooling effect, as the atom's velocity decreases in the direction opposite to the laser beam [9, 10]. The process of repeated photon absorption and spontaneous emission results in a reduction of the atom's velocity, and therefore its kinetic energy, leading to a lower temperature of the atomic ensemble. This cooling effect is particularly effective for certain isotopes, such as Rubidium-87, which are commonly used in laser cooling experiments. The final state, Figure 2-1(c), illustrates the atom after it has undergone multiple cycles of absorption and emission, leading to significant cooling. Laser cooling has enabled researchers to achieve temperatures close to absolute zero, opening up new possibilities in quantum physics, such as the creation of Bose-Einstein condensates and the exploration of new states of matter. The mechanism of cooling atoms below sub Doppler levels in the Fig. 2-2, can be described through the interaction of atoms with resonant laser light. Consider an ensemble of two-level atoms with ground state $|g\rangle$ and excited state $|e\rangle$. The energy difference between these states defines the atomic transition frequency ω_0 . An atom at rest would absorb photons from a laser field that matches this transition frequency. However, due to the Doppler effect, a moving atom with velocity \vec{v} perceives the frequency of the incoming light as $\omega_{\text{Doppler}} = \omega - \vec{k} \cdot \vec{v}$, where ω is the laser frequency and \vec{k} is the wave vector of the light.

The force exerted on an atom by the absorption of a photon from the laser can be written as:

$$\vec{F}_{\text{abs}} = \hbar \vec{k} \Gamma(\delta), \quad (2-1)$$

where \hbar is the reduced Planck constant, and $\Gamma(\delta)$ is the scattering rate of photons, which depends on the detuning $\delta = \omega - \omega_0$. For an atom moving towards the laser, the Doppler effect increases the perceived frequency, reducing the detuning for a red-detuned laser ($\delta < 0$).

When the atom in the excited state $|e\rangle$ spontaneously emits a photon, it experiences a recoil with momentum $\hbar \vec{k}'$, where \vec{k}' represents the wave vector of the emitted photon.

The emission process is isotropic, leading to a net zero average force:

$$\langle \vec{F}_{\text{emit}} \rangle = \langle \hbar \vec{k}' \rangle = 0. \quad (2-2)$$

However, each spontaneous emission event imparts a random kick to the atom, increasing the variance of its momentum. This heating effect is termed as recoil heating and can be characterized by:

$$\Delta p = \sqrt{\langle (\Delta \vec{p})^2 \rangle} = \sqrt{\frac{2}{3}} \hbar k. \quad (2-3)$$

The overall force on an atom due to the absorption and emission of photons can be modeled as a damping force that is proportional to its velocity:

$$\vec{F}_{\text{net}} = -\alpha \vec{v}. \quad (2-4)$$

The coefficient α is the damping coefficient and it determines the rate at which the atomic motion is damped.

The equilibrium temperature T of the atoms can be estimated from the balance between Doppler cooling and recoil heating. It is given by the Doppler limit:

$$k_B T_D = \frac{\hbar \Gamma}{2}, \quad (2-5)$$

where k_B is the Boltzmann constant and Γ is the natural linewidth of the atomic transition.

By applying counter-propagating laser beams, a three-dimensional optical molasses can be formed, allowing cooling in all spatial dimensions. The temperature of the atoms can be reduced to a fraction of the Doppler limit by using sub-Doppler cooling techniques like polarization gradient cooling, which rely on the spatial variation of the polarization of the laser light.

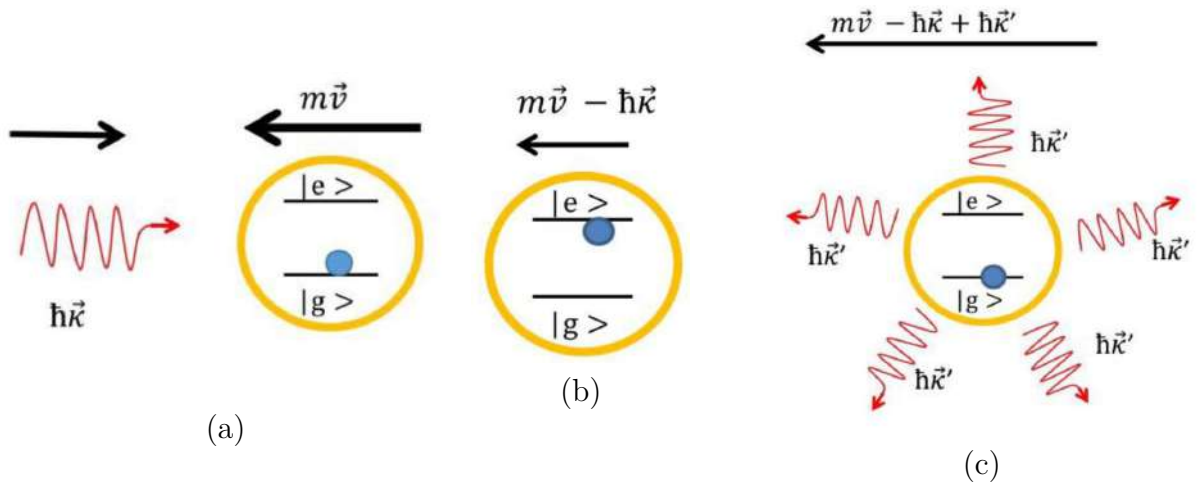
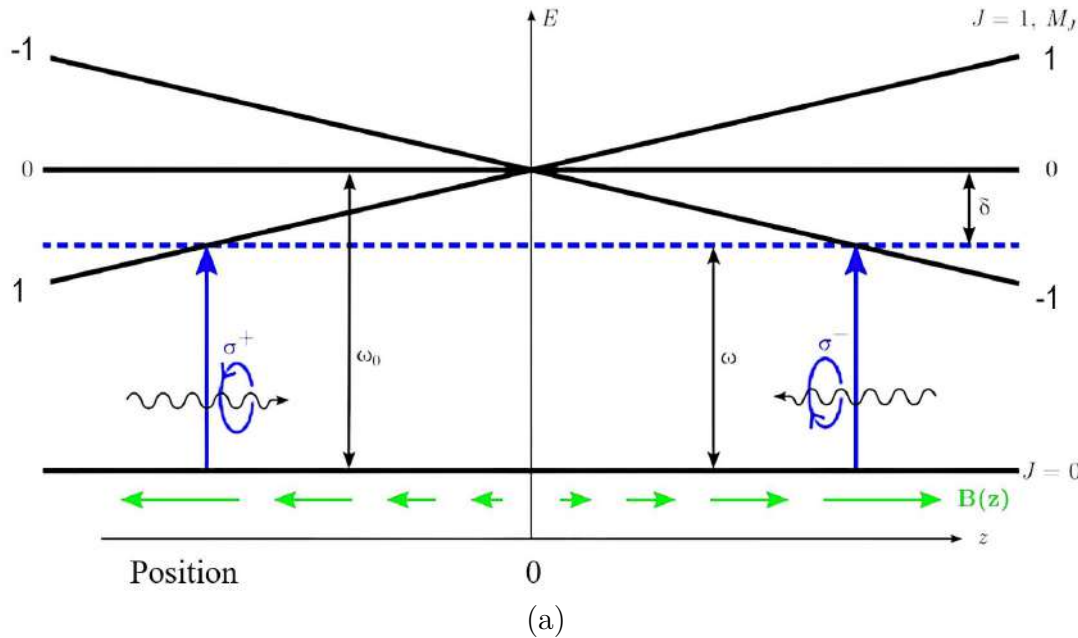


Fig 2-2 Schematic representation of the laser cooling process: in Fig (a) A photon with momentum $\hbar k$ is absorbed by a ^{87}Rb atom, causing the atom to move in the opposite direction due to conservation of momentum. In Fig (b) The atom is in an excited state after absorbing the photon, having a momentum of $m v - \hbar k$. In Fig (c) Spontaneous emission occurs in random directions, resulting in a net recoil momentum that averages to zero in all directions except along the atom's initial movement. Continuous absorption and re-emission of photons in the direction of motion lead to a gradual reduction in the atom's velocity, effectively cooling it down as the kinetic energy decreases.

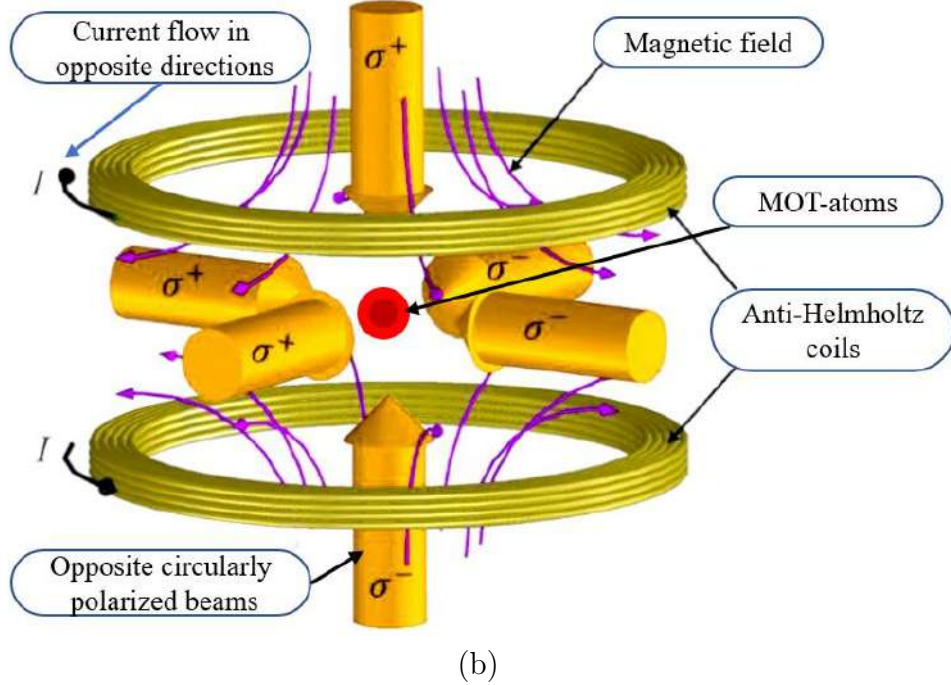
2.3 Three-dimensional cooling and sub-doppler techniques

A key advancement in laser cooling technology is the implementation of three-dimensional cooling, which involves the use of counter-propagating laser beams. These beams are arranged as shown in Fig. 2-3 (b) in such a way that they form an optical lattice, often referred to as "optical molasses" [9, 11, 144, 145], because of the viscous drag it imparts to the atoms moving through it. This setup enables cooling in all three spatial dimensions, as atoms are slowed down regardless of the direction in which they are moving. The technique of optical molasses is depicted by the multidirectional arrows in Figure 2-1(c), indicating the various directions in which the cooling lasers can be applied. By precisely tuning the frequency and intensity of these laser beams, researchers can exert control over the atomic motion in a way that is isotropic, meaning it is uniform in all directions. This isotropic cooling is crucial for experiments that require atoms to be as motionless as possible, such as in atomic clocks or quantum computing applications.

While traditional Doppler cooling is effective, it has a limit to how cold the atoms can get, known as the Doppler limit. However, by employing sub-Doppler cooling techniques like polarization gradient cooling, it is possible to cool the atoms to even lower



(a)



(b)

Fig 2-3 Fig (a) is an illustration of a magneto-optical trap (MOT) for an atom with a $J = 0 \rightarrow J = 1$ transition. The laser frequency ω is red-detuned by δ against the atomic resonance ω_0 . The Zeeman shifts, which are exaggerated for clarity, contribute to a restoring force that drives the atom towards the zero-point of the magnetic field. This force, combined with Doppler cooling, effectively traps and cools the atoms within the MOT. Fig (b) is a schematic representation of a three-dimensional magneto-optical trap (MOT) configuration. The MOT employs a pair of anti-Helmholtz coils to generate a magnetic field gradient necessary for spatial confinement of atoms. The coils carry currents I in opposite directions, creating a quadrupole magnetic field. Circularly-polarized laser beams with σ^+ and σ^- polarizations intersect at the center of the trap, where the field gradient is zero (indicated by the red dot of trapped MOT atoms), to provide the optical cooling and trapping forces.

temperatures. These techniques take advantage of the spatial variation of the polarization of the laser light. Atoms in different parts of the optical molasses experience different polarizations, which affects the way they absorb and emit photons. This can lead to cooling effects that are more refined and can reduce the temperature of the atoms to a fraction of the Doppler limit. Polarization gradient cooling relies on the complex internal structure of the atoms, which includes multiple sublevels of the electronic excited state. The spatially varying polarization of the light creates a pattern of varying energy levels for these substates, which the atoms can move through. As they do, they experience a series of optical pumping and radiation pressure effects that result in a net loss of kinetic energy [9, 11, 144].

2.4 Introduction to atom chip physics

2.4.1 Working principles of atom chips

Atom chips serve as a versatile platform for trapping and manipulating ultracold atoms, primarily Bose-Einstein Condensates (BECs), through micro-fabricated magnetic and electric fields. The fundamental working principle of an atom chip is based on the interaction between the magnetic moments of ultracold atoms and the magnetic fields produced by micro-fabricated structures on the chip [5, 33, 34].

As depicted in the Fig. 2-5, the atom chip typically consists of a current-carrying wire that generates a magnetic field. The field lines around this wire exhibit a circular pattern perpendicular to the current direction. When a homogeneous bias magnetic field B_b is applied perpendicularly to the wire's field, the superposition of the two fields results in a two-dimensional quadrupole field. This combined field is characterized by a line of zero magnetic field strength, which is crucial for creating magnetic traps for neutral atoms [9–14]. The ability to manipulate the configuration of these magnetic fields allows for the formation of various types of magnetic traps, such as the 2D quadrupole trap illustrated in the provided figure. In this trap, atoms are confined in the plane perpendicular to the zero-field line and are free to move along this line. The application of an additional magnetic field can transform this configuration into a more complex trap, such as a Ioffe-Pritchard type or a time-averaged orbiting potential (TOP) trap, which can confine atoms in all three dimensions [26–28].

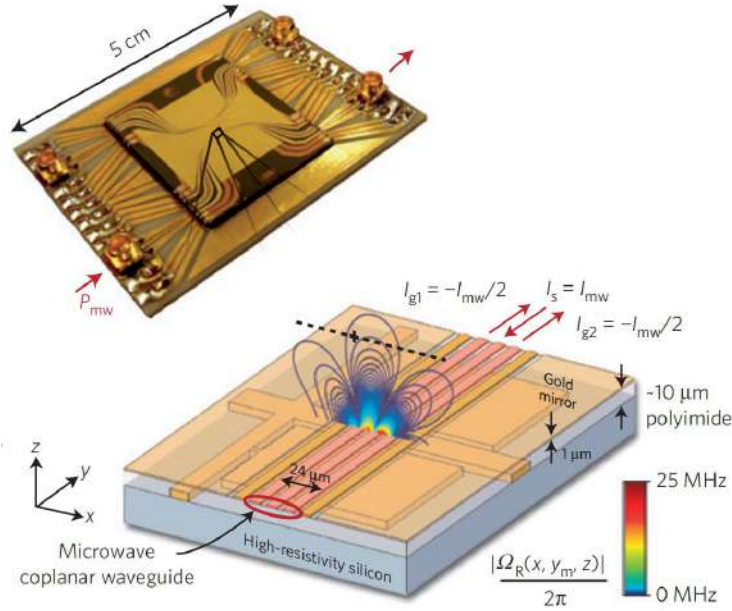


Fig 2-4 Atom chip design by Böhi et al. Nature Phys. 5, 592 (2009).

The bottom graph in the Fig. 2-5(a) shows the magnetic field strength as a function of distance from the wire on the atom chip. The presence of the bias field B_b creates a magnetic potential minimum at a certain distance from the chip's surface, providing a stable trap for the BEC indicated by the yellow spheres. The atom chip allows for fine control over the trap's position and depth by adjusting the current through the wire and the strength of the bias field [35, 36]. Atom chips have enabled significant advances in quantum technology, such as the integration of waveguides for atom interferometry and the development of portable vacuum systems for BECs [38–41]. Moreover, the proximity of the BEC to the chip surface has facilitated studies in quantum degenerate Fermi gases and has been utilized in magnetic field microscopy and sensitive detection techniques [42, 43, 45]. The working principles of atom chips revolve around the precise control of magnetic fields to manipulate ultracold atoms, providing a powerful tool for exploring quantum mechanics and advancing quantum technologies.

The developments in atom chip technology have been instrumental in enhancing our understanding of BECs and have paved the way for new experimental possibilities in the realm of ultracold atom physics [37]. Magnetic trapping is an innovative technique for confining particles, especially neutral atoms, through the application of magnetic fields. This method can be elucidated from both classical and quantum mechanical perspectives. In classical physics, the interaction between a particle's magnetic moment $\vec{\mu}$ and an exter-

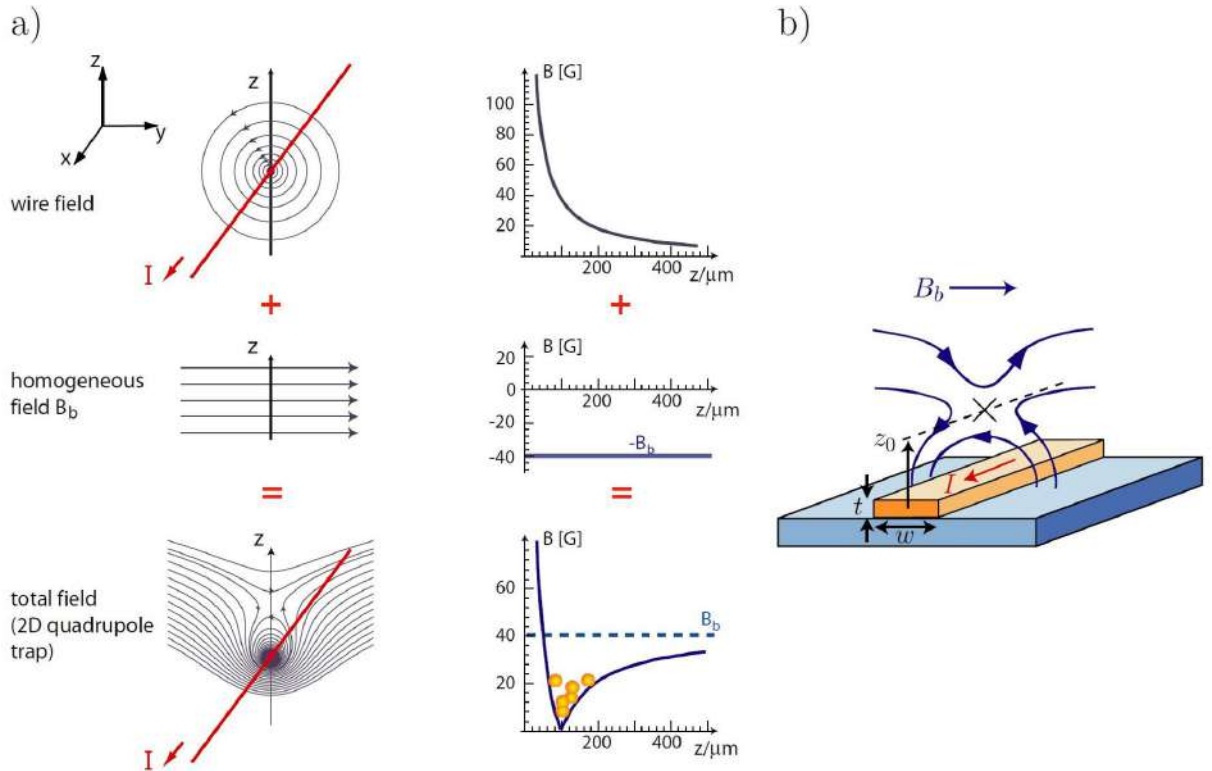


Fig 2-5 A concise illustration of a wire-based magnetic trap that yields planar confinement is presented. Panel (a) demonstrates that a homogeneous bias field, superimposed with the magnetic field emanating radially from a linear conductor, culminates in a planar quadrupole configuration perpendicular to the conductor's axis. The left column depicts the magnetic flux contours, whereas the right column reveals the variation in magnetic field intensity $B(z)$ along the $y = 0$ plane, computed for a current $I = 2 \text{ A}$ through the wire and a bias field $B_b = 40 \text{ G}$. This representation is adapted from [4, 5]. In panel (b), a lithographic technique is employed to construct a wire on the atom chip, which in turn forms a magnetic waveguide. This guide suspends neutral atoms at an established standoff distance z_0 from the wire, offering a conduit for controlled atomic transit.

nal magnetic field \vec{B} is fundamental [146]. The potential energy E of the particle within this field is calculated through the dot product of $\vec{\mu}$ and \vec{B} :

$$E = -\vec{\mu} \cdot \vec{B} = -\mu B \cos(\theta), \quad (2-6)$$

where θ represents the angle between $\vec{\mu}$ and \vec{B} . This scenario leads to Larmor precession, a process where the magnetic moment gyrates around the magnetic field line, stabilizing the angle θ . From the quantum mechanical viewpoint, this phenomenon is analyzed using the Zeeman effect. For a neutral atom possessing total angular momentum \vec{F} , its magnetic moment is delineated as

$$\vec{\mu} = -\mu_B g_F \vec{F}, \quad (2-7)$$

in which μ_B signifies the Bohr magneton and g_F is the Landé g-factor for the angular momentum state F [146]. The Zeeman energy levels are subsequently given by

$$E_{F,m_F} = \mu_B g_F m_F B, \quad (2-8)$$

with m_F being the magnetic quantum number correlated with the projection of \vec{F} on \vec{B} . In this quantum framework, the classical $\cos(\theta)$ term is substituted with discrete values of m_F/F , suggesting that the atom remains in a stable state of m_F . When an atom traverses an inhomogeneous magnetic field $\vec{B}(r)$, it can preserve a steady m_F if the spin precession can adiabatically track the local magnetic field. The energy levels E_{F,m_F} then form an effective magnetic potential energy reliant on the field's magnitude:

$$B(\vec{r}) = \|\vec{B}(r)\|, \quad (2-9)$$

Atoms are entrapped at a potential energy minimum. States with $g_F m_F > 0$, termed "low-field seekers," gravitate towards a magnetic field's minimum. Conversely, states with $g_F m_F < 0$, known as "high-field seekers," are drawn to a magnetic field's maximum. Due to the constraints of Maxwell's equations, which disallow a local magnetic field maximum in a region devoid of sources, only low-field seeking states can be magnetically trapped. Atoms with $g_F m_F = 0$ exhibit no first-order influence from the magnetic field, rendering them untrappable by this technique. In our upcoming sections explaining experimental

design and approach, we focus on two primary types of static magnetic traps. These are distinguished by the characteristics of their magnetic field minimum: one type where the minimum coincides with a zero field crossing, and another where the minimum is at a finite field value.

Quadrupole trap

As shown in Fig. 2-6(a) in a quadrupole trap or U-trap configuration, the magnetic field has a zero crossing at its minimum. The field in the vicinity of this minimum is described by

$$\vec{B}_{quad} = B'_x x \vec{e}_x + B'_y y \vec{e}_y + B'_z z \vec{e}_z, \quad (2-10)$$

where the field gradients B'_x , B'_y , and B'_z comply with Maxwell's equations, specifically $B'_x + B'_y + B'_z = 0$. The potential in the trap is thus proportional to $B_{quad}(\vec{r}) = \sqrt{(B'_x x)^2 + (B'_y y)^2 + (B'_z z)^2}$, creating a linearly confining environment. This arrangement is usually achieved with anti-Helmholtz coil pairs and is notable for its initial application in trapping neutral atoms.

Ioffe-Pritchard or the 'Z' trap

In the Ioffe-Pritchard trap, As shown in Fig. 2-6(b), the magnetic field \vec{B} is a combination of a constant bias field along one axis, a linear field, and a quadrupole field. This can be mathematically represented as:

$$\vec{B} = B_0 \hat{i} + B' \left(-y \hat{j} + z \hat{k} \right) + \frac{B''}{2} \left(\left(x^2 - \frac{y^2 + z^2}{2} \right) \hat{i} - xy \hat{j} - xz \hat{k} \right). \quad (2-11)$$

Here, B_0 is the constant bias field along the x -axis, represented by \hat{i} . The term B' governs the linear components along the y and z axes, denoted by \hat{j} and \hat{k} respectively. Finally, B'' dictates the quadratic, or quadrupole, component of the field, contributing to the complexity of the field structure in all three dimensions. This configuration is achieved by combining a bias field along one axis with a quadrupole field and an additional second-

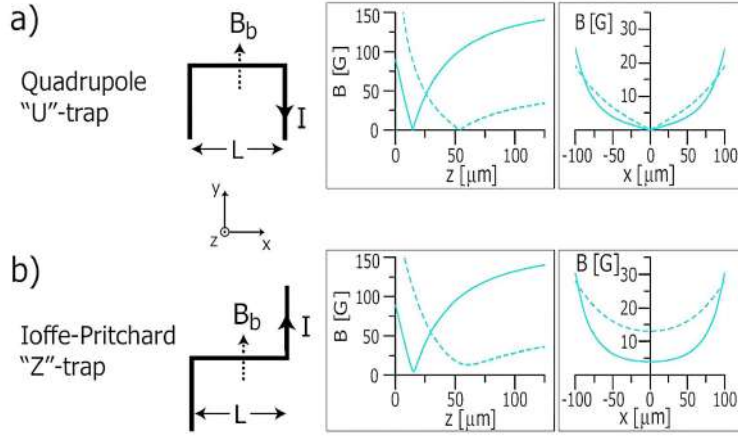


Fig 2-6 Presents two configurations of magnetic traps used for atom confinement in three-dimensional space: (a) displays a Quadrupole "U"-shaped trap, and (b) shows an Ioffe-Pritchard "Z"-shaped trap. The illustrations on the left detail the wire arrangements for both traps, emphasizing their distinct geometrical structures, with the bias magnetic field orientation indicated for clarity. The Quadrupole "U" design and the Ioffe-Pritchard "Z" design each create unique magnetic environments that are conducive to confining neutral atoms. These environments are generated through precise current flows and the application of an external bias magnetic field. The specific field strengths represented by dashed and solid lines correspond to bias fields of 54 G and 162 G, respectively. This figure is an adaptation from source [4,5], highlighting the practical realization of magnetic trapping through wire layout and magnetic field application.

order term. It was first demonstrated in atom trapping by Pritchard and resembles the earlier Ioffe configuration used in plasma confinement. The magnetic field strength, expanded to second order from the trap center, is given by

$$B_{IP}(\vec{r}) = B_0 + \frac{B''}{2}x^2 + \frac{1}{2} \left(\frac{B'^2}{B_0} - B'' \right) (y^2 + z^2), \quad (2-12)$$

leading to harmonic confinement. The corresponding trap frequencies for atoms of mass m and magnetic moment $\mu = \mu_B g_F m_F$ are

$$\omega_x = \sqrt{\frac{\mu}{m} B''}, \quad (2-13)$$

and

$$\omega_{\perp} = \sqrt{\frac{\mu}{m} \left(\frac{B'^2}{B_0} - B'' \right)}. \quad (2-14)$$

In these setups, magnetic traps are generated using current-carrying wires or permanent

magnets. We specifically focus on wire-based traps for our experiment. A single wire carrying a current I creates a radial magnetic field, which, when combined with a perpendicular homogeneous bias field, results in a zero field line at a specific position. This configuration allows for a versatile manipulation of trapped atoms. Fig. 2-4 depicting the chip assembly. The silicon experiment chip features dual layers of gold wires, separated by a slender polyimide layer, and includes coplanar waveguides (CPWs) on the top layer. This chip is affixed and wire bonded to an aluminum nitride (AlN) carrier chip, which has a single gold layer and provides four microwave and 44 DC ports. The detailed schematic shows the experimental area, where the three central wires (colored red and measuring 6 μm by 1 μm) constitute a CPW. All wires, CPW included, are capable of carrying stationary currents for creating static magnetic traps.

2.5 Progress with BEC atom chip combination and quantum entanglement

The combination of Bose-Einstein Condensates (BECs) with atom chips has enabled precise manipulation of ultracold atoms, essential for advancements in quantum entanglement and technology. The integration of atom chips allows for the generation of BECs with high spatial control due to the intricate magnetic potentials created by micro-fabricated surfaces on the chips [33, 34]. Atom chips have been effectively used to produce BECs as demonstrated by the work of T. Hänsch and C. Zimmermann [35, 36]. Subsequent experiments have focused on diverse applications, from atomic waveguides [37] to atom interferometry [65], leveraging the compact nature of atom chips to confine and control BECs.

Entanglement studies in BEC systems have achieved quantum-enhanced magnetometry [60, 61] and the development of atom-optical gyroscopes [62–64]. These studies exploit the coherence properties of BECs to improve measurement sensitivity and precision. The BEC-atom chip combination is recognized for its potential in scalable quantum computing. By manipulating entangled states on atom chips, researchers aim to construct scalable quantum networks [2, 3]. The atom chip's micro-scale control over magnetic fields facilitates this scalability and the implementation of complex quantum algorithms.

Furthermore, the combination has been crucial for testing the intersection of quantum

mechanics and classical physics, with experiments designed to explore this boundary using BECs as a platform [66, 67]. Techniques like magneto-optical trapping (MOT) and evaporative cooling are instrumental in preparing ultracold atoms for BEC formation [9–14, 68]. The BEC-atom chip combination has brought significant technical progress in the field of quantum entanglement and computing. This platform has become instrumental in creating controlled quantum states, serving as a testbed for quantum mechanical principles and the development of quantum technology applications.

3 Quantum information with atomic ensembles control

3.1 Introduction to spatial entanglement and EPR steering in BECs

In quantum mechanics, a notable aspect is the entanglement phenomenon, wherein the quantum state of one entity is intrinsically connected to that of another, making independent descriptions unfeasible. This entanglement is particularly evident in experiments where measurements on entangled entities reveal correlated outcomes. Such phenomena starkly contrast with the predictions of classical physics, especially when these correlations occur between measurements in spatially distant locations [73].

The foundational work by Einstein, Podolsky, and Rosen [73] introduced the concept that strong correlations could lead to an apparent alteration in the quantum state of a distant entity, following local measurements in a separate area. Schrödinger named this interaction “steering” [74]. This concept implies a significant divergence of quantum theory from a local realist perspective of the universe [72, 77]. In practical scenarios, this phenomenon enables an observer in one location to use their local measurement results to predict outcomes in another location with greater accuracy than the Heisenberg uncertainty principle would ordinarily allow [72]. While this has been extensively explored in optical systems, demonstrating EPR steering with larger groups of particles, such as atoms, remains an ongoing research effort [76]. This is particularly significant for testing quantum physics in macroscopic systems and for potential applications in quantum metrology and quantum-information tasks that utilize EPR steering [75]. Recent advancements in ultracold atomic ensembles have facilitated the preparation of nonclassical states [147]. These states are highly relevant for quantum metrology [148], utilizing atom-atom correlations to enhance precision in atom interferometric measurements [78, 149–151]. The challenge lies in the large number of atoms involved, making individual detection and address-

ing nearly impossible. This is particularly true for Bose-Einstein condensates (BECs), where atoms are indistinguishable and share the same spatial mode [79, 152]. Despite these challenges, collective measurements have been successful in revealing entanglement, EPR correlations, and Bell correlations in atomic clouds [78–81]. Direct observation of these correlations in spatially separated subsystems has been achieved in [82] as shown in the Fig 3-3. Additionally, the concept of entanglement in systems of indistinguishable particles has been a topic of debate, especially regarding its utility beyond metrology [83].

3.2 Entanglement of macroscopic objects

In an experiment by Julsgaard, Kozhekin, and Polzik [115] demonstrated the entanglement of two macroscopic objects. The objects in question were two separate samples of cesium gas, each containing approximately 10^{12} atoms. This chapter focuses on the experimental setup as depicted in Figure 1 of their publication, along with the crucial equations that underpin the entanglement process.

The experimental setup Fig. 3-1 in [115] involved two cesium gas samples placed in a highly homogenous magnetic field. These samples were contained in glass cells at approximately room temperature. The cesium atoms in the first cell were optically pumped into the ground state $F = 4, m_F = 4$, and those in the second cell into $F = 4, m_F = -4$, thus orienting the coherent spin states along and against the x-axis, respectively. The entanglement was achieved through the interaction of the cesium gas samples with a polarized light pulse. The critical aspect of this interaction can be encapsulated in the following equations:

$$\mathbf{S}_{\text{out}}^y = \mathbf{S}_{\text{in}}^y + a\mathbf{J}_{z12}, \quad (3-1)$$

where $\mathbf{S}_{\text{out}}^y$ and \mathbf{S}_{in}^y represent the Stokes parameters of the outgoing and incoming light, respectively, \mathbf{J}_{z12} is the sum of the z components of the spins of the two samples, and a is a constant. Equation (3-1) describes the Faraday effect, indicating the rotation of polarization due to the magnetic field induced by the atomic spins.

$$\mathbf{J}_{\text{out}}^y = \mathbf{J}_{\text{in}}^y + b\mathbf{S}_{\text{in}}^z, \quad (3-2)$$

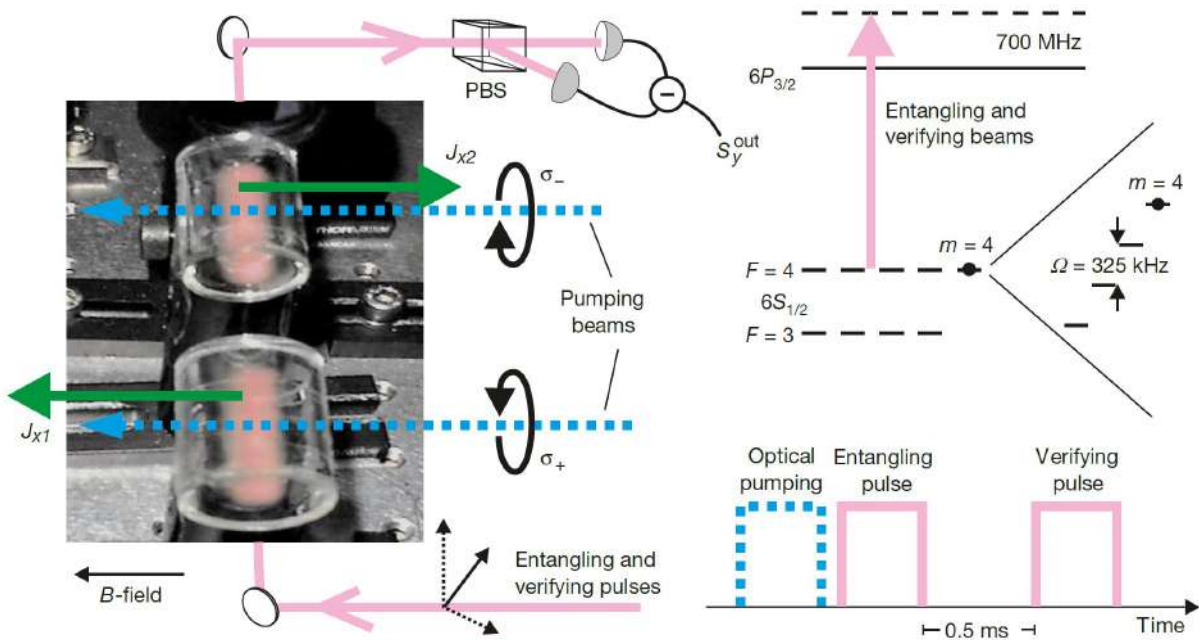


Fig 3-1 Shows an experimental setup for the entanglement of two macroscopic cesium gas samples. The setup features two glass cells placed within a homogenous magnetic field (B-field) with the mean spin values (J_{x1} and J_{x2}) oriented along and against the x-axis, respectively. Optical pumping is performed using circularly polarized light (σ_+ and σ_-), creating coherent spin states in each cell. A linearly polarized probe light (entangling and verifying beams) detuned by 700 MHz interacts with the atomic samples, inducing a Faraday effect observable as a rotation of the probe's polarization S_y^{out} . This interaction is used for non-demolition measurements of the collective spin, facilitating entanglement and subsequent verification. The time sequence below the setup indicates the duration of optical pumping, entangling, and verifying pulses with a 0.5 ms interval between entanglement and verification. Julsgaard, Polzik, et al. Nature 413, 400 (2001)

where $\mathbf{J}_{\text{out}}^y$ and \mathbf{J}_{in}^y are the y components of the atomic spin after and before the light interaction, respectively, and \mathbf{S}_{in}^z is the z component of the Stokes parameter of the incoming light. This equation shows the back-action of light on the atomic spins, a crucial part of the entanglement process. These equations, (3-1) and (3-2), are central to understanding the entanglement mechanism in the experiment. They elucidate the interplay between light and matter at a macroscopic scale, leading to the generation of entangled states.

In conclusion, the experiment by Julsgaard, Kozhekin, and Polzik is demonstrating the possibility of entangling macroscopic objects. In contrast to the groundbreaking experiment by Julsgaard, Kozhekin, and Polzik [153], which demonstrated entanglement in macroscopic objects (cesium gas samples), our approach focuses on entangling individually trapped Bose-Einstein Condensate (BEC) qubits on an atom chip. While Julsgaard et al.'s experiment utilized the interaction of light with the collective spins of the gas samples, our experiment proposes a unique scheme for two-qubit entanglement generation through interaction between BECs confined in the Z-wire trapping potential of the atom chip [2, 3, 6]. This method leverages the precise control and manipulation of qubits in well-separated traps, offering a distinct advantage in scalability and individual qubit control.

Our experimental setup, unlike the cesium gas samples in Julsgaard et al.'s work, allows for the creation of entangled states between spatially separated BECs. This spatial separation is crucial for implementing complex quantum algorithms and multi-qubit gates. Moreover, our method, based on the QND measurement-induced process, provides a more versatile foundation for the future exploration of two-qubit and two-qubit quantum gates [2, 3, 154, 155]. Such capability is essential for advancing the field of quantum information processing, where maneuverability and control at the individual qubit level are paramount. In summary, our approach offers a promising avenue for scalable quantum computing architectures, underlining the differences and potential advancements over the entanglement methods demonstrated in macroscopic systems.

3.3 Spatial entanglement and EPR steering in BECs

This section of the chapter discusses the investigation of spatial entanglement patterns and Einstein-Podolsky-Rosen (EPR) steering in BECs, as shown in [82]. The study focuses on high-resolution imaging techniques to measure spin correlations in spatially

separated parts of a spin-squeezed BEC, observing entanglement sufficient for EPR steering. The experiment involved a sequence of steps [82], illustrated in Fig 3-2 of the work. Initially, a BEC is prepared in a spin-squeezed state on an atom chip. After the trapping potential is switched off, the BEC expands as in Fig. 3-2. The expansion process allows the spatial separation of the atomic cloud into distinct regions, enabling the measurement of spin correlations between these regions. The experiment's crux lies in verifying entanglement and EPR steering through measurements of the two main equations form the foundation of this analysis:

The criterion for detecting entanglement between regions A and B in 3-3 is given by:

$$E_{\text{Ent}} = 4\text{Var}(g_z \hat{S}_z^A + \hat{S}_z^B)\text{Var}(g_y \hat{S}_y^A + \hat{S}_y^B) - |g_z g_y| - |\Delta \hat{S}_x^A| - |\Delta \hat{S}_x^B|^2 \geq 1 \quad (3-3)$$

where Var denotes the variance, and g_z, g_y are real parameters optimized to minimize E_{Ent} . A value of $E_{\text{Ent}} < 1$ certifies entanglement between regions A and B [156].

The criterion for demonstrating EPR steering from A to B is:

$$E_{A \rightarrow B}^{\text{EPR}} = 4\text{Var}(g_z \hat{S}_z^A + \hat{S}_z^B)\text{Var}(g_y \hat{S}_y^A + \hat{S}_y^B) - |\Delta \hat{S}_x^A|^2 \geq 1 \quad (3-4)$$

A violation of this criterion indicates EPR steering, implying that local measurements in region A can predict the outcomes in region Fig. 3-3 with uncertainties below the Heisenberg uncertainty relation for Fig. 3-3B [156]. Fig. 3-3 from the paper work presents the robustness of observed EPR steering A to B, relative to the gap size between regions A and B. This figure demonstrates that EPR steering vanishes as the gap size increases, highlighting the spatial nature of the entangled states in the BEC [82]. This study demonstrates the feasibility of observing spatial entanglement and EPR steering in BECs using high-resolution imaging.

Our experiment seeks to extend these principles to a novel domain: the entanglement between two distinctly separated BEC clouds. Our approach, unlike Fadel et al.'s work that focuses on entanglement within a single expanded cloud, aims to achieve inter-cloud entanglement. This is a groundbreaking step, as entanglement between two distinct BEC clouds [3]. The implementation of our scheme on an atom chip offers greater control and flexibility. It enables the generation of two-qubit entanglement through interactions in a Z-wire trapping potential, a feature not present in the single cloud approach of Fadel et

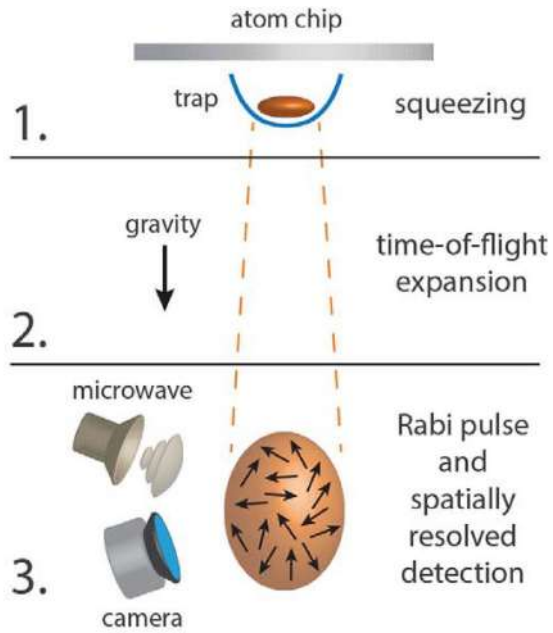


Fig 3-2 Shows an experimental sequence for spin-squeezed state creation and measurement in a Bose-Einstein condensate using an atom chip. (1) A BEC is confined in a trap and a squeezing operation is applied. (2) The trap is released, and under the influence of gravity, the BEC undergoes time-of-flight expansion. (3) A microwave field prepares the atomic spin state, followed by a Rabi pulse to select the spin component for measurement. The spatially resolved detection is performed using a camera, capturing the distribution of spin orientations within the expanded BEC cloud. Time of flight in Fadel et al., Science 360, 409–413 (2018)

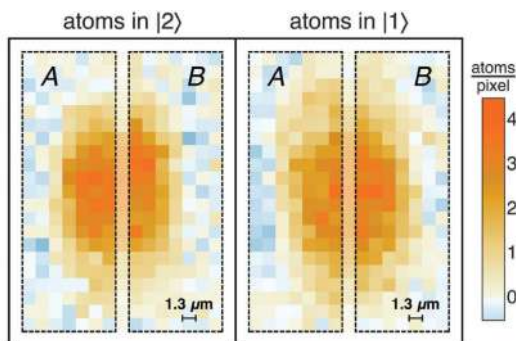


Fig 3-3 Shows a single-shot absorption images showing atomic density distributions in a spin-squeezed Bose-Einstein condensate. The left panel represents the number of atoms in state $|2\rangle$, while the right panel corresponds to atoms in state $|1\rangle$. Regions A and B are delineated by dashed lines, with a gap of $1.3 \mu\text{m}$, indicating the spatial separation of the atomic densities. The color gradient quantifies the atom count per pixel, with warmer colors representing higher densities, thereby visualizing the spin correlations between the separated regions A and B. BEC splitting in Fadel et al., Science 360, 409–413 (2018)

al.

Moreover, our setup 4-19 is designed to address the scalability challenges in quantum computing by enabling the formation of complex multi-qubit states, such as the 2-BEC qubits entangled state. This is achieved through Quantum Non-Demolition (QND) measurement-induced processes, which offer a more advanced and scalable platform for quantum information processing compared to the single BEC setup used by Fadel et al. Our experimental scheme [3] thus represents a significant advancement over the existing methodologies, paving the way for implementing advanced quantum gates and algorithms using multiple BEC qubits.

3.4 Quantum entanglement in spatially separated atomic modes

In the study [157], the generation of quantum entanglement between two spatially separated atomic clouds was demonstrated, marking a significant advancement in the field of quantum mechanics. Figure 1 in their work illustrates the experimental setup and the resulting entanglement phenomenon. The experiment commenced with the preparation of a Bose-Einstein Condensate (BEC) of Rubidium-87 atoms. In the initial state, all atoms were in the hyperfine level $F = 1, m_F = 0$. Through spin-changing collisions, entangled pairs of atoms in the Zeeman levels $m_F = \pm 1$ were generated, as depicted in Fig. 3-4 in [157]. This led to the formation of an ensemble in a twin Fock state, naturally dividing into two spatially separated clouds. The twin Fock state, represented in Fig. 3-4, can be characterized by an equal number of atoms $N_{+1} = N_{-1}$ in the two Zeeman levels. This state is described by the equation:

3.4.1 Analysis and implications

The generation and analysis of entanglement in this system hinge on the indistinguishability of the particles. The fundamental principle underlying this entanglement is the bosonic symmetrization postulate, leading to the creation of entangled states that can potentially violate Bell inequalities. This experiment marks a significant step in utilizing entangled states of indistinguishable particles for advanced quantum information applications. This study [157] analyses the possibilities in quantum metrology and quantum computing, where such entangled states can be harnessed for groundbreaking

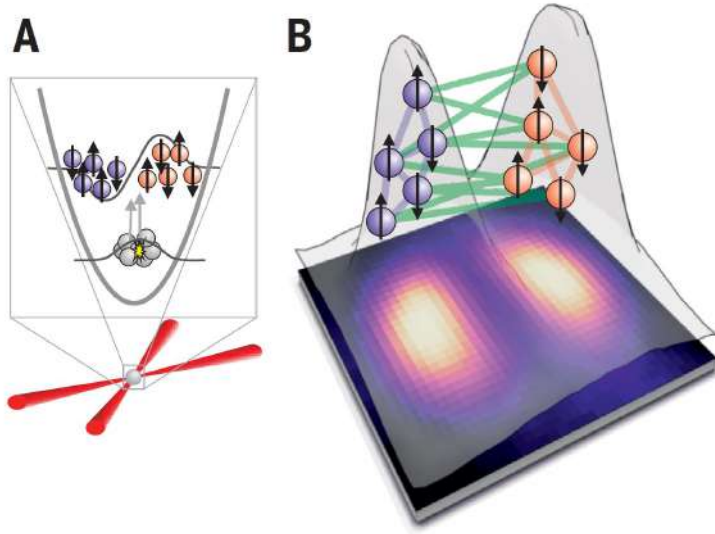


Fig 3-4 Creation of multiparticle entanglement ensemble by naturally dividing the trapping potentials into two thus divided two clouds (red and blue) in Lange et al., Science 360, 416–418 (2018)

applications. However, in our experiment, we propose to extend this concept to generate entanglement between individually trapped BEC qubits on an atom chip. Our scheme, as depicted in Fig. 4-19, involves two-qubit entanglement generation through interaction between BECs confined in the Z-wire trapping potential. We aim to explore the feasibility of implementing two-qubit quantum gates and to form 2- BEC qubits entangled states characterized by the superposition $\frac{1}{\sqrt{2}}(|00\rangle + |11\rangle)$. This approach is not only novel in its application but also critical for the experimental implementation of multiple qubit gates and quantum algorithms. The key advancement of our setup lies in its scalability and the potential to perform fundamental operations of universal quantum computing. Our design aims to address the scaling problem with multiple BECs, a significant limitation in Lange et al.’s approach. The entanglement in our setup is generated through a Quantum Non-Demolition (QND) measurement-induced process, as shown in Fig. 4-18, offering a more versatile and scalable approach compared to the spin-changing collision method used by Lange et al.

3.5 Spatial distribution of entanglement in atomic clouds

In the study conducted by Kunkel et al. [158], a novel approach was implemented to generate and spatially distribute entanglement within a Bose-Einstein condensate (BEC).

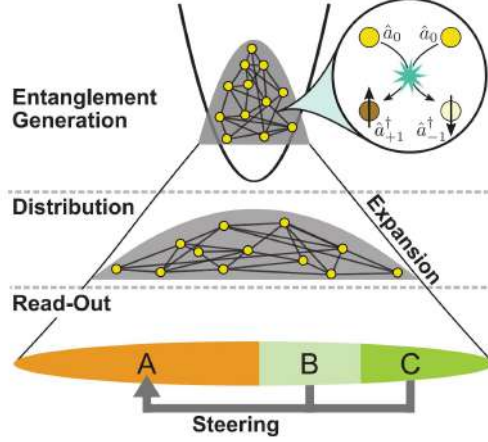


Fig 3-5 EPR steering between spin degree of freedoms in a tightly trapped BEC by local spin-mixing interactions, which evinces the presence of bipartite and multipartite entanglement in Kunkel et al., Science 360, 413–416 (2018)

The core concept revolved around the utilization of spin mixing in a tightly confined BEC to create an entangled state of indistinguishable particles. This entanglement was then spatially distributed through the self-similar expansion of the atomic cloud, as illustrated in Fig. 3-5 of their work. Their experiment commenced with the preparation of a BEC comprising approximately 11,000 ^{87}Rb atoms. The initiation of spin dynamics led to the population of the states $m_F = \pm 1$ with correlated particle pairs, resulting in spin-nematic squeezing and shared entanglement among all atoms in the condensate. The expansion for distributing the entanglement was triggered by deactivating the longitudinal confinement, allowing the atomic cloud to disperse in the waveguide potential.

The key observables in this experiment were the noncommuting spin operators $\hat{F}(0)$ and $\hat{F}(\pi/2)$, defined as:

$$\hat{F}(\varphi) = \frac{1}{\sqrt{2}} \left[(\hat{a}_{+1}^\dagger + \hat{a}_{-1}^\dagger) e^{i(\varphi - \varphi_0)} \hat{a}_0 + \text{h.c.} \right], \quad (3-5)$$

where \hat{a}_j^\dagger is the creation operator for a particle in the spin state $m_F = j$, and h.c. denotes the Hermitian conjugate. These operators satisfy the commutation relation:

$$[\hat{F}(0), \hat{F}(\pi/2)] = 2i\hat{N}(1), \quad (3-6)$$

where $\hat{N}(1)$ is the particle number operator for the $m_F = \pm 1$ states.

The observed variances of the population differences after a spin rotation, as measured

in the experiment, fulfill the uncertainty relation:

$$\frac{\Delta^2 N_-(0)}{N} \frac{\Delta^2 N_-(\pi/2)}{N} \geq 1, \quad (3-7)$$

which holds for any subsystem within the BEC.

This result shows insights into the dynamics and thermalization of quantum many-particle systems. While Kunkel's work [158] represents a significant advancement in generating and distributing entanglement within a single Bose-Einstein condensate (BEC), our experimental approach diverges notably in its aim to create entanglement between individually trapped BEC qubits on an atom chip. Unlike the spatially distributed entanglement in a singular atomic cloud as demonstrated by Kunkel et al., our method focuses on entangling discrete, spatially separated BEC clouds. This approach not only addresses the complex challenge of inter-cloud entanglement but also opens up new possibilities for scalable quantum computing architectures and manipulation of quantum information, which are not directly achievable through the intra-cloud entanglement methods explored in their study.

3.6 Advantages of our BEC qubits entanglement approach

In comparison to the approaches of Kunkel et al. [158], as well as other experiments within a single BEC cloud [82, 157], our experimental scheme focuses on the entanglement between two distinct BEC clouds. This method offers a unique perspective and contributes significantly to the field of quantum information processing [2, 3].

Our future work will explore implementing two-qubit and two-qubit quantum gates, such as CNOT, and entangling these qubits using QND light to form a 2- BEC qubits entangled state, characterized by a superposition state like $\frac{1}{\sqrt{2}}(|00\rangle + |11\rangle)$. This state is crucial for experimental implementations of multiple qubit gates and quantum algorithms. The scalability of our design for fundamental operations in universal quantum computing is a subject of significant interest. Building on the foundations established by previous studies [3, 94, 155], our research focuses on generating entanglement between two BECs. The scheme begins with a QND effective interaction and moves towards solving the scaling problem with multiple BECs, aiming to implement our entangled state in a Mach-Zehnder interferometer setup, as shown in Fig. 4-18. The generation of entanglement between

§3.6 Advantages of our BEC qubits entanglement approach

BECs through QND measurement-induced processes [2, 3] represents a novel approach in the field of quantum information processing. Our experimental setup for cluster state generation using QND measurements between two spatially separated BECs [2,3] promises to open new avenues for quantum computing using BECs as physical qubits.

4 Atom chip and experimental apparatuses design evolution

4.1 Global schema of the experimental setup

The experimental scheme depicted in Fig. 4-1 is designed for the production and manipulation of Bose-Einstein Condensates (BECs) on atom chips. This assembly incorporates various components and systems, each critical for cooling atoms to nanokelvin temperatures to form and control the BECs for quantum experiments. Central to the system is the vacuum chamber that contains the atom chip, a micro-fabricated platform for trapping and cooling atoms. Surrounding the chamber are coils to create the magnetic field necessary for the magnetic trapping and fine manipulation of the atom clouds. An ultra-high vacuum environment, maintained by the vacuum control system, is essential for the BECs' coherence.

The laser lines generation system is a critical component of the setup as it will be discussed in detail in Chapter 5 , comprising various optical elements such as acousto-optic modulators (AOMs), shutters, and lenses. This system is responsible for producing the required optical beams for laser cooling, control, and imaging of the atoms. The laser beams are carefully directed to the vacuum chamber where the atom chip is located, enabling the cooling and trapping processes. The setup includes a primary cooling laser and a secondary repumper laser, both subject to laser line locking techniques to maintain stability and precision—specifically, polarization spectroscopy for the cooling laser and saturated absorption spectroscopy for the repumper laser. Additionally, the setup features an elaborate optics system for entanglement (ENT optics), which is used to manipulate the quantum states of the atoms and to generate entanglement between distinct BECs. The ENT optics include high-precision components that allow for the precise control and steering of the laser beams used in the entanglement processes.

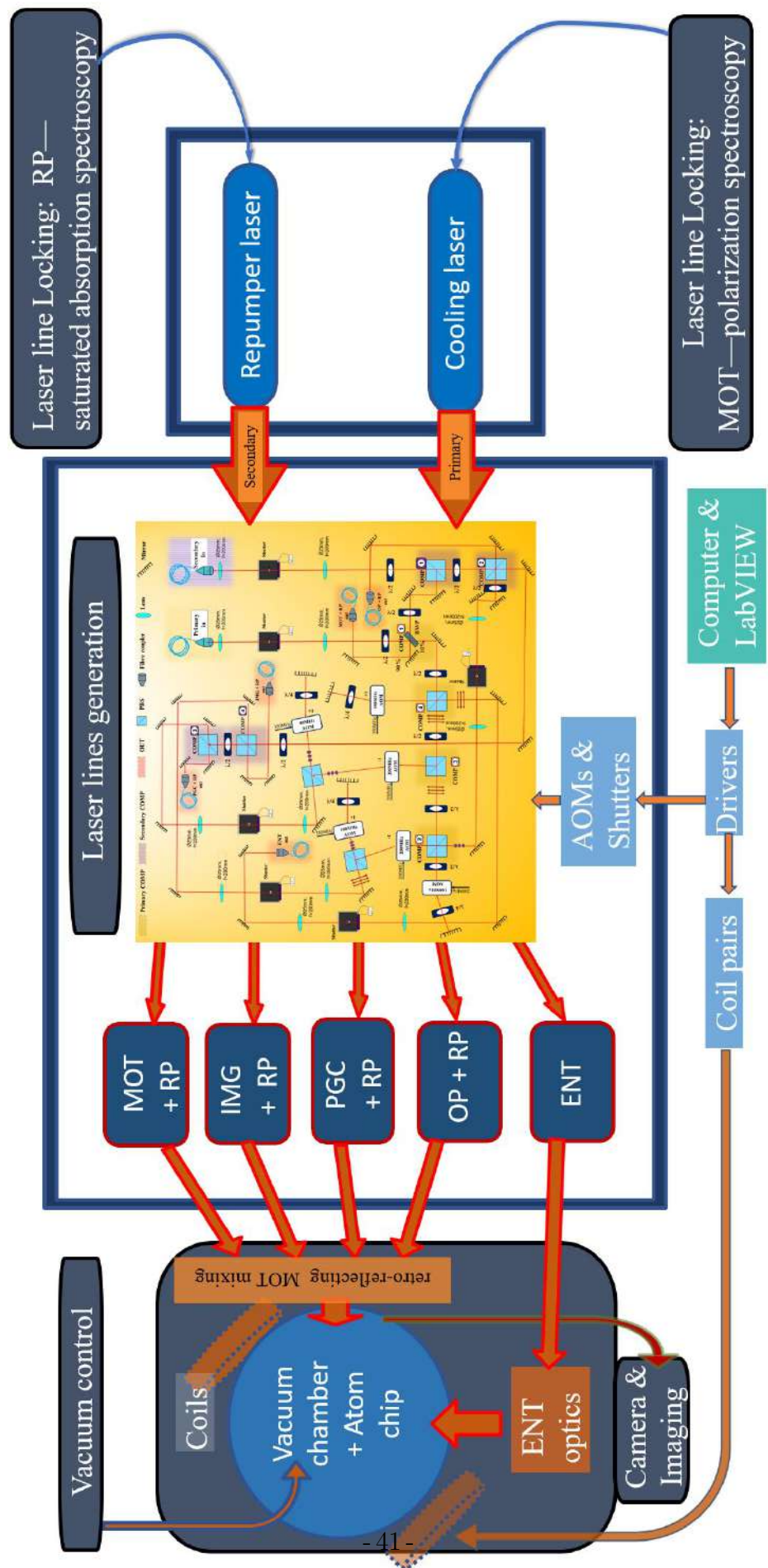


Fig 4-1 Global view of the experimental schema

The magneto-optical trap (MOT), along with the repumping (RP), imaging (IMG), polarization gradient cooling (PGC), and optical pumping (OP) systems, work in conjunction to cool and prepare the atoms for the formation of the BEC. These systems are connected and synchronized, allowing for the sequential and efficient cooling and trapping of the ultracold atoms. A camera and imaging system is included to observe and analyze the atomic clouds and BECs. This system provides real-time feedback on the BEC formation and is crucial for the diagnostics and optimization of the trapping and cooling processes. The entire experimental apparatus is controlled and monitored by a computer system equipped with LabVIEW software. This allows for control over the AOMs, shutters, and coil drivers, as well as the synchronization of the entire process from laser cooling to BEC formation and manipulation. In conclusion, the global experimental setup represents a state-of-the-art apparatus for the study of BECs and quantum mechanics at the microscopic level on atom chip. It incorporates advanced technology and precision engineering to create a platform that is at the forefront of quantum research and experimentation.

4.2 Our atom chip's specific design elements

An atom chip is a device comprising current-carrying wires that produce magnetic fields with spatial variation and strong B-gradients. Fig. 4-2 depicts our atom chip design. For over a decade, atom chips have been used to create microtraps for neutral atoms [159, 160]. The structure at the bottom passes through the top flange of the vacuum

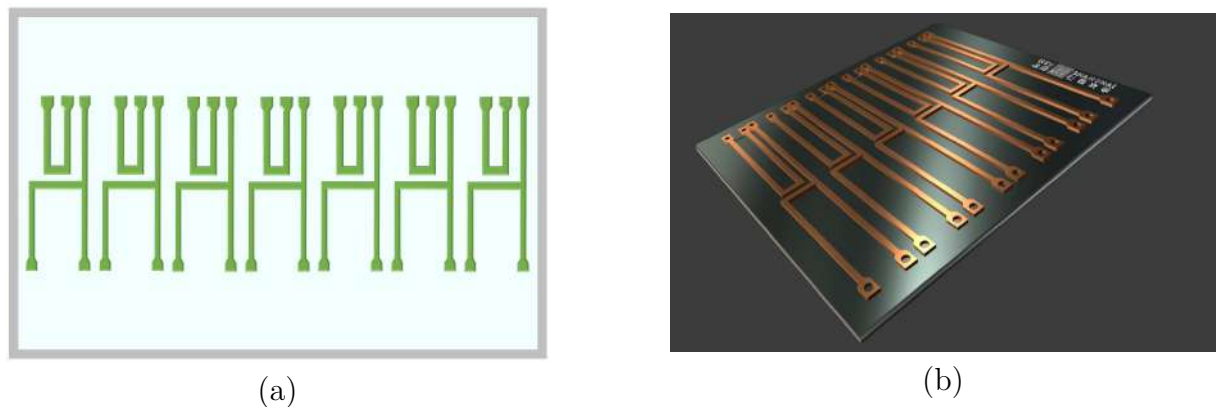


Fig 4-2 Fig (a) show the schematic design of multi-traps version of our atom chip depicting only the core specifics of U and Z wires of the chip. Fig (b) shows the 3D version of schematic design

chamber, along with the current-carrying wires from the chip. The atom chip assembly is mounted on a copper holder, which serves as a heat sink, with a cylindrical hole on top of the vacuum chamber that fits within the dimensions of the top steel flange of the chamber. The chip holder is welded to the top flange of the vacuum chamber.

The design of the atom chip was carried out in L-edit software, and the general elements were composed of current-carrying wires that produce magnetic fields with well-defined spatial distributions and the required field gradients. The atom chip is electrically isolated from the copper heat sink cum holder, mounted on the vacuum chamber's upper flange, by a ceramic layer. This layer's thermal conductivity is significantly higher than other materials with the required properties. As shown in Fig. 4-2, the material is cut in this design to generate current-carrying wires with anchoring pores around the chip perimeter for the wires linking through the flange and the chip. The atom chip dimensions are 50 mm x 50 mm x 1 mm AlN with 0.3 mm ($300\pm30 \mu\text{m}$) thick Cu films creating wire structures on both sides. Material choices are based on electrical and thermal conductivity requirements for the atom chip's stability and performance targets. AlN has been chosen as it is a good match in properties such as thermal conduction and electrical insulation among ceramics. Besides, copper has high electrical and thermal conductivity among metals. The trapping (MOT) beams face a 5 μm gold thin sheet placed on the chip surface as a topmost layer, held and attached to the chip by a holding structure in the corners made up of tiny pieces of wires. The Ioffe-Pritchard trap with the quadrupole characteristic is depicted in Fig. 4-3, essential framework are shown in 4-3. The current coupling via the magnetic field produced by the current density in the wire, as well as the increase of the skin effect in the AC regime and the current coupling via the magnetic field induced by the current density in the wire, are considered.

The quadrupole characteristic, as shown in Fig. 4-3, illustrates the atom chip Z-wire in a bias field. When driven by a current of 2 A, as depicted in Fig. 4-3, it generates an Ioffe-Pritchard trap in conjunction with the quantizing B_y and bias B_x fields. The magnetic field induced by the current density in the wire is considered, including the effects of an anisotropic current distribution within the conductor and the rise of the skin effect in the AC regime. By integrating the Biot-Savart law, the magnetic field of a straight rectangular wire spanning $x_0 \leq x \leq x_1, y_0 \leq y \leq y_1, z_0 \leq z \leq z_1$ can be calculated.

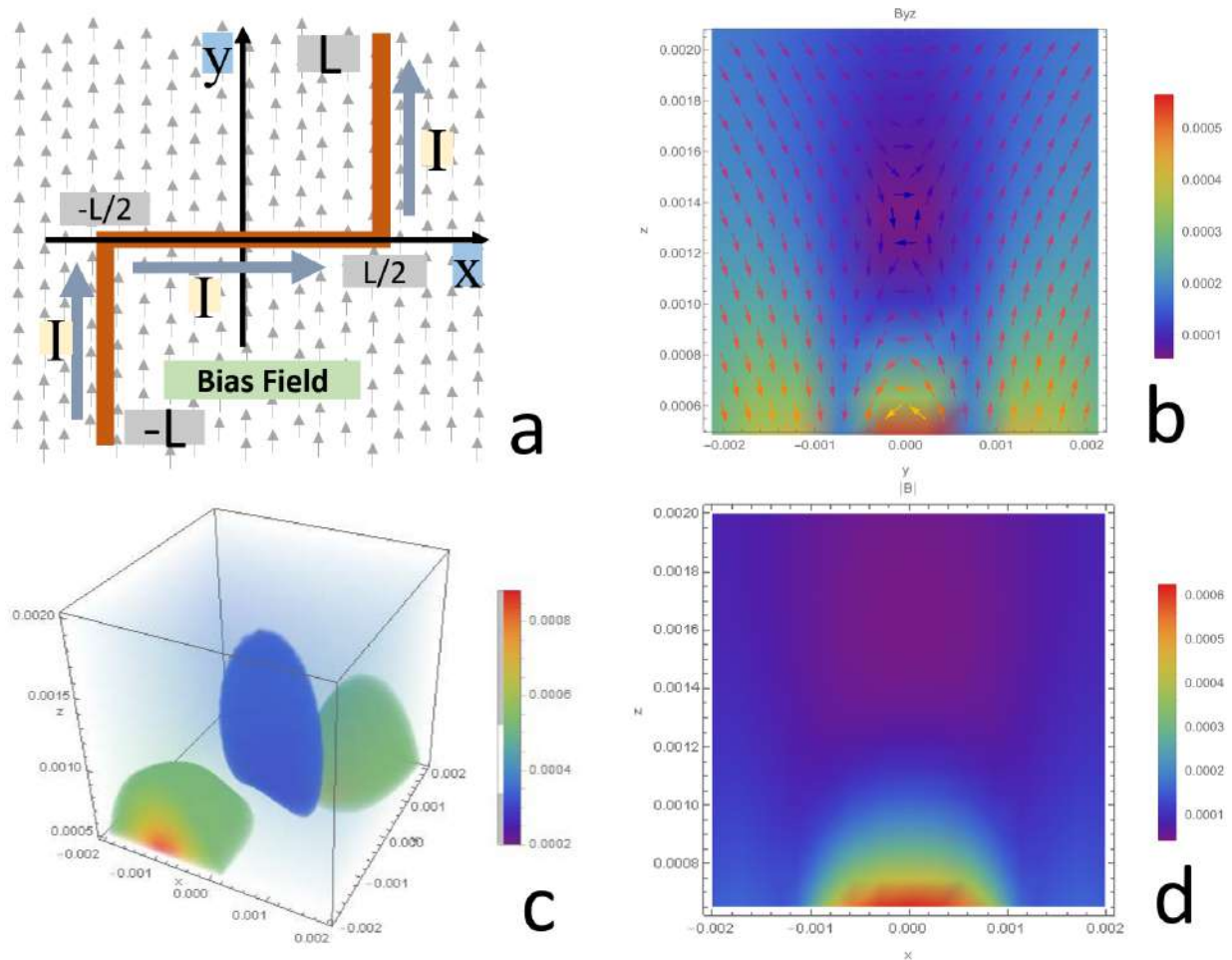


Fig 4-3 a) Z trap is being dissected into a part made up of 3 pieces of wire each of length L , Width is 0.3mm and Height is 0.3 mm as it's wire dimensions., b) Standard Z-wire: B_{yz} field in $y-z$ plane for current $I = 2$ A , bias field $B_{bias} = 0.0002$ T and length $L = 0.002$ m in x,y and z diminutions with measured in meters. c) Standard Z-wire: Magnitude of $|B|$ field in 3D view d) Standard Z-wire: Magnitude of $|B|$ field slices

The Biot-Savart single-wire formula is given by:

$$B_{Zw} = \frac{2\mu_0 I_z}{r} \text{ in G,}$$

where $\mu_0 = 4\pi \times 10^{-3}$ G.m/A, I_z is the Z-wire current in A, and r is the distance from the wire in m. This equation holds in either regime and is not a rough estimate for our topology; this is demonstrated in Fig. 4-3a, where the magnetic field gradient at the trap has substantial ellipticity and carries a homogeneous current density $\mathbf{j} = j\mathbf{e}_x$.

The magnetic field is calculated as follows:

$$\mathbf{B}(\mathbf{r}) = \frac{\mu_0}{4\pi} \int_{x_0}^{x_1} dx' \int_{y_0}^{y_1} dy' \int_{z_0}^{z_1} dz' \frac{\mathbf{j} \times (\mathbf{r} - \mathbf{r}')}{|\mathbf{r} - \mathbf{r}'|^3}. \quad (4-1)$$

$$f(x, y, z) \equiv z \arctan \left[\frac{xy}{z\sqrt{x^2 + y^2 + z^2}} \right] - x \ln \left[y + \sqrt{x^2 + y^2 + z^2} \right] - y \ln \left[x + \sqrt{x^2 + y^2 + z^2} \right], \quad (4-2)$$

Defining $\tilde{x}_k = x - x_k$, $\tilde{y}_l = y - y_l$, $\tilde{z}_m = z - z_m$, we obtain:

$$\begin{aligned} B_x &= 0, \\ B_y &= -\frac{\mu_0 j}{4\pi} \sum_{k,l,m=0}^1 (-1)^{k+l+m} f(\tilde{x}_k, \tilde{y}_l, \tilde{z}_m), \\ B_z &= \frac{\mu_0 j}{4\pi} \sum_{k,l,m=0}^1 (-1)^{k+l+m} f(\tilde{x}_k, \tilde{z}_m, \tilde{y}_l). \end{aligned} \quad (4-3)$$

The divergence of the magnetic field cannot be nullified at the wire ends for a single isolated wire of limited length, thus violating the continuity equation [161]. A true wire carrying a steady current is always connected to leads and a current source, ensuring the validity of the continuity equation and allowing the divergence of the magnetic field to be zero. The wire ends must be sufficiently far from the point of interest where the field is estimated for statistical reasons. Assuming that the ends of the Z wires are infinitely long, this calculation is depicted in Fig. 4-3.

The transversal spatial mode aberration implies a co-planar waveguide mode configu-

ration. The quadrupolar field gradient characteristic of the Ioffe-Pritchard trap, with the quantization axis at the trap height largely determined by the B_y field, is directed along the Z-wire at the coalescence point. Therefore, a test spin particle's trajectory would be magnetically entrapped and oscillating around the trap center. The magnetic field distribution around the Z-wire is more complex than a simple single-wire distribution due to the aforementioned coupling.

4.2.1 Atom chip installation

The chip holder design, featuring advanced-level customized heat dissipation components, appears in the assembly picture. This design aims to integrate the vacuum baking procedures while providing effective shielding for the vacuum-compatible connector pins, including DB25, probe thermocouples, rubidium dispensers, and the core connection pins of the atom chip's U- and Z-wires.

U- and Z-wire connections

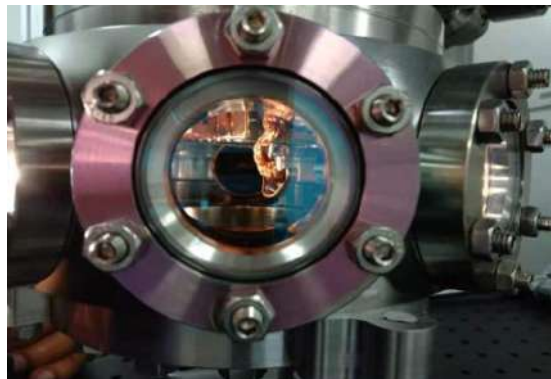
In the Compression stage, the system will be aimed to be compressed by a U-wire with current of around 5 A with DC components. The DC lines labeled as "DCu" and "DCz" would supply the necessary current to the U- and Z-wires, respectively as shown in Fig. 4-5. The control of these currents must be precise since the magnetic fields for atom trapping are sensitive to current fluctuations. The use of Time Division Multiplexing (TDM), which is a technique that allows multiple signals to share the same transmission medium. In the context of an atom chip, TDM could be employed to switch currents rapidly between different wire configurations, allowing dynamic control of the magnetic fields and a quadrupole field ramp down

Temperature-resistance test of Z-wire

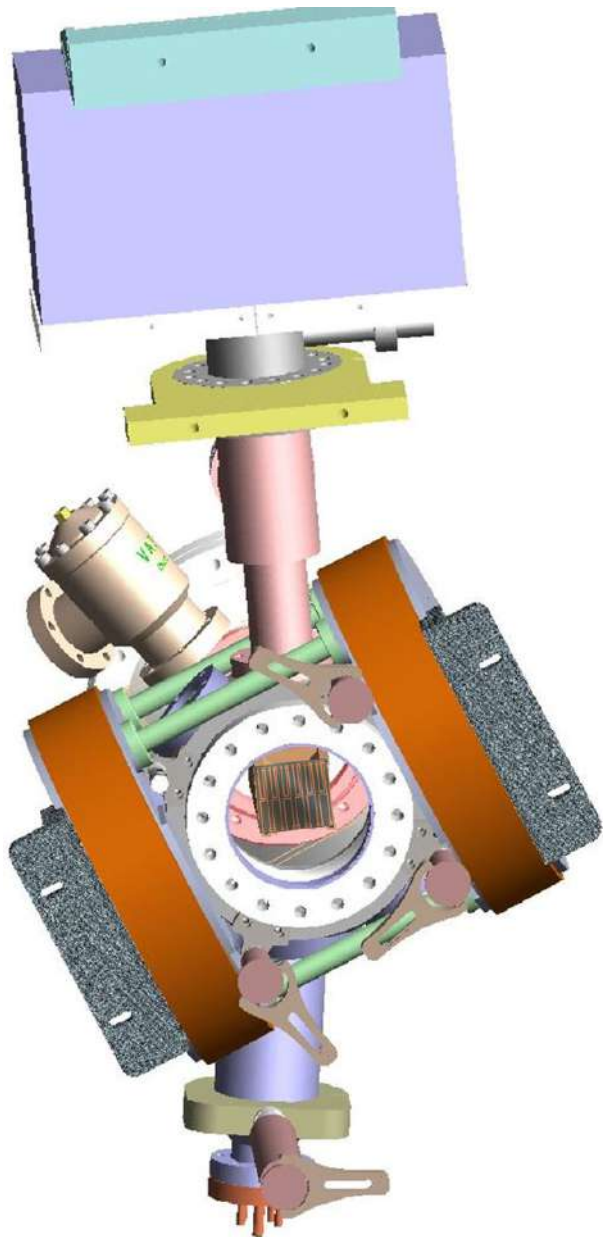
Our atom chip's temperature-resistance test yielded the following characteristics: we chose the Z-wire for the test, applying a current of 30 A for one continuous minute. We measured a resistance $R = 60 \text{ m}\Omega$ with a temperature rise of 18°C (from room temperature 24°C to 42°C over a duration of 60 s).



(a)



(b)



(c)

Fig 4-4 The atom chip installation process. (a) Bottom view of the atom chip installed inside the vacuum chamber. (b) Side view of the atom chip. (c) Shows the chamber design along with the chip install view through the bottom view port of the chamber, designed atom chip and chip holder being assembled together. This assembly seals the bottom of the vacuum chamber, and following the successful assembly of the chip, wire connections, and connector insulators, it will be mounted on top of the vacuum chamber.

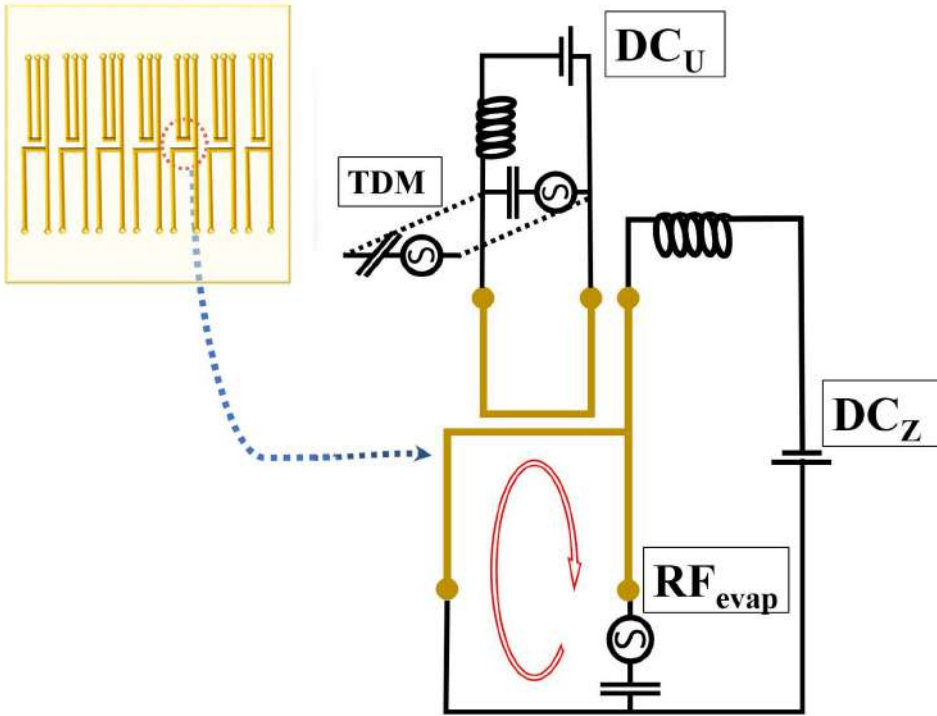


Fig 4-5 U- and Z-wire connections scheme with TDM implementation

Before delving into the intricacies of coherent spin physics in the following chapters, in this section we shall look into what the atomic ensemble undergoes a series of preparatory transformations and placing necessary experimental constraints in place to establish a well-defined BEC quantum states. The experiments detailed here commence with the atoms in the spin state $|F = 1, m_F = -1\rangle$, which are subsequently transitioned to a superposition through coherent population transfer utilizing radio frequency (RF) or microwave (MW) radiation.

4.2.2 Rb dispensers installations and operational parameters

The process begins with the release of rubidium from a 25 mm long dispenser, strategically positioned on the atom chip within the vacuum chamber maintained at a pressure of 1.4×10^{-11} Torr. (with the turbo pump's current level from the UHV particles as 6.5 nA.) The dispenser is heated resistively to approximately 370°C through electrical current pulsing, causing the Rb_2CrO_4 salt within to outgas rubidium through microslits. This system ensures that while heavier chemical particles are retained, the gaseous byproducts, predominantly hydrogen, are absorbed by a titanium layer on the vacuum chamber's inner surfaces, leaving behind a rubidium vapor comprising natural isotopic abundances

of ^{85}Rb (72.2%) and ^{87}Rb (27.8%). The outgassing is regulated by the amplitude and duration of the current pulses to ensure that, following a 1 to 2-minute experimental cycle, the chamber's vacuum level returns from 2×10^{-10} to 2×10^{-11} Torr. Maintaining a low background gas collision rate is crucial, especially for the production of Bose-Einstein Condensates (BECs).

During rubidium vaporization, the gas disperses uniformly across the chamber volume. At roughly 500°C, the Maxwell-Boltzmann distribution predicts the most probable particle velocity to be $v_{th} = \sqrt{2k_B T/m} \approx 400 \text{ m/s}$. This velocity allows particles to reach the farthest extents of the system (1 m) in 2.5 ms, significantly longer than the characteristic MOT-loading stage duration, rendering the dispenser's precise location within the chamber as non-critical. The Rb dispenser is connected to the current supply via vacuum compatible BD25 connectors with coppers wires alongside of the U- and Z-chip wires and flexible copper strain-relief wires, which all the wires are isolated with ceramic barrels to the supply line. This configuration is vital to accommodate for thermal expansion and prevent contact pad breakdown. Adjacent to the atom chip, two dispensers are installed: one in active service and the other as a standby.

Cycle (s)	Pulse (s)	V (V)	I (A)	T (°C)	Vacuum (mBar)
7	5	1	5	360*	8.1×10^{-11}
-	-	0.73	5	340**	-
-	-	-	-	367***	6.2×10^{-11}
20	10	0.87	6	370	1.0×10^{-10}
-	-	-	-	-	$1.8 \times 10^{-11}****$

*Max after 10 mins, **Stable, ***Max when thermalized, ****Min after a full cycle

Table 4-1 Operational parameters for Rb dispenser

The operational parameters of the Rb dispenser are summarized in Table 4.2.2. The dispenser is activated with a 1 V pulse over a 5 s duration within a 7 s cycle, driving a current of 5 A. The temperature of the dispenser rises to a maximum of 360°C after 10 mins and stabilizes at 340°C. The vacuum pressure peaks at 8.1×10^{-11} mBar. A second operational mode with 0.73 V on the dispenser and a total circuit resistance of 0.146Ω results in a power consumption of 3.65 W and a maximal thermalized temperature of 367°C. The vacuum pressure in this regime reaches a maximum of 6.2×10^{-11} mBar. An alternative cycle time of 20 s with a 10 s pulse at 0.87 V produces a maximal temperature of 370°C and a vacuum of 1.0×10^{-10} mBar with a maximal current of 6 A. The minimal vacuum pressure attained after a complete cycle is 1.8×10^{-11} mBar, indicating an almost complete recovery of the vacuum state post-operation.

4.3 AOM drivers

This section provides a brief summary of how we successfully designed and prototyped our AOM drivers, achieving significant amplification gains at a substantial cost reduction compared to market alternatives.

4.3.1 RF synthesizers

In our setup, as shown in Fig. 5-3, we utilized eight AOMs: one 350 MHz AOM required in the entanglement branch of the source generation optical circuit, three 100 MHz, three 200 MHz, and one 80 MHz AOMs in other branches such as OP, IMG, MOT, and PGC. To drive these AOMs, we needed RF signals, sourced from RF synthesizer boards. We employed two types of synthesizers in our experiments: the AD9959 4-channel RF synthesizer and the EVAL-AD9959 DDS board. The AD9959 is a multi-channel frequency synthesizer that incorporates four synchronous direct digital synthesis (DDS) cores with various user-programmable functions. The DDS board is a full-featured evaluation board, with PC evaluation software provided by the developer. The USB interface graphic user interface provided with the device allows for easy control and measurement of the AD9959, offering many user-friendly features such as a mouse-over effect. The hardware and software elements could be practically verified by testing the software modules with frequency sweep capability for board control and data analysis.

4.3.2 Amplifier and filters for DDS AD9958 and AD9959

As depicted in Fig. 4-6, the evaluation synthesizer EVAL-AD9959 DDS board is on the left, with the NWDZ RF-PA amplifier on the right. Our AOM driving frequency requirements necessitated the use of amplifiers to achieve the threshold and desired limits of RF requirements. Hence, we used the NWDZ RF-PA amplifier in both setups shown in Figures 4-7 and 4-8. The setup in Fig. 4-7 employed the DDS AD9958 synthesizer along with the NWDZ RF-PA amplifier to drive the higher frequency needs such as the 350 MHz and 200 MHz AOMs. In contrast, the setup in Fig. 4-8 utilized the AD9959 4-channel O/P synthesizer along with the NWDZ RF-PA amplifier as a low-frequency driving unit, designed to drive the 100 MHz and 80 MHz AOMs.

To reduce amplification noise and achieve a clean output signal from the amplifier, we implemented a multi-stage filtering process. After several trials and errors, we found that a three-stage filtering configuration worked best for our 350 MHz RF signal input. The MCL 3 4H5 SXBP-350 filter was used in this configuration. The input signal from the synthesizer was fed into two filters in series, followed by the amplifier, another filter, an NWDZ RF-PA amplifier, and finally an attenuator of -30 dBm, resulting in a filtered 350 MHz mode signal (+3.5 dBm). This output signal was used to drive the 350 MHz AOM in the system, while the three 200 MHz AOMs were powered directly by the NWDZ RF-PA amplifier without additional filtering. However, no filtering schemes were implemented in the AD9959 4-channel RF synthesizer unit, as shown in Fig. 4-8, where one 80 MHz and three 100 MHz AOMs were powered without filtering. In critical stages, these AOMs functioned with a minimum power requirement of around 1 dB each in the system.

4.3.3 Characterization of the amplifier NWDZ RF-PA V2.0

We used the NWDZ RF-PA amplifier, characterized by a wide frequency range, high gain, and a small noise figure, making it suitable for various RF receiving front ends. Several power tests were conducted to analyze its suitability for our AOMs' power requirements in the system. The amplifier operates across a frequency range of 0.1-2000 MHz, with the gain dependent on the input frequency F : for $F = 0.1$ MHz, the gain is 32 dB; for $F = 500$ MHz, it's 31 dB; for $F = 1000$ MHz, 29 dB; for $F = 1500$ MHz, 25 dB; and for $F = 2000$ MHz, 20 dB. The maximum output power is +10 dBm (10 mW) at the 1 dB compression point, and the noise figure is 1.9 dB. The amplifier requires a power supply voltage range of 6-12V DC and has a system impedance of 50 ohms.

The test results for the NWDZ RF-PA V2.0 amplifier are as follows:

Input Power	Input Frequency	Output Power
1 mW (0 dBm)	700 MHz	0.5 W
1 mW (0 dBm)	350 MHz	2 W
1 mW (0 dBm)	200 MHz	3 W
1 mW (0 dBm)	80 MHz	5 W

Table 4-2 Test Results for NWDZ RF-PA V2.0 Amplifier

The amplifier was tested with both the Agilent technologies synthesizer and our synthesizer boards. The amplification gains with the board are as follows: at 80 MHz,



Fig 4-6 Evaluation board featuring the Analog Devices AD9958 multi channel Direct Digital Frequency Synthesizer IC. The AD9958 incorporates two synchronous DDS cores with many user-programmable functions. Evaluation board software provides a graphical user interface for easy communication with the DDS device along with many user-friendly features and in the right side of the figure RF amplifier NWDZ RF-PA which is employed in the scheme of AOM driver circuits developed to drive the AOMs in the optics blocks

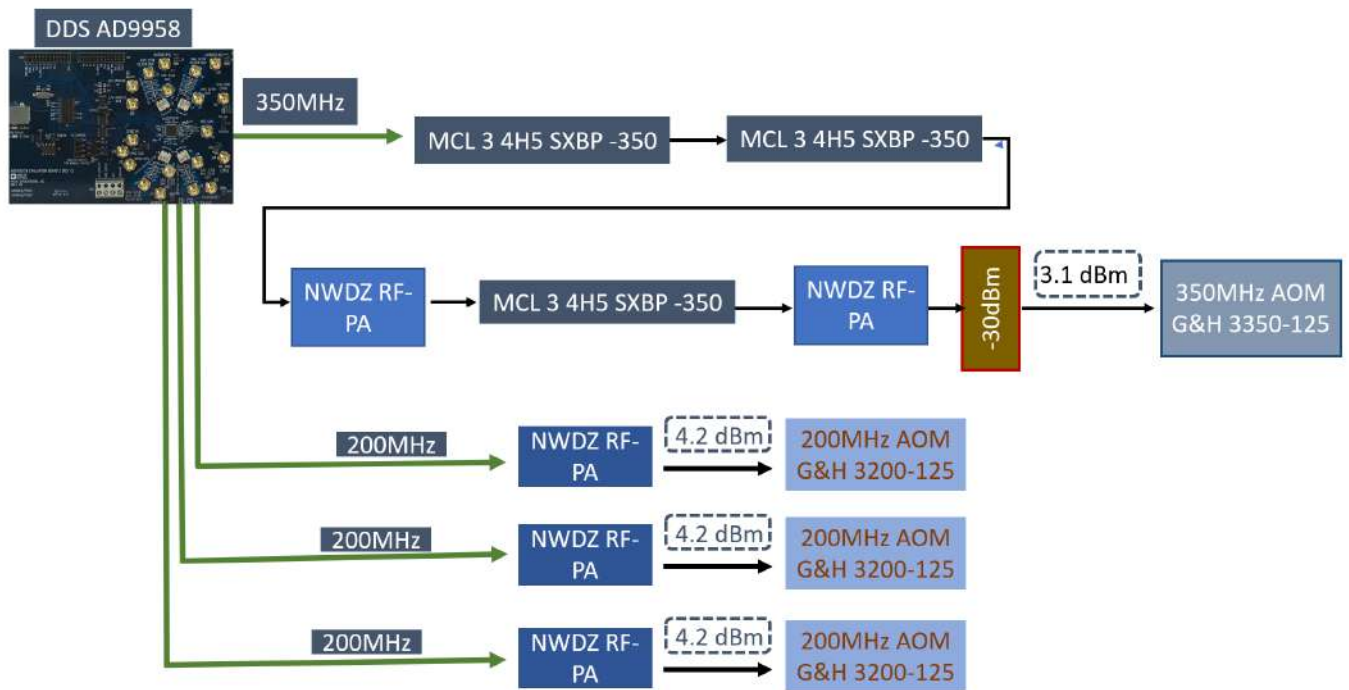


Fig 4-7 Home made design of our experiments' AOM drivers scheme. This Unit is being designed to drive one 350Mhz AOM and three 200MHz AOMs

the gain is 5.1 dBm; at 100 MHz, 5.3 dBm; at 200 MHz, 4.2 dBm; and at 350 MHz, 3.1 dBm (2W+). We also tested the amplifier's ability to work with 80 and 100 MHz frequencies using signals from the 4-channel RF synthesizer, with each channel delivering 2W to 5W for the 100 MHz and 80 MHz frequencies, respectively, as depicted in Fig. 4-8.

4.4 Experimental apparatus

4.4.1 Vacuum chamber and bake-out procedures

Fig. 4-9 illustrates the design of our vacuum chamber used in the experiment. The atom chip, central to our system, is housed in an ultra-high vacuum (UHV) chamber made of stainless steel with minimal relative permeability. This feature is essential to allow external magnetic fields to access the atom chip and surrounding atoms effectively. When the relative permeability equals 1, the material is magnetically flux-transparent, making its value significant to the system's performance. The atom chip is secured by a copper rod on top of the chamber (see Fig. 4-9). The chamber steel, any external conductors, and a common ground are all electrically insulated from the atom chip wires. The chamber is mechanically and acoustically securely attached to the optical table. The windows are anti-reflective and can withstand temperature changes of up to 5 degrees Celsius within a few minutes.

The bake-out was conducted with variac power wires TDGC2-3K (output voltage 0-250V, 3kW), applying a peak maximum voltage of 140V, starting from 50V with a 10V increase at constant intervals of 10 minutes. The temperature on the viewports (bottom) was observed to be 250 °C. Dispensers Rb1 and Rb2 were installed. During the bake-out process, we characterized them with 0.6 V voltage, 10 A current, and 59 mOhm in situ; stability was observed at 475 °C. We employed an Agilent gauge with its driver, the Agilent E8257D PSG Analog Signal Generator. The ion pump, forming plasma vortex filamentations, produced a suction force in the magnetic field, guiding particles away after their breakdown in a high electric field. Along with the Agilent gauge and the ion pump in creating our UHV, we ran a Turbo pump (Limit Vacuum) with run time records starting from valve opening stages to equate with the pressure until the desired vacuum was achieved. The record vacuum attained was 1.4×10^{-11} mbar, or approximately 1×10^{-11} Torr, in the turbo pump, with its current level from the UHV particles as 6.5 nA.

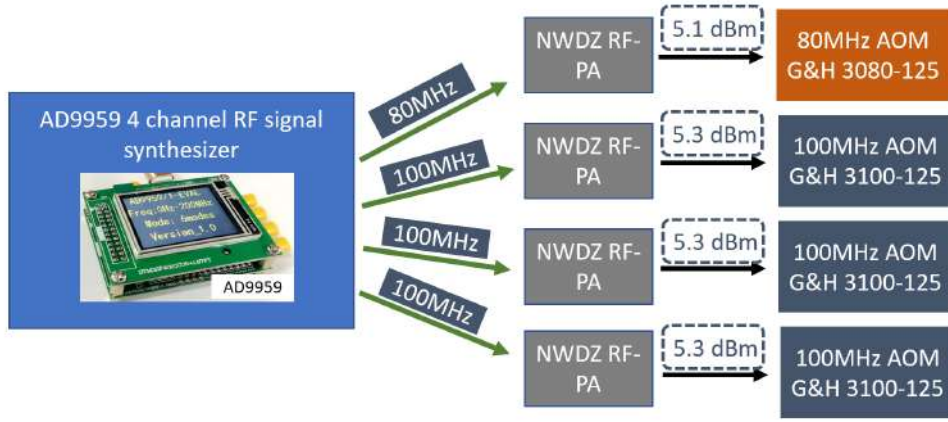


Fig 4-8 Home made design of our experiments' AOM drivers scheme. This Unit is being designed to drive one 80Mhz AOM and three 100MHz AOMs

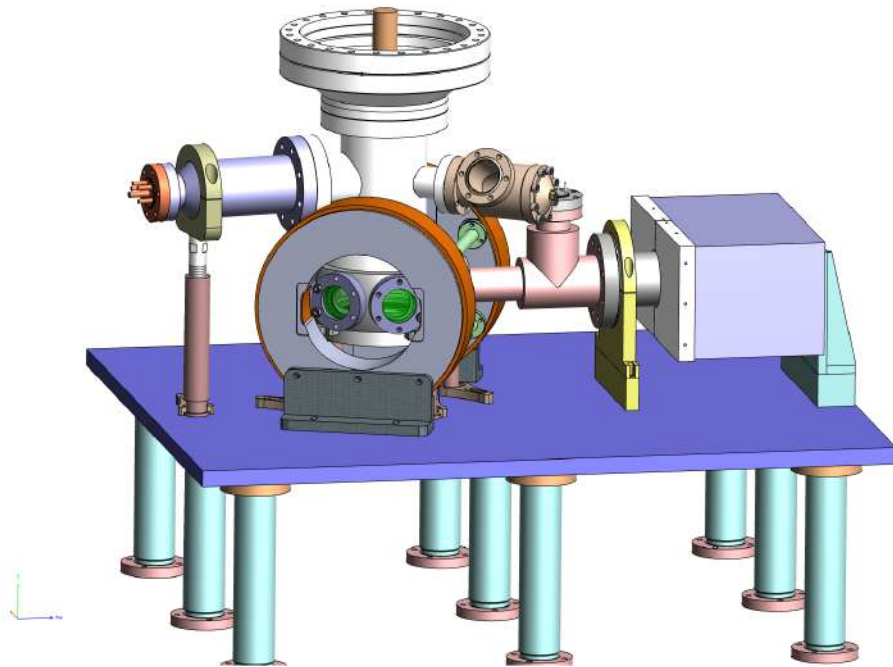


Fig 4-9 3D design of our experimental setup, showing quadrupole coils in brown. The protruding cylindrical copper bar on the upper flange of the vacuum chamber is part of the cooling system for the atom chip, mounted on the bottom edge of the copper holder. The quadrupole-field gradient $|B|$ is shown along the y-axis in units of G/m, calculated against the coil separation distance along the x-axis.

4.4.2 Anti-Helmholtz (quadrupole) coils design

The quadrupole coils, a pair of coaxial coils positioned at an angle to the coordinate planes, have identical magnitudes of current flowing in opposite directions. The fields generated by the coils balance halfway between them, forming a zero-field point due to their symmetrical shape [161, 162]. These coils, driven with a current of 20A and having 600 turns with an effective outer radius of 9 cm (inner radius 7 cm, outer radius 10.3 cm), do not represent the ideal ratio for the largest and most linear gradient of the magnetic field at the geometry's center ($d = R$). However, the gradient is sufficiently strong and linear on a millimeter scale. To characterize the field from a coil, the magnetic field from an infinitely thin circular wire is divided into a succession of multipoles in [161], with the quadrupole being the lowest order that allows a magnetic dipole to be trapped in a local $|B|$ -minimum. The magnetic field potential $|B|$ is calculated using all orders in Fig. 4-10, and the trap lower limit from the analytical formulation is obtained by the Eq. 4-6. From the Biot-Savart result, derived for a single-loop on-axis field component of two coils with co-directed currents, we get a good approximation of the magnetic field at the coil center.

$$B_z = \frac{\mu_0 I}{2\pi} \frac{1}{\sqrt{(R+\rho)^2 + (z-A)^2}} \left(\frac{R^2 - \rho^2 - (z-A)^2}{(R-\rho)^2 + (z-A)^2} E(k^2) + K(k^2) \right) \quad (4-4)$$

$$B_\rho = \frac{\mu_0 I}{2\pi\rho} \frac{z-A}{\sqrt{(R+\rho)^2 + (z-A)^2}} \left(\frac{R^2 + \rho^2 + (z-A)^2}{(R-\rho)^2 + (z-A)^2} E(k^2) - K(k^2) \right) \quad (4-5)$$

$$k^2 = \frac{4R\rho}{(R+\rho)^2 + (z-A)^2} \quad (4-6)$$

and the field potential is given by:

$$|B| = \sqrt{B_z^2 + B_\rho^2}. \quad (4-7)$$

In these equations, B_z and B_ρ represent the magnetic field projections onto the z and ρ axes of cylindrical coordinates, measured in Gauss. The terms $E(k^2)$ and $K(k^2)$ are complete elliptic integrals of the first and second kinds, respectively. Here, the z -axis aligns with the axis of the coils, A denotes the distance from the coil to the origin, and R is the coil radius. The vacuum permeability, μ_0 , is given as $4\pi \times 10^{-7} \text{ T} \cdot \text{m/A}$ (or $4\pi \times 10^{-3} \text{ G} \cdot \text{m/A}$ in mixed units). For the purpose of these calculations, a mixed system

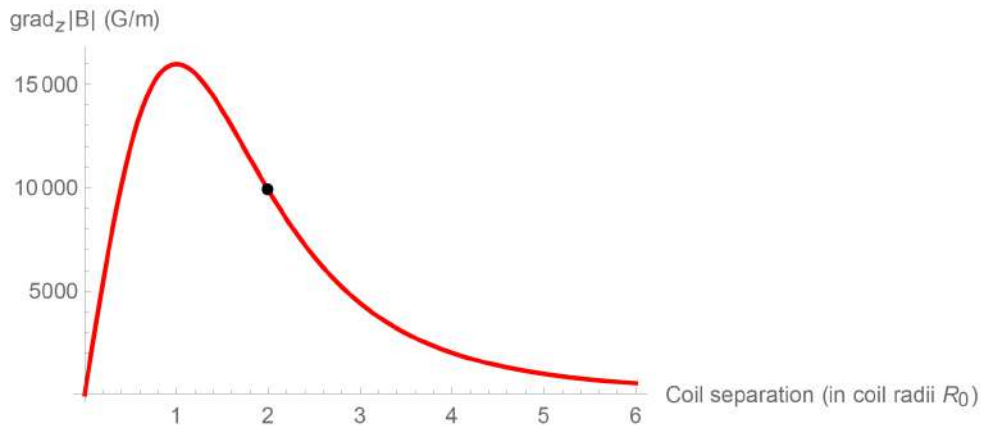


Fig 4-10 Field gradient of the quadrupole (Anti-Helmholtz) coil. The plot was generated with the following parameters per coil: current of 20A, number of turns $n = 600$, and effective outer radius $R = 9\text{cm}$ (inner radius $R = 7\text{cm}$, outer radius $R = 10.3\text{cm}$). The operating point is marked as a black dot. $|\mathbf{B}|$ is shown.

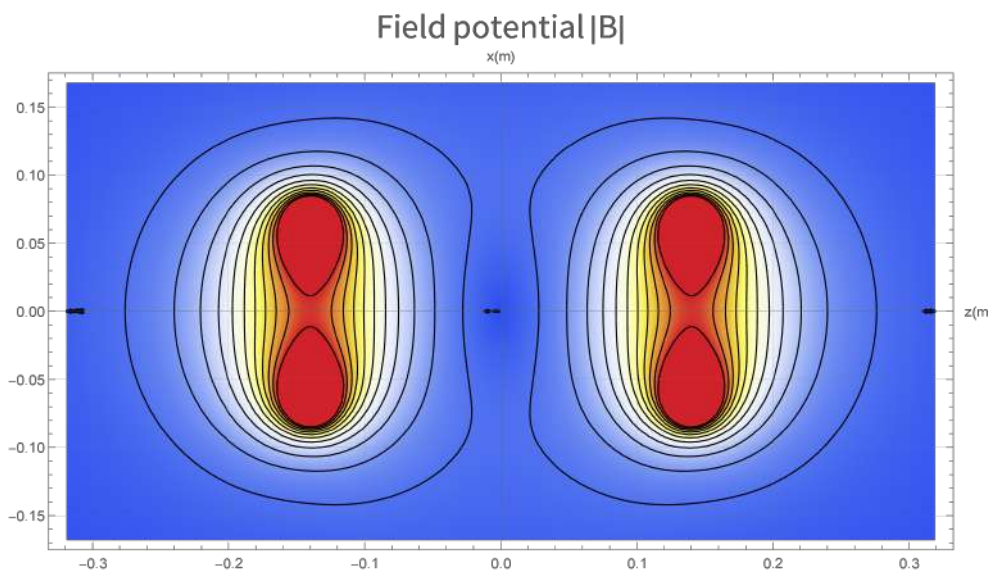


Fig 4-11 Magnetic field potential $|\mathbf{B}|$ of the quadrupole trap.

of units, specifically meters (m), Gauss (G), and Amperes (A), is utilized for its simplicity. Regarding the copper wire, AWG Gauge 12 specifies a wire diameter of $\phi = 2.053$ mm excluding the insulation, and it assumes a square cross-section, able to carry maximum currents of 20 A at 60°C, 25 A at 75°C, and 30 A at 90°C. As depicted in Fig. 4-11, an approximate potential map is provided at a reduced scale. The quadrupole-field gradients created by the coils approximate 100 G/cm along the distance separating the coils.

The high-current source and switch pose significant constraints in the coil geometry design. A complex issue is the absence of low-noise electronic switching techniques in the market. High currents are accompanied by significant thermally produced noise, resulting in trap instabilities. Our current setup operates at 20 amps. In theory, moving the coils closer together to achieve the optimal ratio of $d = R$ at the same currents appears to be a feasible solution, as suggested in [146]. Alternatively, expanding the coil radii could meet the optimal ratio at the expense of increased currents and heating challenges. Our current vacuum chamber design limits such modifications.

4.4.3 Helmholtz coils design

The Helmholtz coil is designed to create a uniformly directed magnetic field through each atom trap in the atom chip. To validate this homogeneity constraint, we calculated the gradient of the magnetic field across the chip's surface, ensuring it is as close to zero as possible. The chip's face is aligned so that the Helmholtz field is directed across it. Considering the on-axis approximation for the magnetic field of a wire coil [163], the exterior pair of uniformly wound coils in the vacuum produces a substantial, homogeneous magnetic field. The spacing between the coils must equal their radius ($d = R$), and equal currents must flow in the same direction, so that the fields of the coils add to the overall axial field in the positive x -direction. The coils are designed with the atomic cigar rotation in the Z-wire of the atom chip in mind, calculated to be 10 cm by 70 cm, thus $\arcsin(1/7) = 8^\circ$.

The Biot-Savart law, derived from a single-loop on-axis field component of two coils with co-directed currents, provides a good approximation of the magnetic field at the coil center in Gauss:

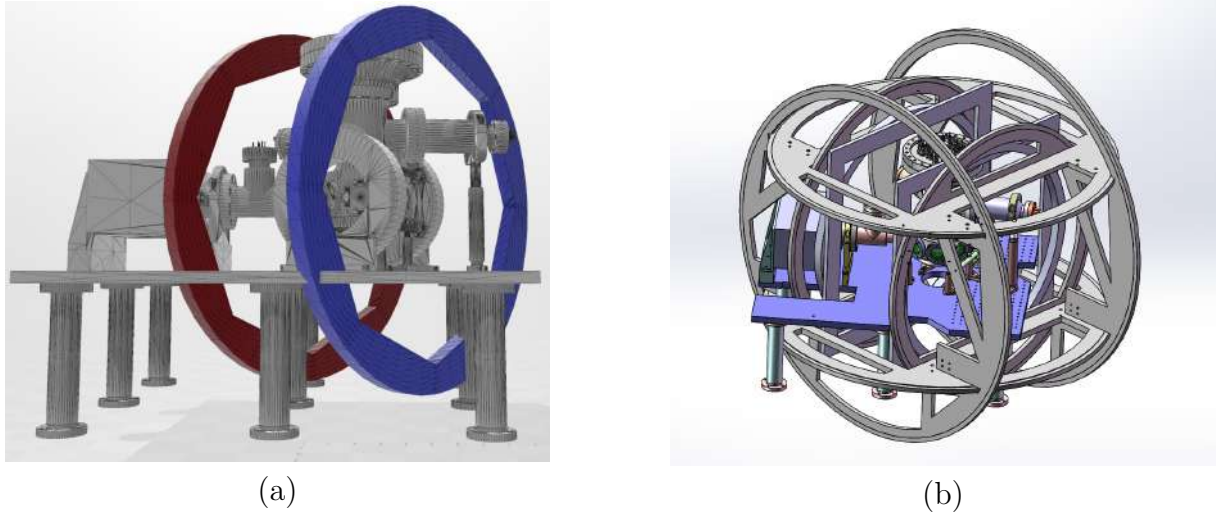


Fig 4-12 Fig. (a) Helmholtz coil design alongside the vacuum chamber. The coil alignment ensures the Helmholtz field is directed across the face of the chip. Given the radius of the Helmholtz coils is much larger than the length of the chip, the coils are intentionally tilted at an 8° angle with respect to the y-axis to match the cigar rotation of the z-wire in the atom chip ($\arcsin(1/7) = 8^\circ$). The on-axis approximation for the magnetic field of a wire coil is justified in this configuration. Fig. (b) shows the assembly design of the 3 pairs of correction coils

$$B_x = \frac{8\mu_0 n R^2}{(d^2 + 4R^2)^{3/2}} I, \quad (4-8)$$

where the field at the center of the coils becomes $B_x = 3.16929I$ G with a vacuum permeability of $\mu_0 = 4\pi \times 10^{-3}$ G · m/A, 80 turns in each coil, a total current I of 30 A through the coils linked in series, a radius R of 0.33 m, and a distance d between the coils of 0.121 m. The Biot-Savart result, with a 3 percent error margin, matches our calibration measurements and the magnetic field potential simulation shown in Fig. 4-15.

It is important to consider that nullifying the effect of other parameters, such as variations in the field due to resistance inaccuracies in the control electronics, is not feasible. Correcting the factor by considering only the potential in combination with the laser field would be inaccurate. Inside the 3 cm MOT-beam diameter, the trap potential is very linear and can be accurately described by its gradient in both directions. Achieving this requires precise control in the electronics, especially controlling the resistors in the control circuits.

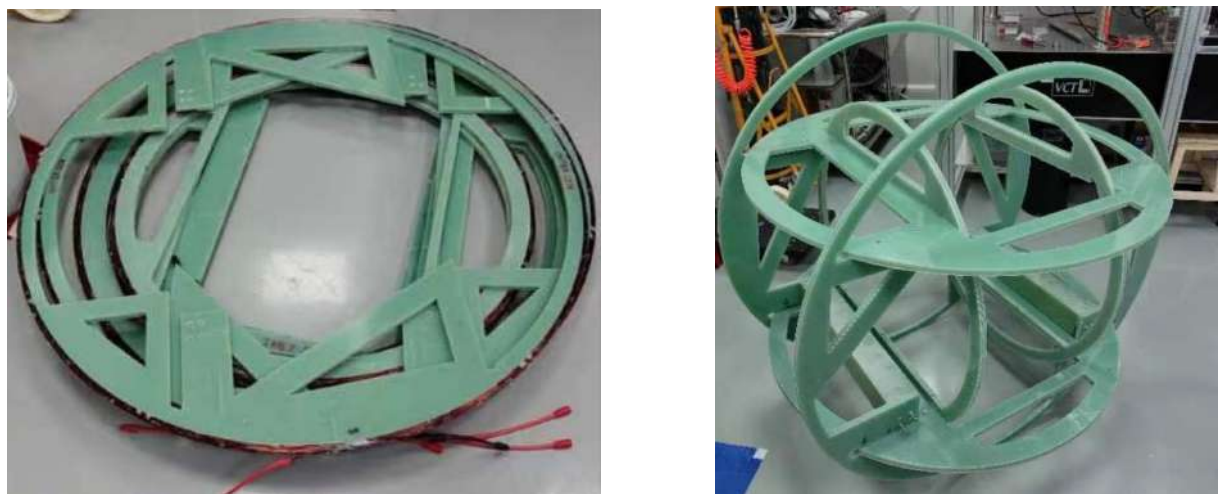


Fig 4-13 The Helmholtz coil design progress steps

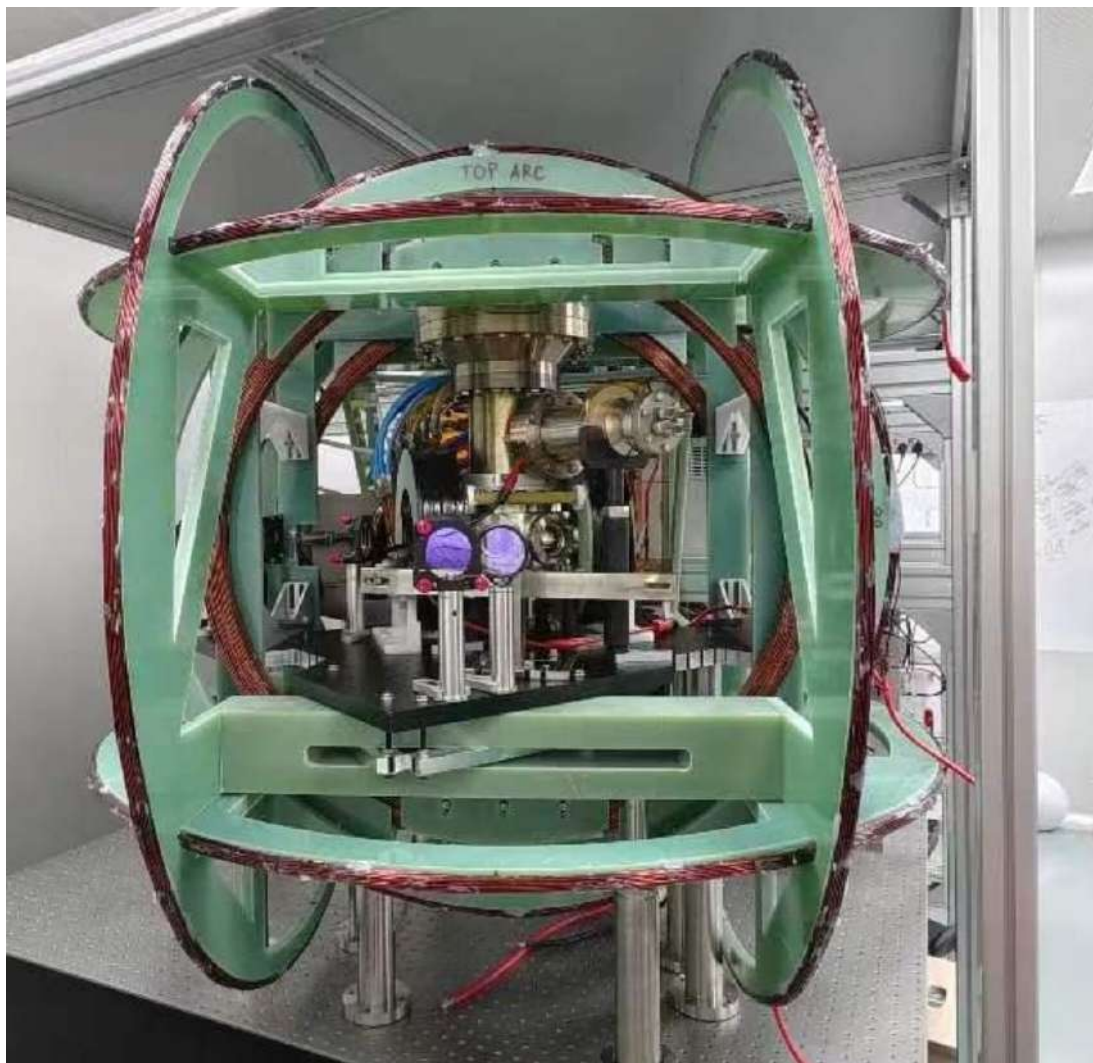


Fig 4-14 The designed Helmholtz coil steps being mounted around the vacuum chamber design

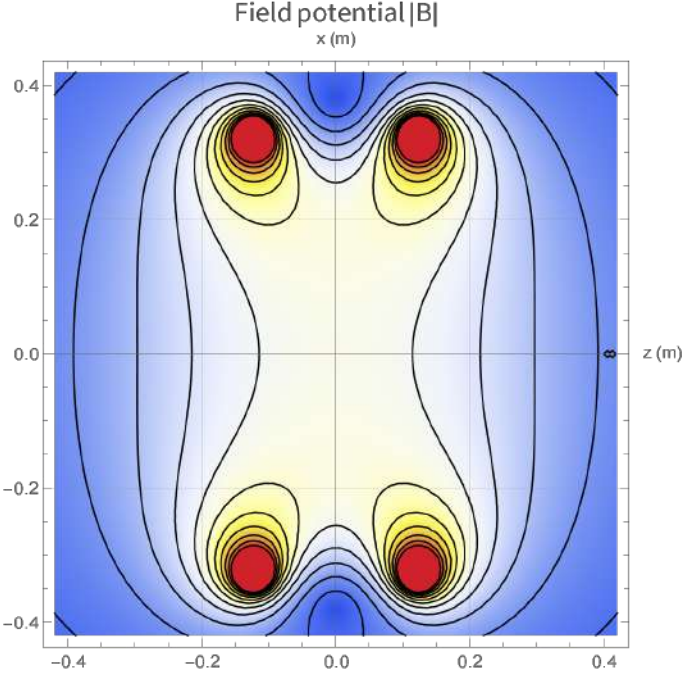


Fig 4-15 Magnetic field potential $|\mathbf{B}|$ of the Helmholtz coil.

4.5 Main experimental scheme

4.5.1 BEC preparation on atom chip

This subsection examines the timeline of achieving a Bose-Einstein Condensate (BEC) on top of the atom chip, starting from creation to entanglement generation between BECs. Our main scheme involves positioning two BECs in the path of a Mach-Zehnder Interferometer. The BEC generation cycle begins with a well-defined spin state $5^2S_{1/2}(F = 1, m_F = -1)$, designated as $|1, -1\rangle$ in the $\{|F, m_F\rangle\}$ basis. We deliver a current to Rubidium dispensers, characterized as follows: for Rb1 and Rb2 with an applied voltage of 0.4 V in parallel, a total current of 6.7 A is applied continuously for 60 s, resulting in a dispenser temperature of 290°C, which is below the vacuum chamber's maximum temperature limit. Our proposed timeline sequence for achieving BEC involves several stages: starting from rubidium vaporization and vacuum recovery for 15 seconds, followed by transfer to a strong-field trap until 34.5 seconds. As shown in Fig. 4-16, the trap beams are halted sequentially at 35.701 seconds and 35.703 seconds. At 35.7032 seconds, the repumper and optical pump beams are halted, transforming the state of the cold atoms in MOT eventually into a BEC state, which is held until the 45th second. The counter-propagating quadrupole magnetic field and MOT-laser beams in left and right

circularly polarized configuration [9], in combination with RP light, are shown in Fig. 5-1. The axial quadrupole-field gradients are 1000 G/m, as shown in Fig. 4-10, confining the MOT within an area of approximately 3 cm across the space irradiated by the trapping beams. This leads to a consistent BEC manufacturing sequence, as proposed in the timeline 4-16. The MOT fluorescence is captured by a calibrated photodiode, used to determine the atom number as per [6, 37]. The cloud temperature rises during compression. Polarization gradient cooling is employed in a small magnetic field, where it is most effective, keeping the field relaxed at about 1 to 2 G for another 1.6 ms for optical pumping (OP). The OP-laser detuning is set at $\text{OP} = +10 \text{ MHz}$, providing optimum pumping for a limited range of parameters [6, 164]. Turning off the U-wire current and the lasers, we then perform frequency measurements of the chip's trap axis as per [6, 164].

4.6 Complete setup

From Fig. 5-6, the overall scheme of our experimental setup is shown. The chip is positioned atop the light beam paths, held by a copper holder which also acts as a heat sink. The beam diameters of the MOT, RP, and PGC are 30 mm, which are mixed via a Brewster plate. The AOMs (from Gooch and Housego) have spot sizes of 1.5 mm for 80 MHz, 1 mm for 100 MHz, 1 mm for 200 MHz, and 1 mm for 350 MHz in the source generation block. Once generated, they are converted to 30 mm with telescope arrangements. The atom chip is installed in a vacuum chamber, surrounded by coils and beams supplied from PM-fibers. To avoid illusory oscillations of cold atoms in the trap, the experiment is positioned on a fixed-base optical table without pneumatic damping. PS14 is mounted on a rotational mount to block linearly polarized light at various angles. In the MOT light block, the entire spectroscopy consumes 1 mW, which is significant since we are limited to about 70 mW of spare power in this block, and some more will be lost at the fiber coupling.

4.6.1 Experimental geometry

Fig. 4-17 shows the atom chip and deployment of laser beams in the experimental setting; blue and red solid lines represent the atom chip. In Fig. 5-6, on the top right, the inserted picture shows the chip as a green rhomb where trapping and entangling laser

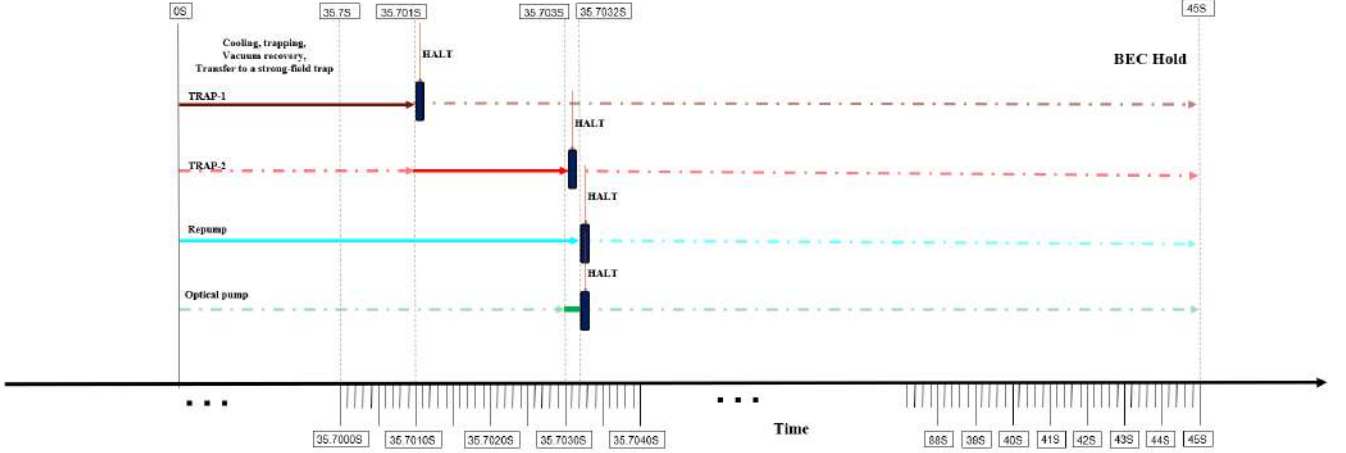


Fig 4-16 A basic timeline diagram for a BEC-BEC entanglement generation experiment, outlining the four stages: i) Cooling and trapping, ii) Vacuum recovery, iii) Transfer of atoms to a strong-field trap, and iv) BEC hold [6].

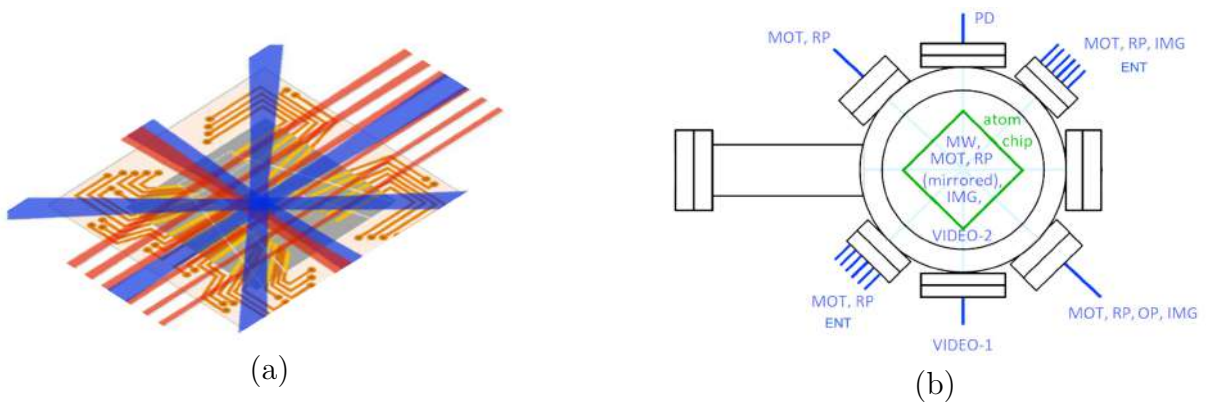


Fig 4-17 Fig.(a) is illustration of the chip and flying beams on top with their appropriate dimensions. Red and blue solid lines are schematically depicted with the atom chip representing mixed MOT and RP beams except the horizontal blue beam will be approaching the chip from the bottom, the z-branch of MOT and RP beams. Fig.(b) is the illustration of the bottom view of chip with the flying beams orientation

beams are depicted in blue. Their functional designations are as follows: MOT –magneto-optical trapping beam, also reused for sub-Doppler cooling. PGC –Polarization Gradient Cooling, RP –repumping laser, and OP –Optical Pumping to a particular well-defined quantum state, specifically a magnetically stretched magnetic substate in the electronic hyperfine ground state. Since there are two doubly polarized magnetic substates in rubidium, we choose between them depending on our specific experimental needs. IMG –source for imaging or probing light, either for absorption or phase-contrast imaging detection. For IMG, we consider a few alternative locations as shown in Fig. 5-6. Additionally, we have an ENT or entanglement beam to generate entanglement between the BECs trapped on top of the atom chip with potential gradients created by chip wires. Additional options for PD –photodiode, VIDEO-1 and VIDEO-2 –tele-macro video cameras of CCTV type for two-plane in-situ real-time fluorescence dynamics observation and MOT alignment purposes are depicted in the scheme.

4.6.2 Preparation of atoms in the atom chip

The initial setup aims to build sources suitable for high-precision optical spectroscopy of the hyperfine-split magnetic levels of ^{87}Rb . The trapping magnetic field, which provides the structural layout of the trapping field, including the atom chip, establishes the relationships between the other elements of the setup. The first step in the process is the magneto-optical trapping (MOT) of a rubidium vapor. Atoms are then transferred to atom chip traps, where they are sub-Doppler cooled and optically pumped to the $|F = 1, m_F = -1\rangle$ state. The atoms are subsequently placed in the magnetic trap. At this final stage, the magnetic field can be tuned to a critical value, shielding the transition from induced magnetic noise and significantly extending its lifetime. A range of strengths in the coil pairs, with varying reaction times, are used to form the trap fields, depending on the control sequence requirements. The optical sources, comprised of specially coated laser diodes and commercial laser heads, have a linewidth of a few hundred kHz.

The initial stage of our experimental steps involves in creating the Magneto-Optical Trap for cooling ^{87}Rb atoms. As we have seen in the previous chapters, this process, which will begin with the atoms at ambient room temperature (approximately 300 K), is expected to employ magnetic fields and laser cooling techniques tailored to the atomic properties of ^{87}Rb . In the MOT phase, the precise locking of laser frequency and magnetic gradients will be crucial for effectively slowing down and trapping the atoms.

4.6.3 Vacuum recovery and optimization

Post-cooling, our experiment will progress into a critical vacuum recovery phase. Here, we anticipate reducing the temperature of the atomic ensembles to around 90 μK , with a vacuum level maintained at 2×10^{-10} Torr. The number of atoms during this phase is expected to be approximately 4×10^8 , a quantity that is crucial for the next steps of the BEC formation process. This phase is pivotal in ensuring minimal interactions with background gases, which could interfere with the cooling process and the formation of BEC.

4.6.4 BEC formation process

As our research moves forward, we will be utilizing strong-field traps, specifically U-MOT and Z-MOT, to further manipulate the atomic cloud. These traps, known for their high control over magnetic field gradients, will be instrumental in cooling and compressing the atoms to conditions conducive to BEC formation. We anticipate that during this phase, the temperature and cloud dimensions will be key factors. For instance, the atomic cloud's radius is expected to be around 1.2 mm in the U wire MOT phase, with a further reduction in the Z-MOT phase.

4.6.5 Advanced cooling techniques

To reach the ultra-cold temperatures necessary for BEC formation, we plan to utilize advanced cooling techniques like polarization gradient cooling and optical pumping. In particular, polarization gradient cooling will be employed to achieve lower temperatures and higher phase-space densities. Optical pumping, which involves the use of laser light to alter the internal states of the atoms, will also play a crucial role in this phase. By adjusting the frequency and polarization of the light, we anticipate transferring the atoms to specific quantum states essential for BEC formation.

4.6.6 Imaging the atoms

In this study, a straightforward absorption imaging technique, referenced in [121, 165–167], employing a system with a magnification factor of three is demonstrated in Fig.

4-18. This methodology captures four distinct components on the imaging plane: a clear depiction of a cloud at the lens' focal point, a probe beam and a scattered shadow, both situated off-focus, and a noticeable mark from some fluorescent light striking the lens aperture.

Fig. 4-18 provides an elaborate representation of two-state imaging using σ^+ light transitioning from $|2, +2\rangle$ to $|3, +3\rangle$, other MZI path configurations elaborations on the concepts introduced in Fig. 4-18 will be explained in the next chapter. This imaging process is conducted in conjunction with either microwave adiabatic passage and Stern-Gerlach state separation or the use of repump light. The aimed approximate duration of the imaging pulse would be $100 \mu\text{s}$, is to prevent blurring of the cloud due to photon recoils. The focal length of the imaging lens and the distance between the CCD camera are aligned.

4.6.7 Expected BEC production stages

In the expected BEC production sequence $5^2S_{1/2}(F = 1, m_F = -1)$, identified as $|1, -1\rangle$. Following this, the MOT-loading stage will start at 34.5 seconds with Rb vaporization at a current of 5 A, aiming to capture 4×10^8 atoms at $140 \mu\text{K}$ at 35.701 s. The process will then proceed to the MOT Saturation stage, which will be aimed to be stopped at photodiode signal saturation, and the pressure is expected to increase to 2×10^{-10} Torr. In the Compression stage, the system will be aimed to be compressed by a U-wire with current of around 5 A with DC components. This will be followed by cooling, where polarization-gradient cooling will be aimed to reduce the temperature to $40 \mu\text{K}$, with MOT-laser detuning projected to change from $\Delta_{\text{MOT}} = -18 \text{ MHz}$ to $\Delta_{\text{PGC}} = -62 \text{ MHz}$. The Optical Pumping stage will then aim to relax the field at 1-2 G, with OP-laser detuning of $\Delta_{\text{OP}} = +10 \text{ MHz}$, leading to an expected accumulation in the $|2, -2\rangle$ state. Subsequently, in the next stage, both the U-wire and lasers will be turned off, and the Z-wire trap will be formed with frequencies $\omega_x = \omega_y = 2\pi \times 97.6 \text{ Hz}$ and $\omega_z = 2\pi \times 11.96 \text{ Hz}$ as in similar case to [6]. Finally, the RF Evaporation stage will involve pre-cooling from 25 MHz to 560 kHz and a second stage from 2.37 MHz to 2.27 MHz, resulting in an anticipated $N_{\text{BEC}} = 30 \times 10^3$ atoms. The following table 4-3 aims explaining our future experimental target steps for ^{87}Rb BEC formation and transferring to atom chip

No.	Time	Procedure aim	Target Trap	Temp
1	0s	Cooling, trapping	MOT	300 K
2	9.5s	Cooling, trapping	MOT	-
3	15s	Vacuum recovery	MOT	90 μ K
4	34.5s	Transfer to strong-field trap	U-MOT	90 μ K
5	35.701s	Polarization gradient cooling	U-MOT	140 μ K
6	35.703s	Optical pumping	U-MOT	40 μ K
7	35.7032s	Transfer to Atom Chip trap	Z-MOT	50 μ K

Table 4-3 Experimental target steps for ^{87}Rb BEC formation and transferring to atom chip.

4.6.8 BEC-BEC entanglement and QND measurements on atom chip

Several experiments have demonstrated entanglement within a single BEC cloud [82, 157, 158], highlighting a significant advancement in quantum mechanics. However, entanglement between two distinct BEC clouds has been a challenging frontier. Notably, our experiment was unique in this regard until the recent work by Treutlein et al. [168], which achieved entanglement between two separate BEC clouds through a novel splitting and freefall experiment. Despite this, our approach remains distinct: we propose a scheme for two-qubit entanglement generation through interaction between BECs confined in the Z-wire trapping potential of the atom chip, as shown in 4-19. This in-situ approach to BEC entanglement in our experiment sets it apart from the methodology used by Treutlein et al. Our experiment, detailed in this subsection, will generate two-qubit entanglement through interaction between BECs confined in the Z-wire trapping potential of the atom chip, representing an in-situ entanglement experiment. Our future work will explore the feasibility of implementing two-qubit quantum gate by properly entangling the two qubits using QND light, a 2- BEC qubits entangled state can be formed. This state would be characterized by the qubits being in a superposition of all being in one state or all in another, e.g., $\frac{1}{\sqrt{2}}(|00\rangle + |11\rangle)$, thus would be used in experimental implementation of multiple qubit gates and quantum algorithms. The scalability of our design structures for fundamental operations of universal quantum computing is also a subject of interest. Quantum entanglement, as established in several studies [3, 94, 155], is crucial for quantum information processing. We aim to elucidate the generation of entanglement between two BECs based on these works. This scheme, shown in Fig. 4-18, begins with establishing a QND effective interaction and later, in Fig. 4-19, addresses the scaling problem with multiple BECs along with the implementation of our entangled state of two BECs in a Mach-Zehnder interferometer.

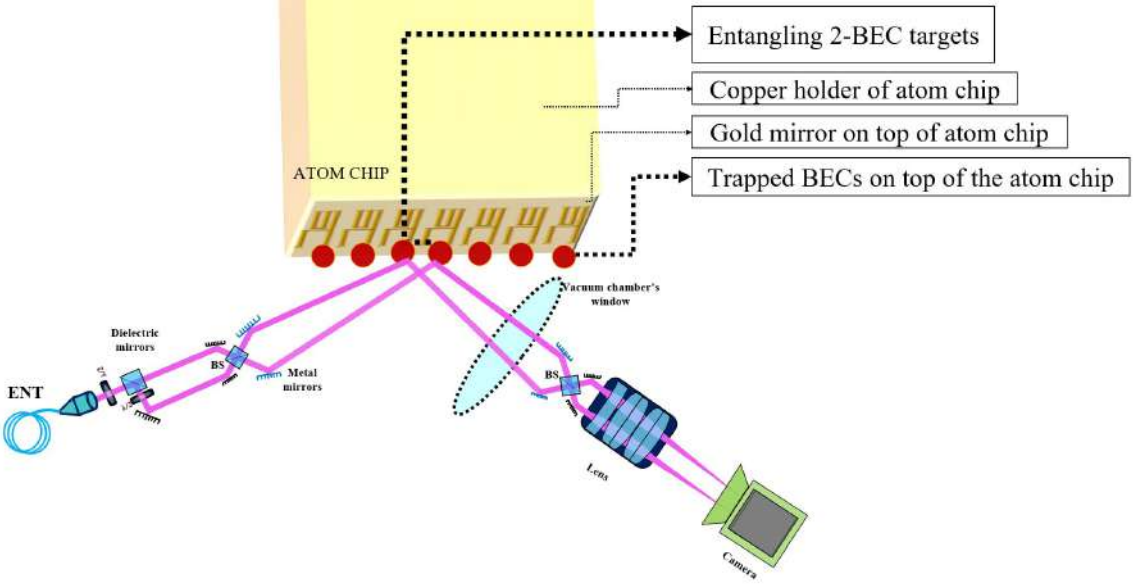


Fig 4-18 shows the configuration scheme for establishing QND effective interactions in an experimental setting. The beamsplitter BS_1 divides coherent light into two modes, top and bottom. Through the QND Hamiltonian, each mode interacts with BEC qubits 1(3rd positioned from left to right) and 2 (4rd positioned from left to right) on their path to BS_1 and mirror, resulting in interfered modes both being projected in parallel towards the lens followed by the camera [3, 7]. Thus the setup configuration would aim for BEC-BEC entanglement of 2 BEC targets with MZI setup

This section explains the generation of entanglement between BECs through the QND measurement-induced process [3]. As a representational experimental scheme for cluster state generation using QND measurement between two BECs [3], we describe the feasibility of the experimental approach for creating entanglement between two distinct BECs separated in space. The setup begins with a laser light source, which after passing through a beamsplitter, splits into two modes a_j (where $j \in \{1, 2\}$), subsequently used to create two BEC clouds. Due to the QND Hamiltonian, each mode interacts with the respective BEC. The BECs' internal states can be configured as neutral atoms to employ a physical qubit and use one of the energy levels to form a cluster state. The modes are then interfered and detected using photodetectors measuring in the Fock basis with outcomes n_c and n_d respectively.

We consider two physical qubits each in well-separated traps, such as optically trapped neutral atoms in dipole traps or BECs in separate magnetic traps on an atom chip, or two BECs in optical dipole traps [169]. Each BEC has two internal energy states, represented by the bosonic annihilation operators g_j, e_j (where $j \in \{1, 2\}$). These internal states could be, for example, the $F = 1, m_F = -1$ and $F' = 2, m_F = 1$ clock states in ^{87}Rb .

The experimental scheme for cluster state generation using QND measurement [3, 94, 155] involves two neutral atom qubits, with qubit-1 having two encoded states and qubit-2 having four encoded states. The additional transition from state $|F = 2, m = 0\rangle$ is used in qubit-2. Z_2^b acts on qubit-2, making a -1 transition between encoded states $|1\rangle$ and $|3\rangle$, while coherent light generated in mode b enters a beam splitter to emerge as two modes a_j (where $j \in \{1, 2\}$). Each mode interacts with the qubits due to the QND Hamiltonian. The modes are then recombined to produce two new modes c, d , which are detected using photodetectors measuring in the Fock basis with outcomes n_c and n_d respectively.

4.7 Entanglement scheme and measurement design on BECs in the systems

A minimal entanglement scheme can be designed where the project involves one entanglement pulse followed by measurements in the J_z and J_x directions. Enhancement of entanglement is feasible through pulses in various finite spin directions, a strategy particularly useful in adverse scenarios. Given that the entanglement pulses are coherent light sources, entanglement is expected as long as there is an interaction producing a J_z -dependent phase shift in both branches of the Mach–Zehnder interferometer (MZI). This phase shift, upon interference facilitated by a beamsplitter (BS), is a precursor to entanglement occurrence. The spin basis alterations in our system would be executed using Microwave (MW) and Radio Frequency (RF) techniques, targeting sub-level magnetic splittings in the rubidium ^{87}Rb energy levels. For entanglement spin directions, the primary consideration is the geometric alignment with the light path. Distinguishing a mere phase shift from genuine entanglement is crucial. If atoms are introduced, they will induce a phase shift, but to verify entanglement, additional evidence is needed. Entanglement generation and detection are distinct processes; detection involves measuring the spins of the entire system in various bases, achievable through absorption imaging. By examining the correlations between the two BECs in J_x and J_y bases, entanglement can be demonstrated, as per the Hoffman Takeuchi criterion ([170]).

Concerning measurement outcomes indicative of entanglement, any result from the MZI should confirm entanglement. This measurement essentially quantifies the spin difference $S_{z1} - S_{z2}$. An outcome of 100/0 corresponds to $S_{z1} - S_{z2} = 0$, signifying $S_{z1} = S_{z2}$. For qubits, this state resembles $|0\rangle|0\rangle + |1\rangle|1\rangle$, as each term in the superposition main-

tains equal spin values. Different spin directions can be measured by initially performing a spin rotation, replacing S_z with J_z in the above discussion about $S_{z1} - S_{z2} = 0$. Our approach deviates from the scheme proposed by Polzik et al. [114]. A minimal scheme in our context would involve one entanglement pulse followed by measurements in the J_z and J_x directions, with potential enhancement through pulses in varied spin directions. In our experimental setup, the pink and red beam pairs are not sent simultaneously. The pink beam first entangles BECs 1 and 2. This sequence culminates in a 2- BEC qubits entangled state, entangling the two qubits. The process resembles a gate sequence, where each step incrementally increases entanglement, the resulting 2-BEC entangled state can be represented as $|00\rangle + |11\rangle$.

The initial preparation of all three target BECs in the $|+\rangle = |0\rangle + |1\rangle$ state is followed by applying the pink pulse, yielding the state $|00\rangle + |11\rangle$ for the first two qubits (ENT12 pulse). The third qubit remains in the $|+\rangle$ state. This projection ensures $J_{z1} = J_{z2}$, resulting in the aforementioned state. Subsequently, applying the ENT23 pulse (red) projects the spins of BECs 2 and 3 to equality. This projection is facilitated by the overlapping arms of the pink and red MZIs. The final state, $|00\rangle + |11\rangle$, signifies entanglement across all three BECs. Our approach is distinct from the methodologies employed in other related works [115], [82], [171]. Typically, these methods involve generating a single entangled BEC through atomic interactions, followed by splitting this state into two BECs, and finally detecting entanglement between them. In Treulein's approach, a spin-squeezed state is utilized, while Klempert employs a twin Fock state. In both cases, atomic interactions are the source of entanglement. In contrast, our method relies on a Quantum Non-Demolition (QND) measurement that partially collapses the wavefunction into an entangled state. In this context, light serves as a mere measurement device without exploiting its quantum properties. This necessitates the use of brighter coherent light for effective measurement.

The atom-photon interaction in our experiment is fundamentally an electromagnetic interaction. To utilize light as a measurement tool, there must be an interaction between the matter (atoms) and the photons. This principle underlies the QND interaction. However, in our setup, light is solely used for measuring the spin difference between the two arms of the MZI. The uncertainty relationship between spin and photon numbers, and the determination of spin through absorption-imaging of photon numbers, allows us to ascertain whether the system is entangled following the second pulse. Our experimental design uniquely considers the entanglement as a triple product of wavefunctions –involv-

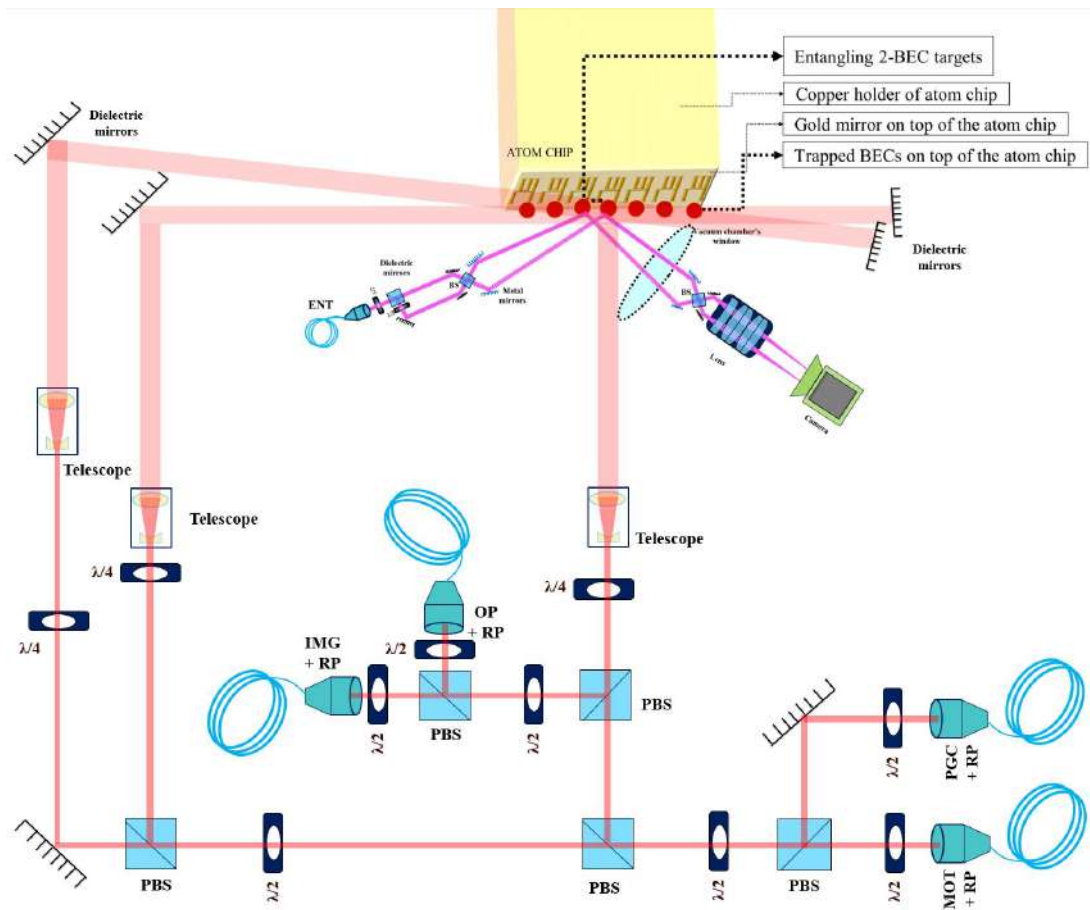


Fig 4-19 BEC-BEC entanglement generation on the chip. The 2- BEC qubits entangled $|00\rangle + |11\rangle$ states produced by two consecutive pulses of ENT beam. The blue mirrors in the MZI setup near the BECs are metal mirrors in the setup and the rest of the mirrors are dielectric mirrors. The wires connecting U and Z wire are not depicted in the picture.

ing two BECs and the spin of light. Unlike typical experiments that focus on the product of two BEC states, our approach considers the long-lived ground states of BECs and treats the photons post-interaction classically, disregarding the quantum properties of the light in the MZI. Decoherence channels in our experiment include atomic loss, dephasing due to magnetic field fluctuations, photon loss in the QND process (resulting in effective dephasing), and spontaneous emission during the QND interaction. Each of these factors contributes to the overall dephasing in the atomic system, and their impacts are carefully considered in the analysis of our experimental results.

4.8 Future experimental design trajectory

Given that BECs possess higher coherence and stability compared to other types of qubits, they are increasingly viewed as promising candidates for quantum computing applications in future quantum information technology devices. With this in mind, we aim to demonstrate the creation of entanglement between two BECs and have successfully laid the technical and theoretical foundations for our experimental setup. We have provided a solid theoretical basis for producing entangled states using quantum non-demolition measurements. Our system’s versatility allows physical qubits to be interlaced with two entirely separate beams, a highly desirable feature. The Mach-Zehnder arrangement permits the entanglement of widely spaced qubits, even when the line-of-sight is obstructed. The resulting entanglement could prove beneficial in quantum information applications such as quantum computing [30, 109] and quantum teleportation [172, 173]. This setup is geared towards creating entangled states as a component of a quantum gate. The Quantum Non-Demolition (QND) photon-BEC interaction serves as a key mechanism in our system for establishing entanglement between two spatially separated, trapped BEC clouds on an atom chip. We conclude that this line of research will progress towards the development of macroscopic quantum information systems, significantly advancing the field of quantum information processing. In summary, our work presents a comprehensive approach to generating and manipulating BECs on an atom chip, with the ultimate goal of achieving quantum entanglement between separate BEC clouds. The techniques and theoretical underpinnings outlined here lay the groundwork for future experiments and applications in the burgeoning field of quantum technology.

Our ongoing research into producing Bose-Einstein Condensates on an atom chip

is a complex process that merges advanced cooling techniques, precise vacuum control, and sophisticated trapping mechanisms. The journey from initial cooling in the MOT to the final stages of polarization gradient cooling and optical pumping is laden with challenges that we are poised to overcome. With the control of crucial parameters such as temperature, atom number, vacuum level, and cloud dimensions, we are on the cusp of making significant strides in understanding and manipulating this quantum phenomenon. The successful creation of BEC on an atom chip in the near future will mark a milestone in our laboratory but also open new avenues and possibilities of testing 3 qubit quantum gates and quantum algorithms. Several quantum algorithms can be tested with only three physical qubits. Quantum Teleportation involves transferring the state ψ of one qubit to another using entanglement and classical communication, represented as $|\psi\rangle_3 = \text{Teleport}(|\psi\rangle_1, |\beta_{00}\rangle_{2,3})$, where $|\beta_{00}\rangle$ is the Bell state [174]. The Deutsch-Josza Algorithm, which determines if a function is constant or balanced, can be demonstrated in a simplified form on a small quantum computer [175]. The 2- BEC qubits entangled state, a type of entangled state useful for illustrating quantum nonlocality, can be formed with three qubits as $\frac{1}{\sqrt{2}}(|000\rangle + |111\rangle)$ [176]. Basic Quantum Error Correction, essential for protecting quantum information, can be implemented with a bit-flip code [139]. The Quantum Fourier Transform, a critical component of more complex algorithms like Shor's algorithm, can be demonstrated in a rudimentary form with three qubits as [84]. Lastly, Entanglement Swapping, a fundamental concept for quantum networking, can be realized in a two-qubit system [177].

5 Optical circuit scheme and development

5.1 Required optical sources for ultracold atom preparation

In an ultracold atom experiment, multiple laser beams are required to cool, image, and entangle the atoms. Fig. 5-1 from our work [2] shows the required beams in the case of ^{87}Rb . For concreteness, we focus on the D2 line $5^2\text{S}_{1/2} \rightarrow 5^2\text{P}_{3/2}$ in ^{87}Rb , although similar transitions and other atomic species could also be used. The first step in an ultracold atom experiment is to create a MOT, where the atoms are cooled to the Doppler limit [9]. A MOT requires two optical sources, the first which performs laser cooling and the second to perform repumping (RP). The MOT transition is red detuned with a frequency $\Delta_{\text{MOT}} = -18$ MHz with respect to the $F_g = 2 \rightarrow F_e = 3$ transition. The RP cycle returns atoms that decay atoms to the $F_g = 1$ state to the $F_e = 2$ state. The atoms absorb photons from the laser in a retro-reflected configuration inside the vacuum chamber, while spontaneous emission puts the atoms in the ground state of the cycle again with external magnetic fields of around 1 G in tandem to slow down by reducing their velocities [11, 145]. This traps the atoms in a confined space. The laser cooling in the MOT stage enables cooling of the atoms to the Doppler limit, typically to microkelvin temperatures in the case of ^{87}Rb . To further cool the atoms below the Doppler limit, polarization gradient cooling (PGC) is employed, which requires a laser source that is detuned a further $\Delta_{\text{PGC}} = -18$ to -62 MHz from the primary laser. To further entangle the atoms, detuned light from the $F_g = 2$ to $F_e = 3$ state with frequencies ranging from $\Delta_{\text{ENT}} = -18$ to $+682$ MHz is used, which may be used for squeezing operations such as quantum nondemolition measurements (QND) [3, 136, 154, 178]. Finally, imaging of the atoms is performed via absorption imaging using a resonant transition from the $F_g = 2$ to the $F_g = 3$ state. This identifies the states that are in the $F_g = 2, m_g = 1$ sublevel and serves to perform a spin readout of the internal states of the atoms.

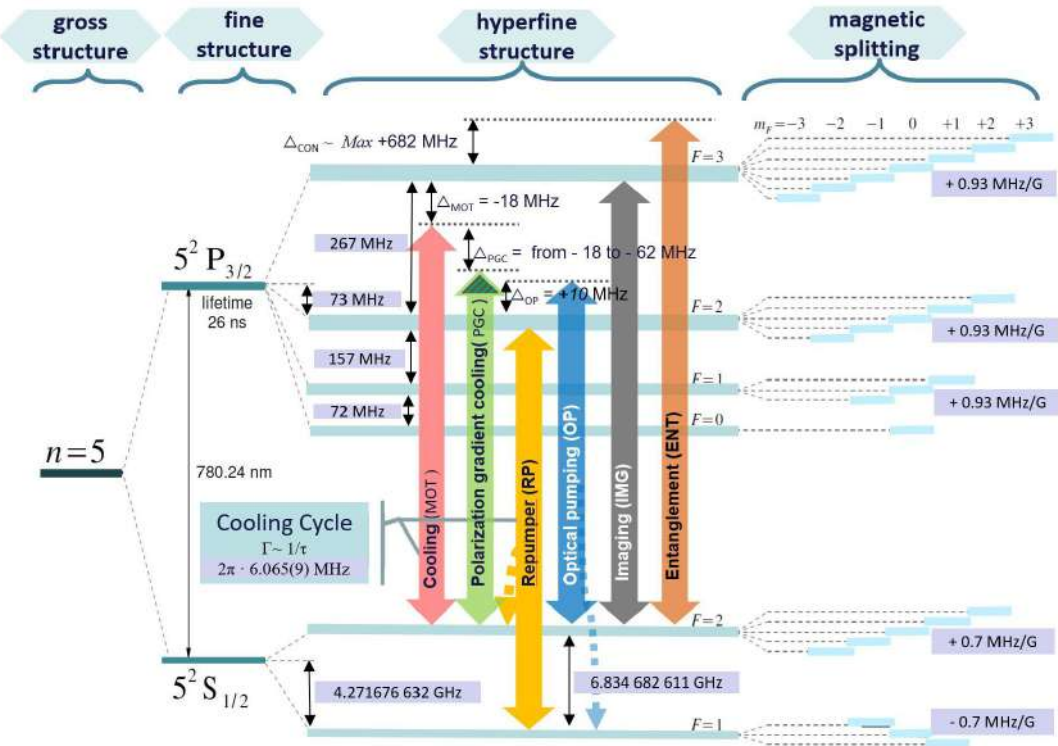


Fig 5-1 ^{87}Rb energy level diagram and required laser lines. Zeeman sublevels show a linear splitting in a weak magnetic field. M Kondappan, V Ivannikov, T Byrnes, Rev Sci Instrum 95, 1 (2024)

5.2 Optical system

5.2.1 Overall optical scheme

Fig. 5-3 shows our design of the optical scheme which generates the sources as described in Fig. 5-1. The two frequency-locked laser inputs are connected by optical fiber to the top right of Fig. 5-1. The overall scheme for the optical circuit then proceeds as follows. For the primary laser, the beam passes through four key components each highlighted in Fig. 5-3, and marked as the yellow COMP-1 to COMP-4. For the secondary laser, four key components are marked as purple COMP-1 to COMP-4. Each of these components is responsible for sending a portion of the input power for further processing, to attain the required frequency, polarization, and power. The beams then proceed to the five different outputs, corresponding to laser cooling (MOT), entanglement(ENT), polarization-gradient cooling (PGC), optical pumping (OP), and imaging (IMG), in order of the components encountered. We summarize the role of the highlighted components in Table 5-1. Throughout the circuit, shutters are used to disable the laser beam paths

temporarily and close off different light paths at different points in the atom cooling sequence.

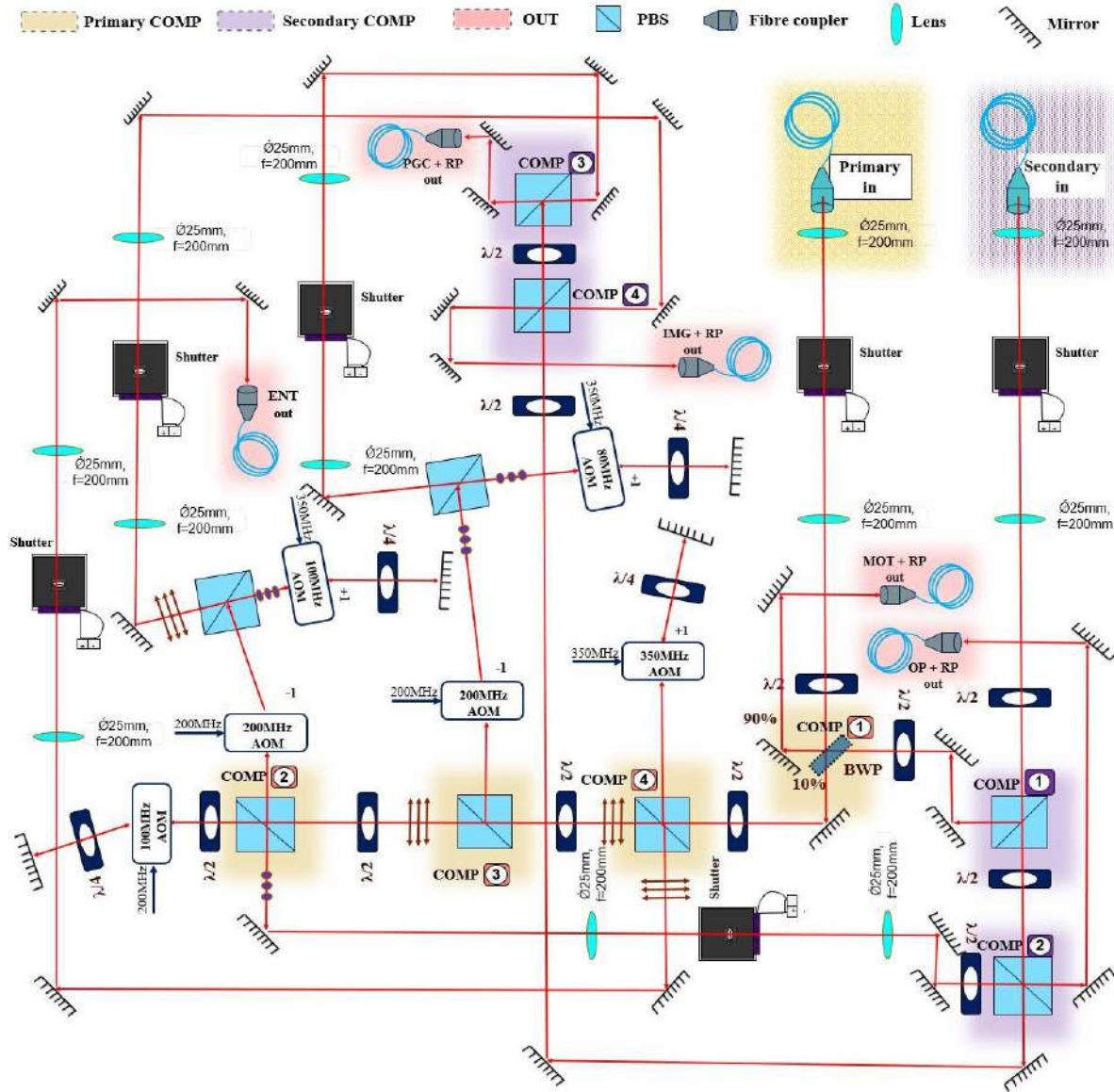


Fig 5-2 Compactified optical source generation for ultracold atoms. The five outputs (highlighted in pink) are generated from two input laser sources (top right) from the Schafter+Kirchhoff collimators. The outputs are labelled as MOT + RP, OP + RP, ENT, PGC + RP, and IMG + RP. Output generations are fiber-coupled, and fiber output fixtures are integrated within the circuit. There are lens sets involved in the circuit, with a corresponding lens acting as a beam focal point for AOMs and shutters. The beams are naturally focused and re-collimated with a lens to have focal spots of around one mm to be matched in the AOM and shutter transmission apertures. The three circular spots depict vertically polarized light and three parallel lines show horizontally polarized light in the diagram. M Kondappan, V Ivannikov, T Byrnes, Rev Sci Instrum 95, 1 (2024)

5.2.2 Optical source generation

We now provide further details on each required laser source. In this section, we introduce the components and their outputs, along with the logic behind their labelling. We also offer a brief explanation of the calculations for the AOM detunings and summarize the requirements for their positions in the circuit. Specific components were selected based on the generated outputs as detailed in the component relationship table (see Table 5-1).

MOT

The primary laser is locked at a frequency of -18 MHz detuning with respect to the $F_g = 2 \rightarrow F_e = 3$ transition as shown in Fig. 5-1. As can be seen in Fig. 5-3, the primary laser is one of the two fiber inputs passing through a shutter placed at the focal point of the Brewster Plate (BWP), which we label as COMP-1. All other branches in the circuit are performed with a polarizing beam splitter (PBS). A half wave plate (HWP) is employed for controlling the polarization of the light passing into the BWP. The relatively high power (1.8 W) involved in the MOT branch creation makes a PBS not an optimal choice for this branch. The Brewster plate reflects 90% of the primary laser beam into the MOT output which will be eventually admixed with repumper (RP). The repumper beam branches from secondary laser path via a PBS (labeled as the purple COMP-1) and gets admixed in the BWP transmitted with a non-Brewster angle, then is admixed with the primary beam to become fiber coupled.

Polarization gradient cooling

We now turn to the polarization gradient cooling (PGC) beam generation. In Fig. 5-3, starting from the primary laser, the optical beam travels through COMP-1, COMP-4, to arrive at COMP-3. The beam spot with a 1 mm diameter then enters an AOM driven by a 200 MHz RF pulse. The polarization of the beam is vertical at this point. The PBS output is regulated by an HWP that is positioned before the PBS, splitting the laser and sending it to a double pass arrangement. After admixing with the RP beam from COMP-3 of the secondary laser, the PGC+RP fiber coupler receives the output beam. This block is used to provide the -18 to -62 MHz dynamic ramped detuning of the PGC laser. To achieve a ramping point reaching -61 MHz detuning,

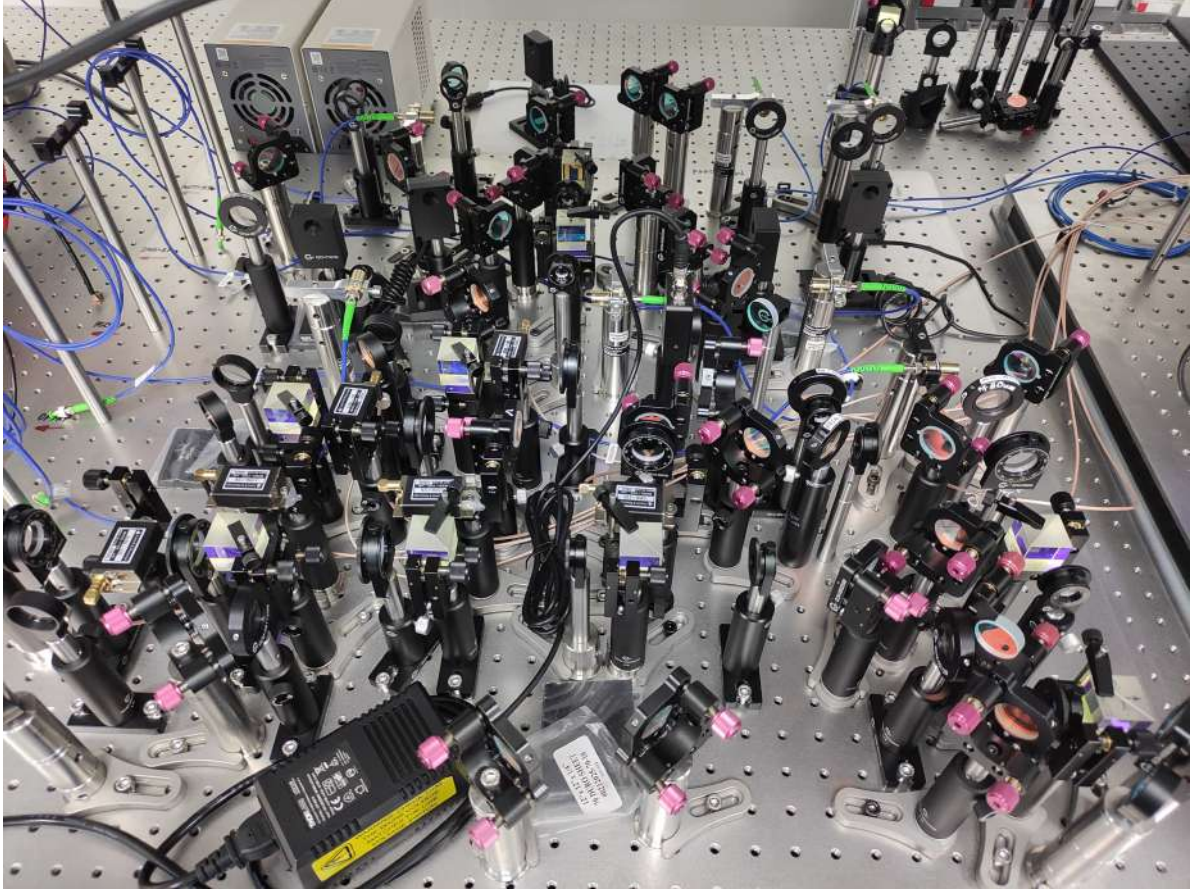


Fig 5-3 Our innovative optical circuit is being built on Viewport table for compactified optical sources generation. The outputs are generated from two input laser sources (top right) from the Schafter+Kirchhoff collimators. The outputs are labelled as shown are being fiber-coupled, and fiber output fixtures are integrated within the circuit.

the 200 MHz AOM and 80 MHz AOM placed after COMP-3 in Fig. 5-3 frequencies shifts should be driven such that $f_1 = -18 - 200 = -218$ MHz and $2f_2 = 78$ MHz, (where $2f_2$ is the variance due to the AOM's double pass configuration) respectively, resulting in $\Delta_{\text{PGC}} = f_1 - 2f_3 = -218 + 2 \times 78 = -62$ MHz. In Fig. 5-1, we show the shaded representation of the PGC light implies that it is being dynamically detuned at a particular time cycle to effectively handle the Doppler cooling limit.

Imaging

Next, we discuss the generation of the imaging (IMG) beam which corresponds to a resonant $5^2\text{S}_{1/2}(F_g = 2) \rightarrow 5^2\text{P}_{3/2}(F_e = 3)$ transition. In Fig. 5-3, the primary laser beam reaches COMP-2 in the primary laser's path, after which it branches into a 200 MHz RF pulse triggers the first AOM, where at this point, the polarization is vertical. This block is

Outputs	primary laser COMP	secondary laser COMP
MOT + RP	1	1
OP + RP	2	2
PGC + RP	3	3
IMG + RP	2	4
ENT	4	-

Table 5-1 Relationship between the component numbers (COMP) in Fig. 5-3 for the primary and secondary lasers and the five outputs of the optical circuit. The labeled components send portions of the input light to different outputs, being processed suitably along the way.

responsible for the +18 MHz frequency shift of the IMG beam which nullifies the primary laser's -18 MHz detuning already present in the primary laser. To achieve a detuning of 0 MHz in the primary laser which is already detuned -18 MHz, the reverse shifts are $f_1 = -18 + 200 = 182$ MHz and $f_4 = 91$ MHz, where $2f_4$ is due to the AOM's double pass configuration. This results in $\Delta_{\text{IMG}} = f_1 - 2f_4 = +182 - 2 \times 91 = 0$ MHz. After nullifying the -18 MHz detuning, the frequency of the laser line is put into the exact resonance with the $F_g = 2 \rightarrow F_3 = 3$ transition. The resultant IMG is an admixer with RP beam from COMP-4 of secondary laser and fiber coupled at IMG + RP fiber coupler.

Entanglement

As shown in Fig. 5-1, the required laser line generation for the cooling and entanglement processes is detuned from the standard frequency spacing of the hyperfine splitting structure. The detunings are for polarization gradient cooling $\Delta_{\text{PGC}} = -62$ MHz and for optical pumping $\Delta_{\text{OP}} = +10$ MHz concerning the D2 transition line. The generation of the entanglement(ENT) beam is accomplished by placing the AOM after COMP-4 for the primary laser path (see Fig. 5-3). The optical entanglement beams are far detuned with a frequency shift of $f_5 = +350$ MHz concerning the transition $F_g = 2 \rightarrow F_3 = 3$ from the starting point is the primary laser, which has a detuning of $f_1 = -18$ MHz. Using the double pass configuration with a 350 MHz AOM, the total possible frequency shift is $\Delta_{\text{ENT}} = f_1 - 2f_5 = -18 \text{ MHz} + 2 \times 350 = +682$ MHz.

Optical pumping

For the optical pumping (OP) beam, we require a +10 MHz detuning from the $F_g = 2 \rightarrow F_e = 2$ transition. We use the same configuration as the entanglement beam

generation, with a double pass 100 MHz AOM after COMP-2 in the primary laser's path of Fig. 5-3. The 200 MHz AOM path is for the IMG beam. The generated OP is then admixed with RP beam from COMP-2 in the secondary laser path then fiber coupled at OP + RP fiber coupler.

Repumping

In the cooling cycle, the population of atoms in the narrow linewidth $5^2P_{3/2}$ level with 26 ns lifetime undergoes spontaneous emission to the dark state $5^2S_{1/2}(F_g = 1)$ following the selection rules: $F_e = 3, 2, 1 \rightarrow F_g = 2$ and $F_e = 2, 1, 0 \rightarrow F_g = 1$ as shown in Fig. 5-3. The transitions to the ground state $F_g = 1, 2$ have 50% probability each to decay from the excited states $\Delta_f = 0, \pm 1$. Thus both of the ground states are populated while the primary laser continues to pump the atoms to the excited state. Since the lifetime of the excited state is of the order of nanoseconds, the trapped atoms become visible to the imaging beam since the saturation to the $F_g = 1$ ground state exponentially.

5.3 Circuit characterization

We now implement the optical circuit design as shown in the previous section and perform some benchmarking to characterize the outputs. A successful implementation of the optical circuit entails the output beams having the beam intensity, polarization, frequency, and a beam profile in the desired range. It is also desirable to have some degree of adjustability, particularly in the frequency outputs, to optimize the various operations that are performed. We show that our optical circuit design successfully implements the required optical beams as desired.

5.3.1 Lasers and frequency locking

We first discuss the nature of the two laser inputs to the optical circuit of Fig. 5-3. The primary laser is a Toptica DLC TA PRO 780 diode laser with a wavelength of 780 nm, an output of 2 W with sub-kHz linewidth, with anti-reflection (AR) coated front facet in a closed thermally stabilized enclosure. The grating inside the laser is positioned on a piezo actuator and features an exterior cavity in the Littrow configuration

design. [144, 179–181] The primary laser’s measured initial power is 1.812 W at 3360 mA at an operational temperature of 20°C. The 1.8 W frequency-locked output is connected to the experimental setup via optical fiber. Peak locking is used at zero-crossing, enabling Doppler-free saturation absorption spectroscopy [181–183] on counter-propagating beams. Due to spontaneous emission, the detuning for the primary laser is -18 MHz to the $F_g = 1 \rightarrow F_g = 2$ transition, the photon scattering rate generated by the MOT light would not be greater. The secondary laser is a Toptica DL100 clone diode laser with a wavelength of 780 nm, a maximum power of 500 mW, and a linewidth of sub-MHz. The photodiode is an external cavity diode laser with a Littrow grating and a direction-correcting mirror [184]. To obtain a sub-MHz linewidth, the diode laser is AR-coated. Laser locking works based on the proportional integral derivative (PID) output signal in the laser controller which is directed to the piezo actuators residing inside the laser [144, 179–181]. The SAS signal, a real-time measure of the laser, is looped back into PID circuitry.

5.3.2 Detuning ranges of the AOMs

We now discuss the attainable detuning ranges of our optical circuit. The AOM work positions result from the collective contribution of the number of AOMs involved in a specific section of the circuit. The operating frequency of each individual AOM is determined based on circuit-specific calculations and the particular AOMs that are used. As a result, the detuning ranges vary for different circuit output generations. Fig. 5-4 shows the tuning ranges of the various AOMs that are used in our optical circuit. We use either one of the ± 1 orders of the AOM as marked in Fig. 5-3, and ignore other orders. The transmission amplitudes without clipping follow a Gaussian relation, and we consider the working ranges obtained from combined work of AOMs in a specific output generating part lie within three standard deviations, which capture $\sim 99.7\%$ of the operation. Based on this, the transmission loss through the AOM’s crystal being as 500:1 (in mW) for a double-pass configuration and 1000:1 in a single-pass configuration in the circuit. We have intentionally omitted the plotting ranges for ENT as it is a variable of choice and also as it has a huge detuning range of $\Delta_{\text{ENT}} = -18$ to $+682$ MHz. Since the transmission loss inside the AOM crystal is significantly less, we neglect the amplitude differences because the maximum power in the MOT branch can be as much as 1350 mW, which is sufficient for our purposes.

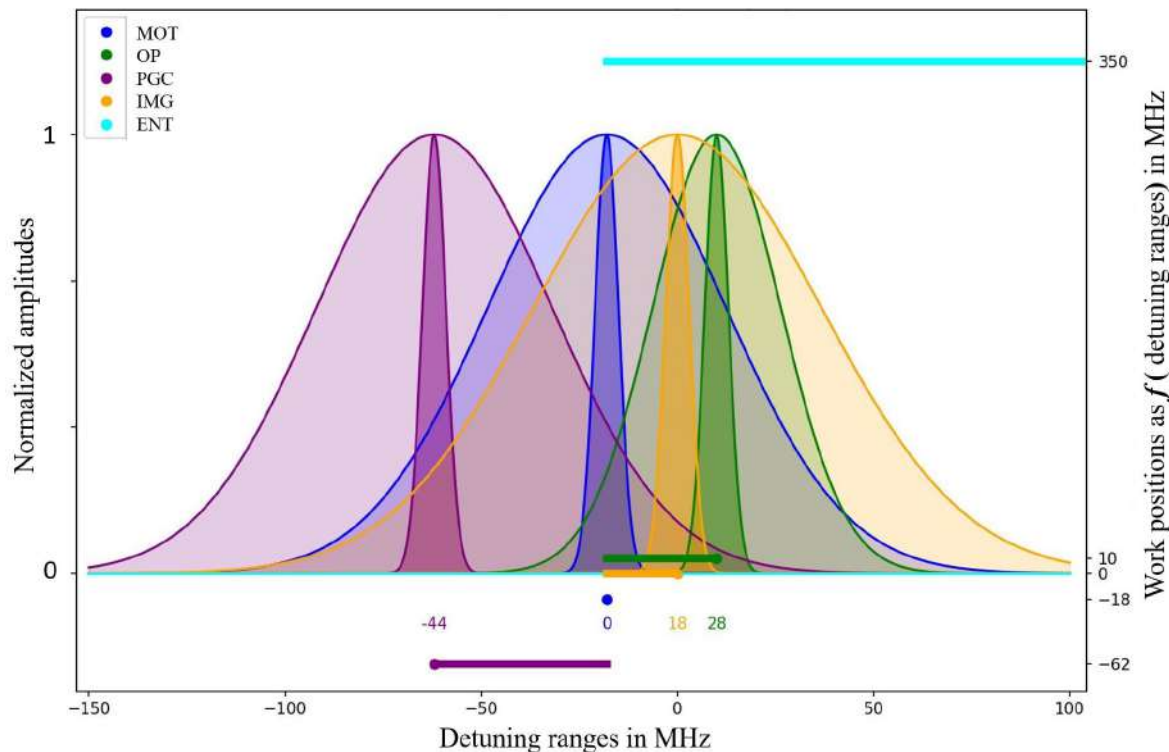


Fig 5-4 Detuning ranges of AOMs and their working positions shown for various optical sources. Four different scales are being used in the plot. The bottom horizontal axis is the frequency for detuning ranges in MHz. The right side vertical axis shows the AOM combined work positions and colored bars as work position ranges as a function of the colored horizontal scale inside the plot. The left vertical scale gives the normalized amplitudes of detuning ranges. The detuning range maximum and minimum of the Gaussian curve shows the AOM transmission amplitude resulting from the combined detuning range. The ENT detuning range is shown here as $\Delta_{\text{ENT}} = +350$ MHz as a simplified representation of $\Delta_{\text{ENT}} = -18$ to $+682$ MHz. The colored numbers inside the plot represent the actual work done by the AOMs from their respective work positions. M Kondappan, V Ivannikov, T Byrnes, Rev Sci Instrum 95, 1 (2024)

5.3.3 Beam profile and power loss

The beam diameters of the MOT, RP, and PGC are maintained as 1 mm except when the beams pass through the lens sets. In our case, $\lambda = 780$ nm, $F = 25$ cm, and $d = 1$ mm = 0.001 m. The calculated focal spot size lies in the shutter apertures is $\approx 4.97 \times 10^{-5}$ m $\approx 49.7\mu m$. We have measured the beam profiles of the output beams. We perform a diffraction-limited spot size calculation for Gaussian and homogeneous profile beams. Initially, we ensured the beam profile of our MOT beam by characterizing it by a 20 cm focal length lens with f-number of 0.510102, a numerical Aperture (NA) of 0.7 for the waist size measurements along the focal point axis and fitting the data to a M^2 Gaussian model as shown in Fig. 5-5. Here we show the measured primary laser beam diameter as a function of displacement from the beam waist. The data was fit to a M^2 Gaussian model as shown. In our circuit design, we have avoided the clipping losses throughout the circuit by utilizing 25 mm lenses with a beam diameter of around 1 mm, thus clipping loses should be negligible. While the HWP is being maintained full transmission throughout all 4 COMPs of the primary laser beam, the efficiency of $97.3\% = 100 \times 1350/1387$ in the primary laser path.

5.3.4 Optical circuit power efficiencies with fiber coupling

Due to the fact that the output power at MOT + RP is the highest in the circuit, the construction and measurements were performed by placing filters of sufficient strength. The output after the fiber coupler was measured as 1150 mW. Based on the comparison with the MOT efficiency $85\% = 100 \times 1150/1350$, Table 5-2 lists all the efficiencies of the different outputs after the five output couplers.

Outputs	Specific output	Efficiency (%)
MOT + RP	MOT	85
	RP	67
OP + RP	OP	80
	RP	65
PGC + RP	Output	66.5
	RP	63
IMG + RP	IMG	62
	RP	62
ENT	ENT	73

Table 5-2 Table shows the efficiencies of fiber coupled outputs

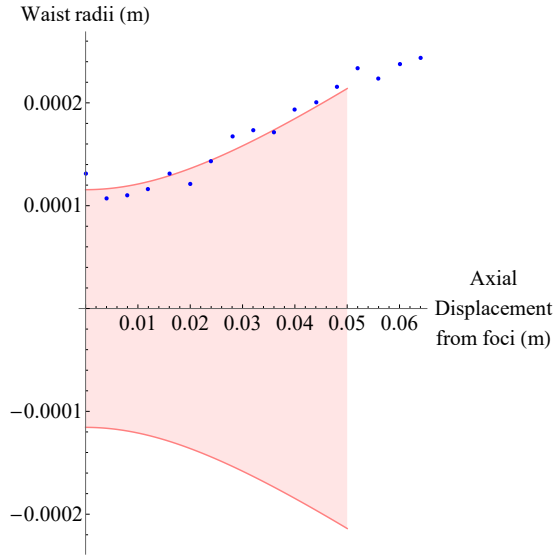


Fig 5-5 Measured cooling MOT beam diameter as a function of displacement from the beam waist. Dots show data points and solid lines show a fit to a diffraction limited spot size calculation for Gaussian and homogeneous profile beams (Airy model). This beam profile of our MOT beam is characterized by a lens of f number of 0.510102, numerical Aperture (NA) 0.7 for the waist size measurements along the focal point axis and fitting data to M^2 Gaussian model, 20cm focal length lens used for the wavelength $\lambda = 780$ nm. M Kondappan, V Ivannikov, T Byrnes, Rev Sci Instrum 95, 1 (2024)

5.3.5 Optimization of fiber coupling

Efficient fiber coupling is paramount to directing optical power precisely where it is needed without significant losses. The fiber coupling's effectiveness is characterized by specific output efficiencies, which reflect the proportion of input power that successfully makes it through the coupling process to be used in the experiment. These efficiencies, as detailed in Table 5-2, are indicative of the system's overall performance and are influenced by several factors, including alignment precision, fiber mode matching, back-reflections, and the physical condition of the fibers themselves.

In our approach, precise alignment is prioritized to minimize power loss, as even micrometer-level misalignments can lead to substantial inefficiencies. We have accomplished this by adjusting the fiber's position and angle to optimize coupling efficiency, a task that becomes particularly complex in multi-beam setups. We have addressed mode mismatch, where the beam and fiber's modal profiles are misaligned, which otherwise leads to power losses. Our techniques include lens adjustments and the use of mode field adapters. To tackle back-reflections, which can destabilize the system, we have implemented anti-reflection coatings and angled interfaces. Additionally, we ensure the fibers

are maintained in good condition, free from stress, bending, or contamination, as this is crucial for efficient coupling. This precise alignment process directly impacts measurement processing, we continuously improved alignment, mode matching, and fiber maintenance to optimize system performance and to have a precise optical power delivery.

In our optical alignment process, we utilize a two-mirror method that optimizes precision in directing laser beams into fiber couplers, crucial for quantum technology applications. The first "steering" mirror, positioned close to the laser source, sets the initial direction of the beam. This mirror's adjustments are vital for aligning the beam along the desired horizontal and vertical paths. Following this, the second "correction" mirror, situated nearer to the fiber coupler, fine-tunes the beam's trajectory, ensuring it enters the coupler at the optimal angle for efficient coupling. It is essential for achieving the high degree of controlling required in quantum technology applications, significantly enhancing fiber coupling efficiency and the reliability of our experimental setups.

5.4 QND implementation inside vacuum chamber

5.4.1 Entanglement generation complexities in experimental setup

The ENT beam shown in the full schema of our experimental setup as shown in the Fig. 5-6 is utilizing a 700MHz blue detuned beam. In advanced quantum experiments involving ^{87}Rb Bose-Einstein Condensates (BECs), the application of a +700 MHz detuning relative to a submagnetic state in the excited state spectrum plays a critical role in the entanglement process. Contrary to red detuning, where the laser frequency is set below the atomic resonance, a +700 MHz blue detuning situates the laser frequency above the atomic resonance. Far-off-resonance traps (FORTs) using blue detuning offer an alternative method to minimize spontaneous emission, crucial for preserving quantum coherence in entanglement experiments with ^{87}Rb atoms. Unlike the conventional red detuning approach, where the laser frequency is set just below the atomic resonance, blue-detuned FORTs operate with a frequency significantly higher than the atomic resonance. For ^{87}Rb , whose atomic transition frequencies are around 384 THz (corresponding to a wavelength of about 780 nm), this means using a laser frequency well above this resonance. The substantial blue detuning, often much greater than the few hundred MHz to GHz range used in red detuning, significantly reduces the probability of spontaneous

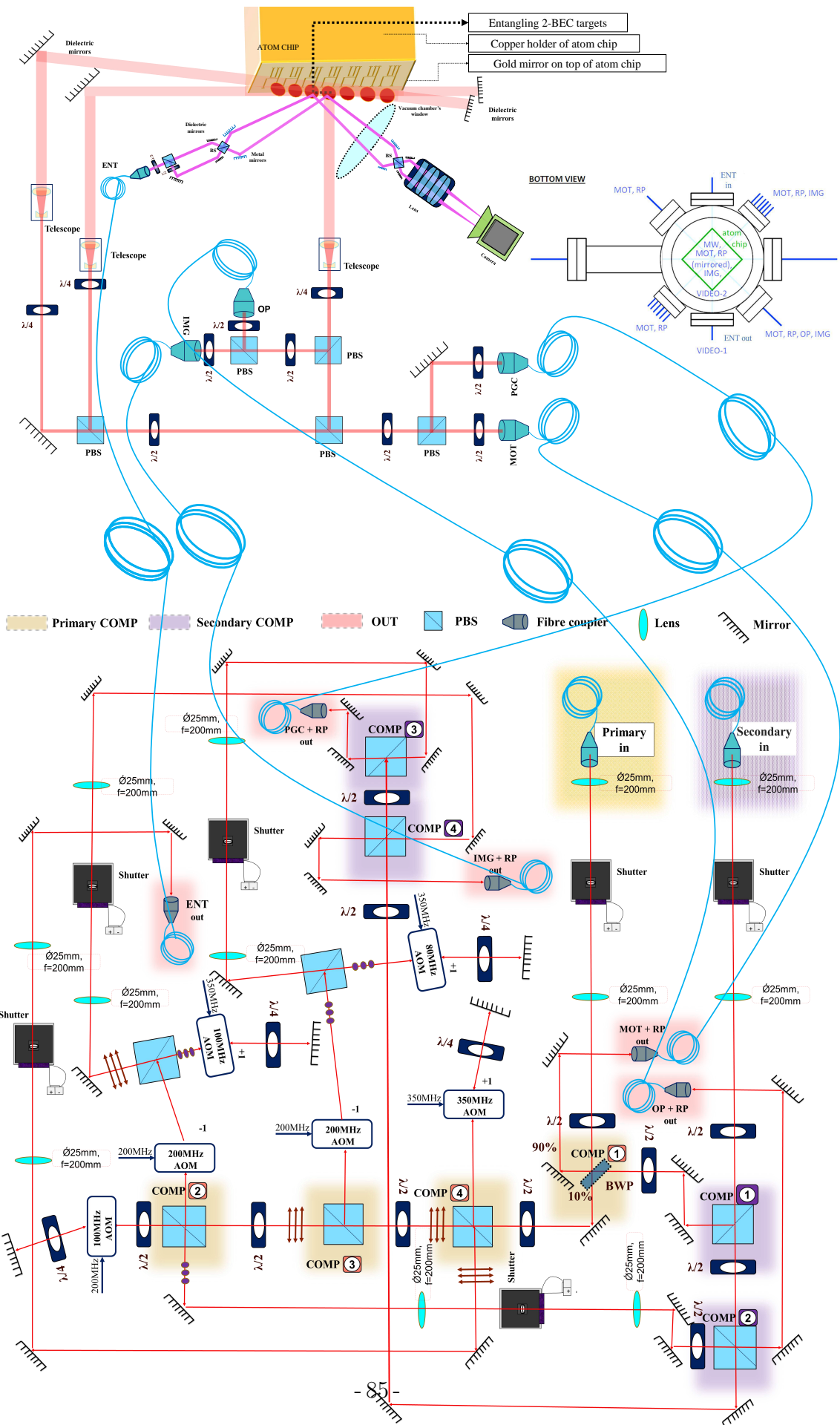


Fig 5-6 Development of full optical setup and entanglement circuit integration

emission while still creating effective optical potentials. The higher energy photons in blue-detuned light result in repulsive optical potentials, as opposed to the attractive potentials formed under red detuning. This method is especially advantageous when the experimental setup requires creating specific trap geometries or manipulating atoms with minimal perturbative effects. Moreover, considering the hyperfine splitting of about 6.8 2- BEC qubits entangled in the ground state of ^{87}Rb , a far-off-resonance blue detuning can be tailored to avoid excitation to unwanted states, thereby reducing decoherence and enhancing control over the atomic states during entanglement operations. This choice of detuning is pivotal in manipulating the atomic states with minimal perturbation and decoherence. Blue-detuned light creates repulsive optical potentials, which can be utilized to engineer specific trap geometries or light-shift potentials essential for controlled interactions between atoms in separate BECs. The precise manipulation of these interactions is a cornerstone in the creation of entanglement between distinct BEC clouds. In such a setup, the blue-detuned light facilitates the creation of well-defined, spatially separated potential wells, allowing for the individual addressing and coherent manipulation of each BEC. Moreover, the +700 MHz offset is specifically chosen to match the energy differences in the hyperfine split levels of the excited states of ^{87}Rb , ensuring that the laser interacts resonantly with the targeted transitions. This resonant interaction is crucial for implementing Quantum Non-Demolition (QND) measurements or coherent Raman processes, which are fundamental techniques in generating and probing entanglement between BECs. Through such finely-tuned laser-BEC interactions, it becomes possible to entangle the macroscopic quantum states of the separate BEC clouds in our setup.

In the precise orchestration of our experimental apparatus, we utilize dual Mach-Zehnder Interferometers (MZIs), designated as MZI_{red} and MZI_{pink} , to coherently manipulate a triad of Bose-Einstein Condensates (BECs) housed within a high-vacuum chamber. The configuration is such that MZI_{red} sequentially addresses BEC_1 and BEC_2 , while MZI_{pink} , with a slight temporal delay Δt , within the coherence window τ_{coh} , targets BEC_2 and subsequently BEC_3 . This delay is critical, fine-tuned to be within the entanglement timeframe τ_{ent} , to ensure the generation of 2- BEC qubits entangled states across the BECs. The experimental intricacies include, but are not limited to, the meticulous alignment of MZI beams to the BEC locations, the synchronization of optical shutters to achieve the requisite Δt , and the precise calibration of beam paths from the output beam splitters (BS) of each MZI to the focusing lenses and camera array. These tasks are rendered more complex by the inversion of the atom chip, denoted as a flipped configu-

ration, within the vacuum chamber, demanding exceptional precision to align the optical elements and achieve the targeted entanglement of BEC states.

The complexity of the experiment is multifaceted, involving not only the alignment of MZIs but also the synchronization of shutter operations to control the delay Δt with high temporal precision in the future when we progress to that stage. Furthermore, the alignment of the output beams from each MZI's Beam Splitters (BS) to the camera through focusing lenses is paramount, necessitating exact positioning to ensure the beams converge on the camera's sensor accurately. These complexities are amplified by the inverted orientation of the atom chip within the vacuum chamber, challenging the typical alignment procedures and demanding a novel approach to achieve the desired entanglement of BEC states. The dielectric mirrors play a pivotal role in steering the beams from the MZIs to the atom chip, while the lens is crucial for beam shaping and expansion as described in section 4.6.6, ensuring that the beam profiles are matched to the spatial dimensions of the BECs. The ENT, IMG + RP, OP + RP, and MOT + RP such various optical components and beam paths for entanglement (ENT), imaging (IMG), repumping (RP), optical pumping (OP), and magneto-optical trapping (MOT) takes their positions as depicted in the sub figure of 5-6. Each path is carefully constructed to maintain the integrity of the beam properties, ensuring that the entanglement process is not compromised. This setup represents a significant advance in the experimental quest to overcome vacuum chamber design limitations.

In our advanced MZI setup, the arms incorporate metallic mirrors after the first BS and before the last BS, chosen for their superior angular and polarization characteristics. Metallic mirrors are favored over their dielectric counterparts due to their broader spectral reflectance and lesser sensitivity to polarization changes upon reflection, a property that is especially beneficial when precise control over the polarization state of photons is required. This attribute is critical in our experiment, as the polarization state of the entangling beams must be preserved to maintain coherence between the BEC states during the entanglement process. Additionally, metallic mirrors typically exhibit higher damage thresholds, providing robustness against high-intensity laser beams that could otherwise damage optical components. This durability is essential in ensuring the longevity and stability of the experimental apparatus, particularly when operating near the laser-induced damage threshold. Furthermore, the choice of metallic mirrors allows for greater flexibility in the alignment process, as these mirrors are less affected by the angle of incidence of the laser beams, thus facilitating the precise steering and shaping of the beams as they prop-

agate through the MZI arms towards the BEC targets. These complexities are further compounded by the use of specialized metal mirrors, depicted in blue within the MZI arms of our schematic, chosen for their superior angle-polarization characteristics over traditional dielectric mirrors. The metal mirrors' enhanced reflectivity for s-polarized light ensures that the polarization state of the laser beams is preserved, which is crucial for the phase stability of the interferometers and the integrity of the entanglement process. Additionally, these mirrors offer the robustness required to withstand the intense laser powers without degradation, a non-negligible factor in the high-precision domain of quantum experiments.

The strategic positioning of these mirrors is calibrated to provide the optimal incident angle for the laser beams, thereby minimizing any polarization-induced phase shifts that could potentially disrupt the entanglement. Furthermore, the selection of these mirrors takes into consideration their ability to handle the specific wavelengths used in the experiment, ensuring that the beams are reflected efficiently with minimal losses. The cumulative effect of these carefully considered optical components and configurations within our setup is the facilitation of a highly controlled and precise environment, conducive to the generation of 2- BEC qubits entangled states across the BECs. In addition to the polarization advantages offered by the metal mirrors, the use of quarter-wave plates (QWP $\lambda/4$) and half-wave plates (HWP $\lambda/2$) along the beam paths in the optical source generation circuitry part setup as shown in the Fig. 5-6 plays a significant role in the manipulation of the polarization states of the photons interacting with the BECs. This level of control over the polarization is essential for certain quantum operations, such as the implementation of Raman transitions or the induction of AC Stark shifts, which are integral to the entanglement protocol. Polarizing beam splitters in the optical source generations circuit might have contributed to some polarization defects so by ensuring that only the correctly polarized light interacts with the BEC, thereby enhancing the fidelity of the entanglement.

5.4.2 Summary and conclusions

Each component in our MZI and overall optical circuitry design is selected and positioned to create a harmonious system capable of exploring the quantum entanglement of BECs. The careful balance of polarization management, timing synchronization, and spatial alignment underscores the experimental prowess required to navigate the and over-

come the possible setbacks by well planned and precisely calculated implementation of our optical design. We have a well compactified optical circuit to generate the principal optical sources that are required to perform cooling, imaging, and entanglement of ultracold atoms. The primary result is shown in Fig. 5-3 which shows our design starting from two sub-kHz linewidth frequency-locked laser sources. One of the advantages of our circuit design is that the repumping beams are admixed with the various optical beams and output in its dedicated single-mode fiber. We implemented the circuit and characterized the outputs in terms of beam profile, power loss, and fiber coupling, and found good performance overall. The present system has a universal design that could be applied to numerous quantum technology applications where it is necessary to produce quantum states of ultracold atomic gases, such as spin squeezed cold atomic ensembles. Utilizing our methods may allow for applications of ultracold atoms to quantum technology more readily available, for various applications, ranging from quantum metrology to quantum simulation.

6 QND background theory

6.1 Introduction to entangled states in BECs

In this chapter, we explore the pivotal role of squeezed states [185–188] in the advancement of quantum optics and their diverse applications, notably in quantum metrology [189–191]. Squeezed states are characterized by reduced quantum fluctuations in one observable at the expense of increased fluctuations in its conjugate variable, as dictated by the Heisenberg uncertainty principle. Such states have been extensively studied and realized in various experimental settings [98, 192–195], leading to a plethora of proposed applications [64, 196–201]. Analogous developments have occurred in atomic systems, where internal spin levels serve as the degrees of freedom. Here, squeezing is manifested as reductions in spin noise fluctuations below those in a coherent spin state [202–208]. Theoretical schemes for producing such squeezed states in atomic ensembles have been proposed and realized in various experiments [23, 60, 61, 80, 209–226]. In the context of quantum information, squeezed states involving multiple physical systems are of significant importance. Two-mode squeezed states are known to produce Einstein-Podolsky-Rosen (EPR) correlated states, which demonstrate correlations in one set of variables and anti-correlations in another. These states, essential in quantum information applications, particularly in continuous variable quantum computing [227], are considered valuable resources due to their entangled nature. In atomic contexts, initial demonstrations by Polzik and colleagues [94, 94, 114, 222, 228–231] utilized two-mode squeezed states under the Holstein-Primakoff approximation. Further, various schemes for entangling atomic ensembles have been proposed and implemented [7, 232–240].

The conceptual experimental scheme [3] aimed at generating entanglement between two Bose-Einstein condensates (BECs). The scheme employs a Mach-Zehnder interferometer setup with two BECs placed in its arms (Fig. 7-1). Through quantum nonde-

molition (QND) interactions and subsequent optical state measurements, the BECs are projected into an entangled state. This approach differs from previous QND-based entangling schemes, offering a unique geometry that facilitates entangling spatially separated BECs. In our work [3] we have demonstrated that it is possible to precisely calculate the resulting wavefunction for any initial state and interaction duration, revealing notable differences from existing theories. For instance, we observe that the variance of certain pairs of variables either saturates at a finite value or even increases due to the interactions. Our understanding of the protocol allows us to propose modifications that significantly improve the level of squeezing. Additionally, we illustrate that the generated states can violate a CHSH-Bell inequality using only joint spin measurements of the two BECs. This chapter also highlights a distinctive aspect of our QND scheme unlike previous approaches, our configuration does not require light to sequentially pass through the atomic clouds, making it more suitable for entangling well-separated BECs.

6.2 Experimental design for BEC entanglement generation

6.2.1 Setup and Hamiltonian

In this section of the thesis, the focus is on a unique experimental setup, as illustrated in Fig. 4-18, aimed at generating two-spin squeezed states in two Bose-Einstein condensates (BECs). The setup involves two separate BECs, each with a pair of internal energy states, denoted as g_j and e_j for $j \in \{1, 2\}$, typically realized in separate magnetic or optical traps [241–243]. The experimental arrangement utilizes a Mach-Zehnder interferometer, where a coherent light mode b is split into modes a_1 and a_2 , interacting with the BECs. The Hamiltonian guiding this interaction, especially under quantum nondestruction dynamics. The spin-dependent interaction is attributed to specific coupling rules in the hyperfine ground states [94, 244].

6.2.2 State preparation and measurement

In the scheme as showed in Fig. 7-1, coherent light is arranged in a Mach-Zehnder interferometer, and two Bose-Einstein Condensates (BECs) are positioned in its arms. The light interacts through a quantum nondemolition (QND) interaction, leading to the

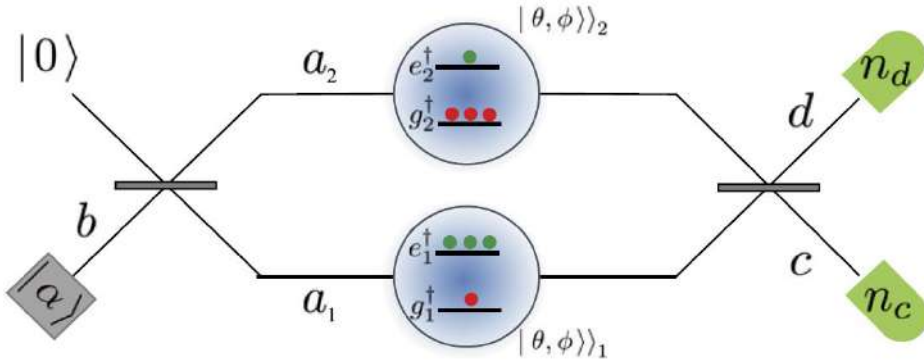


Fig 6-1 Illustration of the experimental setup for generating two-spin squeezed states in two BECs. Coherent light enters a beam splitter, interacts with each BEC, and is then measured in modes c and d at Juan E Aristizabal-Zuluaga, M Kondappan, T Byrnes, et al. J. Phys. B 54 105502 (2021)

entanglement of the two BECs upon measuring the optical state. The use of QND interaction aligns with several established atomic ensemble entangling methods. These include approaches referenced in prior works, emphasizing the experimental and theoretical contributions already made in this field. The modeling typically employs a Holstein-Primakoff approximation, necessitating initial spin polarization in a specific direction and brief light-matter interaction times. This study extends beyond existing theories, providing an exact calculation of the resulting wavefunction for any initial state and evolution time. It reveals that the variance of certain variable pairs can saturate or increase due to interactions. These insights facilitate the proposal of enhanced squeezing techniques. Furthermore, the possibility of violating the CHSH-Bell inequality using the generated states is demonstrated, focusing on joint spin measurements of the two BECs. The geometrical configuration of this scheme differs from previous models, as the light does not sequentially pass through the atomic clouds, an advantage for entangling spatially separated BECs.

Physical system and Hamiltonian

We consider two spatially separated BECs, each in its trap, such as magnetic traps on an atom chip or optical dipole traps. The BECs consist of two internal energy states, represented by bosonic annihilation operators g_j, e_j , where $j \in \{1, 2\}$. These states could correspond to $F = 1, m_F = -1$ and $F = 2, m_F = 1$ clock states in ^{87}Rb . Schwinger boson

operators are introduced:

$$\begin{aligned} S_j^x &= e_j^\dagger g_j + g_j^\dagger e_j, \\ S_j^y &= -ie_j^\dagger g_j + ig_j^\dagger e_j, \\ S_j^z &= e_j^\dagger e_j - g_j^\dagger g_j, \end{aligned} \quad (6-1)$$

with commutation relations $[S^i, S^j] = 2i\epsilon_{ijk}S^k$, where ϵ_{ijk} is the Levi-Civita tensor. The total number of atoms in each BEC is fixed:

$$g_j^\dagger g_j + e_j^\dagger e_j = N. \quad (6-2)$$

Fock states and spin coherent states are used to represent BEC states:

$$\begin{aligned} |k\rangle &= \frac{(e^\dagger)^k (g^\dagger)^{N-k}}{\sqrt{k!(N-k)!}} |\text{vac}\rangle, \\ |\theta, \phi\rangle &= \frac{1}{\sqrt{N!}} \left(e^\dagger \cos \frac{\theta}{2} + g^\dagger \sin \frac{\theta}{2} e^{i\phi} \right)^N |\text{vac}\rangle, \end{aligned} \quad (6-3)$$

where θ and ϕ are spherical angles on the Bloch sphere.

The interaction with light in the Mach-Zehnder configuration involves optical modes represented by bosonic annihilation operators b, a_1, a_2 . After interaction with the BECs, the light modes are transformed:

$$\begin{aligned} a_1 &= \frac{1}{\sqrt{2}}(c + d), \\ a_2 &= \frac{1}{\sqrt{2}}(c - d). \end{aligned} \quad (6-4)$$

The QND interaction Hamiltonian is given by

$$H = \frac{\hbar\Omega}{2} (S_1^z - S_2^z) J^z, \quad (6-5)$$

with the spin dependence arising due to specific transition selection rules. This Hamiltonian forms the basis for the entanglement generation between the BECs.

Dynamics of the BEC System

The dynamics are derived considering a general initial state of the BECs. The laser initially in state $|\alpha\rangle_b$ illuminates the mode b , and after the interaction, the light and BECs' states are given by:

$$|\psi(\tau)\rangle = \sum_{k_1, k_2=0}^N \Psi_{k_1 k_2} |k_1\rangle |k_2\rangle \times |\alpha \cos(k_1 - k_2)\tau\rangle_c | -i\alpha \sin(k_1 - k_2)\tau\rangle_d. \quad (6-6)$$

The final state after photon number measurement in modes c and d is described by:

$$\left| \tilde{\psi}_{n_c n_d}(\tau) \right\rangle = |n_c\rangle |n_d\rangle \times \sum_{k_1, k_2=0}^N \Psi_{k_1 k_2} C_{n_c n_d}[(k_1 - k_2)\tau] |k_1\rangle |k_2\rangle, \quad (6-7)$$

where $C_{n_c n_d}(\chi)$ is defined as

$$C_{n_c n_d}(\chi) \equiv \frac{\alpha^{n_c + n_d} e^{-\alpha^2/2}}{\sqrt{n_c! n_d!}} \cos^{n_c} \chi \sin^{n_d} \chi. \quad (6-8)$$

The normalized state post-measurement is:

$$|\psi_{n_c n_d}(\tau)\rangle \equiv \frac{\left| \tilde{\psi}_{n_c n_d}(\tau) \right\rangle}{\sqrt{p_{n_c n_d}(\tau)}}, \quad (6-9)$$

with the photon detection probability:

$$p_{n_c n_d}(\tau) = \sum_{k_1, k_2=0}^N |\Psi_{k_1 k_2} C_{n_c n_d}[(k_1 - k_2)\tau]|^2. \quad (6-10)$$

For a specific initial state, the photon probability can be simplified to:

$$p_{n_c n_d}(\tau) = \frac{1}{4^N} \sum_{k=0}^{2N} \binom{2N}{k} |C_{n_c n_d}[(N - k)\tau]|^2. \quad (6-11)$$

This formulation allows for arbitrary interaction times, expanding the validity of the model beyond the Holstein-Primakoff approximation, which requires spin-polarized initial states. This exact solution enables the exploration of more complex dynamics and interactions, offering insights into advanced quantum entanglement phenomena. The initial state of

the BECs is generally represented as:

$$|\Psi_0\rangle = \sum_{k_1, k_2=0}^N \Psi_{k_1 k_2} |k_1\rangle |k_2\rangle, \quad (6-12)$$

typically chosen to be BECs polarized in the S^x -direction, expanded in the Fock basis as (0-14).

The experimental procedure involves the BECs interacting with laser-illuminated coherent light. The initial state of photons in mode b is denoted as $|\alpha\rangle_b$, leading to the state post-interaction:

$$|\psi(\tau)\rangle = e^{-iHt/\hbar} |\psi(0)\rangle, \quad (6-13)$$

with $\tau \equiv \Omega t$ as the dimensionless interaction time. This interaction modifies the state as per Eq. (0-11), subsequently transformed by the beam splitter operation (Eq. (0-12)), resulting in the state Eq. (0-13).

Photon detection in modes c, d is the final step, modeled as a projection using $\Pi_{n_c n_d}$. The resulting unnormalized state is:

$$\left| \tilde{\psi}_{n_c n_d}(\tau) \right\rangle = \Pi_{n_c n_d} |\psi(\tau)\rangle, \quad (6-14)$$

with the coefficients $C_{n_c n_d}(\chi)$ defined in Eq. (0-3). The normalized entangled state between the BECs is then given by Eq. (0-9), and its photon detection probability is described by Eq. (0-10). This comprehensive analysis illustrates the precise modulation of the initial BEC wavefunction due to the optical scheme. Further discussions will explore the entangled state properties and photon probability distribution detailed in Eq. (0-10).

6.3 Analysis of short-time interaction dynamics

6.3.1 Analytic approximation for $n_d = 0$

In this thesis section, we address the regime where interaction times are on the order of $\tau \lesssim 1/\sqrt{N}$. This regime is particularly significant for generating entanglement between BECs. Our approach is to simplify the complex dynamics into an analytically tractable form.

Considering the dominant terms in Eq. (0-6) for a spin-polarized initial state (Eq. (0-14)) with large N , we note that the significant coefficients are confined to a specific range around $N/2$. For $\tau \lesssim 1/\sqrt{N}$, the function $C_{n_c n_d}[(k_1 - k_2)\tau]$ simplifies considerably, leading to a scenario where only terms with $n_d = 0$ are significant (Eq. (0-15)). This simplification is evident from Fig. 7-2.

In the presence of bright coherent light ($|\alpha| \gg 1$), the cosine factor in Eq. (0-15) can be approximated by a Gaussian distribution (Eq. (0-1)), yielding an approximate expression for the wavefunction (Eq. (0-2)). This function highlights the correlation between k_1 and k_2 . The interaction time suitable for producing sharp correlations is given by Eq. (0-16), and is consistent with the desired regime as long as condition (0-17) is met, underlining the advantage of using bright coherent light.

6.3.2 Analytic approximation of photon probability

For short interaction times ($\tau \lesssim 1/\sqrt{N}$) and large N , we derive an approximate expression for photon probability, leveraging the approximations in Eqs. (0-15), (0-1), and (0-5). The approximate photon probability distribution, not fully normalized, is given by:

$$p_{n_c n_d}^{\text{approx}}(\tau) \propto \delta_{n_d=0} \frac{|\alpha|^{2n_c} e^{-|\alpha|^2}}{n_c! \sqrt{N\pi}} \vartheta_3(0, e^{-(1/N+n_c\tau^2)}), \quad (6-15)$$

valid under the constraints $N \gg 1$, $|\tau| \lesssim 1/\sqrt{N}$, and $|\alpha| \gg 1$.

Interestingly, as illustrated in Fig. 7-3(a), the photon probability distribution shows minimal variation across different interaction times. This stems from the weak n_c -dependency in Eq. (6-15). Under certain conditions, this leads to a further simplified approximation (Eq. (0-4)), resembling a normalized Poisson distribution for mode c .

6.3.3 Analytic approximation for states with $n_d > 0$

While $n_d = 0$ is the most probable outcome for $N \gg 1$, $|\tau| \lesssim 1/\sqrt{N}$, and $|\alpha| \gg 1$, there is a possibility of obtaining $n_d > 0$. This section examines the atomic wavefunction's response when a non-zero photon number is detected in the d -mode. An approximate form

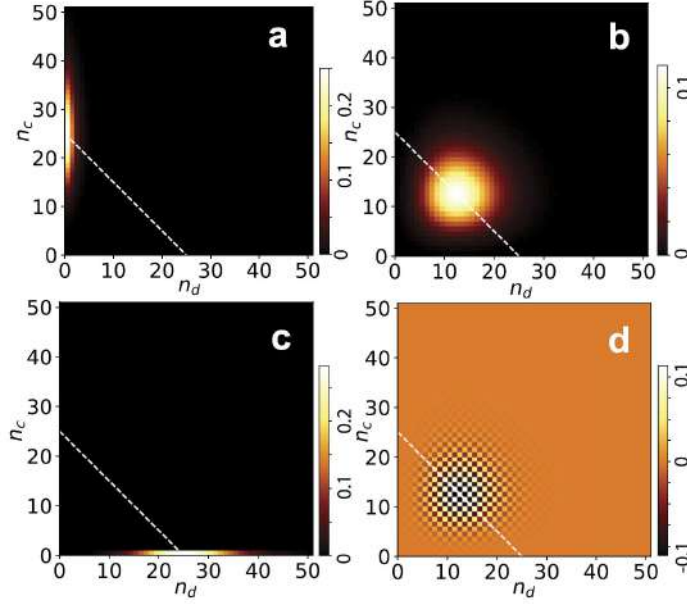


Fig 6-2 The function $C_{n_c n_d}(\chi)$ defined in (0-3) for (a) $\chi = 0.1$; (b) $\chi = \pi/4$; (c) $\chi = \pi/2$; (d) $\chi = 5\pi/4$. All plots use $\alpha = 5$. The dashed line indicates the line $n_c + n_d = |\alpha|^2$, the dominant region where the coefficients have the largest magnitude. at Juan E Aristizabal-Zuluaga, M Kondappan, T Byrnes, et al. J. Phys. B 54 105502 (2021)

of Eq. (0-3) for $n_c, n_d > 0$ is derived as [245]:

$$C_{n_c n_d}(\chi) \approx \frac{\alpha^{n_c + n_d} e^{-|\alpha|^2/2}}{\sqrt{(n_c + n_d)!}} \times \frac{\text{sgn}(\cos^{n_c}(\chi) \sin^{n_d}(\chi))}{\left(\frac{\pi}{2}(n_c + n_d) \sin^2 2\chi\right)^{1/4}} \times \exp\left[-\frac{(n_c + n_d)}{\sin^2 2\chi} \left(\sin^2 \chi - \frac{n_d}{n_c + n_d}\right)^2\right], \quad (6-16)$$

where the Gaussian's peak is at $k_1 - k_2 = \pm \frac{1}{\tau} \arcsin \sqrt{\frac{n_d}{n_c + n_d}}$ (Eq. (??)).

6.3.4 Characteristics of the approximate state

In the high $n_c \tau^2$ limit, the approximate state (0-2) simplifies to:

$$|\psi_{\lim}^{\text{approx}}\rangle \rightarrow \left(\frac{4}{\pi N}\right)^{1/4} \sum_{k=0}^N e^{-\frac{2}{N}(k-\frac{N}{2})^2} |k\rangle |k\rangle, \quad (6-17)$$

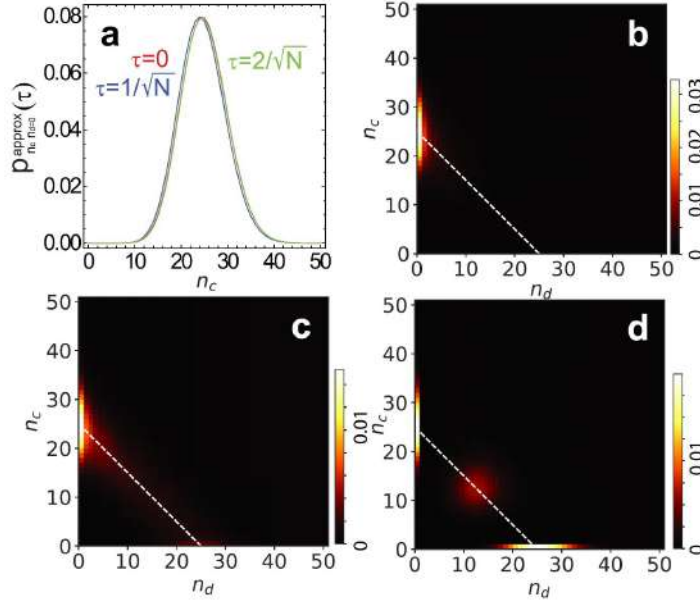


Fig 6-3 Photon probability distribution. (a) Approximate probability distribution (6-15) for the interaction times as marked. (b)(c)(d) Exact probability distribution (0-10) for (b) $\tau = 0.1$; (c) $\tau = 0.23$; (d) $\tau = \pi/4$. All plots use parameters $N = 20$, $\alpha = 5$. The dashed line indicates the line $n_c + n_d = |\alpha|^2$, the dominant region where the coefficients have the largest magnitude. (Juan E Aristizabal-Zuluaga, M Kondappan, T Byrnes, et al. J. Phys. B 54 105502 (2021))

resembling a maximally entangled spin-EPR state [127]:

$$|\text{EPR}\rangle = \frac{1}{\sqrt{N+1}} \sum_{k=0}^N |k\rangle |k\rangle. \quad (6-18)$$

Although similar to the spin-EPR state, (0-2) differs due to its Gaussian amplitude profile. This section delves into the properties of (0-2), specifically focusing on its probability distributions, variances, and entanglement, providing insights into the nature of the unapproximated wavefunction (0-6).

Spin probability distribution

The focus here is on the probability distribution of the state (0-2) in various spin bases, alongside the distribution for the state (0-9) with approximation (6-16). Defining the eigenstates of S^x, S^y operators as:

$$\begin{aligned} S^x |k\rangle^{(x)} &= (2k - N) |k\rangle^{(x)}, \\ S^y |k\rangle^{(y)} &= (2k - N) |k\rangle^{(y)}, \end{aligned} \quad (6-19)$$

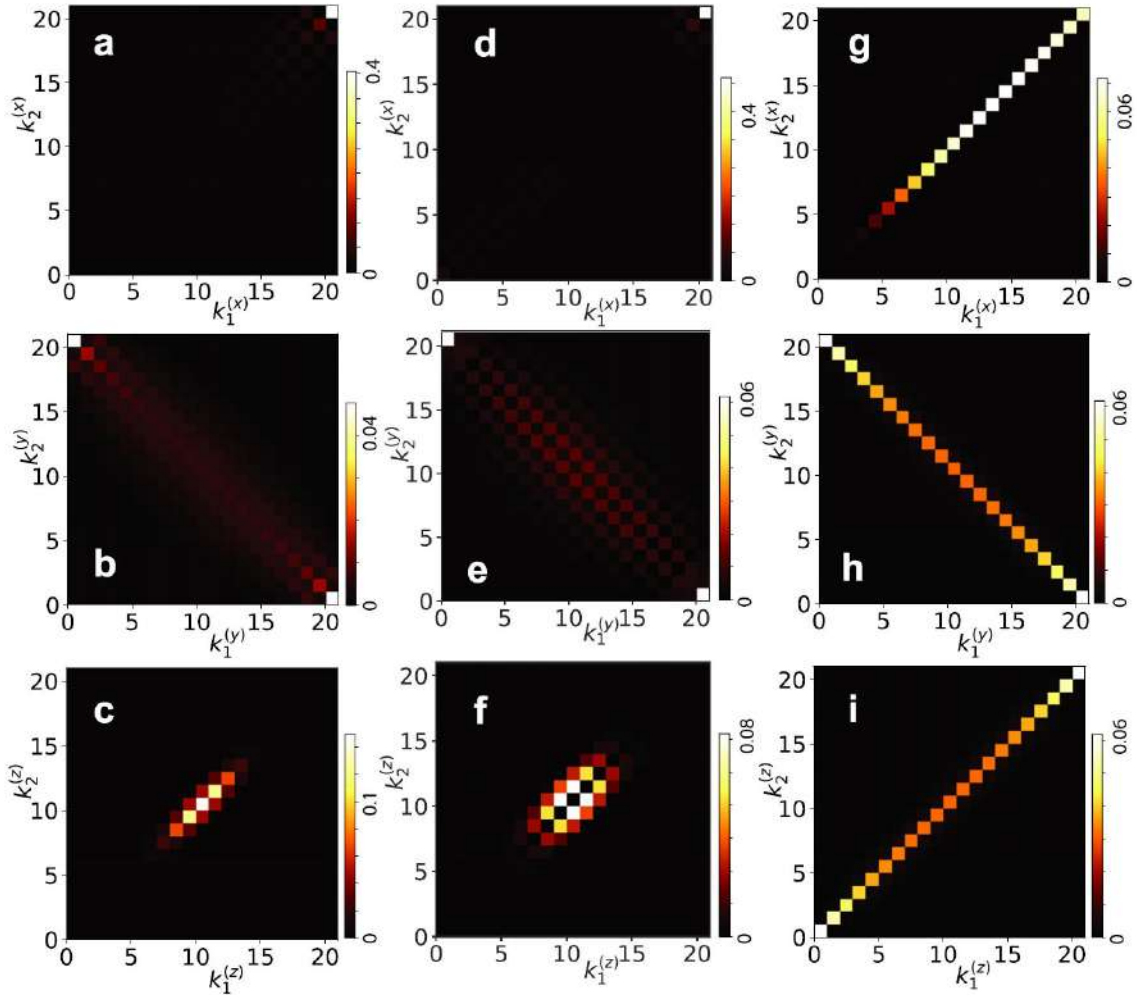


Fig 6-4 (a)(b)(c) Probability distribution for measurements of the state $|\psi_{n_c}^{\text{approx}}(\tau)\rangle$ given in (0-2) for $N = 20$, $n_c = 20$, $\tau = 0.23$, $\alpha = \sqrt{20}$. (d)(e)(f) Probability distribution for measurements of the state (0-9) using the approximation (6-16) for $N = 20$, $n_c = 18$, $n_d = 2$, $\tau = 0.23$, $\alpha = \sqrt{20}$. (g)(h)(i) the 2A2S state given in (6-21) for $N = 20$, $\tau = 2/N$. Measurements are made in the eigenstates of the (a)(d)(g) S^x ; (b)(e)(h) S^y ; (c)(f)(i) S^z operators. (Juan E Aristizabal-Zuluaga, M Kondappan, T Byrnes, et al. J. Phys. B 54 105502 (2021))

the probability for measuring the atoms in these bases is given by

$$p_{\sigma_1\sigma_2}(k_1, k_2) = |\langle \Phi | (|k\rangle^{(\sigma_1)} \otimes |k\rangle^{(\sigma_2)})|^2, \quad (6-20)$$

where $|\Phi\rangle = |\psi_{n_c}^{\text{approx}}(\tau)\rangle$.

A comparison is made with the two-axis two-spin (2A2S) squeezed state [127]:

$$|\psi_{\text{2A2S}}(\tau)\rangle = e^{-i(S_1^z S_2^x + S_1^x S_2^z)\tau} \left| \frac{\pi}{2}, 0 \right\rangle \left| \frac{\pi}{2}, 0 \right\rangle, \quad (6-21)$$

where correlations occur in the $S_{1,2}^z$ variables and anti-correlations in the $S_{1,2}^y$ variables.

The probability distributions of measurements for both the approximate state (0-2) and the 2A2S state (6-21) are analyzed, particularly in the eigenstates of the S^x, S^y, S^z operators. This analysis offers insights into the nature of entanglement and correlations in these states.

Variances and expectation values

In this section of the thesis, we analyze the variances and expectation values derived from the probability distributions of the spin states. Based on Fig. 6-5, we anticipate low variance values for specific spin combinations such as $S_1^x - S_2^x$, $S_1^y + S_2^y$, and $S_1^z - S_2^z$. This expectation aligns with the behavior observed in the 2A2S squeezed state (6-21), where the variances exhibit unique time dependencies. The variances for the approximate state (0-2) are presented in Fig. 6-5, highlighting significant insights into their behavior over time. For instance, the $S_1^z - S_2^z$ variance approaches zero, resembling the trend in the 2A2S squeezed state, while the $S_1^y + S_2^y$ variance converges to a saturation value. This divergence from the 2A2S state is attributed to the broader anti-correlations in the spin states. Spin expectation values, crucial for understanding spin dynamics in the system, are depicted in Fig. 6-5(a) for the approximate state (0-2). These values offer a comparative analysis with the 2A2S squeezed state, particularly noting the decay of initially polarized spins in the S^x -direction and the consistency of other spin expectation values over time.

Entanglement Analysis

In this section of the thesis, the focus is on quantifying entanglement in the state (0-2), using the von Neumann entropy as a measure. The entanglement, represented by $E(\rho)$, where ρ is the reduced density matrix for BEC 1, is a crucial aspect of the analysis. Fig. 6-5(a) illustrates the entanglement as a function of $n_c\tau^2$, indicating a monotonic increase and eventual saturation. For large N , the limiting value of entanglement E_{\lim} is approximated as:

$$E_{\lim} \approx \frac{1}{2} \log_2 \frac{N\pi e}{4} \approx \frac{1}{2} \log_2 N + 0.547. \quad (6-22)$$

This value is significant, indicating substantial entanglement, albeit less than the theoretical maximum for large systems. However, this level of entanglement is still of the same order as the maximal possible, illustrating the efficiency of the optical scheme discussed in this thesis section.

6.4 Spin squeezed states

The concept of spin squeezing, introduced by Kitagawa and Ueda [246], has become a fundamental tool in quantum information processing and precision measurements. The phenomenon is depicted in the context of collective spin states, where the collective spin vector of an ensemble of two-level systems (spins) is represented on the Bloch sphere.

6.4.1 Random vs. correlated spin states

The Fig. 6-6(b*) describe two distinct scenarios of spin ensembles: Fig. 6-6(b*)(a) is random and Fig. 6-6(b*)(b) is correlated, illustrated through their corresponding uncertainty distributions on the Bloch sphere.

Random spin states

Fig. 6-6(a) portrays a random collective spin state, where individual spins are oriented randomly. This randomness leads to a large variance in the collective spin com-

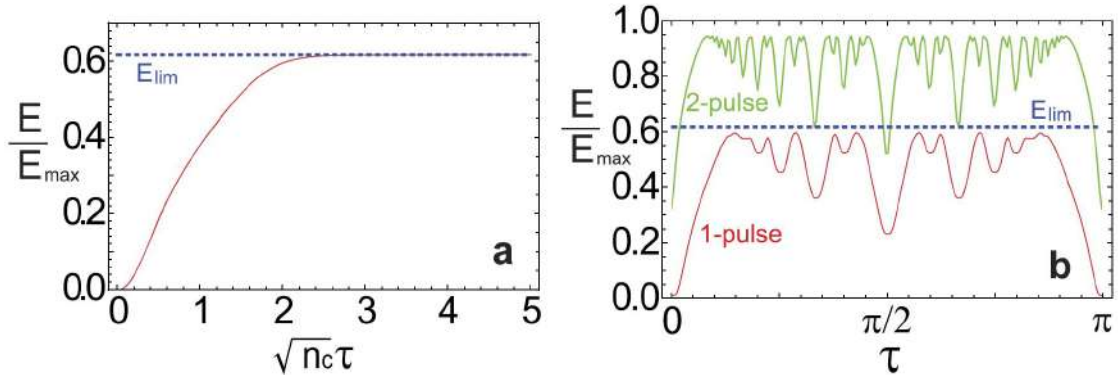


Fig 6-5 Entanglement produced between two BECs using the optical protocol. The von Neumann entropy for (a) the approximate state (0-2) for $N = 20$; (b) the exact state (0-9) for parameters $N = 20$, $n_c = 20$, $n_d = 0$, $\alpha = \sqrt{20}$ and the two-pulse state at [3] for parameters $N = 50$, $n_c^{(1)} = n_c^{(2)} = 50$, $n_d^{(1)} = n_d^{(2)} = 0$, $\tau^{(1)} = 0.1$, $\tau^{(1)} = \tau$, and $\alpha = \sqrt{50}$ as plotted in the figure. (Juan E Aristizabal-Zuluaga, M Kondappan, T Byrnes, et al. J. Phys. B 54 105502 (2021))

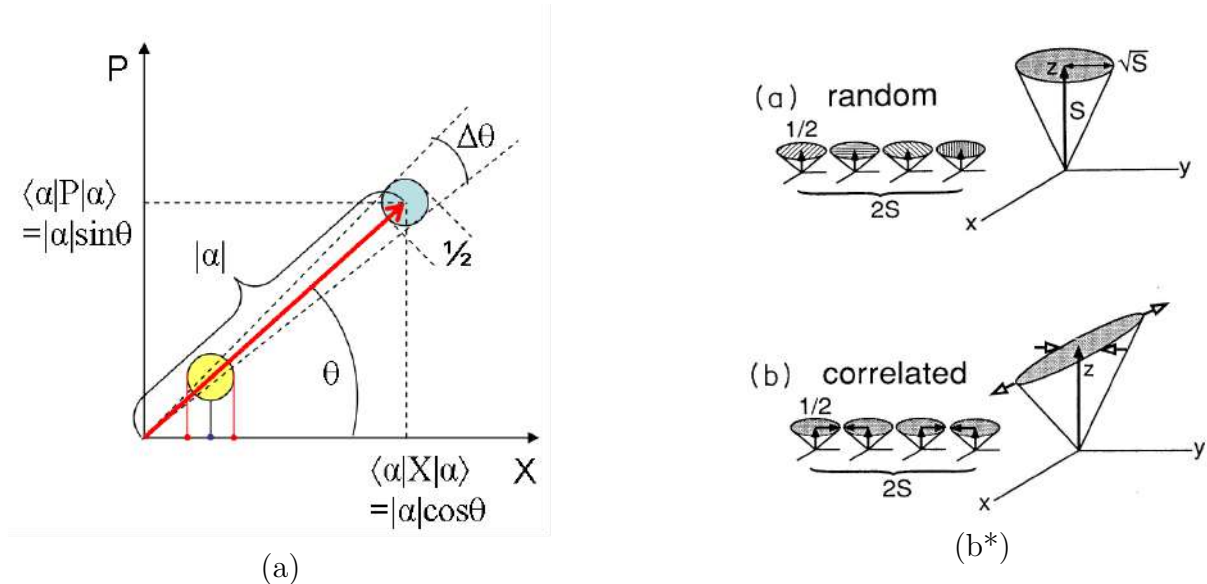


Fig 6-6 Shows the squeezing in spin systems and coherent states, (a) is from Wikipedia: Coherent states and (b*) is spin squeezing from Kitagawa et al., PRA 47, 5138 (1993)

ponents perpendicular to the mean spin direction (denoted as z in the figure). The ensemble's collective spin vector \vec{S} points along the mean spin direction, with a quantum uncertainty that scales with \sqrt{S} , where S is the length of the collective spin vector.

Correlated spin states

Fig. 6-6(b*), on the other hand, shows a correlated spin state, also known as a spin squeezed state. In this configuration, the quantum noise in one of the components perpendicular to the mean spin direction is reduced (squeezed) below the standard quantum limit, at the expense of increased uncertainty in the conjugate component, as per the Heisenberg uncertainty principle. These correlations are indicative of entanglement among the spins, which is a resource for quantum-enhanced measurements.

6.4.2 Quantitative description

Mathematically, the variance of the spin components in the squeezed and anti-squeezed directions are quantified as follows:

$$(\Delta S_{\perp,\text{squeezed}})^2 < \frac{S}{2}, \quad (6-23)$$

$$(\Delta S_{\perp,\text{anti-squeezed}})^2 > \frac{S}{2}. \quad (6-24)$$

These inequalities capture the essence of spin squeezing, where $\Delta S_{\perp,\text{squeezed}}$ is the standard deviation of the spin component in the squeezed direction, and $\Delta S_{\perp,\text{anti-squeezed}}$ is for the anti-squeezed direction.

Fig. 6-6.a illustrates a coherent state in phase space, specifically on a Wigner quasi-probability distribution diagram. Coherent states are paramount in quantum mechanics as they are the closest quantum analog to classical harmonic oscillator states. In the diagram, the axes labeled X and P correspond to the quadrature components of the field, akin to position and momentum. The state is visualized as an ellipse centered at the expectation values $\langle \alpha | X | \alpha \rangle = |\alpha| \cos \theta$ and $\langle \alpha | P | \alpha \rangle = |\alpha| \sin \theta$, where $|\alpha|$ is the amplitude of the coherent state and θ is its phase angle. The ellipse represents the uncertainty in these quadratures, with the standard quantum limit depicted by the circle with a radius of $1/2$. The axis along which the state is squeezed (reduced uncertainty) is marked by $\Delta\theta$,

indicating that this coherent state is also a squeezed state for that particular quadrature.

Coherent states are related to spin squeezing because they can represent the collective state of a spin system under certain conditions. When a spin system is in a squeezed state, similar to the coherent state represented here, the uncertainty in one of the spin components (analogous to the quadrature components in the coherent state) is reduced below the standard quantum limit. This reduction in uncertainty, or squeezing, is a result of quantum correlations between the spins, which can lead to enhanced precision in measurements and is a resource for quantum information processing tasks.

6.5 Two-axis two-spin squeezed spin states

While individual spin squeezing has been extensively explored both theoretically and experimentally, its two-spin counterpart was comparatively underdeveloped until our work [127] has solved the problem. The seminal contributions in the domain of two-spin systems predominantly involve atomic ensembles, spearheaded by Polzik's group [247–249]. These studies primarily engage with atomic ensembles, interpreting spin variables through the lens of bosonic modes, as per the Holstein-Primakoff transformation. Within this framework, the resultant entangled state is akin to a two-mode squeezed state. Contrastingly, the inherent dissimilarity between spins and modes leads to distinct dynamics over prolonged evolution, as evidenced by phenomena like oversqueezing [250–255]. The dual-spin variant of one-axis squeezing, explored in references [256, 257], reveals a complex entanglement structure with fractal time-dependence. Numerous methodologies for generating such states have been investigated [111, 256–261], alongside diverse entangled states for various applications, including quantum computing [108, 109] and quantum information [208, 213, 217, 222, 262, 263]. In the section of this chapter of this thesis, our focus is on the two-axis variant of the two-spin squeezed state, termed as the two-axis two-spin squeezed (2A2S) state. When confined within the Holstein-Primakoff approximation, which is valid for shorter interaction times, this state aligns with the two-mode squeezed state [264]. However, beyond these initial periods, its dynamics diverge markedly from the conventional two-mode squeezing interaction. Our study emphasized longer interaction periods where the Holstein-Primakoff approximation becomes inapplicable. Prior research on prolonged interaction in the one-spin scenario includes references [252, 265]. Our interest lies predominantly in the large but finite spin

regime, relevant to atomic gases, and even in Bose-Einstein Condensates (BECs) with atomic numbers smaller than in thermal atomic ensembles, which still exhibit large spin numbers, often exceeding 10^3 atoms [218, 223, 263].

6.6 The two-axis two-spin squeezed state

Our study centers on two neutral atomic ensembles or Bose-Einstein Condensates (BECs), each comprising atoms with two significant internal states, often hyperfine ground states. For instance, in ^{87}Rb , these states are $F = 1, m_F = -1$ and $F = 2, m_F = 1$ [223]. In BECs, the annihilation operators for these states are denoted as a_j, b_j , where $j \in \{1, 2\}$ for the two BECs. These operators help define an effective spin using Schwinger boson operators:

$$\begin{aligned} S_j^x &= b_j^\dagger a_j + a_j^\dagger b_j \\ S_j^y &= -ib_j^\dagger a_j + ia_j^\dagger b_j \\ S_j^z &= b_j^\dagger b_j - a_j^\dagger a_j. \end{aligned} \tag{6-25}$$

The spin operators follow the commutation relation:

$$[S^j, S^k] = 2i\epsilon_{jkl}S^l, \tag{6-26}$$

with ϵ_{jkl} being the completely antisymmetric tensor. For atomic ensembles, total spin operators are represented as:

$$\begin{aligned} S_j^x &= \sum_{l=1}^N \sigma_{j,l}^x \\ S_j^y &= \sum_{l=1}^N \sigma_{j,l}^y \end{aligned}$$

$$S_j^z = \sum_{l=1}^N \sigma_{j,l}^z, \quad (6-27)$$

where $\sigma_{j,l}^k$ is a Pauli operator for the l th atom in the j th ensemble. We assume equal atom counts in both ensembles. The mathematical convenience of using the BEC will be utilized in this paper, although the results are equally applicable to atomic ensembles.

The two-axis two-spin (2A2S) Hamiltonian is defined as:

$$H = H_{2A2S} = \frac{J}{2}(S_1^x S_2^x - S_1^y S_2^y) = J(S_1^+ S_2^+ + S_1^- S_2^-), \quad (6-28)$$

where:

$$\begin{aligned} S_j^+ &= \frac{1}{2}(S_j^x + iS_j^y) = b_j^\dagger a_j \\ S_j^- &= \frac{1}{2}(S_j^x - iS_j^y) = a_j^\dagger b_j, \end{aligned} \quad (6-29)$$

and J represents an energy constant. This generalizes the two-axis one-spin (2A1S) Hamiltonian studied by Kitagawa and Ueda [266].

The 2A2S squeezed states evolve unitarily as per the Hamiltonian (6-35) over time t , resulting in the state:

$$\begin{aligned} |\psi(t)\rangle &= e^{-iHt/\hbar}|0,0\rangle\langle 0,0|_1|0,0\rangle\langle 0,0|_2 \\ &= e^{-i(S_1^+ S_2^+ + S_1^- S_2^-)\tau}|0,0\rangle\langle 0,0|_1|0,0\rangle\langle 0,0|_2, \end{aligned} \quad (6-30)$$

where $\tau = Jt/\hbar$ is a dimensionless time. The initial states are the maximally polarized states in the S^z -direction.

Analytical expressions for the state at arbitrary evolution times for the 2A2S Hamiltonian are not straightforward due to its inability to be diagonalized using linear transfor-

mations of the bosonic operators. Hence, numerical methods are employed for studying the state and its properties. Our paper will delve into the theoretical aspects of the 2A2S Hamiltonian-produced state. While experimental methods for generating this Hamiltonian will not be discussed here, it's noteworthy that several techniques, including optical interference methods, are viable for producing such states, which we plan to explore in future work. The time deduced for which this regime is valid by expanding the exponential in to second order, and obtain

$$|\psi(t)\rangle \approx (1 - \tau^2 N^2) |N\rangle_1 |N\rangle_2 - i\tau N |N-1\rangle_1 |N-1\rangle_2 - \tau^2 N(N-1) |N-2\rangle_1 |N-2\rangle_2 + \dots, \quad (6-31)$$

where the states we have used are Fock states (6-33). Thus as long as $|\tau| \ll 1/N$, the population of the a -state will be small.

In our study, we introduce a dimensionless time variable τ defined as $\tau = Jt/\hbar$. The starting point of our analysis involves initial states that are fully polarized along the S^z direction, analogous to those used in the 2A1S Hamiltonian framework. To describe the spin coherent states, we use the following formulation:

$$|\theta, \phi\rangle_j = \frac{(\cos \frac{\theta}{2} e^{-i\phi/2} b_j^\dagger + \sin \frac{\theta}{2} e^{i\phi/2} a_j^\dagger)^N}{\sqrt{N!}} |\text{vac}\rangle, \quad (6-32)$$

where θ, ϕ represent the angles on the Bloch sphere, and $|\text{vac}\rangle$ signifies the vacuum state devoid of atoms. The labels $j = 1, 2$ correspond to the respective BECs. Additionally, we define the Fock states as:

$$|k\rangle_j = \frac{(b_j^\dagger)^k (a_j^\dagger)^{N-k}}{\sqrt{k!(N-k)!}} |\text{vac}\rangle. \quad (6-33)$$

The Fock states are eigenstates of the S^z operator according to

$$S_j^z |k\rangle_j = (2k - N) |k\rangle_j. \quad (6-34)$$

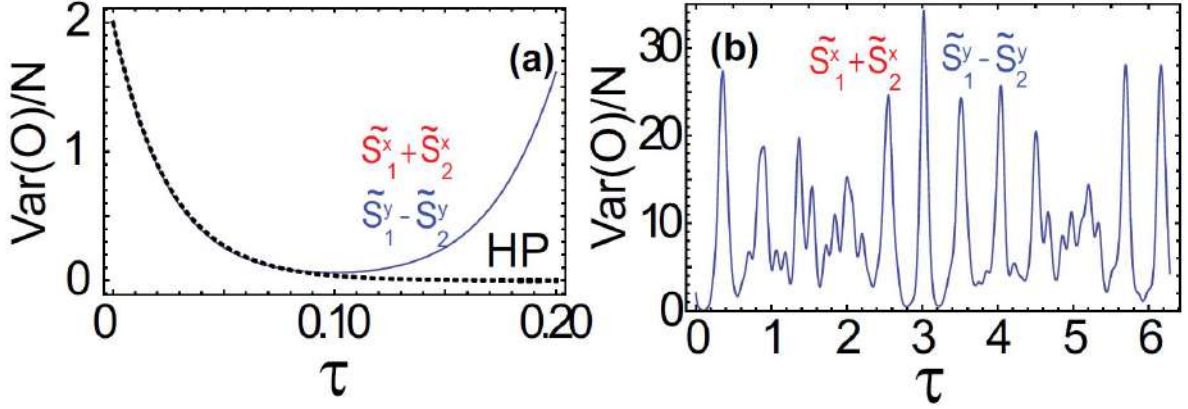


Fig 6-7 Variances of EPR-like observables in the two-axis two-spin squeezed state. The variances of the (a)(b) squeezed variables $\tilde{S}_1^x + \tilde{S}_2^x$ and $\tilde{S}_1^y - \tilde{S}_2^y$. (J Kitzinger, M Kondappan, T Byrnes et al. PRR, 2, 033504 (2020))

6.7 Violation of Bell Inequality in 2A2S squeezed states

In this section of the thesis, the focus is on the non-classical correlations exhibited by two-axis two-spin (2A2S) squeezed states, as evidenced by the violation of the Bell inequality. The 2A2S Hamiltonian, described by the equation

$$H_{2A2S} = \frac{J}{2}(S_1^x S_2^x - S_1^y S_2^y), \quad (6-35)$$

engenders entanglement between two Bose-Einstein condensates (BECs), which can be assessed by the Bell-CHSH inequality.

6.7.1 Bell-CHSH inequality

The Bell-CHSH inequality serves as a fundamental test for entanglement between two systems. For the BECs ruled by the 2A2S Hamiltonian, the Bell-CHSH parameter \mathcal{C} is formulated as

$$\mathcal{C} = \left| \langle M_1^{(1)} M_2^{(1)} \rangle + \langle M_1^{(1)} M_2^{(2)} \rangle - \langle M_1^{(2)} M_2^{(1)} \rangle + \langle M_1^{(2)} M_2^{(2)} \rangle \right| \leq 2, \quad (6-36)$$

with the measurement operators chosen as

$$M_n^{(i)} = (\tilde{S}_n^x \cos \theta_n^{(i)} + \tilde{S}_n^y \sin \theta_n^{(i)}). \quad (6-37)$$

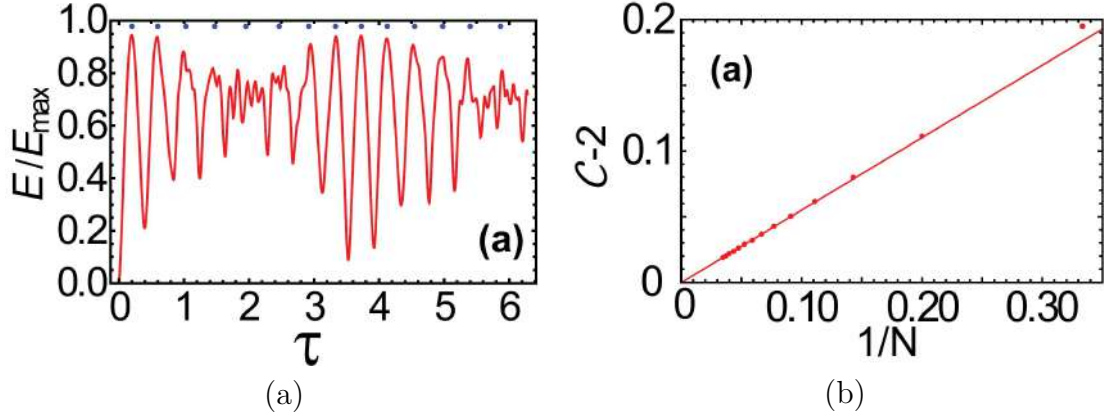


Fig 6-8 Fig. **a** is the entanglement of the two-axis two-spin squeezed state, as measured by the von Neumann entropy E normalized to the maximum value $E_{\max} = \log_2(N + 1)$, as a function of the interaction time τ . The number of atoms in each BEC is $N = 10$. Fig. **b** is Optimized violation of the Bell-CHSH inequality $C - 2$ as a function of $\frac{1}{N}$ for the 2A2S squeezed state. Dots show the numerically calculated values and the solid line is the linear fit. (J Kitzinger, M Kondappan, T Byrnes et al. PRR, 2, 033504 (2020))

6.7.2 Results

The optimized Bell-CHSH violations with respect to the subsystem size N demonstrate that the inequality is violated, as shown in Figure 6-8(a), and follow the empirical scaling

$$C \approx 2 + \frac{0.55}{N}. \quad (6-38)$$

This section underscores the entanglement nature of correlations in 2A2S squeezed states through the violation of the Bell-CHSH inequality, reinforcing the nonlocality inherent in such systems. This contributes to the understanding of entanglement dynamics in macroscopic systems and provides a foundation for future experiments aimed at probing the fundamental aspects of quantum mechanics in BECs.

7 Introduction to quantum non-demolition measurements and imaginary time evolution

The pursuit of a Hamiltonian's ground state is pivotal across various physics domains, including condensed matter, high energy physics, and quantum chemistry [18, 140, 141, 267–269]. It also intersects with optimization problems, focusing on minimizing cost functions [270–272]. Techniques like quantum annealing and adiabatic quantum computing are employed to find complex Hamiltonians' ground states through adiabatic transitions [273–276]. Imaginary time evolution, particularly through the operator e^{-Ht} , amplifies the ground state amplitude, leading to convergence over time [99, 277–281]. While e^{-Ht} represents an unphysical process, methods like Variational Imaginary Time Evolution (VITE) and Quantum Imaginary Time Evolution (QITE) simulate its dynamics. We introduced a novel approach using weak measurements for imaginary time evolution [135]. This method, involving conditional unitary operations based on measurement outcomes, systematically approaches the ground state. Our previous work demonstrated energy estimation via ancilla qubit measurements, with unitary operations adjusting the system towards lower energy states [135]. This section of the thesis explores using quantum nondemolition (QND) measurements for imaginary time evolution [7, 94, 114, 155, 229, 230, 232–240, 282]. QND's integration significantly enhances practical implementation feasibility. Additionally, we extend QND theory, showing its ability to transform single-body Hamiltonians into interacting ones, leveraging quantum measurement nonlinearity. This is crucial for generating states needed in quantum information, such as those involving high-order interactions [20, 137, 138, 283–287]. Our method's efficacy is demonstrated by producing a 4-qubit cluster state requiring a 3-qubit interaction Hamiltonian [287–293].

7.1 Outline and basic idea of this section

Before commencing a more technical discussion of the theory of QND measurements and imaginary time evolution, we give the basic idea of how the measurement-based imaginary time evolution (MITE) technique of Ref. [135] works. We also point out the critical results that are derived in this paper, for the benefit of readers who are not interested in the technical details.

The aim of MITE (as described in Ref. [135]) is to obtain the ground state of a given Hamiltonian H in a controllable quantum system. In the approach, a weak measurement of a quantum state is made in the energy eigenbasis of H , which we call $|E_n\rangle$. The initial state can be an arbitrary state, which can be written

$$|\psi_0\rangle = \sum_n \psi_n^{(0)} |E_n\rangle. \quad (7-1)$$

In Ref. [135], a particular measurement scheme was described, but as we described in this paper, any weak measurement in the energy eigenbasis of the form

$$M(E) \propto \sum_n \exp\left(-\frac{(E_n - E)^2}{2\sigma^2}\right) |E_n\rangle\langle E_n| \quad (7-2)$$

may equally be used. The above measurement has a Gaussian distribution in energy space, centered at energy E and has a width σ . For the purposes of this section, we will not concern ourselves with details such as normalization factors required for $M(E)$ to be a valid quantum measurement for simplicity. We call $M(E)$ a weak measurement because it does not cause total collapse in the energy eigenbasis. In the limit of $\sigma \rightarrow 0$, the measurement approaches a strong measurement which results in a complete collapse of the state to a particular energy eigenstate.

Each measurement outcome E associated with $M(E)$ occurs randomly, since it is a quantum measurement. Hence there is no guarantee that we will obtain the desired outcome for the ground state $E = E_0$. The basic idea of MITE is to cause a “guided collapse” such that multiple measurements of $M(E)$ are made, and adjustments (in the form of unitary operations) are made using the information that is gained from the measurements such as to ensure that the full collapse occurs for $E = E_0$.

Specifically, the procedure proceeds as follows. First, perform a measurement corre-

sponding to $M(E)$ and obtain an estimate of the energy E where the collapse is occurring. The state at this point is

$$M(E)|\psi_0\rangle \propto \sum_n \psi_n^{(0)} \exp\left(-\frac{(E_n - E)^2}{2\sigma^2}\right) |E_n\rangle. \quad (7-3)$$

The parameters of the Gaussian are chosen such that there is still superposition of the energy states, but the amplitudes are more centered around the energy E . If the readout energy E is greater than a threshold energy E_{th} , then this indicates that the collapse is occurring centered at an energy that is higher than desired. In this case, a unitary operation U_C is applied, which redistributes the state in the energy eigenbasis. This has the effect of repopulating the ground state $|E_0\rangle$ and avoiding convergence on any high energy state. If the readout energy $E < E_{\text{th}}$, no unitary is applied, so that the state can continue towards a full collapse towards the ground state $|E_0\rangle$.

Full convergence is attained when the same measurement outcome is consistently attained. Repeated measurements with the same outcome cause a full collapse as may be seen by directly calculating

$$\begin{aligned} M^k(E_0) &\propto \sum_n \exp\left(-\frac{k(E_n - E_0)^2}{2\sigma^2}\right) |E_n\rangle\langle E_n| \\ &\xrightarrow{k \rightarrow \infty} |E_0\rangle\langle E_0| \end{aligned} \quad (7-4)$$

The factor of k in the Gaussian reduces its width by a factor of \sqrt{k} . Once collapse on the energy $E = E_0$ is obtained, all higher energy states are strongly suppressed via the Gaussian factor which is an exponential decay factor in energy. This completes the MITE scheme.

In Ref. [135], an ancilla qubit-based measurement scheme was used to show that it is possible to realize a measurement operator with similar characteristics to (7-2). In this paper, one of the main goals is to show that QND measurements can equally be used to realize a suitable measurement operator to realize the MITE scheme. The POVM for the QND measurement, together with the Gaussian approximations are shown in (7-16) and (7-20). The QND measurement has some additional features, such as the presence of additional Gaussian peaks with a negative phase as illustrated in Fig. 7-2. These require including small modifications of the MITE procedure, such that proper convergence can still be attained. This is explained in Sec. 7.3.2. While these additional Gaussian peaks

may appear to be an undesirable artifact of the QND measurement, these in fact can be taken advantage of to produce multi-body effective interactions. Conventionally, the QND measurements produce two-body interactions, originating from the Gaussian functional form of the measurement (Sec. 7.4.1). However, the additional Gaussian peaks can be used to produce third and higher order interactions, as shown in Sec. 7.4. Finally, we illustrate our methods with an explicit example of generating a four qubit cluster state in Sec. 7.5.

7.2 Generalized quantum nondemolition measurements

We first start by generalizing the theory of QND measurements as developed in Ref. [3, 294] to the measurement of an arbitrary Hamiltonian. This will form the foundation for the measurement-based imaginary time evolution that will be shown in the next section.

7.2.1 Wavefunction evolution

In a QND measurement, coherent light is arranged in a Mach-Zehnder interferometer and the light on one path interacts with the target system (see Fig. 7-1). The form of the interaction is [94, 155]

$$H_{\text{int}} = \hbar\Omega H a^\dagger a, \quad (7-5)$$

where a, b denote the bosonic annihilation operators of the light in the two arms of the interferometer. Here H is a Hamiltonian that specifies the basis of the QND measurement. For typical QND measurements, H is taken to be an operator such as σ^z [3], where $\sigma^{x,y,z}$ are Pauli operators. This Hamiltonian will be eventually that which will be evolved in imaginary time. We note that while not all QND experiments have the exact implementation as shown in Fig. 7-1, many can be reduced to this form, and we consider this to be a generic setup for a QND measurement.

The state of the system after interacting with the light is

$$|\Psi(t)\rangle = e^{-iH_{\text{int}}t/\hbar} \left| \frac{\alpha}{\sqrt{2}} \right\rangle_a \left| \frac{\alpha}{\sqrt{2}} \right\rangle_b |\psi_0\rangle$$

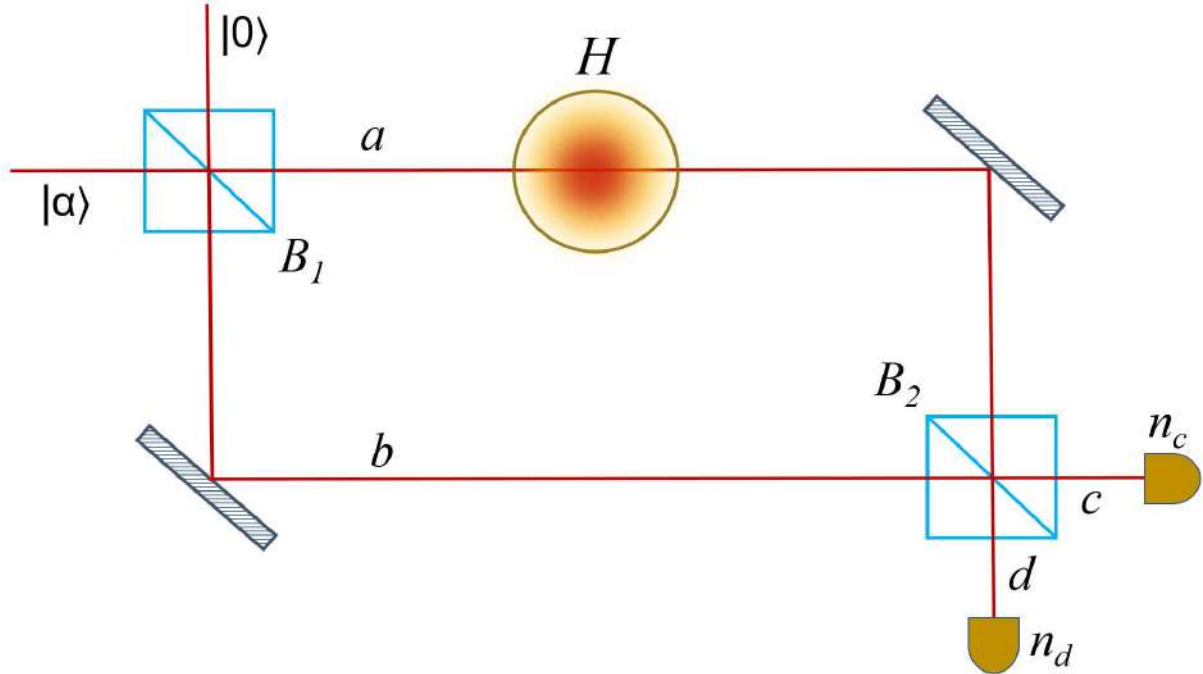


Fig 7-1 Experimental setup for performing a QND measurement. (a) Coherent light $|\alpha\rangle$ is divided into two modes a, b at beamsplitter B_1 . In this generalized scheme of QND of an arbitrary system, the interaction is only through mode a which interacts with qubit via the QND Hamiltonian as depicted in the figure which is an atom cloud in this case (7-5). The modes are then interfered at beamsplitter B_2 that are detected using photon counters with outcomes n_c and n_d respectively. While we show the Mach-Zehnder configuration for conceptual simplicity, any equivalent configuration can also be implemented to realize the QND measurement. M Kondappan, T Byrnes, et al, Phys Rev A 107, 042616 (2023)

$$= \sum_n \psi_n^{(0)} \left| \frac{\alpha e^{-iE_n \tau}}{\sqrt{2}} \right\rangle_a \left| \frac{\alpha}{\sqrt{2}} \right\rangle_b |E_n\rangle \quad (7-6)$$

where $\tau = \Omega t$ is the dimensionless time and the coherent state for the mode a is defined as

$$|\alpha\rangle_a = e^{-|\alpha|^2/2} e^{\alpha a^\dagger} |0\rangle \quad (7-7)$$

and similarly for b . Here, α is the amplitude of the coherent light entering the first beamsplitter in Fig. 7-1. The initial state of the target system is $|\psi_0\rangle$ which can be expanded in terms of energy eigenstates of $H|E_n\rangle = E_n|E_n\rangle$

$$|\psi_0\rangle = \sum_n \psi_n^{(0)} |E_n\rangle, \quad (7-8)$$

where $\psi_n^{(0)} = \langle E_n | \psi_0 \rangle$. After interacting with the atoms, the two modes are interfered via

the second beam splitter which transforms the modes as

$$\begin{aligned} c &= \frac{1}{\sqrt{2}}(a + b) \\ d &= \frac{1}{\sqrt{2}}(a - b). \end{aligned} \quad (7-9)$$

After the second beam splitter, the photons are detected in the Fock basis. The above sequence modulates the quantum state of the atoms due to the atom-light entanglement that is generated by the QND interaction. The final unnormalized state after detection of n_c, n_d photons in modes c, d respectively is

$$|\tilde{\psi}_{n_c n_d}(\tau)\rangle = \sum_n \psi_n^{(0)} C_{n_c n_d}(E_n \tau) |E_n\rangle, \quad (7-10)$$

where we defined the function

$$C_{n_c n_d}(\chi) = \frac{\alpha^{n_c + n_d} e^{-|\alpha|^2/2}}{\sqrt{n_c! n_d!}} \cos^{n_c}(\chi) \sin^{n_d}(\chi). \quad (7-11)$$

The probability of obtaining a photonic measurement outcome n_c, n_d is

$$\begin{aligned} p_{n_c n_d}(\tau) &= \langle \tilde{\psi}_{n_c n_d}(\tau) | \tilde{\psi}_{n_c n_d}(\tau) \rangle \\ &= \sum_n |\psi_n^{(0)} C_{n_c n_d}(E_n \tau)|^2. \end{aligned} \quad (7-12)$$

The function $C_{n_c n_d}(\chi)$ takes a form of a multi-peak Gaussian, peaked at solutions of the equation

$$\cos 2\chi = \frac{n_c - n_d}{n_c + n_d} \quad (7-13)$$

and has a Gaussian width of

$$\sigma_{n_c n_d} \approx \frac{1}{\sqrt{(1 + f_{n_c n_d})(n_c + n_d)}}. \quad (7-14)$$

Here we included a factor of

$$f_{n_c n_d} = \frac{4n_c n_d}{(n_c + n_d)^2} \quad (7-15)$$

which has the range $0 \leq f_{n_c n_d} \leq 1$ and weakly adjusts the Gaussian width. The Gaussian form of the C -function causes a collapse of the initial state into one of the energy eigenstates $|E_n\rangle$ for large $n_c + n_d \approx |\alpha|^2$. For weak coherent light, the state only partially collapses with a modified envelope function as given by $C_{n_c n_d}(E_n \tau)$.

7.2.2 QND measurement operators

The effect of performing the QND measurement can be summarized in a simple way: it introduces an additional factor $C_{n_c n_d}(E_n \tau)$ into the initial wavefunction as given in (7-10). It will be useful to write the QND measurement in terms of a measurement operator, or more precisely a Positive Operator Valued Measure (POVM)

$$M_{n_c n_d}(\tau) = \sum_n C_{n_c n_d}(E_n \tau) |E_n\rangle \langle E_n|. \quad (7-16)$$

The state following the QND measurement (7-10) can then be written as

$$|\tilde{\psi}_{n_c n_d}(\tau)\rangle = M_{n_c n_d}(\tau) |\psi_0\rangle. \quad (7-17)$$

The measurement operators (7-16) satisfy the completeness relation

$$\sum_{n_c, n_d} M_{n_c n_d}(\tau)^\dagger M_{n_c n_d}(\tau) = I, \quad (7-18)$$

which results from the property of the C -functions

$$\sum_{n_c n_d=0}^{\infty} |C_{n_c n_d}(\chi)|^2 = 1. \quad (7-19)$$

In order to connect the QND measurement with imaginary time evolution, it will be illuminating to approximate the C -function as a Gaussian. Using Stirling's approximation we obtain the expression [245]

$$C_{n_c n_d}(\chi) \approx$$

$$s_{n_c n_d}(\chi) A_{n_c n_d} \exp \left(-\frac{\left[|t(\chi)| - \frac{1}{2} \arccos\left(\frac{n_c - n_d}{n_c + n_d}\right) \right]^2}{2\sigma_{n_c n_d}^2} \right) \quad (7-20)$$

where $t(x) = \arcsin(\sin(x))$ is the triangular wave and the amplitude is defined as

$$A_{n_c n_d} = \begin{cases} \frac{\alpha^{n_c + n_d} e^{-|\alpha|^2/2}}{\sqrt{(n_c + n_d)!}} & \text{if } n_c n_d = 0 \\ \frac{\alpha^{n_c + n_d} e^{-|\alpha|^2/2}}{\sqrt{(n_c + n_d)!} (\frac{2\pi n_c n_d}{n_c + n_d})^{1/4}} & \text{otherwise} \end{cases} \quad (7-21)$$

and the sign of the Gaussian is determined by

$$s_{n_c n_d}(\chi) = q^{n_c}(\chi + \pi/2) q^{n_d}(\chi) \quad (7-22)$$

where $q(x) = \text{sgn}(\sin(x))$ is the square wave. The sign function only takes values $s_{n_c n_d}(\chi) = \pm 1$.

A less accurate, but simpler form of the C -function can be obtained according to

$$C_{n_c n_d}(\chi) \approx s_{n_c n_d}(\chi) A_{n_c n_d} \exp \left(-\frac{\left[\cos(2\chi) - \frac{n_c - n_d}{n_c + n_d} \right]^2}{8\tilde{\sigma}_{n_c n_d}^2} \right) \quad (7-23)$$

where we defined the empirical standard deviation factor

$$\tilde{\sigma}_{n_c n_d} = \frac{1}{\sqrt{8 \left(\frac{n_c + n_d}{4} \right)^{2-f_{n_c n_d}}}}. \quad (7-24)$$

The peculiar form of the standard deviation arises due to the fact that at extremal values $n_c = n_d = 0$, the dependence within the exponential (7-23) has a $\sim \chi^4$ dependence, rather than a conventional $\sim \chi^2$ dependence. The exponent in (7-24) adjusts for this such that the width of the peak is of the correct value.

In Fig. 7-2 we show the performance of the two approximations for two parameter values. We see that both (7-20) and (7-23) are peaked at the correct values as given in (7-13), which is guaranteed from the argument of the Gaussian. The primary difference between (7-20) and (7-23) is that in the latter approximation, the form of the peak is

not of Gaussian form in the region of $n_c = n_d = 0$, due to the $\sim \chi^4$ dependence in the exponential. In the cases that we will examine, the precise functional form is not as important as the location of the peaks. For this reason, later Eq. (7-23) will be used to approximate the C -function.

7.3 Imaginary time evolution

In this section we show that the QND measurements described in the previous section can be utilized as the imaginary time evolution measurement operators that were introduced in Ref. [135].

7.3.1 Ancilla qubit based measurement operators

We first review the imaginary time evolution measurement operators introduced in Ref. [135]. There we considered the measurement operators

$$\mathcal{M}_l = \frac{1}{\sqrt{2}}(\cos \tau H - (-1)^l \sin \tau H) \quad (7-25)$$

$$\begin{aligned} &= \frac{1}{\sqrt{2}} \sum_n (\cos \tau E_n - (-1)^l \sin \tau E_n) |E_n\rangle \langle E_n| \\ &= \frac{e^{-(-1)^l H \tau}}{\sqrt{2}} \end{aligned} \quad (7-26)$$

for $l \in \{0, 1\}$. These measurement operators can be realized by interacting an ancilla qubit with the interaction Hamiltonian $H \otimes \sigma^y$ for a time τ and then measuring the ancilla in the σ^z -basis. After a sequence of measurements, the combined effect can be evaluated to be

$$\mathcal{M}_0^{k_0} \mathcal{M}_1^{k_1} = \sum_n A_{k_0 k_1}(\tau E_n) |E_n\rangle \langle E_n| \quad (7-27)$$

where the amplitude function is

$$A_{k_0 k_1}(x) = \cos^{k_0}(x + \pi/4) \sin^{k_1}(x + \pi/4). \quad (7-28)$$

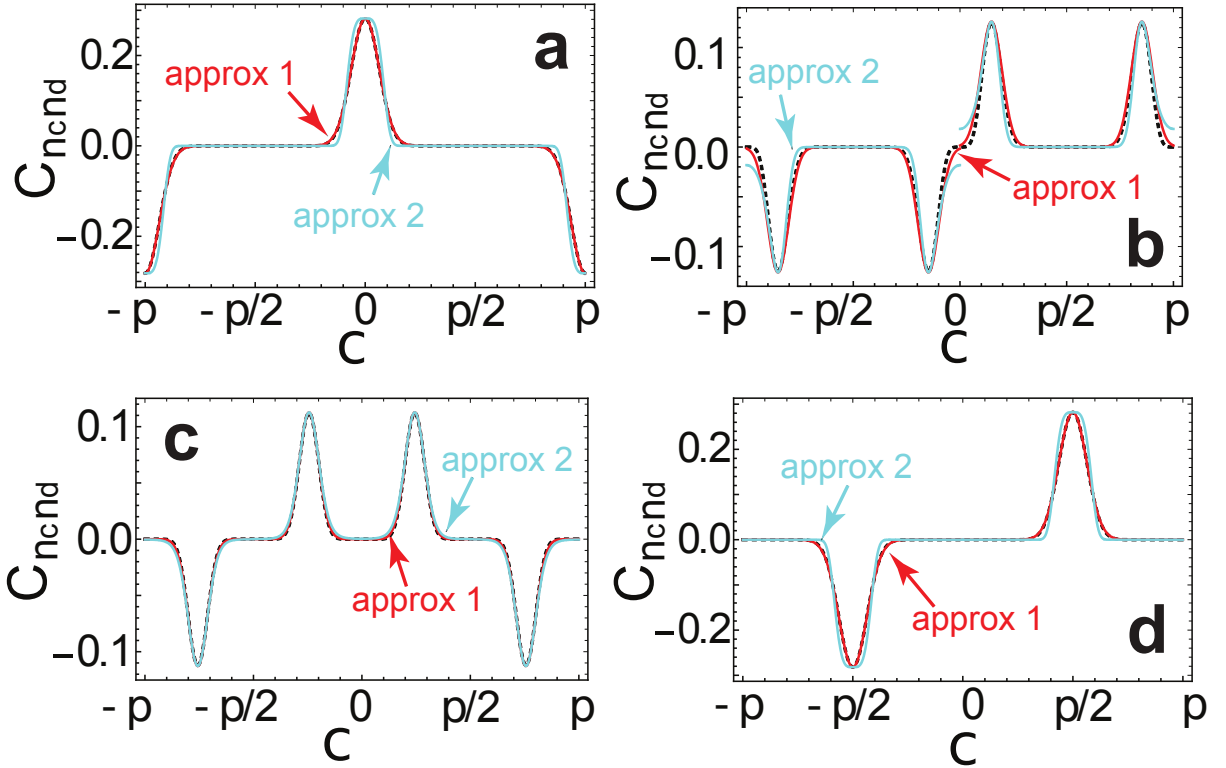


Fig 7-2 Approximating functions to the function $C_{ncnd}(\chi)$. The two approximate expressions (7-20) and (7-23) which we call “approx 1” and “approx 2” respectively, are shown for the measurement outcomes (a) $n_c = 25, n_d = 0$; (b) $n_c = 20, n_d = 5$; (c) $n_c = 13, n_d = 12$; (d) $n_c = 0, n_d = 25$. The dotted line is the exact function (7-11) for comparison. We use $\alpha = 5$ for all plots. C_{ncnd} and χ are dimensionless. M Kondappan, T Byrnes, et al, Phys Rev A 107, 042616 (2023)

The amplitude function is peaked at solutions to the equation

$$\sin 2x = \frac{k_1 - k_0}{k_0 + k_1} \quad (7-29)$$

and has a Gaussian width of

$$\sigma_{k_0 k_1} \approx \frac{1}{\sqrt{(1 + f_{k_0 k_1})(k_0 + k_1)}}. \quad (7-30)$$

In the imaginary time evolution approach of Ref. [135], Eq. (7-29) is used to estimate the energy readout according to

$$E_{\text{est}} = \frac{1}{2\tau} \arcsin \left(\frac{k_1 - k_0}{k_0 + k_1} \right). \quad (7-31)$$

In the scheme as described in Ref. [135], the energy spectrum was limited to the range $-\pi/4 \leq \tau E_n \leq \pi/4$ such that only the principal value of the arcsine needs to be considered. The imaginary time evolution proceeds as follows. If the energy estimate is higher than a particular threshold E_{th} then a corrective unitary U_C is applied, which induces a transition from the existing state to another energy state. If the energy estimate is below E_{th} then the sequence of measurements is allowed to converge and collapse the state. In this way, the system's only fixed point is the ground state and the stochastic evolution due to the measurement operators is converted to a deterministic evolution.

7.3.2 QND based imaginary time evolution

We now show how the QND measurement operators (7-16) can be used in place of the ancilla-based measurement operators for imaginary time evolution. The basic idea of our approach is to replace the imaginary time measurement operators (7-26) by a weak QND measurement specified by (7-16). A very weak coherent light source (e.g. $|\alpha|^2 \sim 1$) is input to the interferometer of Fig. 7-1. This is then repeated a large number of times in a similar way to that given in (7-27). In such a situation the QND measurement-induced collapse occurs very slowly, and it is possible to apply a corrective unitary to drive the system to a desired state deterministically in a similar way to the imaginary time scheme as discussed in Ref. [135].

Let us consider a sequence of T such QND measurements, and evaluate the effect of the combined measurement. Using (7-16) we find that

$$\prod_{t=1}^T M_{n_c^{(t)} n_d^{(t)}}(\tau) = \sum_n C_{\text{tot}}(E_n \tau) |E_n\rangle \langle E_n| \quad (7-32)$$

where the cumulative measurement function is

$$\begin{aligned} C_{\text{tot}}(\chi) &= \prod_{t=1}^T C_{n_c^{(t)} n_d^{(t)}}(\chi) \\ &= \frac{\alpha^{n_c^{\text{tot}} + n_d^{\text{tot}}} e^{-T|\alpha|^2/2}}{\prod_{t=1}^T \sqrt{n_c^{(t)}! n_d^{(t)}!}} \cos^{n_c^{\text{tot}}}(\chi) \sin^{n_d^{\text{tot}}}(\chi) \end{aligned} \quad (7-33)$$

and we defined

$$\begin{aligned} n_c^{\text{tot}} &= \sum_{t=1}^T n_c^{(t)} \\ n_d^{\text{tot}} &= \sum_{t=1}^T n_d^{(t)}. \end{aligned} \quad (7-34)$$

Comparing (7-32) and (7-27), there is an obvious similarity to the form of the operators. They are both diagonal in the energy eigenbasis of H , and the functions $A_{k_0 k_1}(x)$ and $C_{\text{tot}}(\chi)$ have a similar form. In terms of the functional dependence they are completely equivalent up to a constant shift $\chi = x + \pi/4$. This means that the measurement readouts can be done with the cumulative photon counts (7-34) in a similar way to (7-29). Reusing the results from (7-13) and (7-14), we see that the function $C_{\text{tot}}(\chi)$ is peaked at the value

$$\cos 2\chi = \frac{n_c^{\text{tot}} - n_d^{\text{tot}}}{n_c^{\text{tot}} + n_d^{\text{tot}}} \quad (7-35)$$

and has a Gaussian width of

$$\sigma_{n_c^{\text{tot}} n_d^{\text{tot}}} \approx \frac{1}{\sqrt{(1 + f_{n_c^{\text{tot}} n_d^{\text{tot}}})(n_c^{\text{tot}} + n_d^{\text{tot}})}}. \quad (7-36)$$

In the case that the energy range is fixed to $0 \leq \tau E_n \leq \pi/2$, an estimate of the energy can be made from the relation

$$E_{\text{est}}(n_c^{\text{tot}}, n_d^{\text{tot}}) = \frac{1}{2\tau} \arccos \left(\frac{n_c^{\text{tot}} - n_d^{\text{tot}}}{n_c^{\text{tot}} + n_d^{\text{tot}}} \right). \quad (7-37)$$

We will see that it is also possible to utilize long interaction times where the energy range is larger than $0 \leq \tau E_n \leq \pi/2$.

The QND measurement-based imaginary time evolution then proceeds as follows. After the $(t+1)$ th QND measurement is performed, corrective unitaries are applied such that the state becomes

$$|\psi_{t+1}\rangle = \frac{U_{m_c^{(t+1)} m_d^{(t+1)}} V_{n_c n_d} M_{n_c n_d} |\psi_t\rangle}{\sqrt{\langle \psi_t | M_{n_c n_d}^\dagger M_{n_c n_d} |\psi_t \rangle}} \quad (7-38)$$

where the corrective unitary is

$$U_{m_c m_d} = \begin{cases} I & \text{if } |E_{\text{est}}(m_c, m_d) - E_{\text{tgt}}| < \delta_{\text{tgt}} \\ U_C & \text{otherwise} \end{cases} \quad (7-39)$$

and $V_{n_c n_d}$ is a phase correction unitary in the basis of $|E_n\rangle$ that is used to remove the effects of $s_{n_c n_d}$ as given in (7-22). This will only be important in the long interaction time regime and this will be discussed further in the next section. The counters are updated as

$$\begin{aligned} m_c^{(t+1)} &= \begin{cases} m_c^{(t)} + n_c & \text{if } |E_{\text{est}}(m_c^{(t)} + n_c, m_d^{(t)} + n_d) - E_{\text{tgt}}| < \delta_{\text{tgt}} \\ 0 & \text{otherwise} \end{cases} \\ m_d^{(t+1)} &= \begin{cases} m_d^{(t)} + n_d & \text{if } |E_{\text{est}}(m_c^{(t)} + n_c, m_d^{(t)} + n_d) - E_{\text{tgt}}| < \delta_{\text{tgt}} \\ 0 & \text{otherwise} \end{cases}. \end{aligned} \quad (7-40)$$

In the above we have generalized the condition for applying the corrective unitary slightly from what appeared in Ref. [135] such that convergence towards a particular target state with energy E_{tgt} is obtained. The δ_{tgt} is a tolerance for the energy estimate being in the vicinity of the target energy. This modified condition will allow us to target not only the ground state but any state in the energy spectrum.

7.4 QND measurement induced effective interactions

One of the uses of QND measurements has been for generating entanglement between spatially separated quantum systems. For example, in Ref. [114], entanglement was produced between two atomic ensembles using QND measurements. One way to understand how entanglement is produced is that initially entanglement is produced between the two atomic ensembles and light in a tripartite fashion, then the light is measured out, swapping the entanglement to between the two atomic ensembles. In this section, we provide another way of understanding the effective interactions that are produced, making use the measurement operator formalism of Sec. 7.2. We first show how effective interactions can be produced using QND measurements in the short interaction time regime, then show how longer interaction times can produce higher order interactions.

7.4.1 Short interaction time regime

In the previous section, we showed that QND measurements could be used as the basis for imaginary time evolution. In Ref. [135], only the short interaction times were considered, which in the QND formulation corresponds to the energy spectrum being in the range $0 \leq \tau E_n \leq \pi/2$. This range was chosen because the readout of the QND measurement has a multivalued nature and are peaked at the solutions of (7-35). Fixing the energy range as above gives a one-to-one relation between the QND measurement readouts and the energies. For a general Hamiltonian H_0 , this requires adding an energy offset such that the energy spectrum fits in this range. Let us assume that H_0 has a spectrum that has the ground state and the largest eigenvalue of the same magnitude $-E_0 = E_{\max}$. The most sensitive part of the cosine function with respect to the variation of χ in (7-35) is around $\chi = \pi/4$, hence we centre the energy spectrum around this point such that

$$H\tau = H_0\tau + \frac{\pi}{4}I. \quad (7-41)$$

The measurement operator (7-16) can then be written as

$$\begin{aligned} M_{n_c n_d}(\tau) &= C_{n_c n_d}(H\tau) \\ &\approx \pm A_{n_c n_d} \exp\left(-\frac{\left[\sin(2H_0\tau) - \frac{n_d - n_c}{n_c + n_d}\right]^2}{8\tilde{\sigma}_{n_c n_d}^2}\right), \end{aligned} \quad (7-42)$$

where we used the approximate expression (7-23) and we abbreviated the sign dependence $s_{n_c n_d}(H\tau)$ by writing \pm , since it contributes an unimportant global phase in this case. For short times $|E_n\tau| \ll 1$, we may approximate the sine function linearly, giving

$$M_{n_c n_d}(\tau) \approx \pm A_{n_c n_d} \exp\left(-\frac{\left[H_0\tau - \frac{n_d - n_c}{2(n_c + n_d)}\right]^2}{2\sigma_{n_c n_d}^2}\right), \quad (7-43)$$

where we replaced the empirical variance factor with the standard variance (7-14) since the argument of the Gaussian no longer has the issue with the fourth power.

We see from (7-43) that the effect of QND measurements in the short time regime is to produce a Gaussian with respect to the Hamiltonian H_0 , with an offset related to

the measurement readout. This form makes apparent how the imaginary time evolution arises. For measurement outcomes such that $E_0\tau > (n_d - n_c)/(2(n_c + n_d))$, the Gaussian tail causes exponential damping of the excited states. The imaginary time evolution as described in the previous section takes advantage of this by using a feedback approach to drive the system towards the desired outcome.

Let us illustrate the above with a specific example. The fact that the measurement operator involves the *square* of the Hamiltonian H_0 is the reason why entanglement generation is possible using QND measurements, even if H_0 itself does not include interaction terms. Let us show how entanglement generation results using the typical choice for QND measurement

$$H_0 = -(\sigma_1^z + \sigma_2^z). \quad (7-44)$$

Substituting this into (7-43), we see that the effect of the measurement operator is

$$M_{n_c n_d}(\tau) \propto \exp\left(-\frac{\sigma_1^z \sigma_2^z \tau^2 + (\sigma_1^z + \sigma_2^z)\left(\frac{n_d - n_c}{2(n_c + n_d)}\right)\tau}{\sigma_{n_c n_d}^2}\right), \quad (7-45)$$

which involves an interaction term originating from the H_0^2 term in the Gaussian.

Another way to view this is that the state collapses onto one of the energy eigenstates $|E_n\rangle$ of H_0 for large $n_c + n_d$, where the variance $\sigma_{n_c n_d}^2 \rightarrow 0$. The three energy eigenstates of (7-44) are $|00\rangle$, $c_1|01\rangle + c_2|10\rangle$, and $|11\rangle$, where c_1, c_2 are normalized complex coefficients. The second of these eigenstates has the form of an entangled state (for $c_1, c_2 \neq 0$), resulting in entanglement generation.

7.4.2 Long interaction time regime

The form of the measurement operator (7-42) suggests there is another way to produce effective interactions by taking advantage of the sine function in the argument of the Gaussian function. For longer interaction times the contribution of the higher order terms beyond (7-43) become important, giving rise to further a nonlinearity. To illustrate

this, let us consider the example where the Hamiltonian is

$$H_0 = - \sum_{n=1}^N \sigma_n^z \quad (7-46)$$

which is the total spin of an ensemble and is one that is typically considered in QND measurements. Evaluating the sine factor in (7-42) for the interaction time $\tau = \pi/4$ we have

$$\sin\left(\frac{\pi}{2} \sum_{n=1}^N \sigma_n^z\right) = \cos\left(\frac{\pi(N+1)}{2}\right) \prod_{n=1}^N \sigma_n^z. \quad (7-47)$$

This shows that it is possible to produce a highly nonlinear effective interaction from a single particle interaction (7-46).

We may take a different point of view to obtain the same result from an energy point of view. In Fig. 7-3 we contrast the short and long interaction time regimes. In the short interaction time regime (Fig. 7-3(a)), the energy levels are within a limited range $0 \leq \tau E_n \leq \pi/2$, hence for a particular n_c, n_d measurement outcome only one of the levels are picked out at a time. For longer interaction times (Fig. 7-3(b)), the energy levels are more spaced out, and the multivalued nature of the C -function can pick out more than one energy level at a time. For example, for the $n_c = 0, n_d = 101$ outcome, the C -function picks out states with $S^z = 3$ and $S^z = -1$, corresponding to the states $|000\rangle$ and $|011\rangle, |101\rangle, |110\rangle$. These states all satisfy $\sigma_1^z \sigma_2^z \sigma_3^z = 1$ and suppress the remaining states, which satisfy $\sigma_1^z \sigma_2^z \sigma_3^z = -1$. This corresponds to an evolution

$$M_{n_c n_d}(\pi/4) \propto s_{n_c n_d}(H\tau) \exp\left(\frac{\left(\frac{n_d - n_c}{n_c + n_d}\right) \sigma_1^z \sigma_2^z \sigma_3^z}{4\sigma_{n_c n_d}^2}\right) \quad (7-48)$$

according to (7-42). We have reinstated the phase factor $s_{n_c n_d}(H\tau)$ since in this regime this can contribute a relative phase factor that can affect the state. For example, in Fig. 7-3(b), for odd values of n_d , there is a relative minus sign between the $S^z = 3$ and $S^z = -1$ states which can affect the state.

The above is merely a simple example of a way of producing high order interactions by taking advantage of the nonlinearity that is present in (7-42). By choosing interaction times τ that picks out other states in the energy spectrum of the Hamiltonian H , other

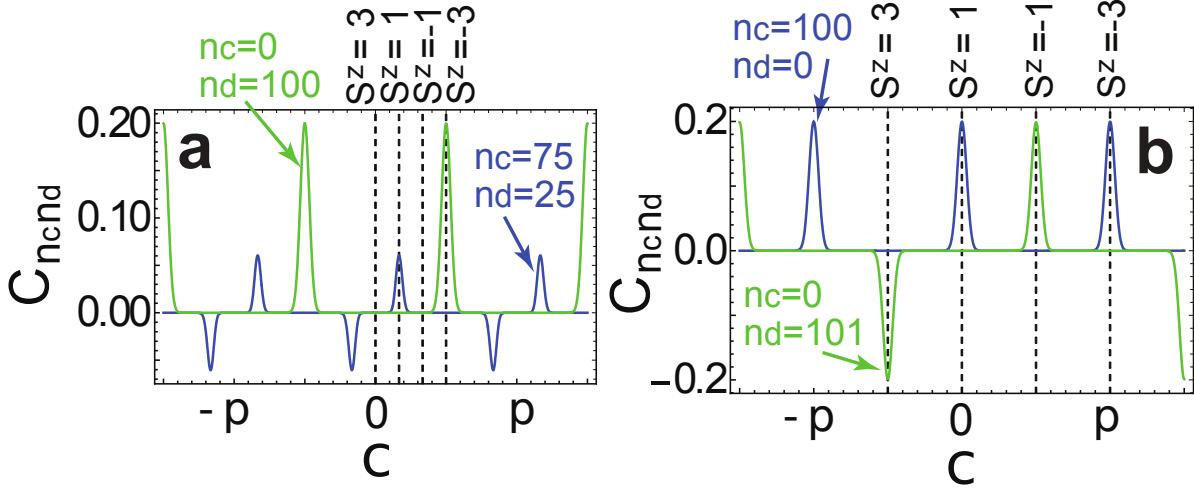


Fig 7-3 Effects of short and long interaction times for QND measurements. The C -function is plotted for different measurement outcomes as marked in the context of the energy levels τE_n marked by the dashed vertical lines. The energy levels are those given by (7-46) with $N = 3$ with the offset (7-41). The interaction times are chosen as (a) $\tau = \pi/12$; (b) $\tau = \pi/4$. The parameters for (a) satisfy the short time regime as $0 \leq \tau E_n \leq \pi/2$, while for (b) the interaction times are in the long time regime. We use $\alpha = 10$ for all calculations. C_{ncnd} and χ are dimensionless. M Kondappan, T Byrnes, et al, Phys Rev A 107, 042616 (2023)

types of interactions can be generated.

7.5 Example: Generation of a four qubit cluster state

We now illustrate our QND measurement-based imaginary time evolution methods for the case of generating a four-qubit cluster state. The four-qubit cluster state is defined as,

$$|C_4\rangle = \frac{1}{2} (|0000\rangle + |0011\rangle + |1101\rangle + |1110\rangle). \quad (7-49)$$

This example serves as not only an illustrative example which shows how QND measurements can be used to generate Hamiltonians involving beyond-second order interactions but is also a practically important example as it is an essential component for gate teleportation of a CNOT gate [295].

7.5.1 Stabilizer Hamiltonian

A useful way to define cluster states is in terms of stabilizers, which are operators that form a group such that the cluster state is their simultaneous eigenstate with eigenvalue +1 [287, 296]. In the case of (7-49), the stabilizers are

$$\mathcal{S} = \{\sigma_1^z \sigma_2^z, \sigma_3^x \sigma_4^x, \sigma_1^x \sigma_2^x \sigma_3^x, \sigma_2^z \sigma_3^z \sigma_4^z\}. \quad (7-50)$$

The stabilizers can be used to construct a Hamiltonian that has the cluster state as its ground state, simply by summing the stabilizer elements

$$H_{C_4} = -\sigma_1^z \sigma_2^z - \sigma_3^x \sigma_4^x - \sigma_1^x \sigma_2^x \sigma_3^x - \sigma_2^z \sigma_3^z \sigma_4^z. \quad (7-51)$$

This can be used in the context of imaginary time evolution, by starting from an arbitrary initial state $|\psi_0\rangle$ the system is driven

$$e^{-H_{C_4}\tilde{t}}|\psi_0\rangle = e^{\sigma_2^z \sigma_3^z \sigma_4^z \tilde{t}} e^{\sigma_1^x \sigma_2^x \sigma_3^x \tilde{t}} e^{\sigma_3^x \sigma_4^x \tilde{t}} e^{\sigma_1^z \sigma_2^z \tilde{t}} |\psi_0\rangle \xrightarrow{\tilde{t} \rightarrow \infty} |C_4\rangle \quad (7-52)$$

where \tilde{t} is a dimensionless time parameter. Here we used the fact that all stabilizers in (7-50) mutually commute. Hence by applying a sequence of imaginary time evolutions, the four qubit cluster state can be prepared.

7.5.2 Measurement and correction operators

We now construct the measurement and correction operators required to realize the imaginary time evolution in (7-52). We see that there are two basic types of operators involved, the two qubit interaction $\sigma_1^z \sigma_2^z, \sigma_3^x \sigma_4^x$ and three qubit interaction $\sigma_1^x \sigma_2^x \sigma_3^x, \sigma_2^z \sigma_3^z \sigma_4^z$. We have already seen that such two and three qubit operators are possible to realize in Sec. 7.4. With some small modifications of what we have already discussed, we will show how these can be implemented.

Two qubit interactions

First let us consider the two qubit imaginary time operator $e^{\sigma_1^z \sigma_2^z \tilde{t}}$. As discussed in Sec. 7.4.1, this can be achieved using a short time evolution and taking advantage of the Gaussian form of the C -function. While the measurement operator (7-45) has the correct basic form, it has the wrong sign on the $\sigma_1^z \sigma_2^z$ term. This can be rectified by instead choosing the Hamiltonian

$$H = \sigma_1^z - \sigma_2^z. \quad (7-53)$$

The three eigenstates of (7-53) are

$$\begin{aligned} |E_0\rangle &= |10\rangle \\ |E_1\rangle &= c_1|00\rangle + c_2|11\rangle \\ |E_2\rangle &= |01\rangle \end{aligned} \quad (7-54)$$

where c_1, c_2 are normalized complex coefficients, and the energies are

$$\begin{aligned} E_0 &= -2 \\ E_1 &= 0 \\ E_2 &= 2. \end{aligned} \quad (7-55)$$

The state we would like to target is the state $c_1|00\rangle + c_2|11\rangle$ which is the ground state of the Hamiltonian $-\sigma_1^z \sigma_2^z$. Hence we target the energy

$$E_{\text{tgt}} = E_1 = 0, \quad (7-56)$$

which corresponds to the measurement outcome $n_c > 0, n_d = 0$ according to (7-37). We choose a time in the short time regime such that the remaining energy levels are not solutions of the location of the peaks given by (7-35). That is, for $E_n = \pm 2$, we choose a time such that

$$\cos 2E_{\text{tgt}}\tau \neq \cos 2E_n\tau. \quad (7-57)$$

This avoids picking up additional states when targeting $|E_1\rangle$. An example of an interaction time that satisfies this is $\tau = \pi/8$.

Finally, we require an operator that induces a transition between non-target energy states and the target state $|\langle E_{\text{tgt}}|U_C|E_n\rangle| > 0, \forall n$. From inspection of the energy eigenstates we may choose

$$U_C = \sigma_1^x. \quad (7-58)$$

The phase correction unitary does not need to be considered for this case since $s_{n_{\text{end}}}(H\tau)$ only contributes a global phase, and we can take

$$V_{n_{\text{end}}} = I. \quad (7-59)$$

With this, we may then follow the procedure described in Sec. 7.3.2, where convergence to the state $c_1|00\rangle + c_2|11\rangle$ is attained.

For the operator $e^{\sigma_3^x \sigma_4^x \tilde{t}}$, the procedure is the same up to a basis change. Specifically, the Hamiltonian for the QND measurement is

$$H = \sigma_3^x - \sigma_4^x. \quad (7-60)$$

while the correction operator is

$$U_C = \sigma_1^z. \quad (7-61)$$

Three qubit interactions

We next show how to perform the imaginary time evolution corresponding to $e^{\sigma_1^x \sigma_2^x \sigma_3^x \tilde{t}}$. The basic approach was already described in Sec. 7.4.2, where a N -qubit interaction in the z basis was realized. In our case, we choose the Hamiltonian

$$H = -(\sigma_1^x + \sigma_2^x + \sigma_3^x) + 3I \quad (7-62)$$

and we choose an interaction time in the long time regime such a three qubit interaction similar to (7-48) is generated. The eigenstates of (7-62) are

$$\begin{aligned} |E_0\rangle &= |+++ \rangle \\ |E_1\rangle &= c_1|++-\rangle + c_2|+-\rangle + c_3|-+\rangle \\ |E_2\rangle &= c_1|---\rangle + c_2|--\rangle + c_3|+-\rangle \\ |E_3\rangle &= |---\rangle \end{aligned} \quad (7-63)$$

where c_1, c_2, c_3 are normalized complex coefficients, and the energies are

$$\begin{aligned} E_0 &= 0 \\ E_1 &= 2 \\ E_2 &= 4 \\ E_3 &= 6. \end{aligned} \quad (7-64)$$

The ground states of the desired Hamiltonian $-\sigma_1^x\sigma_2^x\sigma_3^x$ are $|+++ \rangle, |---\rangle, |--+\rangle, |+--\rangle$, which correspond to the combination of the $|E_0\rangle$ and $|E_2\rangle$ states. To simultaneously target both of these states, we require a time such that a particular outcome n_c, n_d has solutions at multiple values of (7-13). Namely, we require

$$\cos 2E_0\tau = \cos 2E_2\tau \quad (7-65)$$

but

$$\begin{aligned} \cos 2E_0\tau &\neq \cos 2E_1\tau \\ \cos 2E_0\tau &\neq \cos 2E_3\tau \end{aligned} \quad (7-66)$$

which can be satisfied with $\tau = \pi/4$. Then from (7-37), we set the target state to be

$$E_{\text{tgt}} = E_0 = 0, \quad (7-67)$$

which also will target $|E_2\rangle$.

When we work in the long time regime where multiple energy levels are picked out, we must also handle the energy dependent prefactor $s_{n_c n_d}(H\tau)$ that appears in (7-48).

Depending on the parity of n_c, n_d , this adds a relative (-1) phase factor between the $|E_0\rangle$ and $|E_2\rangle$ states, as can be seen from the $n_c = 0, n_d = 101$ curve in Fig. 7-3(b). To eliminate this phase, after performing each three qubit measurement we may apply the conditional unitary

$$V_{n_c n_d} = e^{i((n_c + n_d) \bmod 2)H\tau}, \quad (7-68)$$

where H is given by (7-62). We note that this only involves single qubit rotations which we assume are readily available.

The correction operator should induce a transition between the states $\{|E_0\rangle, |E_2\rangle\}$ and $\{|E_1\rangle, |E_3\rangle\}$ hence we choose

$$U_C = \sigma_1^z \quad (7-69)$$

and otherwise follow the procedure in Sec. 7.3.2.

For the $e^{\sigma_2^z \sigma_3^z \sigma_4^z \tilde{t}}$ operator, the procedure is the same up to a basis change. For example, the Hamiltonian for the QND measurement is

$$H = -(\sigma_2^z + \sigma_3^z + \sigma_4^z) + 3I \quad (7-70)$$

and the correction operator is

$$U_C = \sigma_4^x. \quad (7-71)$$

The conditional operator is the same as (7-68) with the Hamiltonian (7-70).

7.5.3 Numerical evolution

We now use the operators defined in the previous section to perform the measurement-based imaginary time evolution. Our simulation proceeds in four stages, one for each of the imaginary time operators in (7-52). Starting from a random initial state $|\psi_0\rangle$, we first perform the two two-qubit operations following the procedure in Sec. 7.3.2 with the operators as defined in Sec. 7.5.2. This is then followed by the two two-qubit operations following the procedure in Sec. 7.3.2 with the operators as defined in Sec. 7.5.2. The

measurement outcomes are chosen according to Born probabilities, see the Appendix of Ref. [297] for the procedure.

In order to assess the success of the procedure, we evaluate the fidelity of the state during the evolution with respect to the cluster state (7-49) defined as

$$F_C = |\langle C_4 | \psi \rangle|^2. \quad (7-72)$$

We also evaluate whether the state has been projected into the correct subspace using

$$\begin{aligned} F_1 &= \langle \psi | \frac{1}{2} (I + \sigma_1^z \sigma_2^z) | \psi \rangle \\ F_2 &= \langle \psi | \frac{1}{2} (I + \sigma_3^x \sigma_4^x) | \psi \rangle \\ F_3 &= \langle \psi | \frac{1}{2} (I + \sigma_1^x \sigma_2^x \sigma_3^x) | \psi \rangle \\ F_4 &= \langle \psi | \frac{1}{2} (I + \sigma_2^z \sigma_3^z \sigma_4^z) | \psi \rangle. \end{aligned} \quad (7-73)$$

Our results are shown in Fig. 7-4. We show an example of a single run of the algorithm. From the fidelity plots Figs. 7-4(a)-(d) we see that within 10 rounds of measurement and unitary correction, the state settles into a steady state, where further measurement rounds do not affect the state. The associated energy estimates in Figs. 7-4(e)-(h) show that the measurements have converged to the target energy, which is $E_{\text{tgt}} = 0$ for all cases. The fidelities for each subspace (7-73) in each case attain a value of unity at steady state. The fidelity with respect to the cluster state however remains fairly low until the last step, where unit fidelity is attained. Due to the stochastic nature of the imaginary time algorithm, each run produces a different trajectory, but in all cases, the final state is the cluster state (7-52), which is attained with unit fidelity.

7.6 Summary on QND measurements analysis

In this condensed chapter summary, we demonstrate that Quantum Non-Demolition (QND) measurements, integral to the imaginary time evolution scheme as suggested in Mao et al. [135], enable deterministic convergence to a target quantum state. Our adapted approach (Sec. 7.3.2), expands on [135] to target arbitrary energy spectrum states, not just the ground state. This is achieved by utilizing the photon number readouts from

QND measurements to estimate the energy of the QND Hamiltonian, followed by an adaptive unitary operation. We highlight the potential of this technique through the deterministic preparation of a four qubit cluster state, achievable without direct qubit interactions but through collective spin measurements. The employed QND Hamiltonians and correction operators are single qubit Hamiltonians, underscoring the measurement-based nonlinearity of the process [135].

We further discuss the versatility of QND measurements in various platforms [7, 94, 114, 155, 229, 230, 232–240, 282]. Our proposed QND scheme, in contrast to [135], employs a flexible geometry for physical qubit measurement, using two independent laser beams in a Mach-Zehnder configuration. This setup facilitates high order and multipartite entanglement, adaptable to various qubit combinations [298–301]. While focusing on pure states for simplicity, our methodology applies equally to mixed states (Sec. 7.3.2, 7.2, 7.4). Addressing the scheme’s challenges, we note that QND measurements can cause decoherence through photon loss and spontaneous emission [134]. However, the impact of photon loss is mitigated by using coherent light states. The criticality of accurate photodetection is emphasized for energy estimation (7-37) and phase correction (7-68), especially in the long time regime, which presents higher experimental challenges due to increased decoherence rates and the need for near-perfect photon detection efficiency [134].

Lastly, we discuss the scalability of generating larger cluster states, similar to the four qubit example. The process involves sequential application of imaginary time operators (as in 7-52), with each additional vertex adding constant overhead. The scheme’s adaptability for more complex Hamiltonian ground states is also noted, opening avenues for models like spinor quantum computing [25, 243].

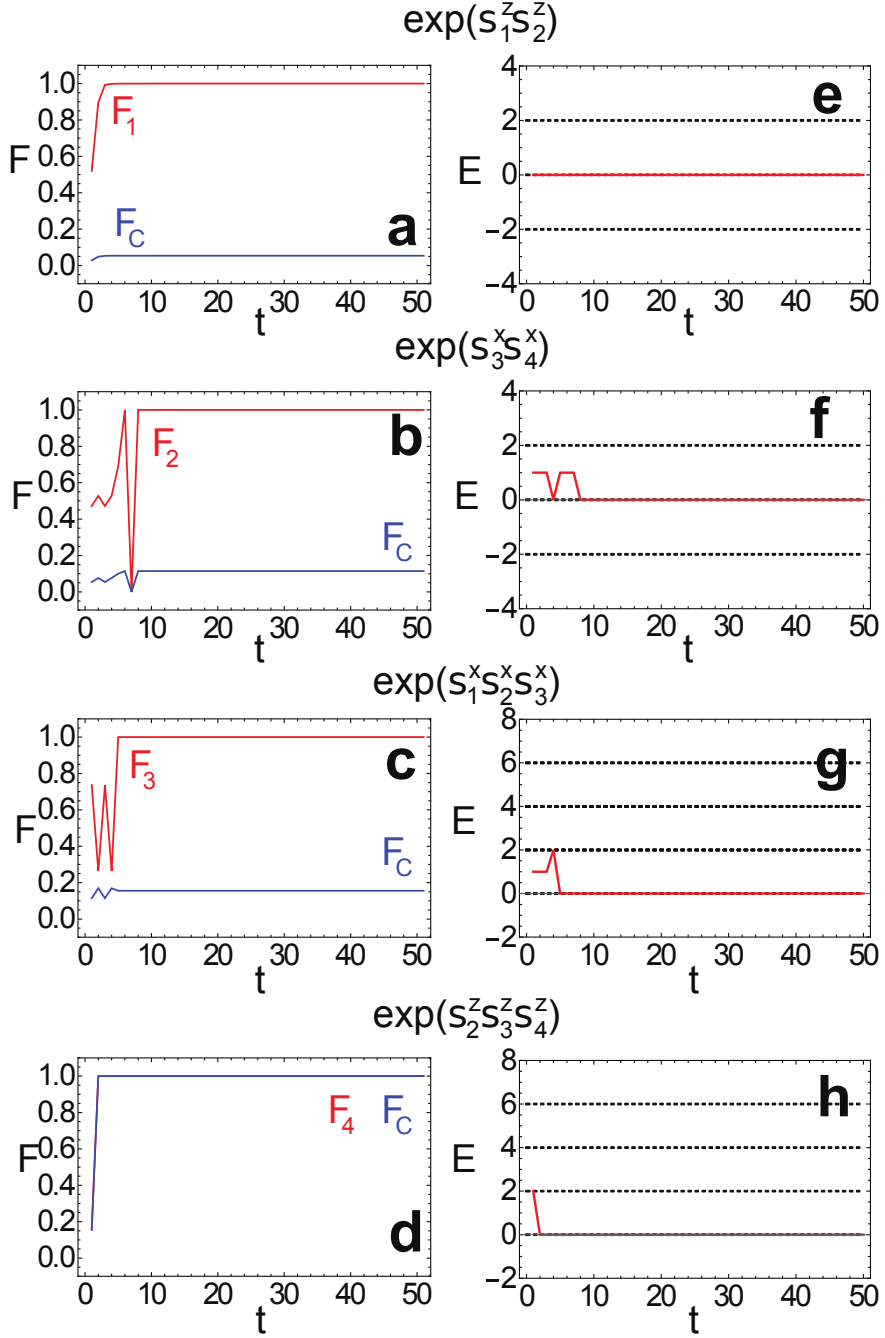


Fig 7-4 Preparing a four qubit cluster state with imaginary time evolution. (a)-(d) show fidelities as defined in (7-72) and (7-73) as marked. (e)-(h) show the energy estimates (7-37) based on the cumulative measurement outcomes (7-40). The procedure starts from a random initial state and applies the imaginary time evolution corresponding to (a)(e) $e^{\sigma_1^z \sigma_2^z \tilde{t}}$, (b)(f) $e^{\sigma_3^x \sigma_4^x \tilde{t}}$, (c)(g) $e^{\sigma_1^x \sigma_2^x \sigma_3^x \tilde{t}}$, (d)(h) $e^{\sigma_2^z \sigma_3^z \sigma_4^z \tilde{t}}$ in sequence. We use parameters $\alpha = 1$, $\delta_{\text{tgt}} = 0.5$ throughout. Numerically we impose a photonic cutoff of 5 photons. Here, the fidelities F and energy E are dimensionless. t is a dimensionless time step parameter (the same as that appearing in Sec. 7.3.2). M Kondappan, T Byrnes, et al, Phys Rev A 107, 042616 (2023)

8 Conclusion

In conclusion, this study establishes new theoretical and experimental methods for QND measurements for BECs on atom chips. First, we have introduced a compactified optical circuit to generate the principal optical sources that are required to perform cooling, imaging, and control of ultracold atoms. The core development in our experimental optical circuits' compactification design starting from two sub-kHz linewidth frequency-locked laser sources. One of the advantages of our circuit design is that the repumping beams are admixed with the various optical beams and outputs in its dedicated single-mode fiber. We implemented the circuit and characterized the outputs in terms of beam profile, power loss, and fiber coupling, and found good performance overall. The present system has a universal design that could be applied to numerous quantum technology applications where it is necessary to produce quantum states of ultracold atomic gases, such as spin squeezed cold atomic ensembles. Utilizing our methods may allow for applications of ultracold atoms to quantum technology that is more readily available for various applications, ranging from quantum metrology to quantum simulation.

The second contribution of this thesis is a development of QND measurements and their applications in state preparation. Our study demonstrated that QND measurements can be effectively used in the imaginary-time evolution scheme for quantum computing. We have shown that photon number readouts from QND measurements can estimate the energy of the QND Hamiltonian. This allows the system to deterministically converge to a target state through adaptive unitary operations based on energy readouts. Our modified scheme enables targeting any state in the energy spectrum, not just the ground state. The method's flexibility is highlighted by its ability to generate high-order effective interactions and specific states like a four-qubit cluster state, using only collective measurements without direct qubit interactions. This approach offers several advantages, such as easy implementation across different platforms and the potential for high-order interactions by integrating more spins. Our method shows promise for scalable and ef-

ficient quantum computing, expanding the possibilities for generating complex quantum states and facilitating various quantum computing models.

Future directions and applications

In closing, the work in this thesis has developed the groundwork for theoretical and experimental approaches to realize the multi-ensemble atom chip platform for quantum information applications. The larger aim is to realize a spinor quantum computing system which is capable of performing arbitrary quantum computation fault tolerantly, which would be a major breakthrough in physics and beyond. Along the way to realizing such a system there is much exciting physics that can be investigated which serve as stepping stones. The immediate goal is to realize in-situ entanglement of two BECs on atom chips, a feat that has never been performed to date. With a single QND measurement, entanglement is generated, but maximally entangled states are not generated. Using a multi-pulse QND protocol there are methods known to generate maximally entangled state which would be another milestone. With the multi-ensemble atom chip platform, this can be extended to multiple ensembles with the same techniques. This would realize elementary examples of spinor generalizations of cluster states, as discussed in this thesis. We hope that the results of this thesis contribute to the set of techniques that will be required to realized the full potential of Bose-Einstein Condensates in quantum applications, setting a new benchmark for future studies in this rapidly evolving field.

Successfully producing BEC on atom chips will enable exploring multi-qubit quantum gates and algorithms, including quantum teleportation and entanglement swapping [177], crucial for quantum networking [174, 176]. Basic Quantum Error Correction employs a bit-flip code [139], with three qubits, Shor's algorithm could be illustrated [84] in this new platform. Our research aims to extend quantum computing frontiers using atomic ensembles. Observing BEC and exploring non-classical correlations in many-body systems have opened new avenues. Our efforts in entanglement generation between atomic clouds and atom chip-based quantum state manipulation are poised to contribute significantly to quantum computing and information processing [69]. Our focus on quantum information science lays the groundwork for future quantum computing explorations, and we aim integrating our findings with broader quantum information science goals to drive further significant advancements in cold atom quantum computing technology. In conclusion, the future goals of our project are not only geared towards advancing our current

understanding and capabilities in the realm of ultracold atoms and quantum computing but also aim to lay a robust foundation for the next generation of quantum technologies.

Bibliography

- [1] KONDAPPAN M CHAUDHARY M ILO-OKEKE E O, et al Imaginary-time evolution with quantum nondemolition measurements: Multiqubit interactions via measurement nonlinearities[J/OL] Physical Review A 2023
<http://dx.doi.org/10.1103/PhysRevA.107.012609>
- [2] KONDAPPAN M IVANNIKOV V BYRNES T Optical circuit compactification for ultracold atoms[J] Review of Scientific Instruments 2024 95(1)
- [3] KONDAPPAN M ARISTIZABAL-ZULUAGA E J S I R L J Y M Y V I T B Quantum nondemolition measurement based generation of entangled states in two Bose-Einstein condensates[J] J. Phys. B 2021 54: 105502
- [4] REICHEL J Microchip traps and Bose-Einstein condensation[J] Applied Physics B 2002 74(6): 469–487
- [5] TREUTLEIN P Coherent manipulation of ultracold atoms on atom chips[J/OL] 2008
<http://nbn-resolving.de/urn:nbn:de:bvb:19-91532>
- [6] IVANNIKOV V Analysis of a trapped atom clock with losses. PhD Thesis[J] Swinburne University of Technology(cited on pp 2013: 20, 36, 39, 40, 151)
- [7] LESTER B J LIN Y BROWN M O, et al Measurement-based entanglement of noninteracting bosonic atoms[J] Physical review letters 2018 120(19): 193602
- [8] STECK D A Rubidium 87 D Line Data[J/OL] version 2003 1: 6
<http://steck.us/alkalidata/>
- [9] DALIBARD J COHEN-TANNOUDJI C Laser cooling below the Doppler limit by polarization gradients: simple theoretical models[J/OL] Journal of the Optical So-

BIBLIOGRAPHY

- society of America B 1989 6 : 11
<http://dx.doi.org/10.1364/JOSAB.6.002023>
- [10] PHILLIPS W D Nobel Lecture: Laser cooling and trapping of neutral atoms[J/OL] Reviews of Modern Physics 1998 70(3) : 721–741
<http://dx.doi.org/10.1103/RevModPhys.70.721>
- [11] LETT P D WATTS R N WESTBROOK C I, et al Observation of atoms laser cooled below the doppler limit[J/OL] Physical Review Letters 1988 61(2) : 169–172
<http://dx.doi.org/10.1103/PhysRevLett.61.169>
- [12] METCALF H J van der STRATEN P Laser cooling and trapping. Graduate Texts in Contemporary Physics[G] // isbn: 9780387987286 (cited on pp. 46, 47 1999
- [13] ADAMS C S RIIS E Laser cooling and trapping of neutral atoms, Prog[J] Quant. Electr. 1997 21 : 1
- [14] METCALF H J van der STRATEN P Laser Cooling and Trapping, Springer, Berlin[J] 1999
- [15] JO G-B SHIN Y WILL S, et al Long Phase Coherence Time and Number Squeezing of Two Bose-Einstein Condensates on an Atom Chip[J/OL] Physical Review Letters 2007 98(3) : 98–101
<http://dx.doi.org/10.1103/PhysRevLett.98.030407>
- [16] DUNNINGHAM J A Using quantum theory to improve measurement precision, Contemp[J] Phys. 2006 47 : 257
- [17] CHILDS A M PRESKILL J RENES J Quantum information and precision measurement, J[J] Mod. Opt 2000 47: 155
- [18] GEORGESCU I M ASHHAB S NORI F Quantum simulation[J] Rev. Mod. Phys. 2014 86 : 153
- [19] LLOYD S SIMULATORS U Q Science 273[J] 1996 1073
- [20] HUANG H-L OTHERS Emulating quantum teleportation of a Majorana zero mode qubit[J] Phys. Rev. Lett. 2021 126 : 090502
- [21] JAN'E E VIDAL G D'UR W, et al Simulation of quantum dynamics with quantum optical systems, Quant[J] Inf. and Comp 2003 3 : 15

- [22] BYRNES T RECHER P KIM N Y, et al Quantum simulator for the Hubbard model with long-range Coulomb interactions using surface acoustic waves[J] Phys. Rev. Lett. 2007 99 : 016405
- [23] DALLA TORRE E G OTTERBACH J DEMLER E, et al Dissipative preparation of spin squeezed atomic ensembles in a steady state[J] Phys. Rev. Lett. 2013 110 : 120402
- [24] SØRENSEN A S van DERWAL C H CHILDRESS L I, et al Capacitive Coupling of Atomic Systems to Mesoscopic Conductors, Phys[J] Rev. Lett. 2004 92 : 063601
- [25] BYRNES T WEN K YAMAMOTO Y Macroscopic quantum computation using Bose-Einstein condensates[J] Phys. Rev. A 2012 85 : 040306
- [26] PHILLIPS W D GOULD P L LETT P D Cooling, stopping, and trapping atoms[J/OL] Science (New York, N.Y.) 1988 239(4842) : 877–883
<http://dx.doi.org/10.1126/science.239.4842.877>
- [27] KETTERLE W Nobel lecture: When atoms behave as waves: Bose-Einstein condensation and the atom laser[J/OL] Reviews of Modern Physics 2002 74(4) : 1131–1151
<http://dx.doi.org/10.1103/RevModPhys.74.1131>
- [28] ARNOLD A S Preparation and manipulation of an 87Rb Bose-Einstein Condensate. PhD Thesis[J] University of Sussex(cited on 1999 90
- [29] CORNELL E A WIEMAN C E Bose-Einstein condensation in a dilute gas, the first 70 years and some recent experiments[J] Review of Modern Physics 2002 74 : 875–893
- [30] BYRNES T ROSSEAU D KHOSLA M, et al Macroscopic quantum information processing using spin coherent states[J] Optics Communications 2015 337 : 102–109
- [31] BYRNES T ILO-OKEKE E O Quantum atom optics: Theory and applications to quantum technology[M] [S.l.] : Cambridge University Press 2021
- [32] WEINSTEIN J D LIBBRECHT K G Microscopic magnetic traps for neutral atoms, Phys[J] Rev. A 1995 52 : 4004

BIBLIOGRAPHY

- [33] HOMMELHOFF P H ANSEL W STEINMETZ T, et al Transporting, splitting and merging of atomic ensembles in a chip trap, *New J[J] Phys.* 2005 7: 3
- [34] FOLMAN R KR UGER P SCHMIEDMAYER J, et al Microscopic Atom Optics: From Wires to an Atom Chip, *Adv[J] At. Mol. Opt* 2002 48: 263
- [35] H ANSEL W HOMMELHOFF P H ANSCH T W, et al Bose- Einstein condensation on a microelectronic chip[J] *Nature* 2001 413: 498
- [36] FORT'AGH J OTT H SCHLOTTERBECK G, et al Microelectromagnets for trapping and manipulating ultracold atomic quantum gases, *Appl[J] Phys. Lett.* 2002 81: 1146
- [37] WHITLOCK S Bose-Einstein condensates on a magnetic film atom chip. PhD Thesis[J] Swinburne University of Technology(cited on pp 2007 19(40): 73
- [38] LEANHARDT A E CHIKKATUR A P KIELPINSKI D, et al Propagation of Bose-Einstein condensates in a magnetic waveguide[J] *Physical Review Letters* 2002 89: 040401
- [39] H ANSEL W REICHEL J HOMMELHOFF P, et al Magnetic Conveyor Belt for Transporting and Merging Trapped Atom Clouds, *Phys[J] Rev. Lett.* 2001 86: 608
- [40] GÜNTHER A KEMMLER M KRAFT S, et al Combined chips for atom optics[J] *Physical Review A* 2005 71: 063619
- [41] DU S SQUIRES M B IMAI Y, et al Atom-chip Bose- Einstein condensation in a portable vacuum cell, *Phys[J] Rev. A* 2004 70: 053606
- [42] AUBIN S MYRSKOG S EXTAVOUR M H T, et al Rapid sympathetic cooling to Fermi degeneracy on a chip, *Nat[J] Phys.* 2006 2: 384
- [43] TEPER I LIN Y-J VULETIĆ V Resonator-Aided Single-Atom Detection on a Microfabricated Chip[J/OL] *Physical Review Letters* 2006 97: 2
<http://dx.doi.org/10.1103/PhysRevLett.97.023002>
- [44] WILDERMUTH S HOFFERBERTH S LESANOVSKY I, et al Microscopic magnetic-field imaging[J] *Nature* 2005 435: 440

- [45] SCHUMM T HOFFERBERTH S ANDERSSON L M, et al Matter-wave interferometry in a double well on an atom chip[J/OL] Nature Physics 2005 1(1): 57–62
<http://dx.doi.org/10.1038/nphys125>
- [46] FORTÁGH J ZIMMERMANN C Magnetic microtraps for ultracold atoms[J/OL] Reviews of Modern Physics 2007 79(1): 235–289
<http://dx.doi.org/10.1103/RevModPhys.79.235>
- [47] WANG D-W LUKIN M D DEMLER E Disordered Bose-Einstein condensates in quasi-one-dimensional magnetic microtraps[J] Physical Review Letters 2004 92: 076802
- [48] EST'EVE J AUSSIBAL C SCHUMM T, et al Role of wire imperfections in micro-magnetic traps for atoms, Phys[J] Rev. A 2004 70: 043629
- [49] KRÜGER P LUO X KLEIN M W, et al Trapping and Manipulating Neutral Atoms with Electrostatic Fields, Phys[J] Rev. Lett. 2003 91(23320): 1
- [50] PIETRA L D AIGNER S C. vom Hagen, S[J] Groth, I. Bar-Joseph, H. J. Lezec, and J. Schmiedmayer, Designing potentials by sculpturing wires, Phys. Rev. A 2007 75: 063604
- [51] HENKEL C P OTTING S WILKENS M Loss and heating of particles in small and noisy traps, Appl[J] Phys. B 1999 69: 379
- [52] JONES M VALE C J SAHAGUN D, et al Spin Coupling between Cold Atoms and the Thermal Fluctuations of a Metal Surface[J/OL] Physical Review Letters 2003 91: 8
<http://dx.doi.org/10.1103/PhysRevLett.91.080401>
- [53] DIKOVSKY V JAPHA Y HENKEL C, et al Reduction of magnetic noise in atom chips by material optimization, Eur[J] Phys. J. D 2005 35: 87
- [54] BLOCH I Ultracold quantum gases in optical lattices, Nat[J] Phys. 2005 1: 23
- [55] LEIBFRIED D KNILL E SEIDELIN S, et al Creation of a six-atom ‘Schrödinger cat’ state[J] Nature 2005 438: 639
- [56] HAFNER H H ANSEL W ROOS C F, et al Scalable multiparticle entanglement of trapped ions[J] Nature 2005 438: 643

BIBLIOGRAPHY

- [57] STEFFEN M ANSMANN M BIALCZAK R C, et al Measurement of the Entanglement of Two Superconducting Qubits via State Tomography[J] *Science* 2006 313: 1423
- [58] MAJER J CHOW J M GAMBETTA J M, et al Coupling superconducting qubits via a cavity bus[J] *Nature* 2007 449: 443
- [59] IVANNIKOV V Analysis of a Trapped Atom Clock with Losses[D] Melbourne, Australia : Swinburne University of Technology 2013
- [60] MUESSEL W STROBEL H LINNEMANN D, et al Scalable spin squeezing for quantum-enhanced magnetometry with Bose-Einstein condensates[J] *Phys. Rev. Lett.* 2014 113: 103004
- [61] WASILEWSKI W OTHERS Quantum noise limited and entanglement-assisted magnetometry[J] *Phys. Rev. Lett.* 2010 104
- [62] TOMILIN V A IL' ICCHOV L V BEC decoherence in hybrid atom-optical quantum gyroscope[J] *Journal of Experimental and Theoretical Physics* 2022 135: 285–290
- [63] THANVANTHRI S KAPALE K T DOWLING J P Ultra-stable matter-wave gyroscope with counter-rotating vortex superpositions in Bose-Einstein condensates[J] *J. Mod. Opt.* 2012 59: 1180–1185
- [64] MOXLEY F I I DOWLING J P DAI W, et al Sagnac interferometry with coherent vortex superposition states in exciton-polariton condensates[J] *Phys. Rev. A* 2016 93: 053603
- [65] YU H KIM S J KIM J B Toward atom interferometer gyroscope built on an atom chip[J] *J. Korean Phys. Soc.* 2023 82: 819–826
- [66] LEWANDOWSKI H J Coherences and correlations in an ultracold Bose gas. PhD Thesis[J] University of Colorado(cited on 2002 90)
- [67] MARQUARDT F ABEL B von DELFT J Measuring the size of a Schrödinger cat state[R] 2006
- [68] MASUHARA N DOYLE J SANDBERG J, et al Evaporative Cooling of Spin-Polarized Atomic Hydrogen[J/OL] *Physical Review Letters* 1988 61(8) : 935–938
<http://dx.doi.org/10.1103/PhysRevLett.61.935>

- [69] NIELSEN M A CHUANG I L Quantum Computation and Quantum Information, Cambridge University Press, Cambridge[J] 2000: 54
- [70] NIELSEN M CHUANG I Quantum Computation and Quantum Information[M] 10th New York, NY, USA : Cambridge University Press 2011
- [71] DIVINCENZO D The Physical Implementation of Quantum Computation, Fortschr[J] Phys. 2000 48: 771
- [72] REID M D E A Colloquium: The Einstein-Podolsky-Rosen paradox: From concepts to applications[J] Rev. Mod. Phys. 2009 81: 1727–1751
- [73] EINSTEIN A PODOLSKY B ROSEN N Can Quantum-Mechanical Description of Physical Reality Be Considered Complete?[J] Phys. Rev. 1935 47: 777–780
- [74] SCHRÖDINGER E BORN M Discussion of Probability Relations between Separated Systems[J] Proc. Camb. Philos. Soc. 1935 31: 555
- [75] CAVALCANTI D SKRZYPCZYK P Quantum steering: a review with focus on semidefinite programming[J] Rep. Prog. Phys. 2017 80(024001)
- [76] HAGLEY E E A Generation of Einstein-Podolsky-Rosen pairs of atoms[J] Phys. Rev. Lett. 1997 79: 1–5
- [77] WISEMAN H M JONES S J DOHERTY A C Steering, Entanglement, Nonlocality, and the Einstein-Podolsky-Rosen Paradox[J] Phys. Rev. Lett. 2007 98(140402)
- [78] GROSS C ZIBOLD T NICKLAS E, et al Nonlinear atom interferometer surpasses classical precision limit[J] Nature 2010 464: 1165–1169
- [79] GÜHNE O TÓTH G Entanglement detection[J] Phys. Rep. 474
- [80] RIEDEL M F E A Atom-chip-based generation of entanglement for quantum metrology[J] Nature 2010 464: 1170–1173
- [81] PEISE J E A Satisfying the Einstein-Podolsky-Rosen criterion with massive particles[J] Nat. Commun. 2015 6(8984)
- [82] FADEL M ZIBOLD T DÉCAMPS B, et al Spatial entanglement patterns and Einstein-Podolsky-Rosen steering in Bose-Einstein condensates[J] Science 2018 360(6387): 409–413

BIBLIOGRAPHY

- [83] SCHMIED R E A Bell correlations in a Bose-Einstein condensate[J] Science 2016 352: 441–444
- [84] COPPERSMITH D An approximate Fourier transform useful in quantum factoring: RC19642[R] [S.I.] : IBM Research Report 1994
- [85] SINGH G A study of encryption algorithms (RSA, DES, 3DES and AES) for information security[J] International Journal of Computer Applications 2013 67(19)
- [86] DIVINCENZO D The physical implementation of quantum computation[J] Fortschr. Phys. 2000 48: 771–783
- [87] BENNETT C H DIVINCENZO D P Quantum information and computation[J] nature 2000 404(6775): 247–255
- [88] BYRNES T Fractality and macroscopic entanglement in two-component Bose-Einstein condensates[J/OL] Physical Review A 2013 88(2): 023609
<http://dx.doi.org/10.1103/PhysRevA.88.023609>
- [89] DIVINCENZO D P BACON D KEMPE J, et al Universal quantum computation with the exchange interaction[J] nature 2000 408(6810): 339–342
- [90] STEANE A Overhead and noise threshold of fault-tolerant quantum error correction, Phys[J] Rev. A 2003 68: 42322
- [91] KNILL E Scalable quantum computing in the presence of large detectederror rates, Phys[J] Rev. A 2005 71: 42322
- [92] SCHINDLER P BARREIRO J T MONZ T, et al Experimental Repetitive Quantum Error Correction[J/OL] Science 2011 332(6033): 1059–1061
<http://dx.doi.org/10.1126/science.1203329>
- [93] ARUTE F ARYA K BABBUSH R, et al Quantum supremacy using a programmable superconducting processor[J] Nature 2019 574(7779): 505–510
- [94] HAMMERER K SØRENSEN A S POLZIK E S Quantum interface between light and atomic ensembles[J/OL] Reviews of Modern Physics 2010 82(2): 1041–1093
<http://dx.doi.org/10.1103/RevModPhys.82.1041>
- [95] SHAW B WILDE M M ORESHKOV O, et al Encoding one logical qubit into six physical qubits[J] Physical Review A 2008 78(1): 012337

- [96] IDZIASZEK Z CALARCO T Two atoms in an anisotropic harmonic trap, Phys[J] Rev. A 2005 71: 050701
- [97] PLEBANSKI J Wave functions of a harmonic oscillator[J/OL] Physical Review 1956 101(6): 1825–1826
<http://dx.doi.org/10.1103/PhysRev.101.1825>
- [98] SCHWARZHANS M RAUCH L WEIMERKIRCH M J J Measurment of the Quantum States of Squeezed Light[J] Nature 1997 387: 471–475
- [99] JONES T ENDO S MCARDLE S, et al Variational quantum algorithms for discovering Hamiltonian spectra[J] Physical Review A 2019 99(6): 062304
- [100] MOHSENI N NAROZNIAK M PYRKOV A N, et al Error suppression in adiabatic quantum computing with qubit ensembles[J/OL] npj Quantum Information 2021 7(1): 71
<http://dx.doi.org/10.1038/s41534-021-00405-2>
- [101] KAMINSKY W M LLOYD S Scalable architecture for adiabatic quantum computing of NP-hard problems[J] Quantum computing and quantum bits in mesoscopic systems 2004: 229–236
- [102] LAUMANN C R MOESSNER R SCARDICCHIO A, et al Quantum annealing: The fastest route to quantum computation?[J] The European Physical Journal Special Topics 2015 224(1): 75–88
- [103] BAN M Quantum dense coding via a two-mode squeezed-vacuum state[J] Journal of Optics B: Quantum and Semiclassical Optics 1999 1(6): L9
- [104] NISHI H KOSUGI T MATSUSHITA Y-I Implementation of quantum imaginary-time evolution method on NISQ devices by introducing nonlocal approximation[J] npj Quantum Information 2021 7(1): 1–7
- [105] DODD J L NIELSEN M A BREMNER M J, et al Universal quantum computation and simulation using any entangling Hamiltonian and local unitaries[J/OL] Phys. Rev. A 2002 65: 040301
<http://dx.doi.org/10.1103/PhysRevA.65.040301>
- [106] CHILDS A M WIEBE N Hamiltonian simulation using linear combinations of unitary operations[J] arXiv preprint arXiv:1202.5822 2012

BIBLIOGRAPHY

- [107] BYRNES T ILO-OKEKE E O Quantum atom optics: Theory and applications to quantum technology[M] [S.l.] : Cambridge university press 2021
- [108] BYRNES T ROSSEAU D KHOSLA M, et al Macroscopic quantum information processing using spin coherent states[J/OL] Optics Communications 2015 337 : 102–109
<http://dx.doi.org/10.1016/j.optcom.2014.08.017>
- [109] BYRNES T WEN K YAMAMOTO Y Macroscopic quantum computation using Bose-Einstein condensates[J] Physical Review A 2012 85(4) : 040306(R)
- [110] SLUSHER R HOLLBERG L YURKE B, et al Observation of squeezed states generated by four-wave mixing in an optical cavity[J] Physical Review Letters 1985 55(22) : 2409
- [111] ROSSEAU D HA Q BYRNES T Entanglement generation between two spinor Bose-Einstein condensates with cavity QED[J] Physical Review A 2014 90(5) : 052315
- [112] DICKE R H Phys. Rev.[J] Phys. Rev. 1954 93 : 99
- [113] WIECZOREK W E A Experimental Observation of a Generalized Schrödinger Cat State[J] Phys. Rev. Lett. 2009 103(020504)
- [114] JULSGAARD B KOZHEKIN A POLZIK E S Experimental long-lived entanglement of two macroscopic objects[J] Nature 2001 413(6854) : 400–403
- [115] THOMAS R A PARNIAK M ØSTFELDT C, et al Entanglement between distant macroscopic mechanical and spin systems[J] Nature Physics 2021 17(2) : 228–233
- [116] VAIDMAN L Teleportation of quantum states[J] Physical Review A 1994 49(2) : 1473
- [117] TREUTLEIN P Coherent Manipulation of Ultracold Atoms on Atom Chips[D] [S.l.] : Ludwig-Maximilians-Universität München and Max-Planck-Institut für Quantenoptik 2008
- [118] BÖHI P E A Coherent manipulation of Bose-Einstein condensates with state-dependent microwave potentials on an atom chip[J] Nat. Phys. 2009 5 : 592–597

- [119] HERRERA I PETROVIC J LOMBARDI P, et al Degenerate quantum gases manipulation on AtomChips[J/OL] Physica Scripta T 2012 149
<http://dx.doi.org/10.1088/0031-8949/2012/T149/014002>
- [120] GERRITSMA R Permanent magnetic atom chips and Bose-Einstein condensation. PhD Thesis[J] University of Amsterdam(cited on 2007 45
- [121] SMITH D A AIGNER S HOFFERBERTH S, et al Absorption imaging of ultracold atoms on atom chips[J/OL] Optics express 2011 19(9) : 8471–8485
<http://dx.doi.org/10.1364/OE.19.008471>
- [122] CORY D G FAHMY A F HAVEL T F Ensemble quantum computing by NMR spectroscopy[J] Proceedings of the National Academy of Sciences 1997 94(5) : 1634–1639
- [123] SATO K NAKAZAWA S RAHIMI R, et al Molecular electron-spin quantum computers and quantum information processing: pulse-based electron magnetic resonance spin technology applied to matter spin-qubits[J] Journal of Materials Chemistry 2009 19(22) : 3739–3754
- [124] KROEZE R M GUO Y VAIDYA V D, et al Spinor self-ordering of a quantum gas in a cavity[J] Physical review letters 2018 121(16) : 163601
- [125] DOWLING J P AGARWAL G S SCHLEICH W P Wigner distribution of a general angular-momentum state: Applications to a collection of two-level atoms[J] Physical Review A 1994 49(5) : 4101
- [126] JULIENNE P S MIES F H TIESINGA E, et al Collisional Stability of Double Bose Condensates, Phys[J] Rev. Lett. 1997 78 : 1880
- [127] KITZINGER J CHAUDHARY M KONDAPPAN M, et al Two-axis two-spin squeezed states[J/OL] Physical Review Letters 2020
<http://dx.doi.org/10.1103/PhysRevLett.124.083604>
- [128] KLEMPT C E A Parametric Amplification of Vacuum Fluctuations in a Spinor Condensate[J] Phys. Rev. Lett. 2009 103(195302)
- [129] STAMPER-KURN D M UEDA M Spinor Bose gases: Symmetries, magnetism, and quantum dynamics[J] Rev. Mod. Phys. 2013 85 : 1191–1244

BIBLIOGRAPHY

- [130] IDLAS S DOMENZAIN L SPREEUW R, et al Entanglement generation between spinor Bose-Einstein condensates using Rydberg excitations[J] Physical Review A 2016 93(2) : 022319
- [131] KRONJ”aGER J Coherent Dynamics of Spinor Bose-Einstein Condensates. PhD Thesis[J] Hamburg University(cited on 2007 48
- [132] UEDA M KAWAGUCHI Y [J] Spinor Bose-Einstein condensates (cited on 2010 73
- [133] ILO-OKEKE E O BYRNES T Theory of single-shot phase contrast imaging in spinor Bose-Einstein condensates[J] Physical review letters 2014 112(23) : 233602
- [134] GAO S ILO-OKEKE E O MAO Y, et al Decoherence effects in quantum nonde-molition measurement induced entanglement between Bose–Einstein condensates[J] Journal of Physics B: Atomic, Molecular and Optical Physics 2022 55(19) : 195501
- [135] MAO Y CHAUDHARY M KONDAPPAN M, et al Deterministic measurement-based imaginary time evolution[J] arXiv preprint arXiv:2022.09100 2022
- [136] KONDAPPAN M CHAUDHARY M ILO-OKEKE E O, et al Imaginary-time evolu-tion with quantum nondemolition measurements: Multiqubit interactions via mea-surement nonlinearities[J] Physical Review A 2023 107(4) : 042616
- [137] KITAEV A Y Fault-tolerant quantum computation by anyons[J] Annals of Physics 2003 303(1) : 2 – 30
- [138] RAUSSENDORF R BRIEGEL H J A one-way quantum computer[J] Physical Re-view Letters 2001 86(22) : 5188
- [139] SHOR P W Scheme for reducing decoherence in quantum computer memory[J] Physical Review A 1995 52(4) : R2493–R2496
- [140] KOKAIL C MAIER C van BIJNEN R, et al Self-verifying variational quantum simulation of lattice models[J] Nature 2019 569(7756) : 355 – 360
- [141] BANULS M C BLATT R CATANI J, et al Simulating lattice gauge theories within quantum technologies[J] The European physical journal D 2020 74(8) : 1 – 42
- [142] MAO Y CHAUDHARY M KONDAPPAN M, et al Measurement-based determin-istic imaginary time evolution[J/OL] Physical Review Letters 2023
<http://dx.doi.org/10.1103/PhysRevLett.131.110602>

- [143] ŻUKOWSKI M ZEILINGER A HORNE M, et al Quest for GHZ states[J] *Acta Physica Polonica A* 1998 93(1): 187–195
- [144] WIEMAN C E H”ANSCH T W Doppler-Free Laser Polarization Spectroscopy[J/OL] *Physical Review Letters* 1976 36(20): 1170–1173
<http://dx.doi.org/10.1103/PhysRevLett.36.1170>
- [145] CASTIN Y WALLIS H DALIBARD J Limit of Doppler cooling[J/OL] *Journal of the Optical Society of America B* 1989 6: 11
<http://dx.doi.org/10.1364/JOSAB.6.002046>
- [146] JACKSON J D ELECTRODYNAMICS C WILEY N Y 3rd edition[H] 1999
- [147] PEZZé L SMERZI A OBERHALER M K, et al Non-classical states of atomic ensembles: fundamentals and applications in quantum metrology[J] arXiv 2016
- [148] GIOVANNETTI V LLOYD S MACCONE L Advances in quantum metrology[J] *Nat. Photonics* 2011 5: 222–229
- [149] LOUCHET-CHAUVET A E A The influence of nonclassical states of light on the spectrum of a single atom[J] *New J. Phys.* 2010 12(065032)
- [150] LEROUX I D SCHLEIER-SMITH M H VULETIć V Implementation of a Nonlinear Interaction between a Single Photon and a Single Atom in Free Space[J] *Phys. Rev. Lett.* 2010 104(250801)
- [151] OCKELOEN C F SCHMIED R RIEDEL M F, et al Quantum metrology with a scanning probe atom interferometer[J] *Phys. Rev. Lett.* 2013 111(143001)
- [152] AMICO L FAZIO R OSTERLOH A, et al Entanglement in many-body systems[J] *Rev. Mod. Phys.* 2008 80: 517–576
- [153] JULSGAARD B KOZHEKIN A POLZIK E S Experimental long-lived entanglement of two macroscopic objects[J] *Nature* 2001 413: 400–403
- [154] HAMMERER K SØRENSEN A S POLZIK E S Quantum interface between light and atomic ensembles[J] *Rev. Mod. Phys.* 2010 82: 1041
- [155] KUZMICH A BIGELOW N MANDEL L Atomic quantum non-demolition measurements and squeezing[J] *EPL (Europhysics Letters)* 1998 42(5): 481

BIBLIOGRAPHY

- [156] FADEL M ZIBOLD T DéCamps B, et al Spatial entanglement patterns and Einstein-Podolsky-Rosen steering in Bose-Einstein condensates[J] Science 2018 360 : 409 – 413
- [157] LANGE K E A Entanglement between two spatially separated atomic modes[J] Science 2018 360 : 416 – 418
- [158] KUNKEL P E A Simultaneously unpolarized and entangled light[J] Science 2018 360 : 413 – 416
- [159] LAU D SIDOROV A I OPAT G, et al Reflection of cold atoms from an array of current-carrying wires[J/OL] The European Physical Journal D - Atomic, Molecular and Optical Physics 1999 5(2) : 193 – 199
<http://dx.doi.org/10.1007/s100530050244>
- [160] DRNDIĆ M ZABOW G LEE C, et al Properties of microelectromagnet mirrors as reflectors of cold Rb atoms[J/OL] Physical Review A 1999 60(5) : 4012 – 4015
<http://dx.doi.org/10.1103/PhysRevA.60.4012>
- [161] BERGEMAN T EREZ G METCALF H J Magnetostatic trapping fields for neutral atoms[J/OL] Physical Review A 1987 35(4) : 1535 – 1546
<http://dx.doi.org/10.1103/PhysRevA.35.1535>
- [162] MIGDALL A PRODAN J PHILLIPS W D, et al First Observation of Magnetically Trapped Neutral Atoms[J/OL] Physical Review Letters 1985 54(24) : 2596 – 2599
<http://dx.doi.org/10.1103/PhysRevLett.54.2596>
- [163] GRIFFITHS D J Introduction to quantum mechanics. 2nd ed[G] // Pearson Prentice Hall isbn: 9780131118928 (cited on p [S.l.] : 76 2005
- [164] ANDERSON R P Nonequilibrium dynamics and relative phase evolution of two-component Bose-Einstein condensates. PhD Thesis[J] Swinburne University of Technology(cited on pp 2009 19 : 25
- [165] KETTERLE W DURFEE D S STAMPER-KURN D M Making, probing and understanding Bose-Einstein condensates[G] // Bose-Einstein condensation in atomic gases S. Stringari, and C. E. Wieman. IOS Press, Amsterdam (cited on p. 45 : by M. Inguscio 1999 : 67 – 176

- [166] DURFEE D S Dynamic Properties of Dilute Bose-Einstein Condensates. PhD Thesis[J] Massachusetts Institute of Technology(cited on 1999 45)
- [167] TREUTLEIN P Coherent manipulation of ultracold atoms on atom chips. PhD Thesis[J] Ludwig-Maximilians-Universit"at M"unchen(cited on pp 2008 45 : 52)
- [168] COLCIAGHI P LI Y TREUTLEIN P, et al Einstein-podolsky-rosen experiment with two bose-einstein condensates[J] Physical Review X 2023 13(2) : 021031
- [169] GRIMM R WEIDEMÜLLER M OVCHINNIKOV Y B Optical dipole traps for neutral atoms[J] Advances in atomic, molecular, and optical physics 2000 42 : 95 – 170
- [170] GAO S ILO-OKEKE E O MAO Y, et al Decoherence effects in quantum nonde-molition measurement induced entanglement between Bose–Einstein condensates[J] Journal of Physics B: Atomic, Molecular and Optical Physics 2022 55(19) : 195501
- [171] LANGE K PEISE J LÜCKE B, et al Entanglement between two spatially separated atomic modes[J] Science 2018 360(6387) : 416 – 418
- [172] PYRKOV A N BYRNES T Quantum teleportation of spin coherent states: beyond continuous variables teleportation[J] New Journal of Physics 2014 16(7) : 073038
- [173] PYRKOV A N BYRNES T Full-Bloch-sphere teleportation of spinor Bose-Einstein condensates and spin ensembles[J] Physical Review A 2014 90(6) : 062336
- [174] BENNETT C H BRASSARD G CRÉPEAU C, et al Teleporting an unknown quantum state via dual classical and Einstein-Podolsky-Rosen channels[J] Physical Review Letters 1993 70(13) : 1895 – 1899
- [175] DEUTSCH D JOZSA R Rapid solution of problems by quantum computation[J] Proceedings of the Royal Society of London. Series A: Mathematical and Physical Sciences 1992 439(1907) : 553 – 558
- [176] GREENBERGER D M HORNE M A ZEILINGER A Going beyond Bell’ s theorem[C] // KAFATOS M Bell’ s Theorem, Quantum Theory and Conceptions of the Universe [S.l.] : Kluwer 1989 : 69 – 72
- [177] ZUKOWSKI M ZEILINGER A HORNE M A, et al ‘Event-ready-detectors’ Bell experiment via entanglement swapping[J] Physical Review Letters 1993 71(26) : 4287 – 4290

BIBLIOGRAPHY

- [178] BRAGINSKY V B KHALILI F Y Quantum nondemolition measurements: the route from toys to tools[J] Rev. Mod. Phys. 1996 68: 1
- [179] REINAUDI G LAHAYE T WANG Z, et al Strong saturation absorption imaging of dense clouds of ultracold atoms[J/OL] Optics Letters 2007 32: 21
<http://dx.doi.org/10.1364/OL.32.003143>
- [180] H'aNSCH T W SHAHIN I S SCHAWLOW A L Optical Resolution of the Lamb Shift in Atomic Hydrogen by Laser Saturation Spectroscopy[J/OL] Nature Physical Science 1972 235: 63–65
<http://dx.doi.org/10.1038/physci235063a0>
- [181] MACADAM K B A narrow-band tunable diode laser system with grating feedback, and a saturated absorption spectrometer for Cs and Rb[J/OL] American Journal of Physics 1992 60: 12
<http://dx.doi.org/10.1119/1.16955>
- [182] SCHAWLOW A L Lasers, light, and matter[J/OL] Journal of the Optical Society of America 1977 67: 2
<http://dx.doi.org/10.1364/JOSA.67.000140>
- [183] SCHAWLOW A L Spectroscopy in a new light[J/OL] Reviews of Modern Physics 1982 54(3): 697–707
<http://dx.doi.org/10.1103/RevModPhys.54.697>
- [184] HAWTHORN C J WEBER K P SCHOLTEN R E Littrow configuration tunable external cavity diode laser with fixed direction output beam[J/OL] Review of Scientific Instruments 2001 72: 12
<http://dx.doi.org/10.1063/1.1419217>
- [185] TAKAHASI H Information theory of quantum-mechanical channels[G] // Advances in Communication Systems: Vol 1 [S.l.]: Elsevier 1965: 227–310
- [186] ROBINSON D W The ground state of the Bose gas[J] Communications in Mathematical Physics 1965 1(2): 159–174
- [187] STOLER D Equivalence classes of minimum-uncertainty packets[J] Physical Review D 1970 1(12): 1925–1926

- [188] WALLS D F Squeezed states of light[J/OL] Nature 1983 306(5939) : 141–146
<http://dx.doi.org/10.1038/306141a0>
- [189] SCULLY M O ZUBAIRY M S Quantum optics[J] 1999
- [190] GERRY C KNIGHT P KNIGHT P L Introductory quantum optics[M] [S.l.] : Cambridge university press 2005
- [191] WALLS D F MILBURN G J Quantum optics[M] [S.l.] : Springer Science & Business Media 2007
- [192] MACHIDA S YAMAMOTO Y Observation of Amplitude Squeezing in a Constant-Current —Driven Semiconductor Laser[J] Physical Review Letters 1987 58(10) : 1000–1003
- [193] SHELBY R M LEVENSON M D PERLMUTTER S H, et al Broad-band parametric deamplification of quantum noise in an optical fiber[J/OL] Physical Review Letters 1986 57(6) : 691–694
<http://dx.doi.org/10.1103/PhysRevLett.57.691>
- [194] SLUSHER R E HOLLBERG L W YURKE B, et al Observation of squeezed states generated by four-wave mixing in an optical cavity[J/OL] Physical Review Letters 1985 55(22) : 2409–2412
<http://dx.doi.org/10.1103/PhysRevLett.55.2409>
- [195] WU L-A KIMBLE H J HALL J L, et al Generation of Squeezed States by Parametric Down Conversion[J] Physical Review Letters 1986 57(20) : 2520–2523
- [196] BONDURANT R S SHAPIRO J H Squeezed states in phase-sensing interferometers[J] Physical Review D 1984 30(12) : 2548
- [197] GIACOBINO E FABRE C LEUCHS G Communication by squeezed light[J/OL] Physics World 1989 2(2) : 31–35
<http://dx.doi.org/10.1088/2058-7058/2/2/25>
- [198] SLUSHER R E YURKE B Squeezed Light for Coherent Communications[J/OL] Journal of Lightwave Technology 1990 8(3) : 466–477
<http://dx.doi.org/10.1109/50.50742>
- [199] HILLERY M Quantum cryptography with squeezed states[J] Physical Review A 2000 61(2) : 022309

BIBLIOGRAPHY

- [200] DOWLING J P Quantum optical metrology—the lowdown on high-N00N states[J] Contemporary physics 2008 49(2) : 125–143
- [201] SCHNABEL R Squeezed states of light and their applications in laser interferometers[J] Physics Reports 2017 684 : 1–51
- [202] MACOMBER J D LYNCH R Squeezed spin states[J/OL] The Journal of Chemical Physics 1985 83(12) : 6514–6519
<http://dx.doi.org/10.1063/1.449838>
- [203] WALLS D F ZOLLER P Reduced Quantum Fluctuations in Resonance Fluorescence[J/OL] Physical Review Letters 1981 47(10) : 709–711
<http://dx.doi.org/10.1103/PhysRevLett.47.709>
- [204] WODKIEWICZ K EBERLY J H Coherent states, squeezed fluctuations, and the SU(2) am SU(1,1) groups in quantum-optics applications[J/OL] Journal of the Optical Society of America B 1985 2(3) : 458
<http://dx.doi.org/10.1364/josab.2.000458>
- [205] WINELAND D J BOLLINGER J J ITANO W M, et al Spin squeezing and reduced quantum noise in spectroscopy[J] Phys. Rev. A 1992 46(R6797-R6800)
- [206] VERNAC L PINARD M GIACOBINO E Spin squeezing in two-level systems[J] Physical Review A 2000 62(6) : 063812
- [207] GROSS C Spin squeezing, entanglement and quantum metrology with Bose-Einstein condensates[J] Journal of Physics B: Atomic, Molecular and Optical Physics 2012 45(10) : 103001
- [208] ZHANG Z DUAN L M Quantum metrology with Dicke squeezed states[J] New Journal of Physics 2014 16(10) : 103037
- [209] KUZMICH A MØLMER K POLZIK E Spin squeezing in an ensemble of atoms illuminated with squeezed light[J] Physical review letters 1997 79(24) : 4782
- [210] FERNHOLZ T KRAUTER H JENSEN K, et al Spin squeezing of atomic ensembles via nuclear-electronic spin entanglement[J] Physical review letters 2008 101(7) : 073601

- [211] SCHLEIER-SMITH M H LEROUX I D VULETIĆ V Squeezing the collective spin of a dilute atomic ensemble by cavity feedback[J] Physical Review A 2010 81(2) : 021804
- [212] PARKINS A SOLANO E CIRAC J Unconditional two-mode squeezing of separated atomic Ensembles[J/OL] Physical Review Letters 2006 96(5)
<http://dx.doi.org/10.1103/PhysRevLett.96.053602>
- [213] HALD J SØRENSEN J SCHORI C, et al Spin squeezed atoms: a macroscopic entangled ensemble created by light[J] Physical review letters 1999 83(7) : 1319
- [214] ORZEL C TUCHMAN A FENSELAU M, et al Squeezed states in a Bose-Einstein condensate[J] Science 2001 291(5512) : 2386 – 2389
- [215] JOSSE V DANTAN A VERNAC L, et al Polarization squeezing with cold atoms[J] Physical review letters 2003 91(10) : 103601
- [216] JO G-B SHIN Y WILL S, et al Long phase coherence time and number squeezing of two Bose-Einstein condensates on an atom chip[J] Physical Review Letters 2007 98(3) : 030407
- [217] ESTEVE J GROSS C WELLER A, et al Squeezing and entanglement in a Bose-Einstein condensate[J] Nature 2008 455(7217) : 1216
- [218] BÖHI P RIEDEL M F HOFFFROGGE J, et al Coherent manipulation of Bose-Einstein condensates with state-dependent microwave potentials on an atom chip[J] Nature Physics 2009 5(8) : 592
- [219] TAKANO T FUYAMA M NAMIKI R, et al Spin squeezing of a cold atomic ensemble with the nuclear spin of one-half[J] Physical review letters 2009 102(3) : 033601
- [220] LEROUX I D SCHLEIER-SMITH M H VULETIĆ V Implementation of cavity squeezing of a collective atomic spin[J] Physical Review Letters 2010 104(7) : 073602
- [221] CHEN Z BOHNET J G SANKAR S R, et al Conditional spin squeezing of a large ensemble via the vacuum Rabi splitting[J] Physical review letters 2011 106(13) : 133601
- [222] KRAUTER H MUSCHIK C A JENSEN K, et al Entanglement generated by dissipation and steady state entanglement of two macroscopic objects[J] Physical review letters 2011 107(8) : 80503

BIBLIOGRAPHY

- [223] PEZZÈ L SMERZI A OBERTHALER M K, et al Quantum metrology with nonclassical states of atomic ensembles[J] *Reviews of Modern Physics* 2018 90(3) : 035005
- [224] LOUCHET-CHAUVENT A APPEL J RENEMA J J, et al Entanglement-assisted atomic clock beyond the projection noise limit[J] *New Journal of Physics* 2010 12
- [225] VASILAKIS G SHEN H JENSEN K, et al Generation of a squeezed state of an oscillator by stroboscopic back-action-avoiding measurement[J/OL] *Nature Physics* 2015 11(5) : 389–392
<http://dx.doi.org/10.1038/nphys3280>
- [226] BOHNET J COX K NORCIA M, et al Reduced spin measurement back-action for a phase sensitivity ten times beyond the standard quantum limit[J/OL] *Nature Photonics* 2014 8(9) : 731–736
<http://dx.doi.org/10.1038/nphoton.2014.151>
- [227] BRAUNSTEIN S L VAN LOOCK P Quantum information with continuous variables[J] *Reviews of modern physics* 2005 77(2) : 513
- [228] KUZMICH A POLZIK E Atomic quantum state teleportation and swapping[J] *Physical review letters* 2000 85(26) : 5639
- [229] DUAN L-M CIRAC J ZOLLER P, et al Quantum communication between atomic ensembles using coherent light[J] *Physical review letters* 2000 85(26) : 5643
- [230] KUZMICH A KENNEDY T Nonsymmetric entanglement of atomic ensembles[J] *Physical review letters* 2004 92(3) : 030407
- [231] KONG J JIMÉNEZ-MARTÍNEZ R TROULLINOU C, et al Measurement-induced, spatially-extended entanglement in a hot, strongly-interacting atomic system[J] *Nature communications* 2020 11(1) : 1–9
- [232] DUAN L-M SØRENSEN A CIRAC J, et al Squeezing and entanglement of atomic beams[J] *Physical Review Letters* 2000 85(19) : 3991
- [233] CHOU C-W de RIEDMATTEN H FELINTO D, et al Measurement-induced entanglement for excitation stored in remote atomic ensembles[J] *Nature* 2005 438(7069) : 828–832
- [234] MATSUKEVICH D CHANNELIERE T JENKINS S, et al Entanglement of remote atomic qubits[J] *Physical review letters* 2006 96(3) : 030405

- [235] MØLLER D MADSEN L B MØLMER K Quantum gates and multiparticle entanglement by Rydberg excitation blockade and adiabatic passage[J] Physical review letters 2008 100(17) : 170504
- [236] HAAS F VOLZ J GEHR R, et al Entangled states of more than 40 atoms in an optical fiber cavity[J] Science 2014 344(6180) : 180 – 183
- [237] KOVACHY T ASENBAUM P OVERSTREET C, et al Quantum superposition at the half-metre scale[J] Nature 2015 528(7583) : 530 – 533
- [238] PU Y WU Y JIANG N, et al Experimental entanglement of 25 individually accessible atomic quantum interfaces[J] Science advances 2018 4(4) : eaar3931
- [239] ZARKESHIAN P DESHMUKH C SINCLAIR N, et al Entanglement between more than two hundred macroscopic atomic ensembles in a solid[J] Nature communications 2017 8(1) : 1 – 10
- [240] OMRAN A LEVINE H KEESLING A, et al Generation and manipulation of Schrödinger cat states in Rydberg atom arrays[J] Science 2019 365(6453) : 570 – 574
- [241] REICHEL J VULETIC V Atom chips[M] [S.l.] : John Wiley & Sons 2011
- [242] WHITLOCK S GERRITSMA R FERNHOLZ T, et al Two-dimensional array of microtraps with atomic shift register on a chip[J] New Journal of Physics 2009 11(2) : 023021
- [243] ABDELRAHMAN A MUKAI T HARTMUT H, et al Coherent all-optical control of ultracold atoms arrays in permanent magnetic traps[J/OL] Optics Express 2014 22(3) : 195 – 200
<http://dx.doi.org/10.1364/OE.22.003501>
- [244] BRAGINSKY V B KHALILI F Y Quantum nondemolition measurements: the route from toys to tools[J/OL] Rev. Mod. Phys. 1996 68 : 1 – 11
<http://dx.doi.org/10.1103/RevModPhys.68.1>
- [245] ILO-OKEKE E O BYRNES T Information and backaction due to phase-contrast-imaging measurements of cold atomic gases: Beyond Gaussian states[J/OL] Physical Review A 2016 94(1) : 013617
<http://dx.doi.org/10.1103/PhysRevA.94.013617>

BIBLIOGRAPHY

- [246] KITAGAWA M UEDA M Spin squeezed states[J] Phys. Rev. A 1993 47: 5138–5143
- [247] JULSGAARD B KOZHEKIN A POLZIK E S Experimental long-lived entanglement of two macroscopic objects[J] Nature 2001 413: 400–403
- [248] CERF N J LEUCHS G POLZIK E S Quantum Information with Continuous Variables of Atoms and Light[M/OL] [S.l.]: Imperial College Press 2007
<http://dx.doi.org/10.1142/p489>
- [249] KRAUTER H SALART D MUSCHIK C, et al Deterministic quantum teleportation between distant atomic objects[J] Nature Physics 2013 9(7): 400–404
- [250] GERVING C S HOANG T M LAND B J, et al Non-equilibrium dynamics of an unstable quantum pendulum explored in a spin-1 Bose–Einstein condensate[J] Nature Comm. 2012 3(May): 1169
- [251] STROBEL H MUESSEL W LINNEMANN D, et al Fisher information and entanglement of non-Gaussian spin states[J] Science 2014 345(6195): 424–427
- [252] KAJTOCH D WITKOWSKA E Quantum dynamics generated by the two-axis countertwisting Hamiltonian[J] Physical Review A 2015 92(1): 013623
- [253] LI S-S Spin Squeezing and Entanglement of Two-Axis Twisting Model[J] International Journal of Theoretical Physics 2017 56(10): 3061–3067
- [254] WANG M QU W LI P, et al Two-axis-twisting spin squeezing by multipass quantum erasure[J] Physical Review A 2017 96(1): 013823
- [255] ZHANG M HELMERSON K YOU L Entanglement and spin squeezing of Bose-Einstein-condensed atoms[J] Physical Review A 2003 68(4): 043622
- [256] BYRNES T Fractality and macroscopic entanglement in two-component Bose-Einstein condensates[J] Physical Review A 2013 88(2): 023609
- [257] KURKJIAN H PAWŁOWSKI K SINATRA A, et al Spin squeezing and Einstein-Podolsky-Rosen entanglement of two bimodal condensates in state-dependent potentials[J] Physical Review A 2013 88(4): 043605
- [258] TREUTLEIN P HÄNSCH T W REICHEL J, et al Microwave potentials and optimal control for robust quantum gates on an atom chip[J] Phys. Rev. A 2006 74: 022312

- [259] PYRKOV A N BYRNES T Quantum teleportation of spin coherent states: beyond continuous variables teleportation[J] New Journal of Physics 2014 16(7) : 073038
- [260] HUSSAIN M I ILO-OKEKE E O BYRNES T Geometric phase gate for entangling two Bose-Einstein condensates[J] Physical Review A 2014 89(5) : 053607
- [261] JING Y FADEL M IVANNIKOV V, et al Split spin-squeezed Bose-Einstein condensates[J] New Journal of Physics 2019 21(9) : 093038
- [262] KUZMICH A MANDEL L BIGELOW N Generation of spin squeezing via continuous quantum nondemolition measurement[J] Physical Review Letters 2000 85(8) : 1594
- [263] RIEDEL M F BÖHI P LI Y, et al Atom-chip-based generation of entanglement for quantum metrology[J] Nature 2010 464(7292) : 1170
- [264] KUPRIYANOV D V SOKOLOV I M SLAVGORODSKII A V Cooperative Raman-type transitions in a system of two four-level atoms: Entanglement in the spin subsystem of two spatially separated atomic ensembles[J/OL] Phys. Rev. A 2001 63 : 063811
<http://dx.doi.org/10.1103/PhysRevA.63.063811>
- [265] YUKAWA E MILBURN G J HOLMES C A, et al Precision measurements using squeezed spin states via two-axis countertwisting interactions[J/OL] Phys. Rev. A 2014 90 : 062132
<http://dx.doi.org/10.1103/PhysRevA.90.062132>
- [266] KITAGAWA M UEDA M Squeezed spin states[J] Physical Review A 1993 47(6) : 5138
- [267] BULUTA I NORI F Quantum simulators[J] Science 2009 326(5949) : 108–111
- [268] AARONSON S Why quantum chemistry is hard[J] Nature Physics 2009 5(10) : 707–708
- [269] ASPURU-GUZIK A WALTHER P Photonic quantum simulators[J] Nature physics 2012 8(4) : 285–291
- [270] PAPADIMITRIOU C H STEIGLITZ K Combinatorial optimization: algorithms and complexity[M] [S.l.] : Courier Corporation 1998

BIBLIOGRAPHY

- [271] KORTE B H VYGEN J KORTE B, et al Combinatorial optimization : Vol 1[M][S.l.] : Springer 2011
- [272] MOHSENI N MCMAHON P L BYRNES T Ising machines as hardware solvers of combinatorial optimization problems[J] Nature Reviews Physics 2022 4(6) : 363–379
- [273] DAS A CHAKRABARTI B K Colloquium: Quantum annealing and analog quantum computation[J] Reviews of Modern Physics 2008 80(3) : 1061
- [274] HAUKE P KATZGRABER H G LECHNER W, et al Perspectives of quantum annealing: Methods and implementations[J] Reports on Progress in Physics 2020 83(5) : 054401
- [275] ALBASH T LIDAR D A Adiabatic quantum computation[J] Reviews of Modern Physics 2018 90(1) : 015002
- [276] YARKONI S RAPONI E BÄCK T, et al Quantum annealing for industry applications: Introduction and review[J] Reports on Progress in Physics 2022
- [277] MCARDLE S JONES T ENDO S, et al Variational ansatz-based quantum simulation of imaginary time evolution[J] npj Quantum Information 2019 5(1) : 1–6
- [278] ENDO S SUN J LI Y, et al Variational quantum simulation of general processes[J] Physical Review Letters 2020 125(1) : 010501
- [279] YUAN X ENDO S ZHAO Q, et al Theory of variational quantum simulation[J] Quantum 2019 3 : 191
- [280] MOTTA M SUN C TAN A T, et al Determining eigenstates and thermal states on a quantum computer using quantum imaginary time evolution[J] Nature Physics 2020 16(2) : 205–210
- [281] LIU T LIU J-G FAN H Probabilistic nonunitary gate in imaginary time evolution[J] Quantum Information Processing 2021 20(6) : 1–21
- [282] BAO H DUAN J JIN S, et al Spin squeezing of 1011 atoms by prediction and retrodiction measurements[J] Nature 2020 581(7807) : 159–163

-
- [283] DECKER K S C KARRASCH C EISERT J, et al Floquet Engineering Topological Many-Body Localized Systems[J/OL] Phys. Rev. Lett. 2020 124: 190601
<http://dx.doi.org/10.1103/PhysRevLett.124.190601>
- [284] LEE T E JOGLEKAR Y N RICHERME P String order via Floquet interactions in atomic systems[J/OL] Phys. Rev. A 2016 94: 023610
<http://dx.doi.org/10.1103/PhysRevA.94.023610>
- [285] TERHAL B M Quantum error correction for quantum memories[J/OL] Rev. Mod. Phys. 2015 87: 307–346
<http://dx.doi.org/10.1103/RevModPhys.87.307>
- [286] BRIEGEL H J RAUSSENDORF R Persistent Entanglement in Arrays of Interacting Particles[J/OL] Phys. Rev. Lett. 2001 86: 910–913
<http://dx.doi.org/10.1103/PhysRevLett.86.910>
- [287] NIELSEN M A Cluster-state quantum computation[J] Reports on Mathematical Physics 2006 57(1): 147–161
- [288] HASELGROVE H L NIELSEN M A OSBORNE T J Quantum states far from the energy eigenstates of any local Hamiltonian[J] Physical review letters 2003 91(21): 210401
- [289] CHEN J CHEN X DUAN R, et al No-go theorem for one-way quantum computing on naturally occurring two-level systems[J] Physical Review A 2011 83(5): 050301
- [290] BARTLETT S D RUDOLPH T Simple nearest-neighbor two-body Hamiltonian system for which the ground state is a universal resource for quantum computation[J] Physical Review A 2006 74(4): 040302
- [291] Van den NEST M LUTTNER K DÜR W, et al Graph states as ground states of many-body spin-1/2 Hamiltonians[J] Physical Review A 2008 77(1): 012301
- [292] KYAW T H LI Y KWEK L-C Measurement-based quantum computation on two-body interacting qubits with adiabatic evolution[J] Physical review letters 2014 113(18): 180501
- [293] KYAW T H KWEK L-C Cluster state generation in one-dimensional Kitaev honeycomb model via shortcut to adiabaticity[J] New Journal of Physics 2018 20(4): 045007

BIBLIOGRAPHY

- [294] CHAUDHARY M MAO Y KONDAPPAN M, et al Stroboscopic quantum non-demolition measurements for enhanced entanglement generation between atomic ensembles[J] *Physical Review A* 2022 105(2): 022443
- [295] GOTTESMAN D CHUANG I L Demonstrating the viability of universal quantum computation using teleportation and single-qubit operations[J] *Nature* 1999 402(6760): 390–393
- [296] FOWLER A G GOYAL K Topological cluster state quantum computing[J] *Quant. Info. Comput.* 2009 9: 721
- [297] ILO-OKEKE E O JI Y CHEN P, et al Deterministic preparation of supersinglets with collective spin projections[J/OL] *Phys. Rev. A* 2022 106: 033314
<http://dx.doi.org/10.1103/PhysRevA.106.033314>
- [298] WALTER M GROSS D EISERT J Multipartite entanglement[J] *Quantum Information: From Foundations to Quantum Technology Applications* 2016: 293–330
- [299] MIYAKE A Classification of multipartite entangled states by multidimensional determinants[J] *Physical Review A* 2003 67(1): 012108
- [300] DÜR W VIDAL G CIRAC J I Three qubits can be entangled in two inequivalent ways[J] *Physical Review A* 2000 62(6): 062314
- [301] RADHAKRISHNAN C LAURIÈRE M BYRNES T Multipartite generalization of quantum discord[J] *Physical Review Letters* 2020 124(11): 110401

Funding and Acknowledgments

This work is supported by the National Natural Science Foundation of China (62071301); NYU-ECNU Institute of Physics at NYU Shanghai; Shanghai Frontiers Science Center of Artificial Intelligence and Deep Learning; the Joint Physics Research Institute Challenge Grant; the Science and Technology Commission of Shanghai Municipality (19XD1423000,22ZR1444600); the NYU Shanghai Boost Fund; the China Foreign Experts Program (G2021013002L); the NYU Shanghai Major-Grants Seed Fund; Tamkeen under the NYU Abu Dhabi Research Institute grant CG008; and the SMEC Scientific Research Innovation Project (2023ZKZD55).

Appendix A: Saturated absorption spectroscopy and laser locking

0.1 Saturated absorption spectroscopy and laser locking

Saturated Absorption Spectroscopy (SAS) is a way of measuring the spectrum of atomic gases that overcomes Doppler constraints. Doppler broadening is dependent on the rate of optical pumping and the lifetimes of the hyperfine states. When a resonant laser beam passes over the sample, power is absorbed by the atoms, resulting in a Doppler-broadened absorption spectrum. In our SAS optical circuit 0-1, the Rubidium cell which contains both ^{87}Rb , ^{85}Rb isotopes. The Rubidium vapor undergoes fluorescence inside the cell when the absorption resonances overlap with the scanned range, which has been steadily shifted by the automated grating tuning of our secondary laser in the case of MOT lines.

By using two distinct beams, saturation absorption spectroscopy overcomes Doppler broadening and obtains the linewidth limited spectrum. The larger intensity pump beam saturates the higher state, such that there are fewer atoms in the zero-velocity state as the probe beam passes through in the opposite direction to absorb photons in the ground state. The detector measures the lower power loss caused by atoms in the sample and the absorption of photons from the probe beam. Because the beams travel in opposing directions, only atoms at rest relative to both beams are in resonance. As a result, the absorption signal received by the probe should have a short, narrow spike at the zero temperature line's point, and its breadth should be similar to the natural line width. We have successfully generated the precise SAS output with our unique design of the surrounding temperature of the Rubidium cell with 40°C higher than the lab's temperature.

This involves comparing atomic transition frequencies with rubidium cell atoms in the SAS setups and using an external cavity grating. The laser spectra are checked with

an optical spectrum analyzer. The grating piezo actuator voltage is modulated to scan a few GHz range (see Fig. 0-2). As rubidium absorption matches this range, it's aligned by the grating. Precision tuning adjusts the piezo's voltages to match laser frequencies with atomic resonances. Only one zero crossing inside one piezo ramp is needed for the locking electronics to lock. The PID controller ensures a tight lock and the laser linewidth is adjusted for the lab temperature. Optical signals are sent through PM fibers to the optical circuit.

The power utilization in the spectroscopy block is 1 mW where it is detuned to 18 MHz with an AOM driven by a 100 MHz RF signal (see Fig. 0-2). At this stage, the polarization of the beam is vertical. After that, it passes through a PBS. The output of the PBS is controlled by a HWP which is placed before the PBS thus the laser being split and sent to a double pass configuration setup. The reflected beam from the PBS maintains the polarization, thus the polarization remains vertical. The double pass configuration employs another 100MHz AOM. After passing the AOM, the beam is reflected by a mirror which rotates the polarization by 180 degrees, then is followed by a quarter wave plate (QWP). The combination of the QWP and mirror changes the beam's polarization to the horizontal orientation. The laser passes back through the same 100 MHz AOM in the configuration and is transmitted out of the PBS as horizontally polarized light passes through the PBS. The output beam goes to the detectors of the spectroscopy unit marked with a blue box in Fig. 0-2.

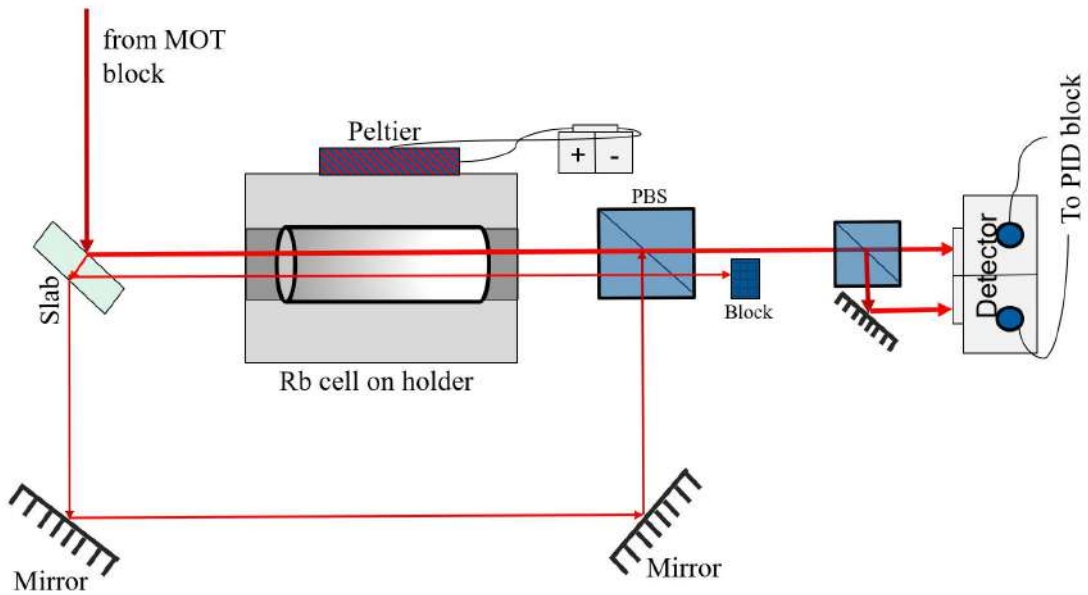


Fig 0-1 SAS scheme used in our experimental setup. A similar configuration is being employed for both the primary and secondary laser to achieve frequency locking. The sub-kHz linewidth diode laser is locked to the cycle transitions $5^2S_{1/2}(F_g = 2) \rightarrow 5^2P_{3/2}(F_e = 3)$ for the cooling cycle. However, it is locked at a detuned wavelength -18 MHz and $5^2S_{1/2}(F_g = 1) \rightarrow 5^2P_{3/2}(F_e = 2)$ is being locked at the exact transition for repumping laser. Of the primary laser's output power, ~ 70 mW is used in the SAS circuit and 1 mW is utilized for repumping locking after the completion of the circuit and utilizing the laser in production mode.

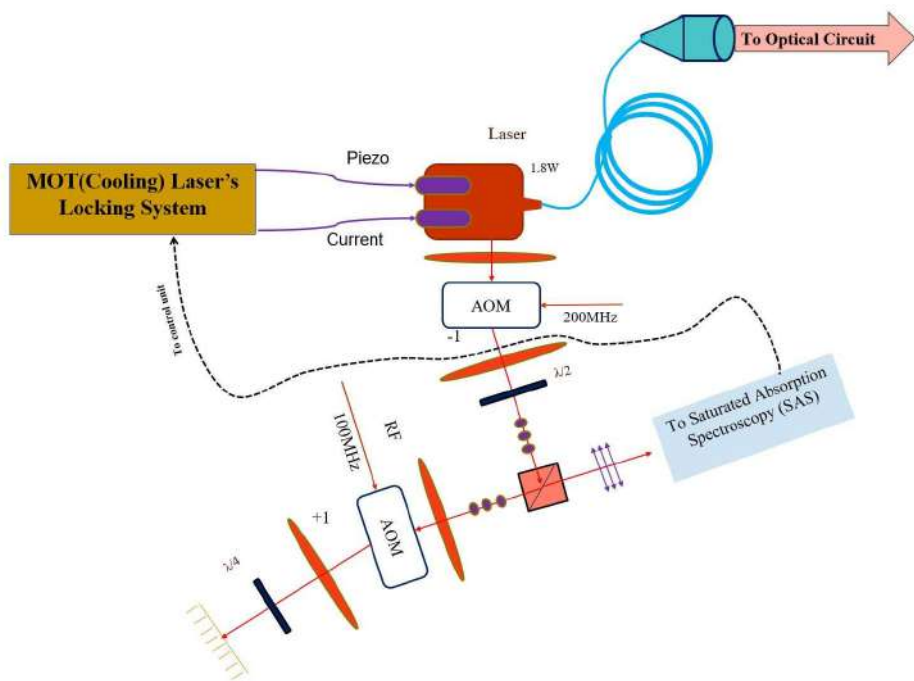


Fig 0-2 Frequency locking of the primary laser. The output of this circuit is sent to the optical circuit of Fig. 5-3. The sub-kHz linewidth diode laser is locked to the cycle transition $5^2S_{1/2}(F_g = 2) \rightarrow 5^2P_{3/2}(F_e = 3)$ with a high polarization resonance. It runs at a detuning of 18 MHz, with a few milliwatts of power being used in this setup branch. The output power of the laser is being maintained at ~ 1.812 W. The frequency scanning range is 7 GHz.

Appendix B: Control electronics

0.2 The Mini-Circuits switch ZASWA-2-50DRA+

The Mini-Circuits switch ZASWA-2-50DRA+ is utilized as a switching circuit to alternate the signal generated from the RF generators. It is positioned between the RF generators and RF amplifiers. TTL signals produced by LabVIEW control this switching circuit. The amplifiers, linked to the Acousto-Optic Modulators (AOMs) in the optical circuit, play a crucial role in managing various laser lines that enter the vacuum chamber, thereby influencing the Magneto-Optical Trap (MOT) formation and various stages of Bose-Einstein Condensate (BEC) formation on the AtomChip. To precisely address the internal states of rubidium atoms, nanosecond-level switching is essential for different laser lines such as MOT, repopulation, Optical Pumping (OP), Entanglement (ENT), and Imaging (IMG). Therefore, these switches are employed for accurate RF signal modulation into the AOMs.

The employed commercial RF switching circuit as shown in Fig. 0-3, Mini-Circuits switch ZASWA-2-50DRA+, operates on DC power within the 100 MHz to 5 GHz range. It is powered by a bipolar power supply of +5/-5 V. The switch requires a TTL signal for operation, toggling from its lowest state (signal off) to its highest state (AOM on) while preventing amplifier termination during switching. The TTL signal from LabVIEW, oscillating between 0 and +5V, is connected to the TTL port of the switch.

Testing: When a 200 MHz RF signal is input into the RF IN port of the device, the outputs from ports 1 and 2 vary from -78dbm to -32dbm with a 0, +5V TTL signal at the TTL input.

Signal Comparison: Oscilloscope analysis reveals that the latency from LabVIEW command to the switching signal is approximately 1500ns. The switching signal's tran-



Fig 0-3 The Mini-Circuits switch ZASWA-2-50DRA+

sition time is around 120ns, indicating how long it takes to switch from the lower to the higher state. This rapid switching is crucial to minimize jitter effects in the AOMs, surpassing the speed of mechanical switches.

0.3 The control circuit

The circuit diagram illustrates 0.3 the generalized version of our three sub varients of coil and Z- wire drivers circuit with $V_{control}$ set to 1. The voltage across resistor R is determined by the equation $V_{set} = (1 + \frac{R_f}{100k}) \cdot V_{sense} \cdot dt$. To mitigate the heat generated by the MOSFETs, the circuits were mounted on heatsinks. Identical circuits were constructed for the x, y, and z bias coils, as well as for the LP MOT coil driver, each equipped with $R_{sense} = 0.5$ and $R_f = 100k$. Their response was $I_{coils} = 1A$ when V_{set} was set to 1V.

An additional driver was utilized to control the Ioffe-Pritchard "extra" bias (IPEB) coils, requiring higher current. For this application, R_{sense} was set to 0.1, and R_f was adjusted to 12k. Current regulation was achieved using four parallel BUK 456-60H MOSFETs, each mounted on a separate heatsink. The response time of this configuration was $I_{coils} = 1A$ for V_{set} at 0.93V. We employ a home made R_{sense} with 36mOhm made out of

$R_{\text{sense}} = 0.5 \text{ Ohm}, 0.1 \text{ Ohm}$ and
32mOhm (constantan)

555 = BUK 456-60H MOS-FET

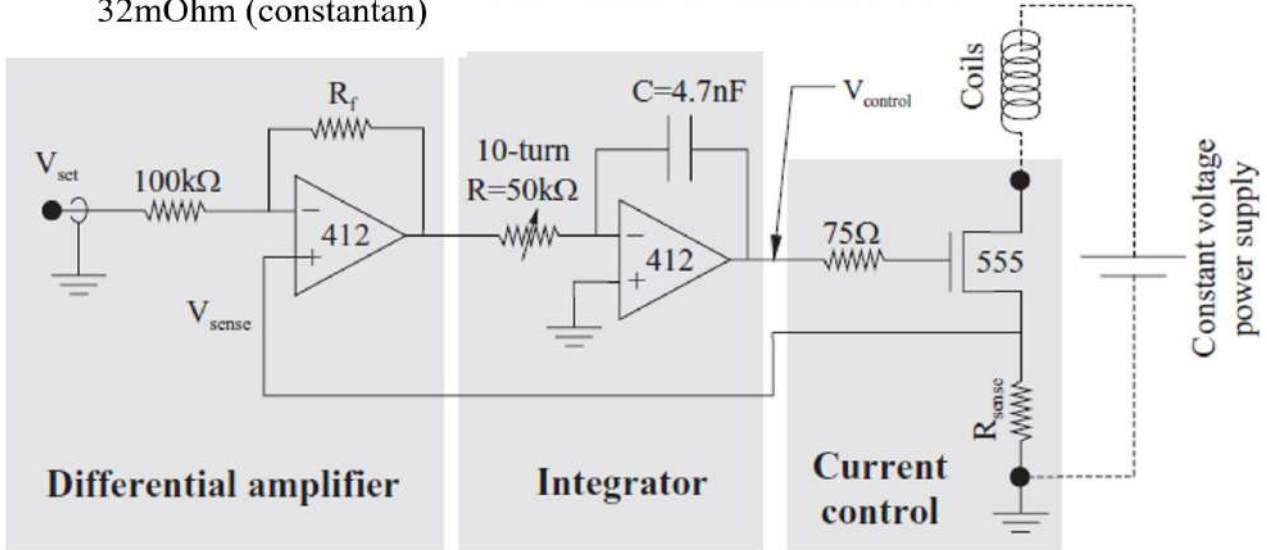


Fig 0-4 Generalized driver control circuit

constantan material for very higher accuracy precise magnetic controls. All drivers shared a common power supply rated at 15V and 200mA. Despite the use of separate DC coil supplies, a single 15V source was utilized in parallel for the x, y, and z bias coils.

0.4 Shutter drivers

The shutter drivers employ IC model numbers IRF 740 and IRF 840 MOSFETs. The control electronics require a minimum V_{set} of 1.25V to open the shutter, with V_{control} connected to a 68 Ohm resistor, and in some cases a 75 Ohm resistor, followed by the gate of the MOSFET. A 56 Ohm resistor is used as the sense resistor. The rated voltage for the beam shutter is 12V, although experimentally, a minimum of 9V is sufficient to open it. The main power supply for the op-amps box is $\pm 15V$. MOSFETs IRF740 and IRF 840 are utilized in six places within our processor circuit. A 75 Ohm resistor is soldered to the gate (G), which controls the current flow to the transistor's drain, connected to the shutter's negative terminal, while the shutter's positive terminal is connected to the 12V power supply.

Similar to the shutter driver, V_{control} for the coil drivers transistor is connected with a 68 Ohm resistor. When not in use in the load circuit, the G(4) and KS(3) are protected

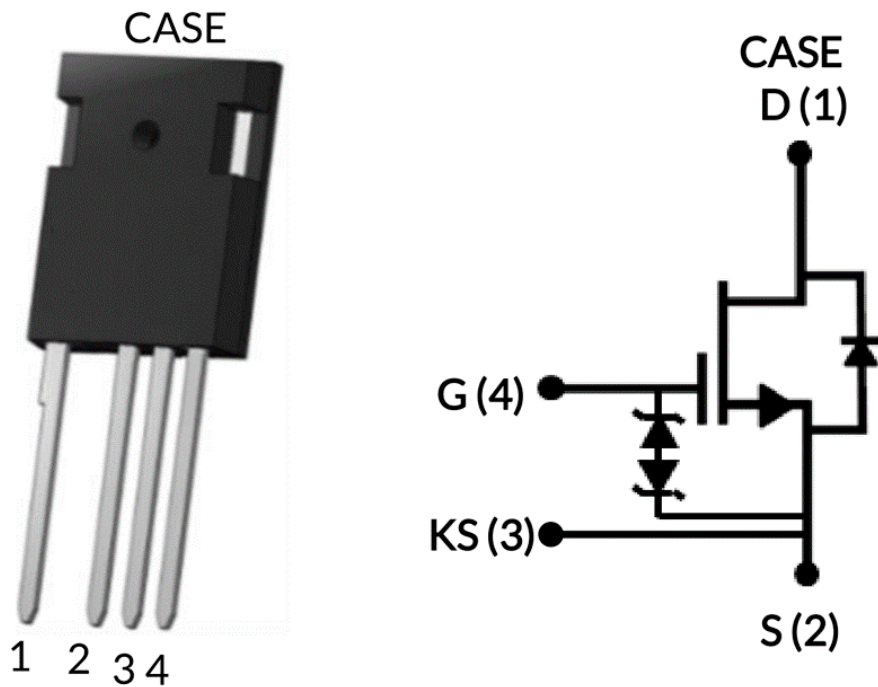


Fig 0-5 UF3SC120009K4S from UnitedSic

with a 50 Ohm resistor. KS(3) would otherwise be connected to the positive input of the first amplifier (identified as 412 in the figure). The R_f 10-turn ramp resistors, referred to as Ramp and R_{tau} in the circuit, are 100kOhm and 50kOhm, respectively. The source (S) is connected to one terminal of a homemade high-precision 36 mOhm resistor, with the other terminal grounded. The drain (D) is connected to one of the connectors of the coils, while the other end of the coil is connected to a 30A ($\sim 200mV$) power supply. To dissipate the energy generated by the MOSFETs, the circuits were constructed on heatsinks. Four circuits, each with identical specifications, were built for the x, y, and z bias coils, as well as for the LP MOT coil driver, equipped with a homemade Rsense value of 36 mOhm and R_f = 100k, yielding a response rate of I_{coils} = 1A when V_{set} is 1V.

The UF3SC120009K4S from UnitedSic [0.4](#) is also employed in the coil-driver circuit. The circuit diagram illustrates the coil-driver circuit with V_{control} set to a range of 1-2V. The voltage across the resistor R can be determined by the equation $V_{set} = (1 + \frac{R_f}{100k}) \times V_{sense} \times dt$. The same driver circuits are used to regulate the Ioffe-Pritchard bias in the atom chip, which requires a greater current. In this scenario, Rsense is set to 0.1, and R_f is adjusted to a range of 10k to 30k. To regulate the current flow, MOSFETs are soldered in parallel and installed on a heatsink. The response time of this circuit yields I_{coils} of 0.8 to 1.5 A when V_{set} is set to a value between 0.8V and 1.5V. All drivers are connected

to the same power supply of 15V and 200mA. Although separate DC coil supplies were employed, a single 15V supply was used in parallel for the x, y, and z bias coils.

RF switches

RF switches used for sandwiching between RF generators and amplifiers. The employed RF switches are P9402A 100 MHz to 8 GHz SPDT PIN switch form Keysight are employed inbetween synthesizers and amplifiers to switch between different amplifiers.

0.5 Automation and reverse engineering element

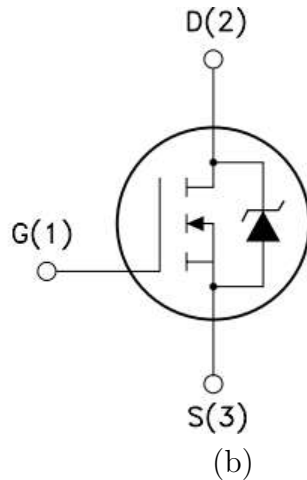
Automation and reverse engineering of a commercial fingerbot [0-6](#) are undertaken to establish independent control within our laboratory setup. The ADAPROX Fingerbot Plus was selected for its ability to toggle switches for lasers and other push-button operations in an online lab environment. Our objective was to bypass the need for third-party software or apps for remote operation, integrating control directly into our main LabVIEW system.

In characterizing the fingerbot's functional requirements for current and voltage, we determined that the ADAPROX's battery outputs 4A at 3V. Measuring the motor's operational current requirements was less straightforward. Upon removing the battery and setting the power supply to 3V and 5A, the fingerbot's operational state was initially tested. Subsequently, the current was reduced to 0.5A while maintaining the voltage at 3V, resulting in the bot's failure to activate upon powering. Observations of the power supply's current indicator suggested rapid fluctuations (noted by red blinks in the c.c. readout LED), which were faster than the load's response time. Upon incrementing the current to 0.7A, the red blinks persisted, but ceased at 1.8A, indicating the fingerbot's operational start. This led us to conclude that the fingerbot's minimum operational current is approximately 2A. To ensure reliability, a 3V power supply capable of delivering 3A was deemed suitable, considering it spans the range from the minimum operational current to the battery's output.

For switching control, the fingerbot's circuitry was modified to respond to LabVIEW-generated pulses. The IRF820 N-channel 500V - 2.5Ω - 4A TO-220 PowerMesh^{TMII} MOS-



(a)



(b)

Fig 0-6 Shows the components of finger bot, (a) is dismantled finger bot and (b) is finger bot's MOSFET

FET 0-6 was incorporated as the switch. Connections were made with the positive from LabVIEW to the IRF820's gate (G) terminal (1), and the negative to the source (S) terminal (3). The drain (D) terminal (2) was connected to the onboard switch button, which is also configured for third-party app access. This setup allows the fingerbot to switch on or off remotely. This is especially convenient as LabVIEW is configured for remote access, facilitated by AnyDesk Co. software installed on a Windows 7 system.

LEM transducer test

Current measurement in our setup is facilitated by a LEM transducer 0.6, with a sense resistor serving as a critical component of the measurement device. The operational principle is based on Ohm's law, where a measured voltage drop across the sense resistor is indicative of the current flowing through it.

In our testing configuration, with a 15 Ohm sense resistor integrated into the sensor loop and a probed current of 5A, a voltage drop of approximately 50 mV is observed. The calculation proceeds as follows:

$$\frac{50\text{mV}}{15 \text{ Ohm}} = 3.\bar{3}\text{mA}$$

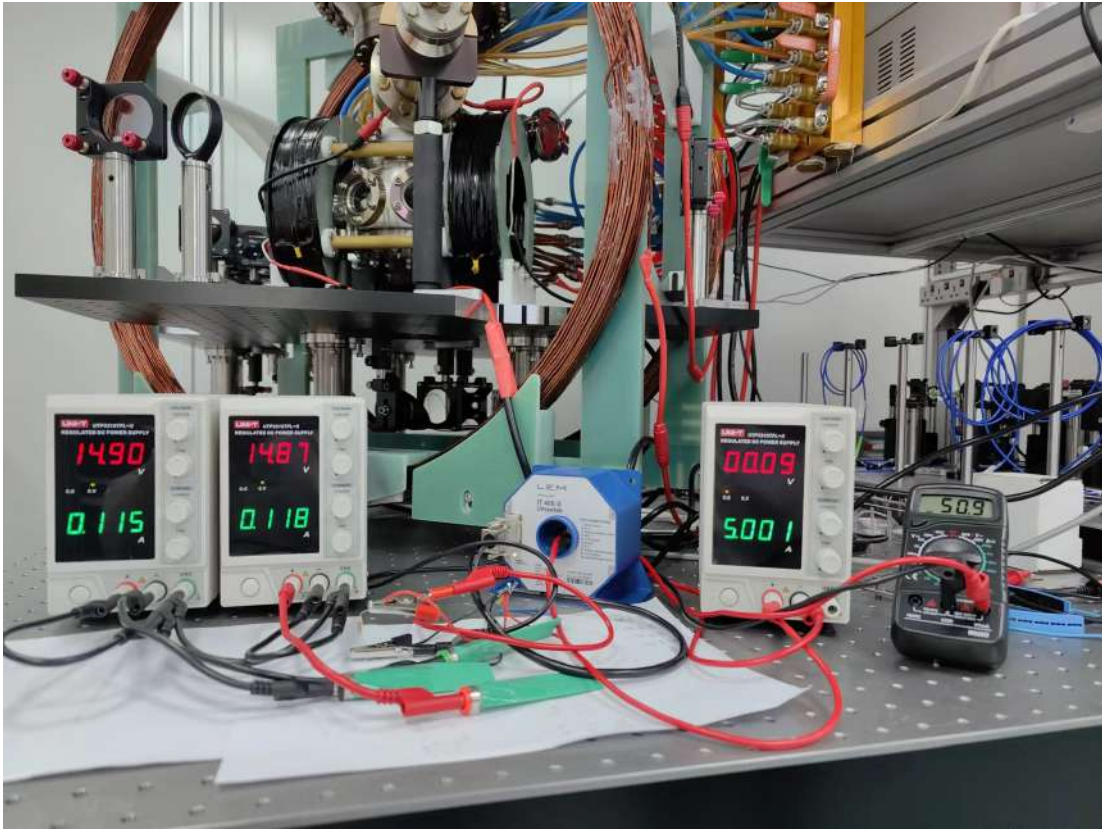


Fig 0-7 LEM transducer

where $3.\overline{3}$ represents a recurring decimal of $3.333333333\cdots$ mA. Multiplying this value by the device's specified ratio of 1500 yields a resultant current of:

$$3.\overline{3}\text{mA} \times 1500 = 5\text{A}$$

This methodology enables the estimation of current through the wire powering Helmholtz coils in the circuit. Such precise measurement is crucial for testing the LEM transducers' performance under various scenarios, ensuring accurate control and monitoring within the system.

0.6 Control VI scheme

The Main control unit(.vi) is compatible with LabVIEW 2009 Service Pack 1, version 9.0.1 (32-bit). This iteration, an advancement of the original LabVIEW script by Shannon/Russell. This handles National Instruments NI PCI-6733 DAQ cards within a single PC. All three cards are interconnected internally via a Real-Time System Integration cable

for synchronized timing and control signal transmission among the boards. Synchronization is achieved using the master board's (M) clock, which governs the two slave boards (S1 and S2), thus maintaining true synchronization. In contrast to the previous setup where each card operated on its own clock, leading to a time base drift between cards ($10\text{s} \pm 100\mu\text{s}$), this approach is more efficient. For installation and configuration details, refer to <http://digital.ni.com/public.nsf/allkb/A120195AAAA9222A86256C69007C8B27>.

The BNC-2110, a desktop and DIN rail-mountable BNC adapter, connects to data acquisition (DAQ) devices. It features 15 BNC connectors, allowing the cards to generate both analog and digital outputs, which are synchronized. The analog output can be ramped, whereas the digital output is limited to switching (20ns). This modification reduces the program's complexity as separate lines for switching devices on/off during ramp execution are no longer needed. Additionally, the digital output's slew rate is faster at 10 ns to 5V, compared to the analog's approximate 500 ns. An indexing function has been incorporated, enabling the linear or random incrementation of a single channel in a single line of an array, between a start and finish value over a specified number of points. Channels are either Time or Analog (no digital). These values are also easily transferable to a spreadsheet. This function facilitates basic operations like time of flight curves, scanning fields, laser frequencies, laser intensity, and atom number, essentially scanning any parameter proportional to an output voltage.

Furthermore, as shown in Fig. 0-8, an external trigger function available at the top of each array (external Trigger switch). This function could halt array execution until a trigger signal is received via the Dev1/PFI0 (a BNC connector in the trigger/counter section of the BNC-2110 connected to Device 1). The trigger signal defaults to a digital edge but can be set to an analog edge in the OUTPUT_ALL.vi. This feature allows array synchronization with the 50 Hz mains line to reduce B noise. It is important to note that modifying the array's timing with the external trigger function active may introduce a phase shift, which must be manually corrected. For example, no phase shift is introduced if the index function steps the time by 20ms intervals ($n2\pi, n = 1, 2, 3, \dots$).

An Array timeout indicator dynamically summing all time intervals of the course array and providing this as the timeout for output_all.vi, the first line (line 0) is not included in the timeout calculation. The wait-until-done VI ensures that the entire output is generated before closing the task, minimizing the time between array outputs, largely independent of array size. The data is with one card as follows.

Array Size samples (1, 2)	20,20	200,200	2000,2000	20000,20000	20000,20000
T (ms)	200	200	200	200	2000
Δt (ms)	10	1	0.1	0.01	0.1
<Latency>(ms)	7	12	12	16	20

A Graphical Output page visualizing array plots, helpful in understanding exported data. This feature is for reading, alternatively, the exporting channel can be connected to an oscilloscope. Export Waveform functionality produces a hardcopy of the data (a CSV file for a single channel). The switch is a push-to-export; however it does not latch on. The External Trigger Function requires an input via the PFI0/AI Start BNC on the Trigger/Counter section of a BNC-2110 breakout connector, typically for the device 1 card (DEV1). The signal type is configurable in output_all.vi, with the default being Digital Edge. If the External Trigger Boolean returns false, the array output task starts immediately. Array 3 / Step size / FIFO Buffer. The minimum attainable step size is limited by the array size in memory.

Step size	100 μ sec	10 μ sec	5 μ sec	2 μ sec	1 μ sec
Samples	4000x8	40,000x8	80,000x8	200,000x8	400,000x8
Run	YES	YES	YES	YES	NO

If the total time is increased by an order of magnitude, the step size must be increased correspondingly; otherwise, the cards crash and cannot output the waveform. Notably, no error message is displayed, and the code continues to cycle but without an output. Unlike previous versions where LabVIEW crashed and required a restart, now the step size can be updated to a larger value for proper functioning.

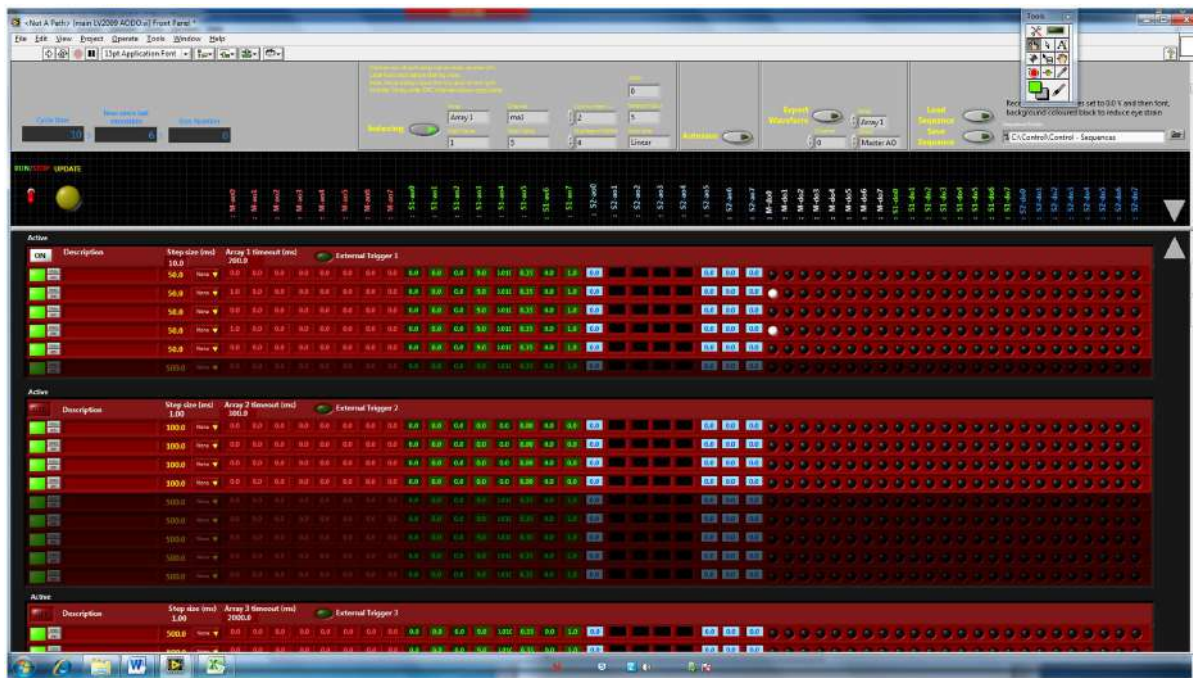


Fig 0-8 LabVIEW control buttons in the main control program's front(vi) page

Appendix : Foundational equations and their context from our works [1–3]

In this section, we consolidate critical equations referenced throughout this thesis. These equations are instrumental in elucidating the interaction dynamics between light and Bose-Einstein Condensates (BECs) well studied in our work [3], serving as the mathematical backbone of our study. We compile all the key equations referenced in previous sections for clarity and coherence. These equations are as a referring point for the discussions presented earlier and later.

0.7 Referenced equations

$$\text{Expression for cosine power: } \cos^{n_c}(k_1 - k_2)\tau \approx e^{-\frac{n_c}{2}[(k_1 - k_2)\tau]^2} \quad (0-1)$$

$$\begin{aligned} \text{Approximate Wavefunction: } & |\psi_{n_c}^{\text{approx}}(\tau)\rangle = \frac{1}{\sqrt{\mathcal{N}}} \sum_{k_1, k_2=0}^N \\ & e^{-\frac{1}{N}[(k_1 - \frac{N}{2})^2 + (k_2 - \frac{N}{2})^2]} e^{-n_c\tau^2(k_1 - k_2)^2/2} |k_1\rangle |k_2\rangle \end{aligned} \quad (0-2)$$

$$\text{C Function: } C_{n_c n_d}(\chi) \approx \delta_{n_d=0} \frac{\alpha^{n_c} e^{-\alpha^2/2}}{\sqrt{n_c!}} \cos^{n_c}(k_1 - k_2)\tau \quad (0-3)$$

$$\text{Poisson Distribution: } p_{n_c n_d}^{\text{approx}}(\tau) \approx \delta_{n_d=0} \frac{|\alpha|^{2n_c} e^{-|\alpha|^2}}{n_c!} \quad (0-4)$$

$$\text{Gaussian Approximations: } \begin{cases} \cos^{n_c}(k_1 - k_2)\tau \approx e^{-\frac{n_c}{2}[(k_1 - k_2)\tau]^2} \\ \frac{1}{2^N} \binom{N}{k} \approx \sqrt{\frac{2}{N\pi}} e^{-\frac{2}{N}(k - \frac{N}{2})^2} \end{cases} \quad (0-5)$$

$$\text{Final Unnormalized State: } |\tilde{\psi}_{n_c n_d}(\tau)\rangle = \Pi_{n_c n_d} |\psi(\tau)\rangle = |n_c\rangle |n_d\rangle$$

$$\sum_{k_1, k_2=0}^N \Psi_{k_1 k_2} C_{n_c n_d}[(k_1 - k_2)\tau] |k_1\rangle |k_2\rangle \quad (0-6)$$

$$(0-7)$$

$$\text{Offset Correlation: } k_1 - k_2 = \pm \frac{1}{\tau} \arcsin \sqrt{\frac{n_d}{n_c + n_d}} \quad (0-8)$$

$$\begin{aligned} \text{Normalized State} & |\psi_{n_c n_d}(\tau)\rangle \equiv \frac{|\tilde{\psi}_{n_c n_d}(\tau)\rangle}{\sqrt{p_{n_c n_d}(\tau)}} \\ \text{After Measurement:} & \end{aligned} \quad (0-9)$$

$$\text{Simpler Photon Probability: } p_{n_c n_d}(\tau) = \frac{1}{4^N} \sum_{k=0}^{2N} \binom{2N}{k} |C_{n_c n_d}[(N-k)\tau]|^2 \quad (0-10)$$

$$\begin{aligned} \text{State After} \\ \text{Interaction:} & |\psi(\tau)\rangle = \sum_{k_1, k_2=0}^N \Psi_{k_1 k_2} |k_1\rangle |k_2\rangle \\ & \times e^{-i\tau(k_1 - k_2)a_1^\dagger a_1} \left| \frac{\alpha}{\sqrt{2}} \right\rangle_{a_1} e^{i\tau(k_1 - k_2)a_2^\dagger a_2} \left| \frac{\alpha}{\sqrt{2}} \right\rangle_{a_2} \end{aligned} \quad (0-11)$$

$$\begin{aligned} \text{Beam Splitter Definition:} & a_1 = \frac{1}{\sqrt{2}}(c + d), \\ & a_2 = \frac{1}{\sqrt{2}}(c - d) \end{aligned} \quad (0-12)$$

$$\begin{aligned} \text{After Beam Splitter:} & |\psi(\tau)\rangle = \sum_{k_1, k_2=0}^N \Psi_{k_1 k_2} |k_1\rangle |k_2\rangle \\ & \times |\alpha \cos(k_1 - k_2)\tau\rangle_c |-\imath\alpha \sin(k_1 - k_2)\tau\rangle_d \end{aligned} \quad (0-13)$$

$$\text{Two Coherent State Initial: } \Psi_{k_1 k_2} = \frac{1}{2^N} \sqrt{\binom{N}{k_1} \binom{N}{k_2}} \quad (0-14)$$

$$\text{C Function for } n_d > 0: \quad C_{n_c n_d}[(k_1 - k_2)\tau] \approx \delta_{n_d \neq 0} \frac{\alpha^{n_c} e^{-\alpha^2/2}}{\sqrt{n_c!}} \cos^{n_c}(k_1 - k_2)\tau \quad (0-15)$$

$$\tau > \frac{1}{\sqrt{n_c}} \approx \frac{1}{|\alpha|}, \quad (0-16)$$

$$N < |\alpha|^2. \quad (0-17)$$

For the understanding and development of the concepts discussed the brief explanation on these equations are as follows since these are pivotal in exploring various regimes

of light-BEC interactions, aiding in both theoretical and experimental inquiries. Equation (0-3) defines the $C_{n_c n_d}$ function, which is central to understanding photon statistics. Equation (0-4) simplifies the photon probability distribution, while equations (0-1) and (0-5) provide Gaussian approximations essential for analyzing the BECs' state distributions. Equation (0-2) gives an insightful approximate expression for the BEC wavefunction post-interaction. Lastly, equations (0-6) and (0-9) offer a comprehensive.

- The equation (0-3) defines the function $C_{n_c n_d}(\chi)$, capturing the essence of photon statistics in the interplay between light and BECs. This function is crucial in understanding the behavior of the system at different interaction scales.
- Equation (0-4) provides an approximation of the photon probability. This approximation is particularly insightful for analyzing the likely outcomes in photon measurement, revealing how the system's behavior shifts under various conditions.
- The cosine power approximation in (0-1) reflects how the interaction time influences the state of the system. It bridges the gap between theoretical predictions and practical outcomes, especially in short interaction time regimes.
- The binomial approximation given by (0-5) simplifies our understanding of the BEC's state distribution. It's a mathematical tool that brings clarity to the complex quantum states involved.
- Equation (0-2) gives an approximate expression for the BEC wavefunction. This is central to grasping the resultant state post-interaction, laying the groundwork for further explorations into the quantum characteristics of the system.
- Finally, (0-16) and (0-17) provide criteria for selecting interaction times and the relationship between the intensity of the coherent light ($|\alpha|$) and the number of particles (N). These equations are pivotal in optimizing the experimental setup for desired outcomes.

International Conferences

Paper Published in International Conference on Quantum Technologies ICQT 2019, World Trade Center, 12, Krasnopresnenskaya Naberezhnaya, Moscow, 123610, Russia.

1. S. Mandal, M. Narozniak, C. Radhakrishnan, M. Kondappan, Z. Jiao, X. Jin, and T. Byrnes. An observable based approach to evaluating quantum coherence, *AIP Conference Proceedings*, 2020, AIP Publishing, 2241(1).

Publishers of the author

1. Review of Scientific Instruments, 2024, AIP Publishing, 95(1)
2. Physical Review A, 2023, American Physical Society, 107(4), 042616
3. Physical Review A, 2023, American Physical Society, 107(5), 052604.
4. Physical Review Research, 2020, APS, 2(3), 033504.
5. Physical Review Letters, 2023, American Physical Society, 131(11), 110602.
6. Physical Review A, 2022, American Physical Society, 105(2), 022443
7. Journal of Physics B: Atomic, Molecular and Optical Physics, 2021, IOP Publishing, 54(10), 105502.
8. AIP Conference Proceedings, 2020, AIP Publishing, 2241(1).
9. Grupo de Física Atómica y Molecular, 2020.
10. Physical Review A, 2022, American Physical Society, 106(3), 033314.

11. Journal of East China Normal University (Natural Science), 2022(2), 93.
12. Journal of Physics B: Atomic, Molecular and Optical Physics, 2022, IOP Publishing, 55(19), 195501.